Nuclear Structure Studies At High Angular Momentum

By

ANINDITA KARMAKAR

PHYS05201904009

Saha Institute of Nuclear Physics, Kolkata

A thesis submitted to the

Board of Studies in Physical Sciences

In partial fulfilment of requirements

For the Degree of

DOCTOR OF PHILOSOPHY

of

HOMI BHABHA NATIONAL INSTITUTE

October 21, 2024

Homi Bhabha National Institute[1]

Recommendations of the Viva Voce Committee

As members of the Viva Voce Committee, we certify that we have read the dissertation prepared by **Anindita Karmakar** entitled **Nuclear structure studies at high angular momentum** and recommend that it may be accepted as fulfilling the dissertation requirement for the Degree of Doctor of Philosophy.

Pradip Kr. Roy Date: 21/10/2024

Chair - Prof. Pradip Kr. Roy

Chattopadhyay Date: 21/10/2024

Guide/Convener - Prof. Sukalyan Chattopadhyay

Date: 21/10/2024

Co-Guide - Prof. Gopal Mukherjee

Anjali Mukherjee Date: 21/10/24

Member 1 - Prof. Anjali Mukherjee

Subir Sarkar Date: 21/10/2024

Member 2 - Prof. Subir Sarkar

G. Gangopadhyay Date: 21/10/2024

Member 3 - Prof. Gautam Gangopadhyay

Vandana Date: 21/10/2024

External Examiner - Prof. Vandana Nanal

Final approval and acceptance of this dissertation are contingent upon the candidate's submission of the final copies to HBNI.

I hereby certify that I have read this dissertation prepared under my direction and recommend that it may be accepted as fulfilling the dissertation requirement.

Date: 21/10/2024 Guide: Chattopadhyay

Place: KOLKATA Prof. Sukalyan Chattopadhyay

[1]This page is to be included only for final submission after successful completion of viva voce.

STATEMENT BY AUTHOR

This dissertation has been submitted in partial fulfilment of requirements for an advanced degree at Homi Bhabha National Institute (HBNI) and is deposited in the Library to be made available to borrowers under the rules of the HBNI.

Brief quotations from this dissertation are allowable without special permission, provided that accurate acknowledgement of the source is made. Requests for permission for extended quotation from or reproduction of this manuscript in whole or in part may be granted by the Competent Authority of HBNI when in his or her judgment the proposed use of the material is in the interests of scholarship. In all other instances, however, permission must be obtained from the author.

Anindita Karmakar

DECLARATION

I, hereby declare that the investigation presented in the thesis has been carried out by me. The work is original and has not been submitted earlier as a whole or in part for a degree/diploma at this or any other Institution / University.

Anindita Karmakar

List of Publications arising from the thesis

Journal

1. Possibility of stable octupole deformation in ^{100}Ru by **A. Karmakar**, P. Datta, Soumik Bhattacharya, Shabir Dar, S. Bhattacharyya, G. Mukherjee, H. Pai, S. Basu, S. Nandi, S. S. Nayak, Sneha Das, R. Raut, S. S. Ghugre, Sajad Ali, R. Banik, W. Shaikh, and S. Chattopadhyay arXiv:2306.07670 [nucl-ex] Phys. Rev. C **109**, 054312 (2024)

2. First identification of a doublet wobbling excitation mode in ^{105}Pd by A. Karmakar, P. Datta, N. Rather, S. Pal, R. Palit, A. Goswami, G.H. Bhat, J. A. Sheikh, S. Jehangir, S. Chattopadhyay and S. Frauendorf (arXiv:2403.08235 [nucl-ex]) (Under review)

3. Octupole deformation in ^{100}Ru **A. Karmakar**, Nazira Nazir, P. Datta, G.H. Bhat, J. A. Sheikh, S. Jehangir, S. S. Nayak, Soumik Bhattacharya, Suchorita Paul, Snigdha Pal, S. Bhattacharyya, G. Mukherjee, S. Basu, S. Chakraborty, S. Panwar, Pankaj K. Giri, R. Raut, S. S. Ghugre, R. Palit, S. Ali, W. Shaikh, S. Chattopadhyay and S. Frauendorf (Under review)

4. Observation of transition from wobbling mode to principle axis rotation in ^{101}Ru **A. Karmakar**, P. Datta, G.H. Bhat, J. A. Sheikh, S. Jehangir, S. S. Nayak, Soumik Bhattacharya, Suchorita Paul, Snigdha Pal, S. Bhattacharyya, G. Mukherjee, S. Basu, S. Chakraborty, S. Panwar, Pankaj K. Giri, R. Raut, S. S. Ghugre, R. Palit, S. Ali, W. Shaikh, S. Chattopadhyay and S. Frauendorf (Manuscript under preparation)

Chapters in books and lectures notes N. A.

Conferences

1. Coexistence of γ and octupole band in ^{100}Ru, **A. Karmakar**, P. Datta, H. Pai, S. Ali, W. Shaikh, S. Bhattacharya, G. Mukherjee, S. Dar, S. Basu, S. Nandi, S.S. Nayak, Soumik Bhattacharya, S. Das, R. Raut, S.S. Ghugre, R. Banik, B. Das, S. Chattopadhyay Proc. of DAE- BRNS Symp. on Nucl. Phys., Vol. 65, page 40 (2021)

2. First observation of multiple E3 transitions in ^{100}Ru, **A. Karmakar**, P. Datta, S. Ali, W. Shaikh, S. Bhattacharya, G. Mukherjee, S. Dar, S. Basu, S. Nandi, S. S. Nayak, Soumik Bhattacharya, S. Das, R. Raut, S. S. Ghugre, R. Banik, G. Gangopadhyay, S. Chattopadhyay Proc. of DAE- BRNS Symp. on Nucl. Phys., Vol. 66, page 62 (2022)

3. Observation of signature partner bands in ^{105}Pd with one wobbling phonon configuration **A. Karmakar**, P. Datta, N. Rather, S. Pal, R. Palit and S. Chattopadhyay Proc. of DAE- BRNS Symp. on Nucl. Phys., Vol. 67, page 51 (2023)

Others

Jounral

1. Revealing new structures in odd–odd ^{54}Mn nucleus by S. Basu, G. Mukherjee, S. Nandi, S. S. Nayak, S. Bhattacharyya, Soumik Bhattacharya, Shabir Dar, Sneha Das, S. Basak, D. Kumar, D. Paul, K. Banerjee, Pratap Roy, S. Manna, Samir Kundu, T. K. Rana, R. Pandey, S. Chatterjee, R. Raut, S. S. Ghugre, S. Samanta, R. Banik, **A. Karmakar**, S. Chattopadhyay, S. Das Gupta, P. Pallav, S. Rajbanshi, S. Ali and H. Pai Eur Phys. Jour. A 59, 229 (2023)

2. Nuclear Structure and Decay Data for A = 222 Isobars by Balraj Singh, M.S. Basunia, Jun Chen, P. Dimitriou, B.M.S. Amro, S. Basu, S. Das, Diwanshu, **A. Karmakar**, M.J. Lazaric, S.R. Leblond, S.S. Nayak, C. Ngwetsheni, A. Rathi, P.S. Rawat, B. Rohila, V. Vallet Nuclear Data Sheets 192, 315-421(2023)

3. Coexistence of low-K oblate and high-K prolate $g_{9/2}$ proton-hole bands in ^{115}Sb by Shabir Dar, S. Bhattacharyya, S. Chakraborty, S. Jehangir, Soumik Bhattacharya, G.H. Bhat, J.A. Sheikh, N. Rather, S.S. Nayak, Sneha Das, S. Basu, G. Mukherjee, S. Nandi, R. Banik, S. Basak, C. Bhattacharya, S. Chattopadhyay, S. Das Gupta, **A. Karmakar**, S.S. Ghugre, R. Raut Phys. Lett. B 851, 138565 (2024)

Conferences

1. Deformed nuclear shapes around N, Z = 28 in A = 50 - 60 region, S. Basu, G. Mukherjee, S. Nandi, S.S. Nayak, S. Bhattacharyya, Soumik Bhattacharya, Shabir Dar, Sneha Das, S. Basak, D. Kumar, D. Paul, K. Banerjee, Pratap Roy, S. Manna, Samir Kundu, T.K. Rana, T. Bhattacharjee, R. Pandey, S. Samanta, S. Chatterjee, R. Raut, S.S. Ghugre, H. Pai, **A. Karmakar**, S Chattopadhyay, S. Das Gupta, P. Pallav, R. Banik, S. Rajbanshi, S. Ali, Q.B. Chen, C. Bhattacharya Proc. of DAE-BRNS Symp. on Nucl. Phys., Vol. 65, page 46 (2021)

2. First observation of the πg7/2 band in ^{115}Sb, Shabir Dar, S. Bhattacharyya, Soumik Bhattacharya, Sneha Das, S. Basu, G. Mukherjee, S. Nandi, S. S. Nayak, R. Banik, S. Chakraborty, S. Das Gupta, S. Basak, T. Bhattacharjee, C. Bhattacharya, S. Chattopadhyay, **A. Karmakar**, S. S. Ghugre, D. Kumar, D. Mondal, S. Mukhopadhyay, D. Pandit, S. Rajbanshi, R. Raut Proc. of DAE- BRNS Symp. on Nucl. Phys., Vol. 65, page 52 (2021)

3. Observation of the oblate $g_{9/2}$ proton-hole band in ^{115}Sb, Shabir Dar, S. Bhattacharyya, Soumik Bhattacharya, S. Chakraborty, Sneha Das, S. Basu, G. Mukherjee, S. Nandi, S. S. Nayak, R. Banik, S. Basak, C. Bhattacharya, S. Chattopadhyay, S. Das Gupta, **A. Karmakar**, S. S. Ghugre, D. Kumar, D. Mondal, S. Mukhopadhyay, D. Pandit, S. Rajbanshi, R. Raut Proc. of DAE- BRNS Symp. on Nucl. Phys., Vol. 66, page 112 (2022)

4. Rotational band structure in odd A ^{55}Mn, S. Basu, G. Mukherjee, S. Nandi, S. S.

Nayak, S. Bhattacharyya, Soumik Bhattacharya, Shabir Dar, Sneha Das, S. Basak, D. Kumar, D. Paul, K. Banerjee, Pratap Roy, S. Manna, Samir Kundu, T. K. Rana, T. Bhattacharjee, R. Pandey, S. Samanta, S. Chatterjee, R. Raut, S. S. Ghugre, H. Pai, **A. Karmakar**, S. Chattopadhyay, S. Das Gupta, P. Pallav, R. Banik, S. Rajbanshi, S. Ali, Q. B. Chen Proc. of DAE- BRNS Symp. on Nucl. Phys., Vol. 66, page 140 (2022)

5. Lifetime measurements of g9/2 positive parity band in ^{57}Fe, S. Basu, G. Mukherjee, S. Nandi, S. S. Nayak, S. Bhattacharyya, Soumik Bhattacharya, Shabir Dar, Sneha Das, S. Basak, D. Kumar, D. Paul, K. Banerjee, Pratap Roy, S. Manna, Samir Kundu, T. K. Rana, R. Pandey, S. Samanta, S. Chatterjee, R. Raut, S. S. Ghugre, H. Pai, **A. Karmakar**, S. Chattopadhyay, S. Das Gupta, P. Pallav, R. Banik, S. Rajbanshi, S. Ali, Q. B. Chen, C. Bhattacharya Proc. of DAE- BRNS Sym Nucl.Phys., Vol. 66, page 156 (2022)

6. Level scheme of ^{128}Cs below the isomeric $I^{\pi} = (9^{+})$ state S. Chakraborty, S. Bhattacharyya, G. Mukherjee, S.S. Nayak, Shabir Dar, Sneha Das, S. Basu, Suchorita Paul, Snigdha Pal, S. Basak, A. Pal, D. Kumar, Soumik Bhattacharya, Debasish Mondal, R. Raut, Pankaj K. Giri, A. Sharma, S.S. Ghugre, C. Majumder, R. Banik, S.Das Gupta, **A. Karmakar**, J. Dey, U. Dutta, S. Chattopadhyay, S. Ganguly, S. Rajbanshi DAE- BRNS Symp. on Nucl. Phys., Vol. 67, page 39 (2023)

7. Newly observed M1 band in odd-A ^{57}Fe S. Basu, G. Mukherjee, S. Nandi, S.S. Nayak, S. Bhattacharyya, Soumik Bhattacharya, S. Dar, Sneha Das, S. Basak, D. Kumar, D. Paul, K. Banerjee, Pratap Roy, S. Manna, Samir Kundu, T.K. Rana, R. Pandey, S. Samanta, S. Chatterjee, R. Raut, S.S. Ghugre, H. Pai, **A. Karmakar**, S. Chattopadhyay, S. Das Gupta, P. Pallav, R. Banik, S. Rajbanshi, S. Ali DAE- BRNS Symp. on Nucl. Phys., Vol. 67, page 101 (2023)

8. In-beam spectroscopic study of ^{209}At Sneha Das, S. Bhattacharyya, S. Chakraborty, S.S. Nayak, Soumik Bhattacharya, Shabir Dar, R. Banik, S. Ali, S. Basak, S. Basu,

S. Chatterjee, S. Chattopadhyay, S.Das Gupta, S.S. Ghugre, **A. Karmakar**, D. Kumar, Debasish Mondal, G. Mukherjee, S. Mukhopadhyay, S. Nandi, P. Pallav, Deepak Pandit, S. Rajbanshi, R. Raut, S. Samanta DAE-BRNS Symp. on Nucl. Phys., Vol. 67, page 123 (2023)

9. Observation of signature partner of $i_{13/2}$ band in ^{199}Hg Soumik Bhattacharya, S. Bhattacharyya, S. Das Gupta, R. Banik, G. Mukherjee, S. Chakraborty, S.S. Nayak, Shabir Dar, A. Dhal, S. Nandi, Md. A. Asgar, R. Raut, S.S. Ghugre, S.K. Das, S. Chatterjee, S. Samanta, Sajad Ali, S. Chattopadhyay, **A. Karmakar**, D. Kumar, S. Basu, S. Basak, S. Mukhopadhyay, P. Pallav, Debasish Mondal, S.S. Alam, T. Bhattacharjee, A. Saha, S. Rajbanshi DAE- BRNS Symp. on Nucl. Phys., Vol. 67, page 127 (2023)

Anindita Karmakar

To my grandfather...

ACKNOWLEDGEMENTS

If we do meet again, why, we shall smile; If not, why then, this parting was well made.

Like any good thing, the PhD life also comes to an end. But I am thankful to encounter many great people who made the navigation quite enjoyable.

First of all, I would like to express my sincere gratitude to my supervisor Prof. Sukalyan Chattopadhyay for inspiring me to find interest in Nuclear Physics. I am grateful that he held his patience through many mistakes and lack of understanding on my part. As I had no seniors in my research area during my tenure, he was always one call away for any physics discussion, night and day. I feel fortunate to have him as my guide. Next, I would convey my gratitude to Dr. Pradip Datta who made me learn and enjoy the analysis process. The first thing he ever said to me was "In nuclear physics, you first measure energy precisely, the Rest will follow". How true these words are for a spectroscopist. This thesis exists because both Pradip Da and Sukalyan Sir had kept their faith and physics motivation by my side. I thank all of my doctoral committee members Dr. Gopal Mukherjee, Prof. Anjali Mukhejee, Prof. Subir Sarkar, Prof. Pradip Kr. Roy and Prof. Gautam Gangopadhyay for their valuable suggestion throughout my tenure. As I am part of the INGA collaboration, I have come across a lot of inspiring people for both experimental and theoretical purposes. I would like to thank Dr. Sarmistha Bhattachharya, Dr. Gowhar Bhat, Dr. Javed Sheikh, Prof. Rudrajyoti Palit, Prof. Stefan Frauendorf, Ms Nazira Nazir and all the other members of my collaboration. Thanks to my long-distance seniors Biswarup Da and Sajad Da who did their best to guide me through some really difficult times.

I am a typical ambivert in nature. I take time to know people, but once I do, the bonds remain. I would try to mention all the people close to my heart and ask for sincere apologies if I mistakenly forgot to mention any names.

Firstly, I would like to pay my tributes to Late Sunil Sir. You introduced me to the world of mathematics in class 5 and I have never stopped to be mesmerised by that. From my

school days, I have come across some wonderful teachers like Camelia Di, Jagadish Sir, Tapas Sir (both bio and chemistry) and Niladri Sir. Not only did they make me curious about their respective subjects, but they also ignited a tiny flame within me that one day I could teach someone just like they taught me. You all are my inspirations. My school life also gave me friends like Aindrila, Nilanjana, Sayeri, Sata, Moitrayanidi and Dibyo. I cherish your presence in my life.

I owe a lot to my college and my tuition batch. I would like to thank Sanoar Sir for making me fall in love with mathematical physics and quantum mechanics, AMR Sir for wonderful electronics lessons and SB Sir for introducing me to the world of coding at a time when I was unsure if I did the right thing by choosing physics. In that time, I have made some wonderful bonds with Debanjali, Partha, Shayam, Reshma, Imran, Asmita, Puspita, Ayan, Manojit, Medha, Geetu and many other young enthusiasts like me. I got my brothers from another mother, Rupam and Khursid; and my beloved juniors Rajeshree and Ayesha. To Debanjali and Shayam, we may have parted ways, but the time we had together will be part of my core memories.

The initial days of IIT Roorkee would have been impossible to overcome without Srishti, Debjani, Divya, Rupak Da and Nataraj Sir. Thank you for being there for me when I myself could not.

The list of names of people from SINP is truly never-ending. I am very very fortunate to have Sweta, Pritam Da, Gourab Da, Promita Di, Suman, Debu Da, Wadut Da, Laltu and Sanjeev. 249 is something I will cherish forever. Nothing can replace those impromptu plans for food, discussion on literally everything and the laughter and joys. I am not part of CMS like every other person in 249, but never once I have felt out of place for that. Koustav, Sweta, Saikat, Soumya, Habib, Soumen, Suman and all my other batchmates of Post MSC 2019 will forever be very close to my heart. I will miss those impromptu house parties and the plans in progress for a "batch tour outside Digha" that will definitely happen, someday. Kousik da, you truly are our Hagrid. I look forward to our dinner plan. I would like to thank Nilanjan Da, Subhashish Da, Pappu Da, Sagar Da, Lipi Di, Arindam

Da, Sudam Da and Pradip Da (accounts) for helping me through all kinds of work at SINP. I thank Hari Da, Saikat Da, Subhoraj Da, Shubham Da, Pooja Di, Sabyasachi Da, Arka, Saikat Ghosh and my beloved seniors and juniors for making such wonderful acquaintances. Last but not least, I would like to thank Munmun. Although we met at IIT Roorkee, we truly have made some great memories in my SINP days.

My RFA days take a huge place in my heart. I thank Saikat for his constant help and support during those days. I am grateful to all SINP employees and fellows who assisted me in improving the RFA community.

I have also worked on some experiments at VECC. Among the many people I met there, I would like to thank Shabir Da, Sneha Di, Soumen Da, Saikat Da, Soumik Da, Devesh Da, Suchorita and Shefali Di. Snigdha, Satya and Pankaj Da:: let's meet and have one of those never-ending conversations at BF ground. Shall we?

Now, I would like to mention my three gems. Neha, Koustav and Samarpita. I sincerely do not know how will I endure the hardship of life without you three being by my side. Thank you for everything. Neha and Sampu, thank you for accepting me not only as a friend but as a sister. It is for you two I have Dipudi, Babin and Gopu who are like my family.

I would like to express my sincere gratitude to my close friends and relatives. I have never been very close to my family, but I am still glad that I got to be a part of your circle. Masi, I know you would have been immensely proud to see this day. Tinni, Susmidi and I miss your musur dal and lote maccher jhuri, and we all miss you.

And lastly, I mention the two most important people of my life. Baba, no matter how often we get into misunderstandings, I owe it to you for my personality of mixing with people easily. Ma, I may not have been the best daughter in the world, but you are the **best mother** one can get. I love you both. You are the reason I could achieve anything in life without any pressure.

Contents

List of Figures **xvi**

List of Tables **xxvi**

1 Introduction **9**

2 Angular Momentum Generation Mechanisms **14**

2.1 Nuclei at shell closure 15

2.2 Deformation and Nilsson Model 17

2.2.1 Shape parameterisation 18

2.2.2 Nilsson Model 19

2.3 Angular Momentum Generation 21

2.3.1 Non Collective or single particle excitation 21

2.3.2 Collective modes of excitation 26

2.4 The origin of exotic shapes 37

2.4.1 Reflection Asymmetry 38

2.4.2 Axial asymmetry 42

2.4.3 Interplay between single-particle and collective contributions . . . 47

3 Experimental Techniques **54**

3.1 Fusion-evaporation reaction 55

3.2 Interactions of γ-ray with matter 55

3.3 Experimental set-up 58

3.3.1 Clover Detectors 59

3.3.2 Detector Geometry at INGA 60
3.3.3 Target 62
3.3.4 Data Acquisition 64
3.4 Data Analysis 65
3.4.1 Calibration 65
3.4.2 Coincidence technique between the γ transitions 68
3.4.3 Identification of Spin and Parity of the excited states 69
3.4.4 Level Lifetime Measurements 81
3.4.5 Transition probability 83

4 Spectroscopic Studies in ^{100}Ru **87**
4.1 Introduction 87
4.2 Experimental details 88
4.3 Results 90
4.4 Discussion 98
4.4.1 Octupole and strongly couple bands 98
4.4.2 Band4 and Band5 - the signature partner bands 110
4.4.3 Band6 and Band7 - the γ - soft bands 111

5 Spectroscopic Studies in ^{98}Mo **119**
5.1 Experimental details 119
5.2 Results 120
5.3 Discussion 126

6 Spectroscopic Studies in ^{105}Pd **132**
6.1 Experimental Results 135
6.2 Discussion 142

7 Spectroscopic Studies in ^{101}Ru **153**
7.1 Experimental details and results 153
7.2 Discussion of the Results 164

8 Summary **174**

List of Figures

2.1 The Shell model states for a basic harmonic oscillator potential, a simple harmonic potential with l^2, and spin-orbit interaction terms are illustrated (Bottom) Schematic diagram of the two shell model potentials: the S. H. O. potential and the modified harmonic oscillator, which approximates the influence of the l^2 term. The figure is adapted from Ref [14]. 15

2.2 The deformation parameters β and γ for various nuclear shapes are displayed according to the Lund convention [14]. 17

2.3 Pictorial representation of an axially symmetric deformed nucleus and the relevant quantum numbers proposed by Nilsson. 19

2.4 The effect of the deformed nuclear potential and rotation on the $h_{11/2}$ shell model state. The deformation ϵ is related to the β_2 deformation as $\epsilon = 0.946\beta_2$ in the limit of small deformation. 20

2.5 The excited states generated via collective rotation in deformed nuclei ^{158}Er, (left panel) and non-collective single-particle excitation in nearly-spherical nuclei ^{146}Gd (right panel) [19, 20] 21

2.6 Experimental observations showing a regular band-like structure of M1 transitions and the gated spectrum for ^{199}Pb [20, 21] 23

2.7 Illustration of the spin-coupling scheme for the shears mechanism. Figure courtesy: Ref. [24] 23

2.8 The M1 transition probabilities, B(M1), for intraband transitions in isotopes $^{193-199}$Pb, are presented as a function of the spin of the initial state. The figure is taken from Ref. [28]. 25

2.9 The left panel shows the decreasing trend of experimental B(E2) values as a function spin I along with the I vs. ω plot in ^{104}Pd. The lines represent the numerical values obtained from the theoretical calculations. The right panel shows how the gradual closing of the shears angle generates the spin states [31]. 26

2.10 The nuclear potential for (a) dynamic (vibration) and (b) stable deformation. Here the minima of the potential V represents the deformation for which the shape is stable. 27

2.11 A pictorial representation of the various nuclear vibration modes observed in nuclear structure studies [14]. 28

2.12 Alignment of the quasi-particle angular momentum for the nucleus's (a) prolate and (b) oblate core shapes, respectively. The projection of the quasi-particle angular momentum along the symmetry axis ($\hat{z}$) is represented by Ω. [20] 29

2.13 The orientation of the particle angular momentum with respect to the core in the (a) weak and (b) strong coupling limits. 29

2.14 The quasiparticle energies (routhians) 56 neutrons of ^{100}Ru considering β_2 = 0.2 and γ = 0.0 plotted as a function of rotational frequency. The spins and signatures of the routhians are indicated following the prescription: (-, +1/2): red dashed, (-, -1/2): red dot-dashed, (+, +1/2): green solid, (+, -1/2): green dots. 33

2.15 The pictorial representation of the nuclear potential energy as a function of octupole deformation. The figure demonstrates how the barrier height between the two minima increases with the decrease of pairing interactions. 39

2.16 Experimental level schemes of dynamic octupole deformed nucleus showing only unidirectional E1 transitions decaying from negative to positive parity partner [43]. 39

2.17 The level schemes for a stable octupole deformed nuclei ^{222}Th, showing the interleaving of the E1 transitions [44]. 40

2.18 Parity splitting (keV), S(J) and the ratio of rotational frequency plotted as a function of spin (I) for ^{226}Th. At I = 15$\hbar$, also denoted at I_c, S(J) as well as parity splitting nearly becomes zero, which signifies the onset of strong octupole correlations. 42

2.19 Pictorial representation of a simple wobbler where l, m, and s correspond to the long, medium, and short axes. I is the total angular momentum of nuclei, which processes about the medium axis. 43

2.20 Pictorial representation of a longitudinal (left) and a transverse (right) wobbler. j, R and I are the odd particle, rotor and total angular momenta, respectively. 44

2.21 Schematic representation of left and right handed chiral systems for a triaxial odd-odd nucleus. R, j_ν, j_π and J are the rotor, neutron, proton and total angular momentum, respectively. 45

2.22 Partial level schemes showing chiral doublet bands in N = 73 isotones [50]. 46

2.23 The measured I(ω) plot (shown in (a)) and B(E2) rates (shown in (b)) in ^{110}Cd. The calculated B(E2) values for AMR + rotation and pure AMR are shown in panel (b) by the solid and dotted lines, respectively [53]. . . 47

2.24 The partial level scheme of ^{144}Ba illustrating both symmetric and reflection asymmetric band structures. Figure taken from Ref. [56]. 48

3.1 Schematic diagram depicting the mechanism of fusion evaporation reaction. 56

3.2 The decay scheme of a compound nucleus. 57

3.3 The three mechanisms through which a γ-ray interacts with matter are illustrated as follows: (a) Photoelectric Effect; (b) Compton Scattering; and (c) Pair Production. 58

3.4 Schematic diagram of a typical clover detector. The four crystals have been depicted in distinct colours. 61

3.5 Experimental setup of VECC - INGA (left panel) and TIFR - INGA (right panel). 62

3.6 The mounting of the self - supporting ^{100}Mo target used in the first experiment at VECC 63

3.7 On panel (a): before gain matching and energy calibration, On panel (b): after the said processes. The data were acquired for the ^{152}Eu radioactive source during the VECC-INGA campaign 2020. 66

3.8 The relative efficiency of clover detectors in the VECC-INGA as a function of γ-ray energy as obtained using the radioactive source ^{152}Eu. 68

3.9 Example of a typical level scheme constructed using coincidence method. 69

3.10 Geometry of angular correlation where angles θ_1 and θ_2 represent respective angles of the two detectors with beam axis. ϕ represents the angle between the two planes containing the detectors. 70

3.11 Theoretical angular distributions of γ-rays with different multipolarities and mixing ratios. 72

3.12 Angular distribution fit of 991 keV γ-ray in ^{105}Pd from the dataset of TIFR-INGA. Here, the angle is plotted up to 90° as the plot is symmetric around $\theta = 90°$. 74

3.13 The contour plots for different combinations of initial and final levels as a function of mixing ratio (δ) with R_{DCO} in one axis and polarization in another. The black point indicates the experimental value for the 888 keV transition in ^{100}Ru which matches with the contour for $6^- \rightarrow 6^+$ transition. 75

3.14 A schematic representation of the angles and planes relevant to the linear polarization measurement of a γ-ray [12]. 76

3.15 The values of the geometrical asymmetry correction factor a(E_γ) for various energies of ^{152}Eu source. The data points are fitted with a linear function, represented by the solid line 78

3.16 A typical gated spectrum for an electric type (left panel) and a magnetic type (right panel) transition. 79

3.17 The energy-dependent polarization sensitivity of the Clover detectors used in the experiments. 80

3.18 The experimental lineshapes of a γ transition depopulating from a state with a sub-picosecond lifetime are schematically represented in (a) the shape at the backward angle (-θ) detector, (b) the unshifted peak of energy E_0 at the 90° detector, and (c) the shape at the forward angle (+θ) detector, as the recoil velocity (β) decreases continuously to zero. 81

3.19 Typical experimental line-shapes and the corresponding fits produced using Wells and Johnson's LINESHAPE algorithm. The background is represented by the colour magenta, the contamination peak(s) by green, the line shape fit by blue, and the overall experimental data fit by red. 82

4.1 The partial level scheme of ^{100}Ru established from the present work. Seven inter-leaved transitions between Band2 and Band3 have been observed in the present work. The level and transition energies are expressed in keV. Gamma-ray energies have been rounded off to their closest integer. The thicknesses of the arrows are proportional to the relative intensities of the de-exciting γ-rays. The transitions marked in red are newly observed in the present data set. The high spin levels beyond I = 20$\hbar$ were reported in Ref. [19] but not observed in the present experiment. 89

4.2 The γ-ray spectrum in coincidence with the 552- keV ($9^- \rightarrow 7^-$) transition. The gamma energies have been rounded off to the nearest integer. The higher energy section of the gated spectrum is shown in the inset. The γ rays marked with * are from other excited levels of ^{100}Ru [25], which are not part of the partial level scheme shown in Fig. 4.1. 91

4.3 The measured values of Ratio of Directional Correlations from Oriented states (R_{DCO}) and integrated Polarization from the Directional Correlation of Oriented states (iPDCO) for different γ transitions of ^{100}Ru. The vertical lines represent the calculated R_{DCO} values of 0.65 and 1.0 for pure ΔI = 1 and ΔI = 2 transitions, respectively, in a stretched E2 gate. 97

4.4 Coincident γ spectra observed with the detectors of the 90° ring. The E1 transitions connecting Band2 and Band3 are marked by the dotted line. Each E1 transition is shown in two gamma-gated spectra. The numbers in the rectangular box represent the γ-ray energy of the gating transitions. The gamma energies have been rounded off to their closest integer. 99

4.5 Ratios of the inter-band E1 and the intra-band E2 transition rates from the excited levels of ^{100}Ru as a function of spin, I. The lower value of the ratio for the 9^- level corresponds to Band4. The values for I $\leq 9\hbar$ corresponds to $\Delta\nu$ =2 E1 transitions between Band3 and Band1, while for the higher spins, $\Delta\nu$ = 0 E1 transitions between Band3 and Band4 are considered. . . 101

4.6 Moment of inertia $J^{(1)}$ and parity splitting index S(I) for the positive (black dots) and the negative parity (red diamonds) partner bands of ^{226}Ra, ^{144}Ba and ^{100}Ru are plotted on the left and right panels as a function of rotational frequency (ω) and angular momentum I, respectively. 102

4.7 The line-shape fits for 1001 keV of Band2, 1036 keV of Band3 and 986 keV of Band5 at 40°, 90° and 157° to the beam direction. The fitted Doppler broadened line shapes are drawn in blue lines while the contaminant peaks are shown in green lines. The result of the fit to the experimental data is shown in red lines. 104

4.8 Intrinsic quadrupole moment (Q_0) values as a function of spin for Band2 and Band3. The solid line represents the values from TPSM calculations. 105

4.9 Intrinsic quadrupole moment (Q_0) values as a function of spin for Band4 and Band5. The solid line represents the values from the TPSM calculations. 106

4.10 Level energies minus rotor contribution values and angular momentum as a function of spin (I) and rotational frequency (ω), respectively for positive parity Band1 and Band2 (black circles) and negative parity Band3 (red diamond). The solid line represents the values from TPSM calculations. 107

4.11 B(E1) values vs spin for Band2 and Band3. The solid line represents theoretical calculations using the TPSM framework. 107

4.12 Energy staggering S(I) for the negative parity partners (black square) and the positive parity γ (red diamonds) partner bands of ^{100}Ru are plotted as a function of angular momentum I. 111

5.1 The partial level scheme of ^{98}Mo established from the present work. The level and transition energies are expressed in keV. The thicknesses of the arrows are proportional to the relative intensities of the de-exciting γ-rays. The transitions marked in red are newly observed in the present data set. . 120

5.2 Gated spectrum of ^{98}Mo using 787.2 keV gate. The transitions marked in red are newly placed from the present experiment. However, those marked in green, are transitions from ^{98}Mo but not part of the partial level scheme. Transition energies are rounded off to the nearest integer value. . 121

5.3 Spectrum for calculating R_{DCO} values showing four possible combinations of multipolarity of gating and observed transition. Panel (a), (b), (c) and (d) represent dipole transition (D) gated with the quadrupole transition (Q) gate, D in D gate, Q in Q gate and Q in D gate, respectively. The red and black lines represent the counts corresponding to 125° and 90°, respectively. 122

5.4 Typical polarisation spectrum for one magnetic type (left panel) and one electric type (right panel) transition of ^{98}Mo. 123

5.5 Contour plots of polarisation vs R_{DCO} as a function of varying mixing ratio for four different transitions. 124

5.6 The moment of inertia $J^{(1)}$ as a function of rotational frequency (ω) for the negative parity partner of the alternate parity bands in^{98}Mo (black diamonds) and ^{100}Ru (red diamonds). 128

5.7 The ratio of the inter-band E1 and the intra-band E2 transition rates from the low spin excited levels of ^{98}Mo and ^{100}Ru as a function of spin, I. . . . 129

5.8 The parity splitting index S(I) as a function of angular momentum for the positive (black dots) and negative parity (red diamonds) partner bands of ^{98}Mo, ^{100}Ru, and ^{144}Ba. 130

6.1 The partial level scheme of ^{105}Pd established from the present work. The level and transition energies are expressed in keV and have been rounded off to their nearest integer. The levels and transitions marked in Black were reported in [19] while those marked in Blue were reported [20] by the same group. Our data confirms all these levels and transitions and we have added three more transitions, which are marked in red. The spin and parities of Band 2 have been adapted from Ref. [19] 134

6.2 The gamma spectra in coincidence with (a) 1046 keV ($31/2^- \rightarrow 27/2^-$) keV and (b) 1006 ($27/2^- \rightarrow 23/2^-$) keV transitions of Band 4. The newly placed gamma transitions from Band 4 to Band 2 have been marked in red. The transitions marked in green belong to ^{102}Ru. This contamination is due to the presence of 1047 keV ($15^- \rightarrow 13^-$) and 1005 keV ($14^- \rightarrow 12^-$) transitions in ^{102}Ru. 135

6.3 A typical polarisation spectrum for an electric (left) and a mixed (right) transition. 138

6.4 Values of the DCO ratios (R_{DCO}) and linear polarization (P) of the ΔI = 1 transitions that decay from the negative parity wobbling band to the positive parity ground state band, computed (solid line) and experimental (symbol) for various mixing ratios (δ). 139

6.5 The χ^2 minimization plots for (a) 991 keV (b) 1034 keV (c) 994 keV and (d) 603 keV. The horizontal lines correspond to the +1 of the minima value for determining the uncertainties. For the first three transitions, the lower minima correspond to the higher δ values. However, for 603 keV, the lower delta value is more preferable. 141

6.6 Variation of the calculated R_{DCO} as a function of mixing ratio (δ) for the $\Delta I = 1$ transitions from Band 3 to Band 1 ((a) 991, (b) 1034 keV) and from Band 4 to Band 2 ((c) 300, (b) 254 keV). The horizontal lines correspond to the R_{DCO} values at 40° along with their uncertainties. 141

6.7 The ratio of the rates of the out-band $\Delta I = 1$ transitions and the in-band E2 transitions of ^{105}Pd are plotted as a function of spin, I. The E2 and M1 rates for the $\Delta I = 1$ transitions have been estimated using the evaluated values of the mixing ratios (Table 6.1) and are shown on the left and right panels, respectively. The values for the Band 3 → Band 1 transitions are shown in (a) and (d), the values for Band 4 → Band 2 transitions in (b) and (e), and the values for the Band 3 → 4 transition in (c) and (f). Fig. 6.7(f) also includes the value for the Band 2 → Band 1 transition (shown in green), assuming the E2 mixing to be negligible. In Fig. 6.7(c), the upper bounds correspond to the upper limit of the uncertainties of the mixing ratio values given in Table 6.1. The dotted line on each panel represents the calculated values from TPSM. 142

6.8 The ratio of the rates of the out-band $\Delta I = 0$ and $\Delta I = 2$ transitions from Band 4 to Band 1, Band 2 to Band 3 and the in-band E2 transition of Band 4 as a function of spin, I. The M1 and E2 rates have been estimated using the evaluated values of the mixing ratios (Table. 6.1) and plotted in (a) and (b), respectively. The dotted line on each panel represents the calculated values from TPSM. 143

6.9 Experimental and calculated values from TPSM for the rotational frequency (upper panel) and the level energies minus the rotor contribution (lower panel) as functions of the spin I for Bands 1, 2, 3 and 4. 145

6.10 Energies of the projected K configurations, where the short axis is chosen as the quantization axis 3 to which K refers. The curves are labelled by three quantities: quasiparticle character, K quantum number and energy of the quasiparticle state. For instance, [1,1/2,1.31] designates the one quasineutron state with K= 1/2 having intrinsic energy of 1.31 MeV. . . . 146

6.11 Probabilities of various projected K configurations in the orthonormal basis shown in Fig. 6.10. The curves are labelled by three quantities: quasiparticle character, K quantum number and energy of the quasiparticle state. For instance, [1,1/2,1.31] designates one quasineutron state with K= 1/2 having an intrinsic energy of 1.31 MeV. The symbols and line types agree with Fig. 6.10. 148

7.1 The partial level scheme of ^{101}Ru established from the present work. The level and transition energies are expressed in keV. The thicknesses of the arrows are proportional to the relative intensities of the de-exciting γ-rays. The transitions and levels marked in red are newly observed in the present data set. The high spin levels beyond 39/2 were reported in Ref. [1] but not observed in the present experiment. 154

7.2 γ - γ coincidence spectra with 663.6, 815.4 and 858.7 keV gates in ^{101}Ru. The transitions marked in black, green and blue belong to Bands 1, 2 and 3 respectively, while those marked in magenta are from the other bands of ^{101}Ru, which are not shown in the current level scheme. It may be noted that the 858.7 keV gate has contamination from the strong 861 keV transition ($15/2^+ \rightarrow 11/2^+$) in positive parity sequence of ^{101}Ru. The transitions marked in red are contamination from ^{98}Mo. 155

7.3 γ - γ coincidence spectra with (a) 923.8 and (b) 1138.2 keV gates in ^{101}Ru. The transitions marked in red are newly placed from the present experiment. The transitions marked in green represent previously placed transitions used for confirmation of placements of new transitions. 156

7.4 Experimental (symbol) and calculated (solid line) values of DCO ratios and linear polarization (P) for varying mixing ratios δ for transitions decaying from Band 4 to Band 3. In the top two panels, previously established magnetic dipole (M1) and electric quadrupole (E2) transitions are shown in order to validate the present measurements. 157

7.5 The χ^2 analysis to establish the true minima of the mixing ratio values for the transitions from Band 4 to Band 3. The horizontal lines correspond to the +1 of the minima value for determining the uncertainties. 158

7.6 Variation of the calculated R_{DCO} as a function of mixing ratio (δ) for the $\Delta I = 1$ transitions from Band 4 to Band 3 (i.e. 473.7 keV) and from Band 5 to Band 3 (i.e. 1022.5 keV). The horizontal lines correspond to the R_{DCO} values at 125° along with their uncertainties. 158

7.7 The line-shape fits for 815.4 keV, 671.5 keV of Band 4 and 1138.2 keV, 1214.6 keV transitions of Band 3 at 40°, 90° and 157° to the beam direction. The fitted Doppler broadened line shapes are drawn in blue lines while the contaminant peaks are shown in green lines. The result of the fit to the experimental data is shown in red lines. 162

7.8 Experimental transitional rate ratios of $\Delta I = 1$ transitions decaying from Band 5 (plotted in black) and Band 4 (plotted in red) to Band 3. The ratio for the $29/2^-$ level for Band 5 has been extracted assuming pure M1 character for the 946.6 keV transition. The solid and dashed lines represent calculated values using the Triaxial Projected Shell Model (TPSM) approach. 164

7.9 The variation of the three derived parameters with increasing spin from Bands 3 and 4 of ^{101}Ru namely, aligned angular momentum (panel (a)), wobbling energy (panel (b)) and signature spitting (panel (c)). α is the favoured signature and the arrow in Fig. 7.9(c) marks the signature inversion point in ^{101}Ru. The calculated values from TPSM, shown as solid lines in the figures, show good agreement with the experimental values. . 165

7.10 Experimental and calculated values from TPSM for the rotational frequency (upper panel) and the level energies minus the rotor contribution (lower panel) as functions of the spin I for Bands 1, 2 and 3 166

7.11 Energies of the projected K configurations for the negative parity levels, where the short axis is chosen as the quantization axis, to which the "K" refers. The curves are labelled by three quantities: quasiparticle character, K quantum number and energy of the quasiparticle state. For instance, [1,1/2,1.01] designates the one quasineutron state with K= 1/2 having intrinsic energy 1.01 MeV. 167

7.12 Probabilities of various projected K configurations for the negative parity levels in the orthonormal basis shown in Fig. 7.11. The curves are labelled by three quantities: quasiparticle character, K quantum number and energy of the quasiparticle state for the negative levels. For instance, [1,1/2,1.01] designates one quasineutron state with K= 1/2 having an intrinsic energy of 1.01 MeV. The symbols and line types agree with Fig.7.11. 168

7.13 Ratios of the interband E1 and the intraband E2 transition rates from the excited levels of ^{100}Ru (red circles) and ^{101}Ru (black diamonds) as a function of spin, I. 169

7.14 Variation of the parity splitting between the simplex partners as a function of the spin I. The wobbling energy has been subtracted from the corresponding level energies of Band 4. 170

List of Tables

4.1 The energy (E_γ) and the relative intensity (I_γ) of the γ rays of ^{100}Ru along with the spin and parity of the initial (J^i_π) and the nal (J^f_π) states, measured values of R_{DCO}, Δ_{iPDCO} and the energy of the initial state (E_i) are shown. R_{DCO} values are obtained with gates on pure quadrupole transitions except as noted. The quoted uncertainties in the intensities include statistical and fitting errors only. The systematic error due to the efficiency determination has been estimated to be around 3%. 92

4.2 E1 and E2 branching ratios and the estimated values of B(E1)/B(E2) for the low spin levels of ^{100}Ru. The gamma energies were expressed in MeV for calculating the B(E1)/B(E2) ratios. 95

4.3 E1 and E2 branching ratios and the estimated values of B(E1)/B(E2) for the levels of the alternate parity band. The gamma energies were expressed in MeV for calculating the B(E1)/B(E2) ratios. The evaluated branching ratio is the weighted average of the values obtained from the two independent gates. 96

4.4 M1 and E2 branching ratios and the estimated values of B(M1)/B(E2) for the spin levels of Band4 and 5 of ^{100}Ru. The gamma energies were expressed in MeV to calculate the B(M1)/B(E2) ratios. 98

4.5 M1 and E2 branching ratios and the estimated values of B(M1)/B(E2) for the spin levels of Band6 and 7 of ^{100}Ru. The gamma energies were expressed in MeV to calculate the B(M1)/B(E2) ratios. 98

4.6 The measured lifetimes of electric quadrupole transitions of the ^{100}Ru levels for Band2, Band3, Band4 and Band5. The uncertainties in the lifetime measurements were derived from the behaviour of the χ^2 in the vicinity of the minimum for the simultaneous fit at the three angles. 104

4.7 The measured lifetimes of dipole transitions of the ^{100}Ru levels for Band2 and Band3 along with the values from the two TPSM calculations; one considering only quadrupole-quadrupole and pairing term and the other one additionally considering octupole perturbation. The uncertainties in the lifetime measurements were derived from the behaviour of the χ^2 in the vicinity of the minimum for the simultaneous fit at the three angles. . 108

4.8 The measured lifetimes of dipole transitions of the ^{100}Ru levels for Band4 and Band5. The uncertainties in the lifetime measurements were derived from the behaviour of the χ^2 in the vicinity of the minimum for the simultaneous fit at the three angles. 111

5.1 The energy (E_γ) and the relative intensity (I_γ) of the γ rays of Band2 and Band3 of ^{98}Mo along with the spin and parity of the initial (J^i_π) and the nal (J^f_π) states, measured values of R_{DCO}, Δ_{iPDCO} and the energy of the initial state (E_i) are shown. R_{DCO} values are obtained with gates on pure quadrupole transition except as noted. The quoted uncertainties in the intensities include statistical and fitting errors only. A systematic error due to the efficiency determination has been estimated to be around 4%. . 125

5.2 The E3 and E2 branching ratios and the estimated values of B(E3)/B(E2) for the low spin levels of ^{98}Mo and ^{100}Ru. 127

5.3 The E1 and E2 branching ratios and the estimated values of B(E1)/B(E2) for the low spin levels 128

6.1 Energies, relative intensities, DCO ratios using the detectors at 40° and 157° ring along with the detectors at 90° ring, linear polarizations, mixing ratios and deduced multipolarities of transitions of ^{105}Pd shown in Fig. 6.1. 136

6.2 Transition rates of different bands from TPSM Calculations used for the comparison plots with experimental values. 144

7.1 Energies, relative intensities, DCO ratios using the detectors at 125° ring and the detectors at 90° rings, linear polarization, mixing ratios and deduced multipolarities of transitions of the five reported bands of ^{101}Ru. The quoted uncertainties in the intensities include statistical and fitting errors only. The systematic error due to the efficiency determination has been estimated to be around 4%. 159

7.2 The measured lifetimes of the levels of Bands 1, 3, 4 and 5 of ^{101}Ru and the derived transition rates. 163

SYNOPSIS

The aim of science is to understand the world around us through simple laws of nature. In this endeavour, the microscopic and macroscopic properties of matter are investigated as a function of length, time and energy scale. At the microscopic level, all matter is made up of atoms. Each atom consists of a central nucleus surrounded by a cloud of electrons. The nuclei have neutrons and protons as their constituents, which in turn, are made up of quarks. All these constituents are spin half particles called fermions, while all the mediators of their interactions are integer spin particles named bosons. Hence, all matter can be modelled as a system of interacting fermions. However, such Ab Initio models are enormously complex and numerically intensive and these calculations lead to approximate solutions of the real matter. The more common approach is to perform the exact calculations of an ideal system, which has a close resemblance to the real matter [1]. This approach has been followed to understand the microscopic structure of a nucleus, which is a finite fermionic system whose constituents (protons and neutrons) interact through strong, electromagnetic and weak interactions.

Our national accelerators produce beams with 3-10 MeV/nucleon and in this energy domain, we can probe the macroscopic structure of the nucleus but not the individual nucleon-nucleon interactions. The first significant structural information was found in the 1930s when nuclei with specific nucleon numbers were found to exhibit increased stability i.e. higher binding energy compared to others. These numbers - 2, 8, 20, 28, 50, 82 and 126 - became known as the magic numbers. This information led to the development of the "Nuclear Shell Model" by Jensen and Mayer in 1949 and were awarded the Nobel Prize in 1963. This framework depicts the independent motion of a nucleon in a mean-field potential generated by the other nucleons. The shell model calculations using a harmonic oscillator potential could reproduce the spin and parity of the low spin levels of the nuclei, whose nucleon numbers are close or equal to the magic numbers up to 20. However, to reproduce the higher magic numbers, the inclusion of the spin-orbit interaction term was necessary, which lifts the degeneracy of total angular momentum by an energy difference between the aligned and the anti-aligned state. The next crucial observation was the large enhancement of electric quadrupole (E2) rates for certain transitional (i.e. away from the magic numbers) nuclei, which the spherical mean field potential of the shell model could not predict. In order to reproduce these results, Nils-

son developed the deformed shell model in 1953, where the radius term of the harmonic oscillator potential (later replaced by the more realistic Woods-Saxon potential) was expressed through an expansion in the spherical harmonics. This deformed mean field led to the visualization of permanent and transient deformed shapes like oblate (orange-shaped) or prolate (rugby ball-shaped) nuclei, instead of perfect spheres. The permanent deformation supports collective rotation as the nucleus changes its orientation under rotation, while the transient shape represents collective vibrations around the spherical shape. Subsequently, Bohr, Mottelson and Rainwater developed the unified theory of the structure of the atomic nucleus by incorporating the connection between the particle motion and the collective excitations. They were awarded the Nobel prize in 1975.

The non-spherical shape of a nucleus can be realized by representing

$$R(\theta, \phi) = R_0[1 + \sum_{lm} \alpha_{lm} Y_{lm}]$$

where $R(\theta, \phi)$ is the deformed radius, R_0 is the radius of the spherical nucleus of the same volume and Y_{lm} and α_{lm} are the normalized spherical harmonics and the corresponding expansion coefficients. Here, Y_{10} term i.e. the dipole term, represents the translation of the centre of mass of nuclei and does not contribute to the shape of the nuclei. For the case of axially symmetric deformation (rugby ball for quadrupole deformation and pear shape for both quadrupole and octupole deformation), the $m \neq 0$ coefficients are absent. Thus, for axially symmetric nuclei, the two lowest non-zero coefficients are α_{20} and α_{30}, which can be associated with deformation parameters β_2 and β_3, respectively. Their values can be estimated from the measured electric quadrupole and octupole transition moments, which arise due to the non-spherical charge distribution. For finite values of β_2 and β_3, the Y_{20} and Y_{30} leads to the mixing of the $\Delta l = 2$ and $\Delta l = 3$ orbitals, respectively. The effects of these two types of deformation are different in terms of parity. Parity is the characteristic property of a wave function in quantum mechanics, which is defined by the change in the sign of the corresponding wave function after the sign reversal of the spatial coordinates of the system. The parity of a nucleon orbital is given by $(-1)^l$, which implies that the β_3 term mixes orbitals with different parities and the intrinsic configuration of an octupole nucleus does not have a definite parity. For the case of reflection symmetric nuclei where only Y_{20} term is involved, the levels of the same parity are mixed and hence the parity remains a good quantum number. On the other hand, the incorporation of the

term Y_{2m} leads to the triaxial nuclei, which are axially asymmetric.

The collective rotation of a deformed nucleus manifests in the characteristic angular momentum (I) dependence of the excited energy levels (E) given by E $\propto$ I(I+1), where the proportionality constant is the inverse of the moment of inertia (MOI). It is generated by the motion of the constituent nucleons. At low angular momentum (analogously called 'spin'), the MOI of an even-even nucleus is considerably smaller than the rigid body value due to long-range pairing correlations between the nucleons. This correlation originates due to the scattering of a pair of nucleons between the nucleon orbitals near the Fermi surface. As the nucleus starts to rotate faster, the motions of the nucleons in the intrinsic frame are strongly influenced by the Coriolis force, which breaks the nucleon pairs in the time-reversed orbitals and starts to align them along the rotation axis. This way the angular momentum gets generated by the contributions from both the collective rotation and the orbital angular momenta of the aligning nucleons. Thus, in general, the effective MOI increases with increasing angular momentum due to the Coriolis force and the nucleus behaves as a soft rotor. Only in rare cases, the moment of inertia can become the constant of motion over an angular momentum interval if the Coriolis force fails to affect the orbital occupancies of the nucleons due to the Pauli blocking. In this domain, the nucleus can be assumed to be rigid as the angular momentum gets generated only through the nuclear rotation.

The nuclear structure studies involve the synthesis of a specific nucleus of interest, exciting it to high angular momentum, detecting the decay gamma-rays and building the discrete level structure of the nucleus. The excited levels originating from different mechanisms for angular momentum generation have characteristic electromagnetic decay properties. The enhancement in the E2 or E3 transition rates is the marker for the rotation of a quadrupole or octupole shape, respectively. On the other hand, the magnetic dipole (M1) transitions depend on the intrinsic nucleonic currents and thus, are a good identifier for the occupancy of the nuclear orbitals. These transition rates can be estimated through the measurement of the lifetime of the decaying state. Thus, the level lifetime is an important spectroscopic information needed for nuclear structure studies.

For the neutron-rich isotopes in mass 100, the level energies of the intruder negative parity $h_{11/2}$ orbital of the neutron sector become significantly lower for $\beta_2 \approx 0.2$. Thus, the shears mechanism becomes a dominant mechanism for the angular momentum generation

in these nuclei, where the neutrons occupy the lower levels of the $h_{11/2}$ orbital, while the protons occupy the higher levels of the ($d_{5/2}/g_{7/2}$) orbitals [10, 11, 12, 13]. On the other hand, the occupancy of the $h_{11/2}$ orbital induces nuclear deformation through the polarization of the core and leads to the emergence of several exotic shapes in this mass region. For example, ^{96}Zr (N = 56) shows an enhanced electric octupole transition rate B(E3) for the low-lying 3^- state, which is the experimental evidence of octupole instability [7]. This observation indicates that reflection asymmetric characteristics can be present in this mass region. Another recent work on ^{105}Pd reported a transverse wobbling band, which is a signature of a triaxially deformed nucleus [14]. Thus, the search and study of exotic shapes in A $\approx$ 100 region through discrete γ-ray spectroscopy, is the primary goal for this thesis work.

The thesis will report high spin spectroscopy of ^{98}Mo, ^{100}Ru, ^{101}Ru and ^{105}Pd. The high spin levels of these nuclei were populated in three separate experiments. The first nucleus of interest in the thesis, ^{100}Ru, was populated in a fusion-evaporation reaction with a high cross-section ($\approx$ 1 b) due to the availability of a suitable target-projectile combination. A 2.5 mg/cm^2 ^{100}Mo was bombarded with a stable α beam of 50 MeV from the K-130 cyclotron at VECC. In the second experiment, the same target projectile combination was used but this time, a target of thickness 10 mg/cm^2 along with a beam energy of 45 MeV was chosen so that two evaporation channels other than ^{100}Ru, ^{101}Ru($\approx$ 600 mb) and ^{98}Mo ($\approx$ 150 mb), were also populated. In addition, the thick target data were utilized to measure the sub-picosecond lifetimes for the excited levels of ^{100}Ru and ^{101}Ru using the Doppler Shift Attenuation Method (DSAM). The high-spin states of ^{105}Pd were populated by a 63-MeV ^{13}C beam from the 14-UD Pelletron at the Tata Institute of Fundamental Research (TIFR) [8]. The target was 1 mg/cm^2 of enriched ^{96}Zr with a backing of ^{206}Pb of thickness 9 mg/cm^2. The gamma rays deexciting the high spin states were detected by the Compton-suppressed Clover detectors of the Indian National Gamma Array (INGA). The spins of different excited states were determined through Directional COrrelation (DCO) measurements. The clover detectors can also act as a Compton polarimeter. Hence, polarisation direction correlation (PDCO) measurements were also performed to determine the electromagnetic character of the de-exciting γ-rays.

In ^{100}Ru (N = 56, Z = 44), seven interleaved E1 transitions have been observed between the two alternating parity bands whose moments of inertia are nearly identical. The

$B(E1)_{out}/B(E2)_{in}$ values for these transitions are nearly constant for both $I^+ \rightarrow (I-1)^-$ and $(I-1)^- \rightarrow (I-2)^+$. There is also a sudden enhancement in this transition rate ratio above spin $I = 16\hbar$. It is interesting to note that the parity splitting also vanishes in this spin range. The rates along with the vanishing parity splitting indicate a possible emergence of stable octupole deformation in ^{100}Ru in high spins based on a rotationally aligned configuration. From the second experiment with the thick target, the level lifetimes of these bands were estimated. The comparison of the measured B(E1) rates with the calculated values from the Triaxial Projected Shell Model (TPSM), establishes the presence of octupole collectivity at high spins in ^{100}Ru. This is the only nucleus outside the Lanthanide and Actinide regions, where this effect has been observed. In addition to that, there are two negative parity bands which are inter-connected by strong M1 transitions and also have similar quadrupole moments as estimated from the DSAM analysis. Thus, these two bands are the signature partners based on $\nu[\{d_{5/2}/g_{7/2}\} \bigotimes h_{11/2}]$ configuration and originate due to the reflection of a symmetric shape. This implies that ^{100}Ru exhibits the coexistence of reflection symmetrical and asymmetrical shapes.

Another N = 56 nucleus of A $\approx$ 100, ^{98}Mo has been studied in the present thesis. The spins and multipolarity of the excited levels [9] were established from the present data and few additional transitions were identified. However, due to inadequate statistics, the weak interleaving E1 transitions were not observed. On the other hand, the identification of two alternating parity bands along with two newly placed electric octupole (E3) transitions indicates the possibility of octupole collectivity in ^{98}Mo. Systematic studies like parity staggering and moment of inertia (MOI) plots, enhance the prospect of establishing this nucleus as another reflection asymmetric shape in the mass $\approx$ 100 region.

These two nuclei namely ^{98}Mo and ^{100}Ru, are axially symmetric and the axis of rotation is perpendicular to the symmetry axis. A triaxial nucleus, on the other hand, can rotate about any of the three principal axes. This generalized rotation opens up the possibility of nuclear wobbling. In the case of transverse wobbling in an odd mass nucleus, the odd nucleon aligns along the short axis, while the nucleus rotates predominantly perpendicular to the medium axis with the largest MOI. The current experimental investigation of ^{105}Pd has revealed, for the first time, the existence of two wobbling bands both having one phonon configuration and originating from the coupling of the wobbling phonon to the ground state band and to its signature partner. The doublet one-phonon wobbling bands

are, in turn, found to be the signature partner bands. These observations have been drawn from the measured ratios of the inter-band and intra-band gamma transition rates. The numerical calculations based on the triaxial projected shell model (TPSM) approach have been performed and the obtained results are found to be in good agreement with the experimental observations. These calculations provide an insight into the nature of the observed structures at a microscopic level and establish that the new band originates due to the combined particle-wobbling excitation. This is the first observation of this interplay.

In ^{101}Ru, two new bands have been established and the level lifetimes have been measured using DSAM from the present data. These two bands represent the signature and wobbling partners of the yrast band and have one quasineutron configuration ($h_{11/2}$). At higher spins, the wobbled band exhibits large mixing with the three-quasiparticle configuration of $\nu h^1_{11/2} \bigotimes \pi g^2_{9/2}$. This is the first observation of the smooth evolution from collective rotation (γ-band) at high spin ($I > 31/2\hbar$) to the interplay of collective rotation and wobbling in the intermediate spin ($31/2\hbar \leq I \leq 27/2\hbar$) to pure wobbling in the low spin domain ($I < 27/2\hbar$).

In summary, the present thesis reports the existence of exotic shapes in $A \approx 100$ mass region. The experimental observations and comparison with the TPSM calculations, establish the reflection asymmetric shape for ^{100}Ru and the non-axial shapes for ^{105}Pd and ^{101}Ru. The experimental data on ^{98}Mo indicate the possibility of octupole collectivity.

The thesis will be organized in the following way. After a brief introduction chapter, the second chapter of the thesis will outline the distinct mechanisms for the generation of high angular momentum states and the basics of the Triaxial Projected Shell Model (TPSM), which has been used extensively during the present thesis work. The details of the experimental methods and analysis tools will be discussed in Chapter 3. The experimental findings and the interpretation of the results on ^{100}Ru, ^{98}Mo, ^{105}Pd and ^{101}Ru will be discussed in Chapters 4, 5, 6 and 7, respectively. The summary of the present thesis work will be presented in Chapter 8 along with a future direction for further experimental investigations.

Bibliography

[1] Joachim Alexander Maruhn, Paul-Gerhard Reinhard, Eric Suraud - *Simple Models of Many-Fermion Systems* Springer (2010)

[2] A. Bohr and B. R. Mottelson, *Nuclear Structure* (W. A. Benjamin, New York, 1975), Vol. II.

[3] R. F. Casten - *Nuclear Structure from a Simple Perspective* , Oxford University Press (1990).

[4] S. G. Nilsson, Binding states of individual nucleons in strongly deformed nuclei, Kgl. Danske Videnskab. Selskab. Mat.-fys. Medd, **29**, 16 (1955).

[5] S. Das *et. al.* Nuclear Instruments and Methods in Physics Research Section A: Accelerators, Spectrometers, Detectors and Associated Equipment **893**, 138 (2018).

[6] S. S. Nayak and G. Mukherjee, "Development of an Advanced, Multi-Function, Multi-DAQ-Compatible Data Sorting and Analysis Software Suite-BiNDAS," in IEEE Transactions on Nuclear Science, vol. **70**, no. 12, pp. 2561-2571, Dec. 2023

[7] Ł. W. Iskra *et. al.* Revised B(E3) transition rate and structure of the 3^- level in ^{96}Zr, Physics Letters B, Volume **788**, 2019.

[8] N. Rather *et. al.* Antimagnetic rotation in ^{104}Pd, Phys. Rev. C Volume **89**, 2014.

[9] S. Lalkovski *et. al.* Octupole collectivity in ^{98,100,102}Mo, Phys. Rev. C Volume **75**, 2007.

[10] P. Datta *et al.*, Observation of magnetic rotation in odd-odd ^{104}Ag Phys. Rev. C **69** (2004)

[11] S. Roy Systematics of antimagnetic rotation in even – even Cd isotopes *et al.*, Phys. Lett. B **694** (2011)

[12] N. Rather *et al.*, Exploring the Origin of Nearly Degenerate Doublet Bands in ^{106}Ag Phys. Rev. Lett **112** (2014)

[13] B. Das *et al.*, Novel evolution of the positive parity shears band in ^{106}Ag Phys. Rev. C **95** (R), (2017) 014326

[14] J. Timár *et. al.* Experimental Evidence for Transverse Wobbling in ^{105}Pd, Phys. Rev. Lett. **122**, 062501 (2019).

Summary

The present thesis reports the existence of exotic shapes in A $\approx$ 100 mass region, namely, ^{98}Mo, ^{100}Ru, ^{101}Ru and ^{105}Pd. The thesis is organized in the following way. After a brief introduction, the thesis outlines the distinct mechanisms for the generation of high angular momentum states and the basics of the Triaxial Projected Shell Model (TPSM), which has been used extensively during the present thesis work.

The details of the experimental methods and necessary analysis tools is also discussed. The high spin levels of the nuclei discussed in this thesis were populated in three separate experiments at Variable Energy Cyclotron Centre (VECC) and Tata Institute of Fundamental Research (TIFR). The gamma rays deexciting the high spin states were detected by the Compton-suppressed Clover detectors of the Indian National Gamma Array (INGA). The spins of different excited states were determined through Directional COrrelation (DCO) measurements. The clover detectors can also act as a Compton polarimeter. Hence, polarisation direction correlation (PDCO) measurements were also performed to determine the electromagnetic character of the de-exciting γ-rays.

The experimental results, combined with TPSM calculations, confirmed the reflection-asymmetric shape for ^{100}Ru and axial asymmetric-shapes for ^{105}Pd and ^{101}Ru. The data also suggest the possibility of octupole collectivity in ^{98}Mo. The summary of the present thesis work is presented along with a future direction for further experimental investigations.

Chapter 1

Introduction

The atomic nucleus is a finite, quantal system of interacting fermions. The research in nuclear physics primarily focuses on comprehending various properties of this complex system through the nucleon-nucleon interaction. The advancements in modern accelerators and detection methodologies facilitate detailed investigations of this interaction. These include exploring nuclear fusion dynamics and nuclear reaction mechanisms spanning a wide energy spectrum and studying nuclear structure at high angular momenta while maintaining low excitation energies. The study of high angular momentum (analogously called 'spin') states of atomic nuclei has emerged as a particularly significant area of interest as the radiative transitions between these excited states provide clear evidence of perturbations over the average mean field potential. The multipole nature of this perturbation is the origin of various excitation modes of atomic nuclei [1].

The presence of symmetry in nature is associated with a conservation law. In nuclear physics, there are three fundamental symmetries, namely charge, mass and current distribution. For example, the charge symmetry of nuclear force essentially means that the strong forces between proton-proton, neutron-neutron and neutron-proton are approximately the same. However, the multipole nature of the perturbative Hamiltonian leads to the spontaneous symmetry-breaking phenomena [2]. A notable example is the formation

of rotational bands when the spherical symmetry is lost. These bands exhibit specific level structures corresponding to different symmetries linked to the shape of the nucleus like π-rotation symmetry [2]. Recent experimental findings have revealed two new categories: magnetic and chiral bands [3, 4, 5]. The magnetic bands possess significant dipole moment, originating from highly uneven current distributions. On the other hand, the chiral bands are linked to the breakdown of spin chiral symmetry in axially asymmetric odd-odd nuclei. The macroscopic models based on such symmetries offer precise solutions for an ideal nucleus. However, these models rely on multiple free parameters, adjusted through comparison with experimental data. The credibility of a model is strengthened if these parameters show consistent variation across a wide range of nuclei in the periodic table. The effectiveness of this approach can be attributed to two key factors:

1) The creation of a mean-field by all nucleons, wherein the nucleon motion accurately reproduces the observed nuclear traits. The success of the shell model in reproducing "magic numbers" validates this concept.

2) The consistent observation of zero ground state spin in even-even nuclei highlights the strong pairing interaction between protons and neutrons.

Thus, a nucleus may be envisioned as an even-even core responsible for generating the mean field, along with valence nucleons primarily influencing nuclear properties. The deformation of the core introduces additional collective degrees of freedom for the nucleus notably, rotation and vibration [6]. These macroscopic descriptions and associated models undergo rigorous testing under extreme conditions of very high angular momentum, significant isospin values, and notable deformation.

High-resolution γ-spectroscopy emerges as a valuable tool for these tests [7]. Investigations into nuclear properties, such as quadrupole moments, excitation energy, angular momentum, and transition probabilities of discrete excited states, help in evaluating the validity of the macroscopic models.

The excitation modes depend on the occupation of nuclear orbitals near the Fermi surface

by valence particles, leading to different band structures for different nuclear shapes. For example, at shell closure, a nucleus is spherical in nature and hence a change in orientation can not be defined due to a lack of an axis of reference. As a result, no rotational band can be observed in a spherical nucleus. Thus, in this case, the coupling of the angular momenta of the valence nucleons gives rise to higher spin states, which leads to the observation of randomly spaced energy-level structures. On the other hand, Aage Bohr's seminal work in 1951 [8] provided insights into the rotational spectra of nuclei and their relationship to stable nuclear deformations. The deformed nuclei, characterized by asymmetric mass distributions, exhibit a variety of shapes, including prolate, oblate, and triaxial forms. Most deformed nuclei exhibit axial and reflection-symmetric spheroidal shapes, which can be deduced from the experimentally observed properties of their band structures. These symmetric shapes, being invariant under space inversion, yield rotational bands with unique parity. However, reflection-asymmetric shapes can arise from the octupole term of the interaction potential, albeit less stable than the well-known quadrupole deformations. This mode of excitation originates from the interactions between the orbitals of opposite parity with $\Delta l = \Delta j = 3$ near the Fermi surface. Consequently, it leads to a separation between the nucleus's centre of mass and centre of charge, resulting in the observation of alternating parity bands connected by enhanced E1 transitions [9].

Thus, the various angular momentum generation mechanisms are reflected in the high-spin level structures of deformed nuclei, which also affect the electromagnetic transition rates. In the mass $A \approx 100$ region, the close proximity of the positive parity $d_{5/2}$ and negative parity $h_{11/2}$ neutron orbitals near the Fermi surface enhances the possibility to observe strong octupole correlations, leading to β_3 deformations.

It may be noted that an axially asymmetric nucleus can exhibit three-dimensional rotation i.e. it can rotate about any one of the principal axes. Uniform rotation around the medium axis with the largest Moment of Inertia (MoI) represents the lowest energy state for a given angular momentum. The precession of the total angular momentum around any

of the three axes leads to the phenomenon of nuclear wobbling [10]. The occupation of quasineutrons in the low- Ω $h_{11/2}$ orbitals establishes nuclei of A $\approx$ 100 mass region as potential candidates for observing the wobbling phenomenon. The primary aim of the present thesis is to explore the possibility of the existence of these exotic reflection and axially asymmetric shapes in this mass region.

To achieve this goal, experimental investigations were conducted employing in-beam γ-ray spectroscopy. The thesis work presents spectroscopic studies of two N = 56 isotones ^{100}Ru and ^{98}Mo, as well as ^{105}Pd (N = 59) and ^{101}Ru (N = 57), which were populated via fusion-evaporation reactions with different target projectile combinations. The emitted γ-rays were detected utilizing the Indian National Gamma Array (INGA), comprising a Compton-suppressed Clover detector array. All the experimental procedures are discussed in detail in Chapter 3. The next chapter delves into the emergence of octupole collectivity in the high spin domain of the alternate parity band in ^{100}Ru. This is a rare observation in the Segre Chart and the first such identification in this mass region. Chapter 5 establishes ^{98}Mo as another potential candidate for the observation of permanent octupole deformation in the A $\approx$ 100 mass region. On the other hand, Chapter 6 describes a unique observation of a band built from combined particle-wobbling excitation in ^{105}Pd. Finally, Chapter 7 elucidates the newly observed wobbling band in ^{101}Ru and the gradual evolution from pure collective rotation at high spins to wobbling at low spin levels. The thesis will also include a summary chapter which will discuss some future prospects of structure studies in this mass region using stable target-beam combinations.

Bibliography

[1] M. Roberts, P. Taylor, G. P. Barwood, W. R. C. Rowley, and P. Gill. Observation of the $2S_{1/2} - 2F_{7/2}$ electric octupole transition in a single ^{171}Yb+ ion. Phys. Rev. A, **62**:020501, Jul 2000.

[2] Stefan Frauendorf. Spontaneous symmetry breaking in rotating nuclei. Rev. Mod. Phys., **73**:463–514, Jun 2001.

[3] H. Hübel. Magnetic rotation in nuclei. Progress in Particle and Nuclear Physics, **54**(1):1–69, 2005.

[4] S. Frauendorf. Tilted cranking. Nucl. Phys. A, **557**:259–276, 1993.

[5] S. Frauendorf and Jie Meng. Tilted rotation of triaxial nuclei. Nucl. Phys. A, **617**(2):131–147, 1997.

[6] R. F., Casten, 'Collective excitations in even-even nuclei: vibrational and rotational motion', Nuclear Structure from a Simple Perspective, 2nd edn (Oxford, 2001; online edn, Oxford Academic, 1 Jan. 2010).

[7] W.L. Dunn, D.S. McGregor, J.K. Shultis, . Gamma-Ray Spectroscopy. In: I. Fleck, M. Titov, C. Grupen, I. Buvat, (eds) Handbook of Particle Detection and Imaging. Springer (2021).

[8] Aage Bohr. On the quantization of angular momenta in heavy nuclei. Phys. Rev., **81**: 134 – 138, Jan 1951.

[9] A V Afanasjev and S Mizutori. Octupole correlations at medium spin in odd-proton ^{153}Eu nucleus. Z. Physik A - Hadrons and Nuclei, **353**(3):267–271, September 1995.

[10] Nirupama Sensharma Wobbling Motion in Nuclei: Transverse, Longitudinal and Chiral. University of Notre Dame. Thesis. https://doi.org/10.7274/mg74qj7626t (2021).

Chapter 2

Angular Momentum Generation Mechanisms

Nuclear shape and structure studies at high angular momentum provide insights into the mechanisms that generate angular momentum. No ab initio theory has been developed to describe these processes accurately. However, advances have been and continue to be made using phenomenological models, which give a fair description of the fundamental physics of this intrinsically complicated problem. In nuclear physics, the discovery of the magic numbers resulted in the development of the Shell model [1, 2]. However, the progress of the shell model suggested that even in the ground state, extra configuration mixing can result from the accumulation of p-n interaction strength. This results in an asymmetry in the mass distribution of the nuclei, which causes a permanent deformed shape. For the axially symmetric prolate or oblate nuclei, the collective rotation can be observed around an axis perpendicular to the symmetry axis. Regular level sequences connected by intraband electric quadrupole (E2) transitions have been found in the mid-shell nuclei, which experience the highest concentration of the p-n interaction strength [3, 4, 5]. A more generalized rotation is possible for an axially asymmetric mass distribution (triaxial shape), which can rotate along any of the three - the short, long, and

intermediate axes [6]. The moment of inertia, defined by the deformation parameters β and γ, determines the rotational energy (discussed in section 2.2.1). For $\gamma = 30°$, the rotational energy around the shortest primary axis becomes advantageous for nuclei in mass areas A $\approx$ 60, 100, 140, and 160 [7, 8, 9, 10]. As shown recently in ^{77}Kr [11] and ^{138}Nd [12], the rotation around the intermediate axis may become energetically beneficial when pairing correlations are taken into account [13].

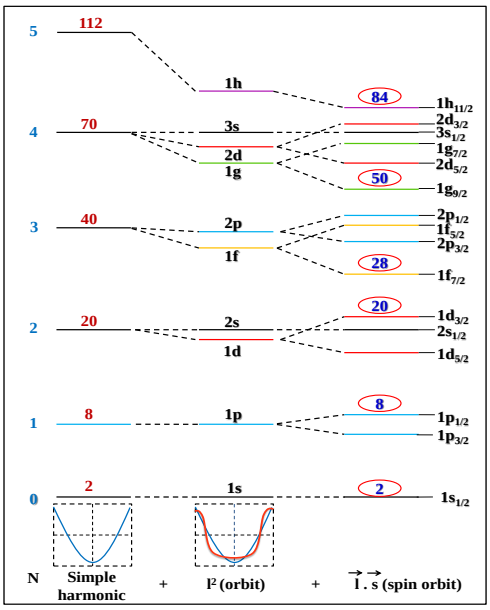

Figure 2.1: The Shell model states for a basic harmonic oscillator potential, a simple harmonic potential with l^2, and spin-orbit interaction terms are illustrated (Bottom) Schematic diagram of the two shell model potentials: the S. H. O. potential and the modified harmonic oscillator, which approximates the influence of the l^2 term. The figure is adapted from Ref [14].

This chapter will focus on several exotic excitation mechanisms that manifest due to the various nuclear shapes.

2.1 Nuclei at shell closure

The nuclear shell structure can be described by obtaining the wave functions and eigenvalues corresponding to single-particle motion in the nuclear mean field potential. The short-range character of the nucleonic forces suggests that the potential can be considered

a square well potential as a first approximation since it roughly resembles the density distribution. There is widespread use of a harmonic oscillator potential with similar specifications. Fig. 2.1 shows that the primary shell closures occur at nucleon numbers 2, 8, 20, 40, 70, 112, and 168 [14] if the nuclear potential resembles that of a harmonic oscillator. The observed magic numbers are consistent with the first three members of the series, but not with the higher ones.

The elaborate orbital sequence is slightly altered by the selection of a more realistic radial dependence. The primary step is the elimination of the harmonic oscillator degeneracy, which results in a depressed orbit for higher orbital angular momentum (l) relative to lower l orbits. The inclusion of strong spin-orbit interaction in the nucleonic motion — which provided a logical explanation for the magic numbers was the crucial turning point in developing the nuclear shell model [15, 16, 17]. The levels with $j = l \pm 1/2$, which are degenerate in a spin-independent potential, are split by this coupling, and the observed magic numbers are reproduced if the sign is selected to lower the levels with $j = l + 1/2$. The lowest states of an odd-A nucleus can be qualitatively described in terms of the orbits that the unpaired odd nucleon can occupy. Assuming that the other nucleons stay paired with $I^{\pi} = 0^{+}$, the degrees of freedom of these nucleons are discarded in this approximation. This assumption covers the majority of the features of the lower levels in odd and odd-odd spherical nuclei. One may anticipate a somewhat complex pattern of levels for nuclei containing several particles outside of closed shells, related to the various ways in which these particles' angular momenta are coupled. However, the presence of non-yrast levels in the low-energy spectra, rotational bands, and large quadrupole moments in many nuclei highlight the shortcomings of this straightforward explanation and indicate the possibility of broken symmetries.

2.2 Deformation and Nilsson Model

The spontaneous symmetry breaking is a fundamental phenomenon in physics, wherein a system selects a symmetry-violating state while attempting to achieve the lowest energy. The nature of the interactions that govern the system dictates which symmetries are broken and under what circumstances. Thus, the study of symmetry-violating states is essential for understanding the interactions.

In nuclear structure physics, the existence of deformed nuclei is the most common example of a spontaneous symmetry breaking. Similar to molecules, breaking the spherical symmetry in nuclei leads to the appearance of rotational excitation, which is observed as specific sequences of levels called the rotational bands.

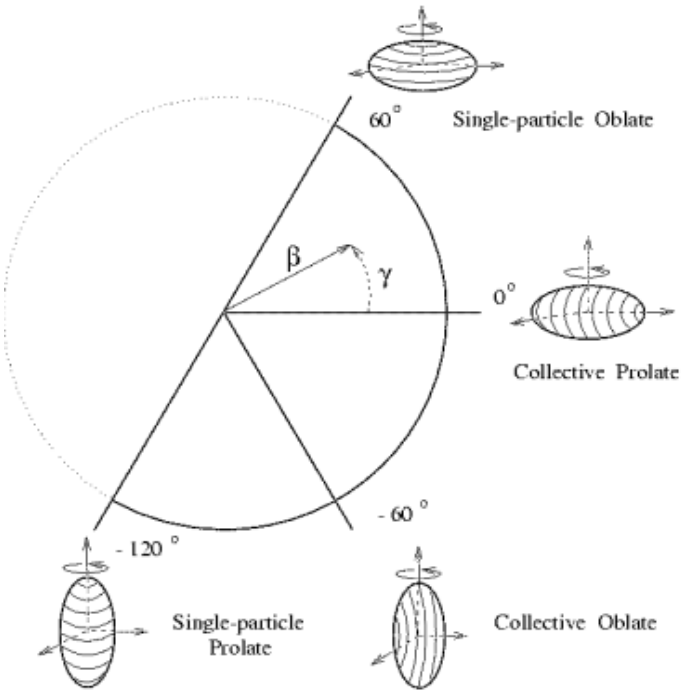

Figure 2.2: The deformation parameters β and γ for various nuclear shapes are displayed according to the Lund convention [14].

2.2.1 Shape parameterisation

The rotational degrees of freedom in a nucleus are connected to the mass anisotropy in the nuclear equilibrium shape. As a result, a deformed potential must be adopted instead of the spherical potential [14].

The non-spherical potential can be realized by replacing the radius term of the Harmonic Oscillator or Woods-Saxon potential by

$$R(\theta, \phi) = R_0[1 + \sum_{lm} \alpha_{lm} Y_{lm}(\theta, \phi)] \tag{2.1}$$

where $R(\theta, \phi)$ is the deformed radius, R_0 is the radius of the spherical nucleus of the same volume and Y_{lm} and α_{lm} are the normalized spherical harmonics and the corresponding expansion coefficients, respectively. The dipole term, or Y_{10} term, in this case, denotes the translation of the centre of mass of nuclei and has no impact on the nuclei's shape. The quadrupole deformation is represented by $\lambda = 2$, while an octupole deformation is represented by $\lambda = 3$. For quadrupole deformation, Eq. (2.1) takes the form:

$$R(\theta, \phi) = R_0[1 + \sum_{m=-2}^{m=2} \alpha_{2m} Y_{2m}(\theta, \phi)] \tag{2.2}$$

The five coefficients of Y_{2m} reduce to two parameters ($\alpha_{22} = \alpha_{2-2}$ and $\alpha_{21} = \alpha_{2-1} = 0$) when the principal axes (x, y, z) are aligned with the nuclear axes (1, 2, 3). Thus, the independent and conventional parameters for characterizing quadrupole deformation are:

$$\alpha_{20} = \beta cos\gamma \quad and \quad \alpha_{22} = \frac{1}{\sqrt{2}} \beta sin\gamma$$

where γ represents the deviation from axial symmetry and β represents the deviation from the spherical surface. The Lund convention [14] is a widely used convention to characterize the range of shapes for $\lambda = 2$ in terms of the β and γ variables. The shapes resulting from quadrupole deformation are depicted in Fig. 2.2, using the (β - γ) plane. It

is clear from this convention that $R_1 = R_2 = R_0$ if $\gamma = 0$ (axial symmetry). For an oblate nucleus, $R_3 > R_0$, while for prolate, $R_3 < R_0$. The nucleus has a triaxial structure for $\gamma = 30°$ ($R_1 > R_2 > R_3$), meaning that rotation around any of the three axes is permitted and there is no preferred axis of symmetry.

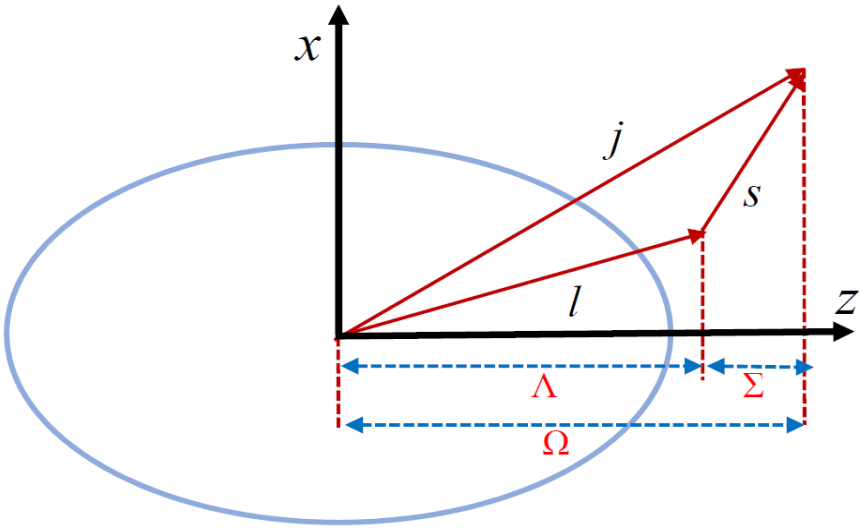

Figure 2.3: Pictorial representation of an axially symmetric deformed nucleus and the relevant quantum numbers proposed by Nilsson.

2.2.2 Nilsson Model

The definition and classification of nuclear deformation serve as a central concept for the theoretical construction of the Nilsson model [18]. According to Nilson's proposal of a non-spherical mean field, the nuclear shape and orientation have to be taken into account as the dynamical variables. These variables correspond to the different kinds of nuclear motion that reflect changes in the binding energy. Nilsson's first framework only addressed prolate or oblate quadrupole deformations (Y_{20}). With a spin-orbit coupling term, it was modelled as a modified harmonic oscillator potential [18]. The Nilsson model's subsequent developments also made it possible to generalize it to higher-order nuclear deformations, which are dependent on the configuration of a single particle. However, it is important to note that, unlike the shell model, the Nilsson model considers the motion of a single nucleon which moves in a deformed mean field generated by the interactions

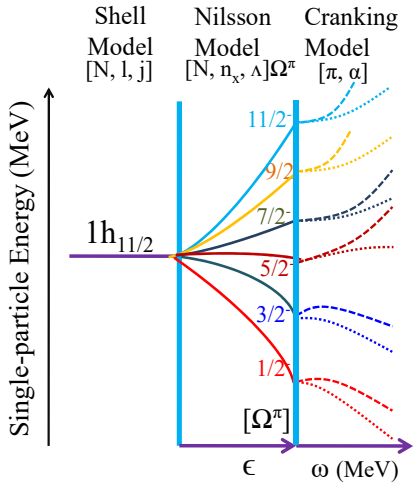

Figure 2.4: The effect of the deformed nuclear potential and rotation on the $h_{11/2}$ shell model state. The deformation ϵ is related to the β_2 deformation as $\epsilon = 0.946\beta_2$ in the limit of small deformation.

of all the other nucleons. Thus, the Nilsson orbitals are often referred to as single-particle (SP) orbitals. Nilsson's proposed model of a symmetrically deformed nucleus, with the z-axis as the symmetry axis, is depicted in Fig. 2.3. Nilsson orbitals are commonly described by the asymptotic quantum numbers (also shown in Fig. 2.4) as follows:

$$\Omega^{\Pi}[Nn_z\Lambda] \tag{2.3}$$

where N is the principle quantum number, Λ and Ω are the projections of orbital (l) and total (j) angular momentum along the z-axis and Π is the parity. There is no favoured direction for a spherical nucleus, and the energy of all (2j+1) sub-states for a given j is degenerate. On the other hand, the symmetry axis in an axially deformed nucleus can be identified, and the 2j+1 degeneracy of sub-levels is lifted. The only degenerate orbits are $+\Omega$ and $-\Omega$, which are time-reversed. It makes intuitive sense that the energy of a nucleon orbiting a deformed core will depend on the overlap or the direction of the single-particle

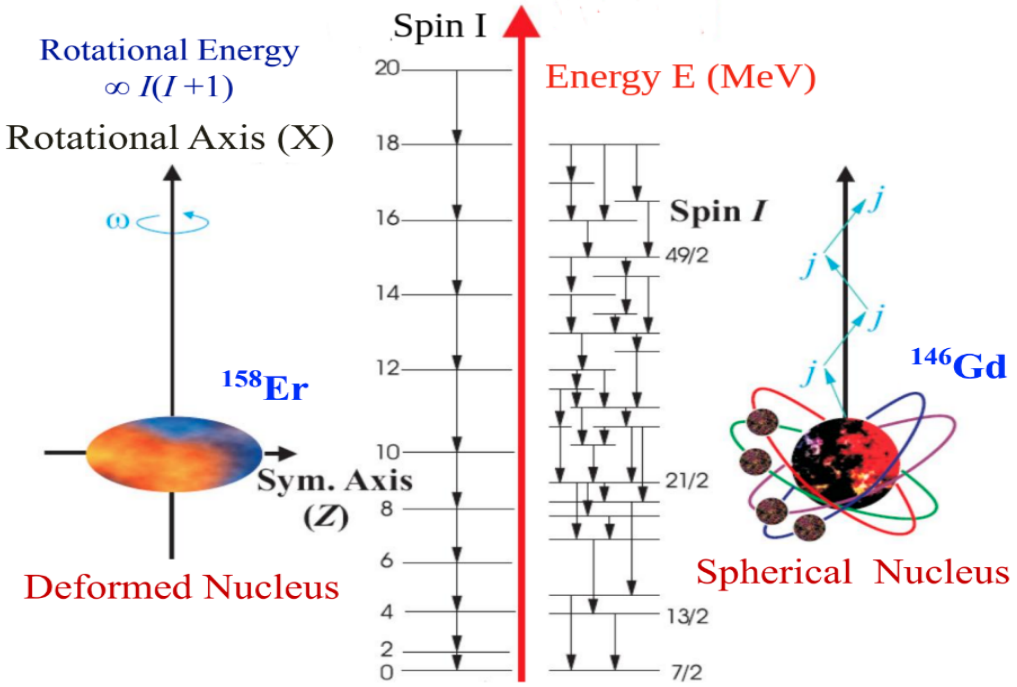

Figure 2.5: The excited states generated via collective rotation in deformed nuclei ^{158}Er, (left panel) and non-collective single-particle excitation in nearly-spherical nuclei ^{146}Gd (right panel) [19, 20]

orbit with respect to the core if the matter distribution within the core is not uniform. As a result, the energy of the states will only differ depending on Ω.

2.3 Angular Momentum Generation

The angular momentum in the atomic nucleus is generated by single particle or collective excitations or through their interplay. In the following sections, the different angular momentum generation mechanisms are discussed.

2.3.1 Non Collective or single particle excitation

Nuclei that are spherical or nearly spherical are typically found near the closed shells. These nuclei generate angular momentum by rearranging their valence nucleons. Fig. 2.5

(right panel) shows an example of such an excitation. The total angular momentum is the sum of the individual angular momentum of the valence nucleons that are not coupled to spin-zero. The majority of the nucleons form the rest of the nuclear matter i.e. the core and do not contribute to the generation of angular momentum.

The pairing interaction forms pairs of particles that are coupled to a total magnetic sub-state of M = 0, where M is the projection of total angular momentum along the symmetry axis. Therefore, when the pairing interaction is strong near closed shells, it inhibits the tendency to deform.

The breaking of a nucleon pair leaves a hole in the occupied level and creates a particle in an excited level. Thus, it is convenient to represent the energy required for single particle and hole excitations by the quasi-particle energy. This leads to the replacement of particles and holes with quasi-particles that represent partially filled levels. This transformation from particles to quasi-particles greatly simplifies the shell model calculations as only the quasi-particle excitations relative to the Fermi surface are considered.

Magnetic Rotation

In the early 1990s, scientists identified rotational-like patterns of γ rays in $^{193-200}$Pb nuclei that were determined to be magnetic dipole (M1) transitions, indicating that the states in these bands had identical parity but varied by just one unit of angular momentum [21, 22, 23]. Such a band structure for ^{199}Pb is shown in Fig. 2.6. Subsequent electron conversion and γ-ray polarization experiments provided further evidence supporting the M1 characters of these transitions. The absent or weak stretched E2 transitions indicate a small quadrupole deformation.

These bands have the following unique characteristics:
(i) Despite their low quadrupole collectivity, they form regular band structures across the observed spin range for $I \geq 10\hbar$. Indeed, neighbouring nuclei with similar deformation do

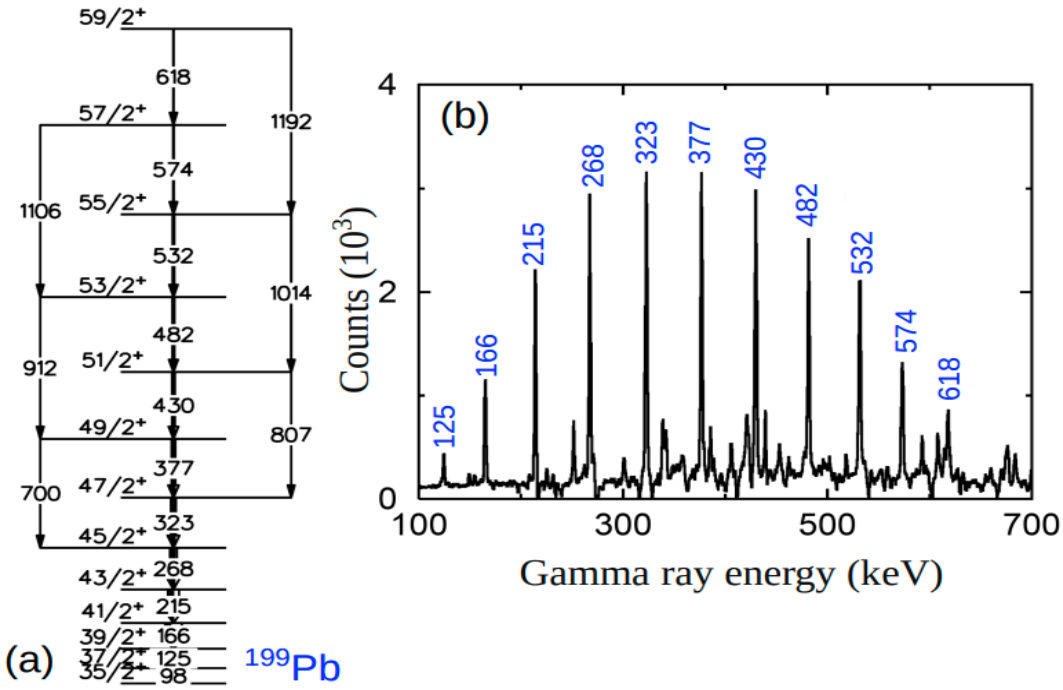

Figure 2.6: Experimental observations showing a regular band-like structure of M1 transitions and the gated spectrum for ^{199}Pb [20, 21]

not exhibit any bands of comparable regularity.

(ii) The ratio of their MOI to the B(E2) value is approximately 10 times greater than that of typical well-deformed nuclei. At first, these bands were proposed to originate

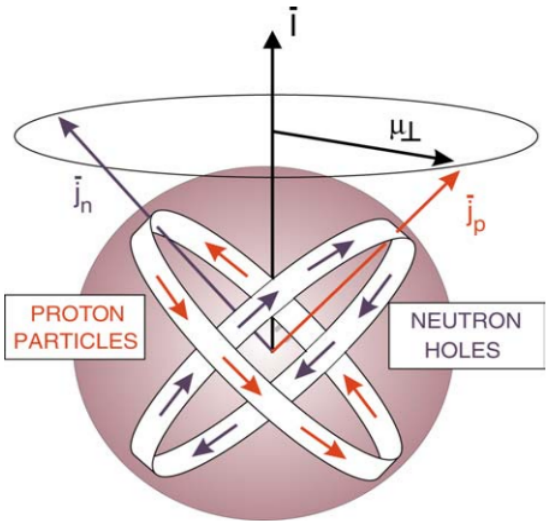

Figure 2.7: Illustration of the spin-coupling scheme for the shears mechanism. Figure courtesy: Ref. [24]

from proton configurations that involved $h_{9/2}$ and $i_{13/2}$ orbitals with the angular momenta

aligned with the symmetry axis, which leads to non-collective rotation. However, the observation of the uniform band structures over a wide spin range suggested that these bands originate from a novel method for generating angular momentum in atomic nuclei. Frauendorf gave the first theoretical explanation for these $\Delta I = 1$ rotational bands, known as Magnetic Rotational (MR) bands, using the framework of tilted axis cranking (TAC) [25]. Macchiavelli et al. [26] have later proposed a more phenomenological approach of the shears mechanism, which explains the interaction between the current loops (shown in Fig. 2.7) using the concept of exchange of quadrupole phonons. Their prescription offers a logical explanation of the observed energies, B(M1) and B(E2) values. It relies on just a few parameters, namely the particle-phonon coupling strength, effective charges, and g factors. The proton hole (particle) and neutron particle (hole) angular momenta align perpendicular to one another in weakly deformed nuclei, as shown by the vectors $\vec{j_\pi}$ and $\vec{j_\nu}$ in Figure 2.7. The minimal spatial overlap between the two loops is ensured by this perpendicular alignment, which is favoured by the repulsive potential between the particles and the holes. The gradual alignment of $\vec{j_\pi}$ and $\vec{j_\nu}$ produces the higher angular momentum states of the band. The shear mechanism is so named due to its similarity to the closing of a sheep's shear with the spring representing the repulsive interaction. The shears bands are often called the magnetic dipole (M1) bands. The behaviour of the M1 transition rates (B(M1)) transition probabilities as a function of spin has provided the definitive test of this theory. The B(M1) values in these bands decrease with increasing spin [21, 22, 23] as seen in Fig. 2.8. Furthermore, these bands have large K values (projection of total angular momentum on the symmetry axis) for the band heads, implying multi-quasiparticle configurations, and smaller dynamical moments of inertia than those of typically deformed nuclei [27].

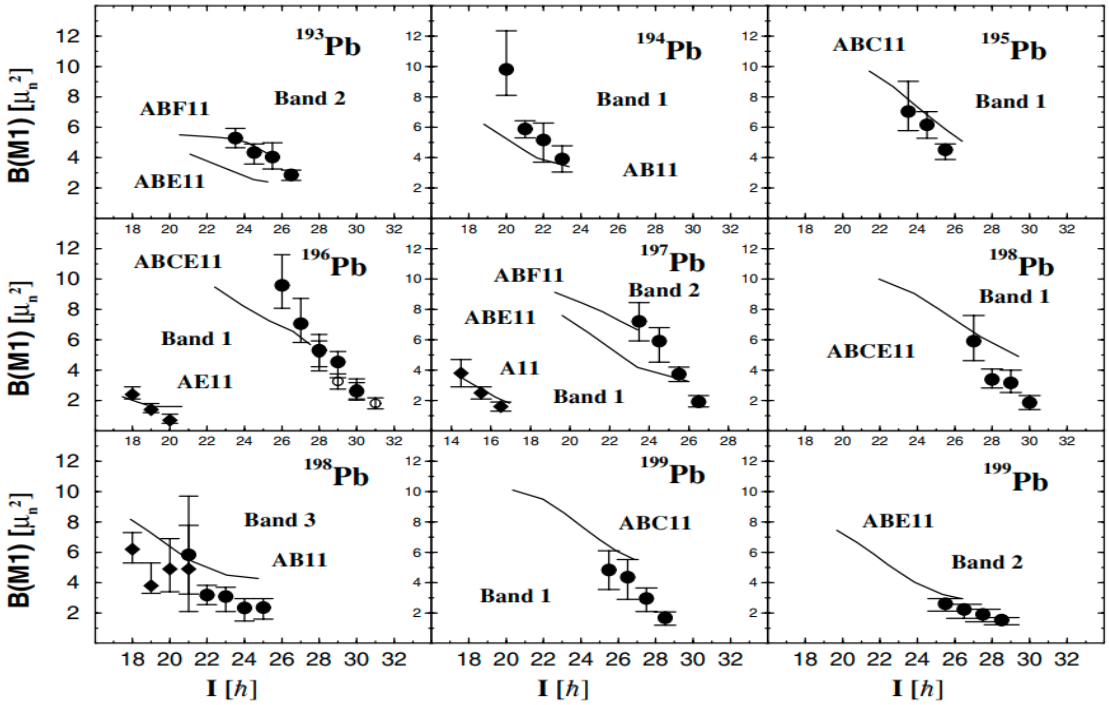

Figure 2.8: The M1 transition probabilities, B(M1), for intraband transitions in isotopes $^{193-199}$Pb, are presented as a function of the spin of the initial state. The figure is taken from Ref. [28].

Anti-Magnetic Rotation

The strong electric quadrupole E2 transitions which build up the rotational bands in atomic nuclei are understood to represent the coherent collective rotation of many nucleons about an axis perpendicular to the symmetry axis [1, 29]. One of the important experimental features of these bands is the observation of the almost constant and enhanced electric quadrupole transition rates [B(E2)] for the levels of the band. Remarkably, a few weakly deformed nuclei near shell closure have also shown regular E2 transition sequences, but the B(E2) values were found to decrease with spin. Zhu et al. [30] originally described this kind of excitation from their spectroscopic study of the ^{100}Pd nucleus. The observed characteristic of the decreasing tendency of B(E2) values (as shown in Fig. 2.9) [31] of these sequences has also been understood within the framework of a shear mechanism.

In this case, the angular momentum is produced by the valence particles and holes ar-

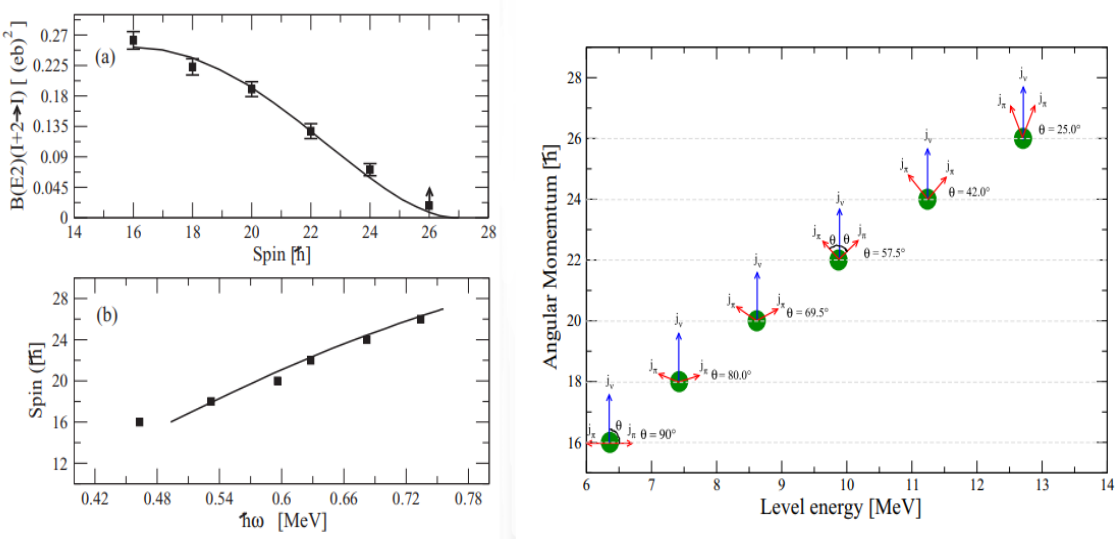

Figure 2.9: The left panel shows the decreasing trend of experimental B(E2) values as a function spin I along with the I vs. ω plot in ^{104}Pd. The lines represent the numerical values obtained from the theoretical calculations. The right panel shows how the gradual closing of the shears angle generates the spin states [31].

ranged in a double shears structure, which has π rotational symmetry along the axis of the total angular momentum. The high spin states are generated by the simultaneous closing of the two blades of the conjugate shears. The transverse magnetic dipole moments ($\mu_\perp$) generated by the two shears are oriented in opposite directions and so cancel each other. This scenario bears similarities to that of an antiferromagnetic material, in which half of the atomic dipole moments are aligned on one sublattice within the crystalline structure, while the other half are aligned in the opposite direction. Due to this similarity, the phenomenon is called antimagnetic rotation [6, 30, 31, 32].

It is important to note that these above-mentioned mechanisms are purely single-particle excitations and no collectivity of the core is involved.

2.3.2 Collective modes of excitation

The atomic nucleus exhibits both collective vibration and rotation. The vibration mode can be interpreted as dynamic deformation, which involves shape oscillations. A small departure from the nuclear potential energy minimum (shown in Fig. 2.10(a)) causes the

shape oscillation around the spherical shape ($\beta_2 = 0$).

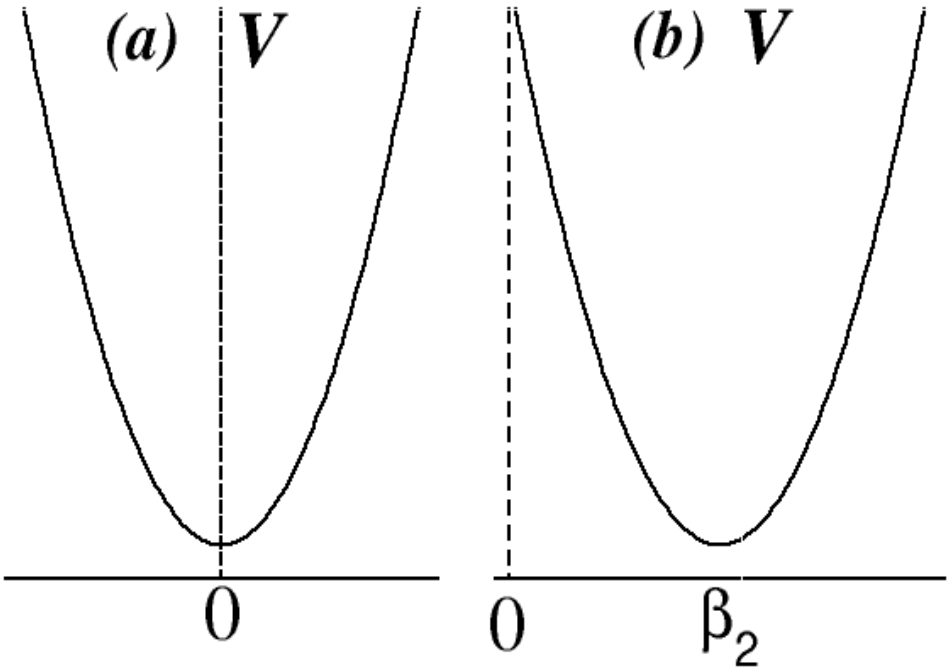

Figure 2.10: The nuclear potential for (a) dynamic (vibration) and (b) stable deformation. Here the minima of the potential V represents the deformation for which the shape is stable.

The coefficients α_{lm} in Eq. 2.1 can be used to describe the magnitude of this vibration. Fig. 2.11 shows the different low-order vibrational excitation modes (l = 0, 1, 2). The quanta of vibration are known as phonons, and the vibrational energy for the multipole λ is represented by $\hbar\omega_\lambda$. Every phonon is a boson with parity $\pi = (-1)^\lambda$ and angular momentum $\lambda\hbar$. The present thesis work aims to explore exotic shapes with permanent deformation (as represented in Fig. 2.10(b)). Thus, the features of collective rotation have been described in detail, in the following sections.

The collective rotation leads to the characteristic angular momentum (I) dependence of the excited energy levels (E) given by $E \propto 1/2\ I(I+1)$. The proportionality constant is the inverse of the moment of inertia (MOI) and is generated by the motions of the constituent nucleons. At low spins, the MOI of an even-even nucleus is considerably smaller than that of a rigid rotor having the same mass because of the long-range pairing correlations

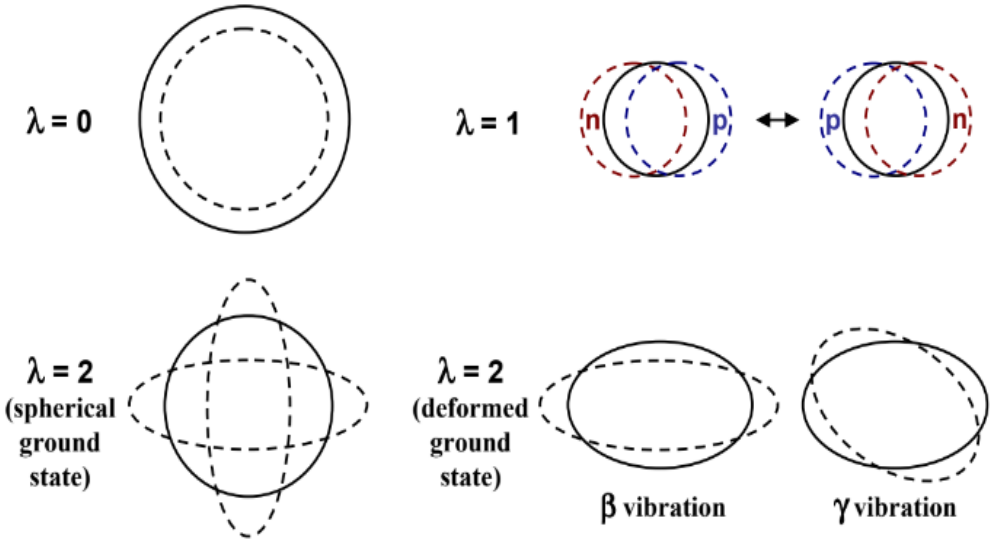

Figure 2.11: A pictorial representation of the various nuclear vibration modes observed in nuclear structure studies [14].

between the nucleons. These correlations originate due to the scattering of a pair of nucleons between the nucleon orbitals near the Fermi surface. As the nucleus starts to rotate faster, the Coriolis interaction breaks the nucleon pairs in the time-reversed orbitals. Thus, in general, the MOI increases with spin. In principle, rigid nuclear rotation can be observed at high angular momentum when the pairing correlations are quenched as a result of the rotational alignment of the nucleons.

The Coriolis force aligns the angular momenta of the quasi-particles parallel or perpendicular to either the symmetry or rotational axis, depending on the shape of the core (whether it is prolate or oblate) and the nature of the quasi-particle (whether it is a hole or a particle). This maximizes the overlap of the quasi-particle with the mass distribution of the core, as depicted in Fig. 2.12. Thus, it is important to note that the high spin levels are generated both from the collective rotation of nuclei and single particle contributions.

Description of Collective Rotation

The valence nucleon(s) of an odd (odd-odd) nucleus can couple to the rotating deformed core at two extreme limits. Fig. 2.13 shows the limits of the two coupling schemes. These

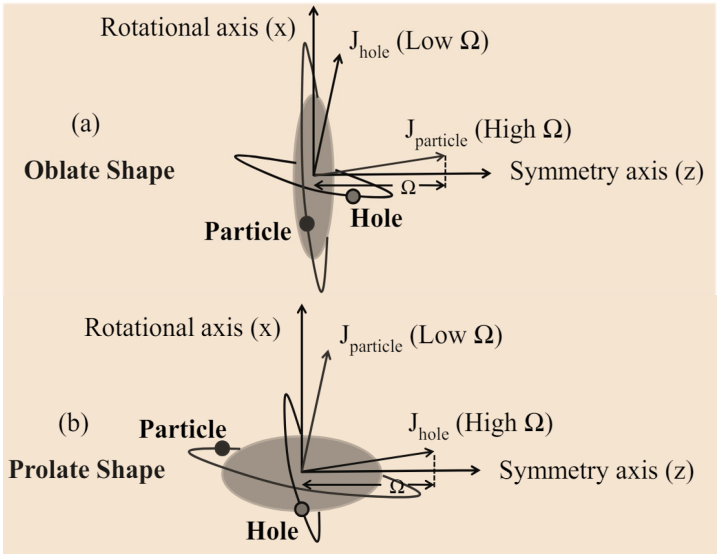

Figure 2.12: Alignment of the quasi-particle angular momentum for the nucleus's (a) prolate and (b) oblate core shapes, respectively. The projection of the quasi-particle angular momentum along the symmetry axis ($\hat{z}$) is represented by Ω. [20]

schemes do not consider the effects of a short-range pairing force and instead assume that the valence nucleon's motion is solely influenced by the Coriolis force and the deformed nuclear field. As seen in Fig. 2.13(a), nucleonic motion and core deformation are coupled when the projection of the particle angular momentum along the symmetry axis is large. This is known as the strong coupling limit. At high spins, the Coriolis force aligns the particle rotation axis as shown in Fig. 2.13(b). This is the weak coupling or decoupling limit.

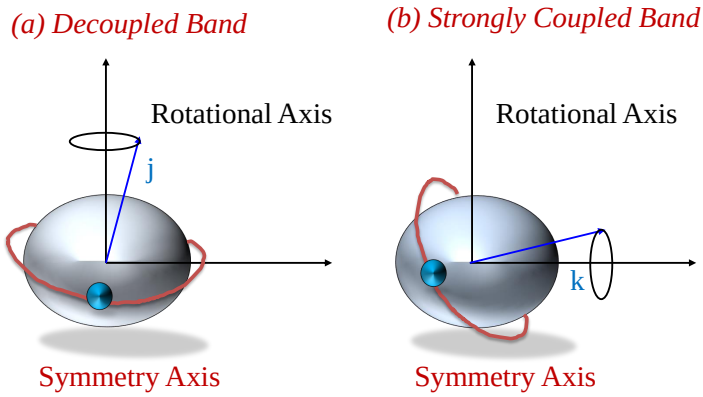

Figure 2.13: The orientation of the particle angular momentum with respect to the core in the (a) weak and (b) strong coupling limits.

Particle Rotor Model

This rotational dynamics of these nuclei can be well described by the Particle Rotor Model (PRM), where the particle-core coupling is described as

$$\vec{I} = \vec{R} + \vec{J} \tag{2.4}$$

where $\vec{R}$ is the rotational angular momentum of the core which is perpendicular to the symmetry axis and $\vec{J}$ is the sum of all intrinsic particle angular momentum ($\sum \vec{j_n}+\vec{j_p}$) coupled to the core. For this system, the Hamiltonian may be expressed as considering both collective and intrinsic Hamiltonian as [33]:

$$H_{tot} = H_{col} + H_{int} \tag{2.5}$$

where H_{int} is the nucleon Hamiltonian in the absence of collective rotation. For two particles coupled to the rotor, H_{int} takes the form

$$H_{int} = \sum_{\Omega}^{(p)} E_\Omega \alpha^\dagger_\Omega \alpha_\Omega + \sum_{\Omega}^{(n)} E_\Omega \beta^\dagger_\Omega \beta_\Omega \tag{2.6}$$

where E_Ω is the Bardeen-Cooper-Schriefer (BCS) quasiparticle energies [34]. H_{col} can be expressed as follows using Eq. (2.4):

$$H_{col} = \frac{\hbar^2}{2\mathcal{J}}(\vec{I} - \vec{J})^2 \tag{2.7}$$

In the limit of no particle-core coupling ($\vec{I}.\vec{J} = 0$), the expectation value of the H_{col} becomes

$$\langle H_{col} \rangle = E_{col}(I) = \frac{\hbar^2}{2\mathcal{J}}(I(I+1) - K^2) \tag{2.8}$$

where the MOI ($\mathcal{J}$) remains constant. In PRM, the Coriolis force originates due to the

particle-core coupling and corresponds to

$$H_{cor} = \frac{\hbar^2}{\mathcal{J}} \vec{I}.\vec{J} \tag{2.9}$$

This force strongly affects the high-j and low-ω orbitals leading to the origin of signature partner bands. The signature quantum number has been discussed in detail in the next section. The PRM has been successful in describing a wide range of observations at low and indeterminate spins for deformed odd or odd-odd nuclei.

However, in this model, which is described in the laboratory frame, the intrinsic particle angular momentum $\vec{J}$ is the sum of the individual angular momentum of all the valence nucleons ($\sum \vec{j_i}$) outside the core. As a result, the dimensionality of the calculation diverges and also becomes complicated when the number of valence nucleons becomes three or more. To overcome this problem, a rotating deformed nucleus may be described in the body-fixed frame by the variation of the energy of the single particle (Nilsson) orbitals in a rotating mean field.

Cranking Model

In this microscopic model, the total angular momentum (I) is not a good quantum number and the whole formalism is described in terms of rotational frequency (ω), which is not observable for quantum rotation. The single particle Cranking Hamiltonian can be written as

$$h^{\omega} = h_{intr} - \omega J'_x \tag{2.10}$$

where J'_x stands for the x component of the total angular momentum on the rotational axis, h_{ω} is the Hamiltonian in the rotating frame, and h_{intr} is the intrinsic Hamiltonian in the body-fixed frame given by the Nilsson Hamiltonian.

It is observed from Eqn. (2.10) that because of the "-$\omega j'_x$" term, which is analogous to the classical Coriolis force, the cranked Hamiltonian breaks the time-reversal symmetry

[4, 5]. Hence, Ω is no longer a good quantum number. Only parity invariance remains, which characterizes the symmetry under space inversion. The second symmetry concerns invariance of H_ω under a 180° rotation about the axis perpendicular to the symmetry axis and the associated operator can be expressed as follows:

$$R|\pi\alpha\rangle = e^{-i\pi J_{x'}}|\pi\alpha\rangle \tag{2.11}$$

As we are dealing with a system of fermions, a rotation of 2π gives a negative sign to the wavefunction. Hence,

$$e^{-i2\pi\alpha} = -1 = e^{\pm i\pi} \tag{2.12}$$

so, $\alpha = \pm 1/2$. Hence, given the operation described in Eqn. 2.11, α is conserved and is called the signature quantum number [13]. This separates the bands depending on the direction of rotation. The band which comes down in energy is known as the favoured signature band and $\alpha = +1/2$ corresponds to I = 1/2, 5/2, ... while $\alpha = -1/2$ corresponds to the states I = 3/2, 7/2, ... for odd mass nuclei. For odd-odd nuclei, $\alpha = 0$ denotes the states I = 0, 2, 4,... and $\alpha = 1$ corresponds to the states with I = 1, 3, 5... . The nuclear spin and α are connected through the relation:

$$I = \alpha \, mod 2 \tag{2.13}$$

Thus, the parity π and the signature α serve to characterize the rotation of the SP orbitals as shown in Fig. 2.4. The expectation values to the operators in Eq. 2.10 correspond to the variation of the SP energy levels (routhians) and I_x as a function of ω. A typical routhian plot for N = 56 is shown in Fig. 2.14. The solid horizontal line defines the Fermi surface. The configuration is defined as the one for which all the levels below the Fermi surface are filled. Thus, the reference configuration corresponds to the ground state band for an even-even nucleus. However, at higher frequencies, the intrinsic SP configurations change where the positive and negative energy levels cross. The predictions from this

body-fixed model can not be compared with experimental data as in the lab frame, where the level energies are measured as a function of angular momentum I. Thus, the rotational frequency is obtained as a function of angular momentum (I) as follows

$$E'(\omega) = \frac{1}{2}[E_{I+1} + E_{I-1}] - \omega(I)I_x(I) \tag{2.14}$$

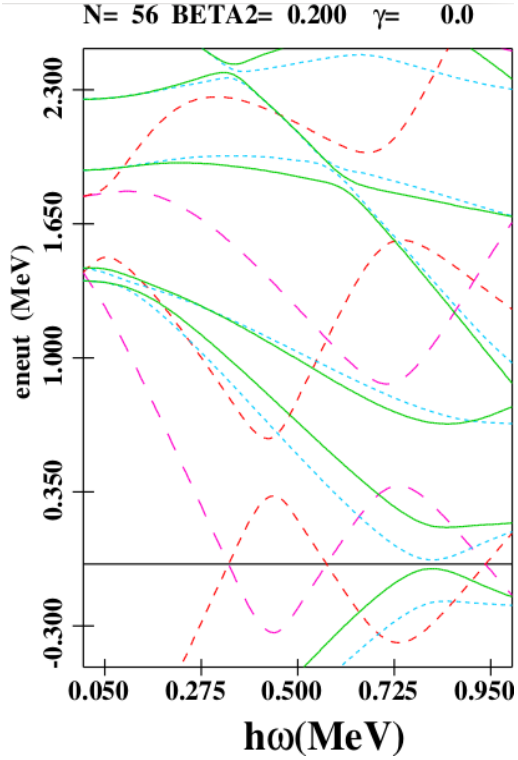

Figure 2.14: The quasiparticle energies (routhians) 56 neutrons of ^{100}Ru considering β_2 = 0.2 and γ = 0.0 plotted as a function of rotational frequency. The spins and signatures of the routhians are indicated following the prescription: (-, +1/2): red dashed, (-, -1/2): red dot-dashed, (+, +1/2): green solid, (+, -1/2): green dots.

where I_x and ω follow the expressions:

$$\hbar\omega = \frac{E_{I+1} - E_{I-1}}{I_x(I+1) - I_x(I+1)} \tag{2.15}$$

$$I_x = \sqrt{I(I+1) - K^2} \tag{2.16}$$

To compare the experimental routhian with the theoretical single particle routhian, the core contribution has to be removed from the total energy. After the transformation from variable I to ω, the routhian energy is defined as

$$e'(\omega) = E'(\omega) - E^{ref}(\omega) \tag{2.17}$$

For this purpose, reference energy $E^{ref}(\omega)$ as a function of rotational frequency using two parameters is obtained from the fully paired ground state band of the neighbouring even-even nucleus [35]. These quantities, also known as Harris Parameters, are based on the assumption that at low spins, the reference MOI of a nuclei is approximately proportional to ω^2 and can be written as:

$$\mathcal{J}^{ref}(\omega) = \mathcal{J}_0 + \mathcal{J}_1\omega^2 \tag{2.18}$$

Thus, the reference-aligned angular momentum takes the form:

$$I_x^{ref}(\omega) = (\mathcal{J}_0 + \mathcal{J}_1\omega^2)\omega \tag{2.19}$$

and the quasi-particle aligned angular momentum can be defined as

$$i_x(\omega) = I_x(\omega) - I_x^{ref}(\omega) \tag{2.20}$$

Finally, the reference energy can be calculated using the following relation:

$$E^{ref}(\omega) = -\hbar \int I_x^{ref}(\omega) d\omega \tag{2.21}$$

Thus, it is possible to compare experimental level schemes with theoretical routhians. It is also instructive to study the change of slope of the routhians as a function of ω. The kinematic moment of inertia $\mathcal{J}^{(1)}$ is the first order derivative and can be identified with

experimental level energies as follows:

$$\mathcal{J}^{(1)}(I) = \left(\frac{dE}{dI_x}\right)^{-1} \hbar^2 = \hbar\frac{I_x}{\omega} \approx \hbar^2 \frac{2I-1}{E_{I+1} - E_{I-1}} \tag{2.22}$$

Additionally, the dynamic moment of inertia ($\mathcal{J}^{(2)}$) is the second-order derivative which is given by:

$$\mathcal{J}^{(2)}(I) = \left(\frac{d^2E}{dI_x^2}\right)^{-1} \hbar^2 = \hbar\frac{dI_x}{d\omega} \approx \hbar^2 \frac{4}{(E_{I+2} - E_I) - (E_I - E_{I-2})} \tag{2.23}$$

This quantity is independent of the absolute spin of the levels and solely depends on the energy difference between transitions between two successive decays as follows.

$$\mathcal{J}^{(2)} \approx \frac{4\hbar^2}{\Delta E_\gamma} \; for\; \Delta I = 2 \;\; band \tag{2.24}$$

As a result, it is a useful variable when band head spin is not known, and the level spins are not precisely determined. Thus, crucial information regarding the structural alterations occurring inside a rotating band can be obtained from the variation of the moment of inertia with rotational frequency. This imparts a distinctive configuration to the energy levels and serves as a valuable experimental indicator for rotational bands.

As demonstrated above, the experimental data needs to be suitably adopted to compare with Cranking Shell Model (CSM) predictions. This remains the major shortcoming of this body fixed model, although it gives a satisfactory description of the high spin physics involving rotational alignments. The other shortcoming is the absence of interaction between the multi-quasiparticle configurations. These issues can be better addressed in the models based on angular momentum projections from intrinsic configurations followed by band mixing calculations. In the present thesis, the Triaxial Projected Shell Model (TPSM) calculations [36, 37] have been used to describe the experimental observations in ^{100,101}Ru and ^{105}Pd. .

Triaxial Projected Shell Model

In this model, the single particle configurations and corresponding energies are evaluated in the body-fixed frame. After that, the rotational bands based on each single particle configuration are projected to obtain the good I basis. This is followed by the band mixing calculations. The generalized scheme followed by TPSM is described in brief for the completeness of this discussion. The details of this model can be found in Ref. [36].

The one-neutron and one-proton quasiparticle configurations make up the basis space of the TPSM method for odd-odd nuclei:

$$|\phi_K\rangle = a_\nu^\dagger a_\pi^\dagger |0\rangle \tag{2.25}$$

The diagonalization of the deformed Nilsson Hamiltonian and subsequent BCS computations yield the triaxial quasi-particle (qp)-vacuum $|0\rangle$ in Eq. (2.25) [36]. The number of levels close to the corresponding Fermi levels of protons and neutrons determines the number of basis configurations.

The states $|\phi_\kappa\rangle$ from deformed Nilsson computations lack rotational symmetry. To restore this symmetry, three-dimensional angular momentum projection is used. Using the projection technique, a band is formed from each intrinsic state in Eq. (2.25). The interaction between bands with certain spin is accounted for by diagonalizing the Hamiltonian shell model in the projected basis. The TPSM wave function has the form of

$$|IM\rangle = \sum_{K,\kappa} f^I_{K,\kappa} P^I_{M,K} |\kappa\rangle \tag{2.26}$$

where, the angular momentum- -projection operator $P^I_{M,K}$ is defined as,

$$P^I_{M,K} = \frac{2I+1}{8\pi^2} \int D^I_{M,K}(\Omega) R(\Omega) d\Omega \tag{2.27}$$

The following eigenvalue equation can be solved to get rotational band energies and cor-

responding wave functions:

$$\sum_{K,\kappa} f^{I}_{K,\kappa}(\kappa'|HP^{I}_{K',K}|\kappa\rangle - E^{I}\kappa'|P^{I}_{K',K}|\kappa\rangle) = 0 \tag{2.28}$$

where the Hamiltonian H contains four terms as follows:

$$H = H_0 - \frac{1}{2}\chi \sum_{\mu} \hat{Q}^{\dagger}_{\mu}\hat{Q}_{\mu} - G_M \hat{P}^{\dagger}\hat{P} - G_Q \sum_{\mu} \hat{P}^{\dagger}_{\mu}\hat{P}_{\mu} \tag{2.29}$$

The Nilsson Hamiltonian is denoted by the first term, while the second term represents multipole-multipole interactions. The third and fourth terms account for monopole and quadrupole pairings, respectively. In the calculations for ^{100}Ru, the Hamiltonian also included the octupole-octupole interaction term (used as a perturbation), with the mean-field having well-defined parity. In this manner, the octupole correlations have currently been incorporated. However, the octupole mean field can be defined in the Nilsson state by explicitly breaking the reflection symmetry and the parity projection formalism can be employed to restore this broken symmetry [37]. This development of TPSM is in progress [38].

2.4 The origin of exotic shapes

As discussed in previous sections, the most commonly observed shapes in the Segre chart are prolate and oblate, which are both axially and reflection symmetric. The exotic shapes with triaxial (axially asymmetric) or octupole (reflection asymmetric) deformations have been observed in a few nuclei, which are concentrated in specific mass regions. The rotational characteristics of these shapes have been discussed in the next sections.

2.4.1 Reflection Asymmetry

The octupole deformation, which results from the spontaneous breaking of intrinsic reflection symmetry in nuclei with pear-like shapes, is due to the Y_{30} term of Eq. 2.1. The octupole coupling between the regular parity subshell (l - 3, j - 3) and the intruder orbital (l, j) close to the Fermi energy surface gives rise to the reflection asymmetric bands. "Octupole correlation", a dynamical interaction between these orbitals, can result in reflection symmetry-breaking bands connected by enhanced electric dipole (E1) transitions [39]. The origin of the band structure of a rotating pear-shaped nucleus can be understood from the variation of the nuclear potential energy of this reflection-asymmetric shape as a function of the octupole deformation parameter [40, 41, 42]. The potential energy has two degenerate minima at $\pm\beta_3^{min}$ separated by a finite barrier at $\beta_3 = 0$ (shown in Fig. 2.15). Reflection-symmetric nuclei exhibit the rotational invariance under parity (P) operation and rotation (π) about an axis perpendicular to the symmetry axis (R). The rotation of a reflection-asymmetric nucleus is invariant only under the product of these two operations (RP), giving rise to the simplex quantum number (s) [39]. Two minima correspond to the s = ±i values and give rise to a pair of alternate parity bands.

Thus, for stable octupole deformation, the MOI for simplex partners at high spins are expected to be identical. However, as the barrier height is finite at low spins, tunnelling is possible between the two minima, which leads to parity splitting among the simplex partners in the laboratory frame.

The presence of low-lying quantum states in several nuclei with an even number of protons and neutrons, characterized by a total angular momentum (spin) and parity of $I^{\pi} = 3^{-}$, suggests that these nuclei are exhibiting octupole collectivity. Two such level schemes are shown in Fig. 2.16. For octupole vibration (dynamic octupole deformation), fast E1 transitions will be present only from the negative parity partner to the positive parity partner. However, for a stable octupole deformation (pear-shaped nuclei), interleaved E1 transitions are expected between the alternate parity bands as shown in Fig. 2.17.

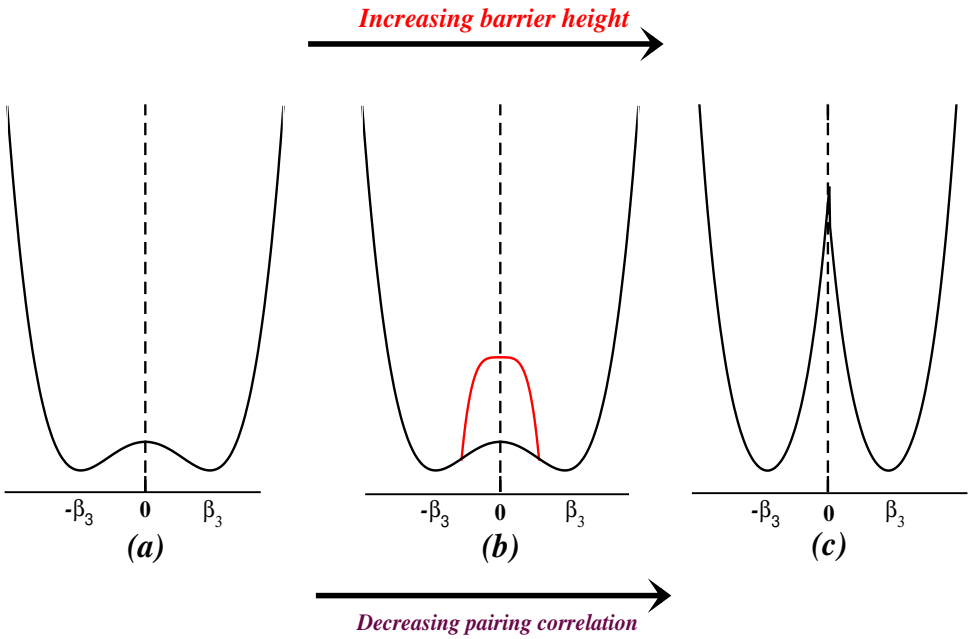

Figure 2.15: The pictorial representation of the nuclear potential energy as a function of octupole deformation. The figure demonstrates how the barrier height between the two minima increases with the decrease of pairing interactions.

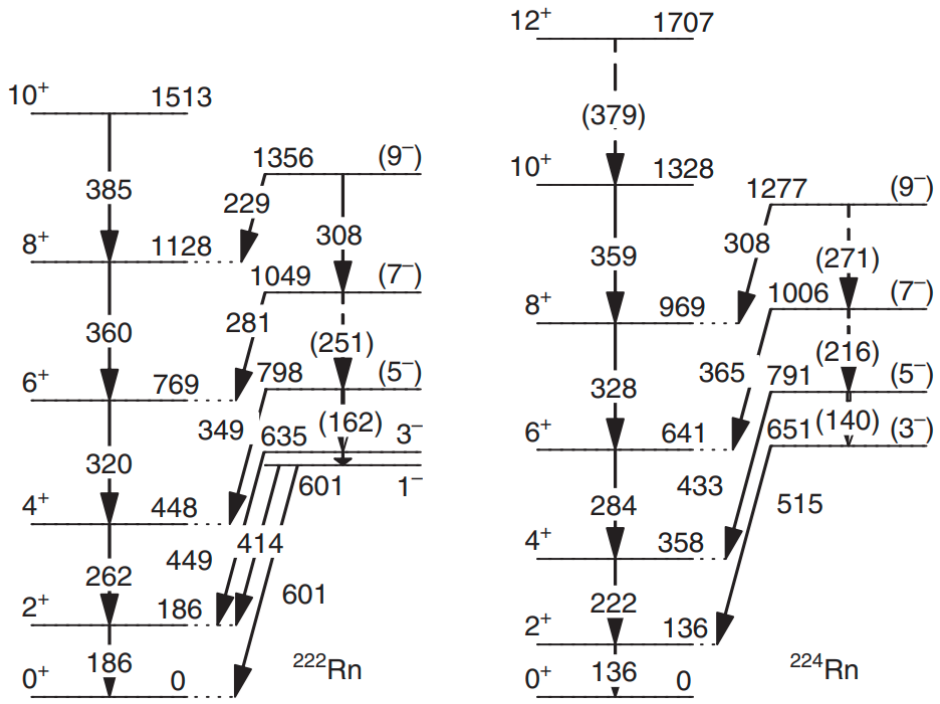

Figure 2.16: Experimental level schemes of dynamic octupole deformed nucleus showing only unidirectional E1 transitions decaying from negative to positive parity partner [43].

The alternate bands have been observed in a few nuclei of the Actinide and Lanthanide mass regions. In these mass regions, B(E1) values vary from 10^{-4} to 10^{-2} w. u. (single

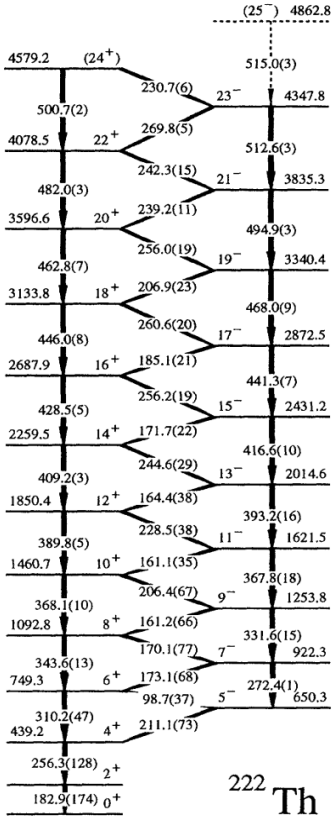

Figure 2.17: The level schemes for a stable octupole deformed nuclei ^{222}Th, showing the interleaving of the E1 transitions [44].

particle unit). Usually, retardation in B(E1) values is more than 10^6 w.u. An increased E1 transition strength between the opposing parity levels is a signature of an intrinsic electric dipole moment [44, 45]. It arises due to the separation between the centre of mass and the centre of charge as the concentration of protons is higher in the region of higher curvature, which is the narrower end of the pear [46]. For a system that is axially deformed, $\langle x \rangle = \langle y \rangle = 0$ and the z-axis possesses the inherent dipole moment. There is a straightforward correlation between the inherent dipole moment D_0 of state I and the reduced transition probability B(E1), assuming the axial shape of the nuclei [45]:

$$B(E1; IK \rightarrow I'K) = \frac{3}{4\pi} D_0^2 \langle IK10|I'K\rangle^2 \tag{2.30}$$

Although it may not always be possible to determine the B(E1) value experimentally, the D_0 value can usually be obtained from the B(E1)/B(E2) branching ratios, where B(E2) is

given by:

$$B(E2; IK \rightarrow I'K) = \frac{5}{16\pi} Q_0^2 \langle IK20|I'K\rangle^2 \tag{2.31}$$

where Q_0, the intrinsic quadrupole moment, can be found from the B(E2) rates for the $2^+ \rightarrow 0^+$ or $3^- \rightarrow 1^-$ as the value is assumed to be constant across the two alternating parity bands.

The rotational behaviour of reflection-asymmetric nuclear shapes can be explored more quantitatively by plotting the spin-dependent signature splitting index (S(I)) proposed by Zamfir and Casten [47]. The quantity is defined by

$$S(I) = \frac{(E(I) - E(I-1)) - (E(I-1) - E(I-2))}{E_2^+} \tag{2.32}$$

For lower spin levels, the negative parity partner is shifted to higher energies with respect to the positive parity partner. The critical angular momentum at which $S(J) \approx 0$ is denoted by the critical spin (I_c) (shown in Fig. 2.18) which signifies the onset of strong octupole correlations.

Alternatively, the ratio of the rotational frequencies of the positive and negative parity partners are defined as follows:

$$\frac{\omega_-(I^-)}{\omega_+(I^+)} = 2\frac{E(I+1)^- - E(I-1)^-}{E(I+2)^+ - E(I-2)^+} \tag{2.33}$$

For stable octupole deformation, this frequency ratio should approach one as shown in Fig. 2.18. This is a rare phenomenon in even-even nuclei and the static octupole deformation has only been observed in a few even Radium and Thorium isotopes of $A \approx 220$ (for example ^{224,226}Th, ^{226}Ra), for which this limiting value has been observed [48].

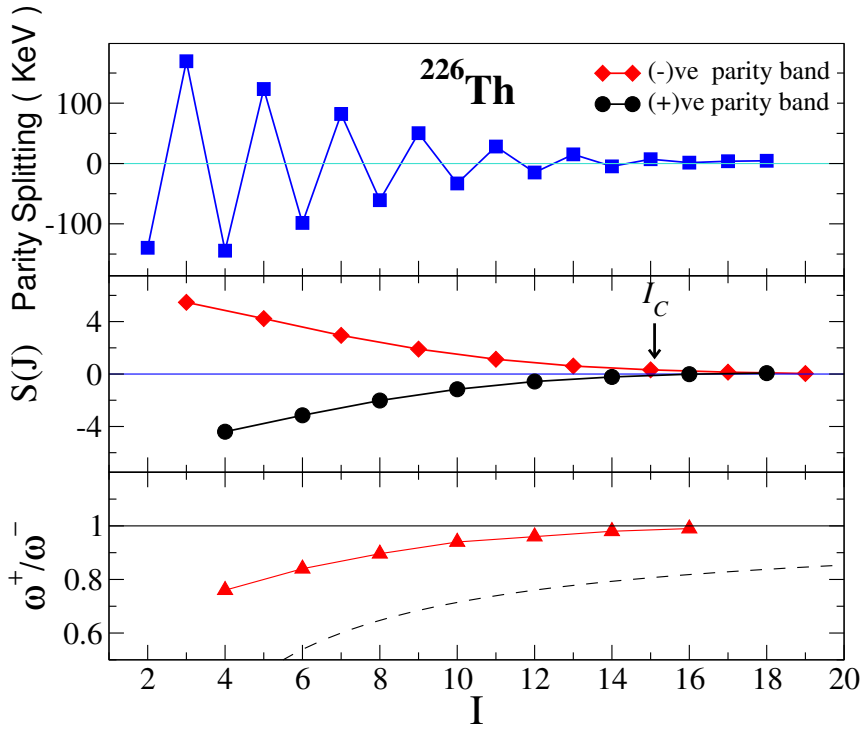

Figure 2.18: Parity splitting (keV), S(J) and the ratio of rotational frequency plotted as a function of spin (I) for ^{226}Th. At I = 15$\hbar$, also denoted at I_c, S(J) as well as parity splitting nearly becomes zero, which signifies the onset of strong octupole correlations.

2.4.2 Axial asymmetry

The inclusion of the $Y_{2\mu}$ term in Eq. 2.1 breaks the axial symmetry in a quadrupole-deformed nucleus, which leads to the triaxial shape. The experimental signatures of triaxiality are based on the observation of two phenomena, namely.

i) Wobbling mode of excitation

ii) Breaking of the chiral symmetry

Nuclear wobbling

The wobbling motion of a triaxial nucleus was first discussed by Bohr and Mottelson [1]. There are three unequal moments of inertia in the triaxial nucleus along the three principal axes: medium, long, and short. To minimize its rotational energy, a triaxial nucleus

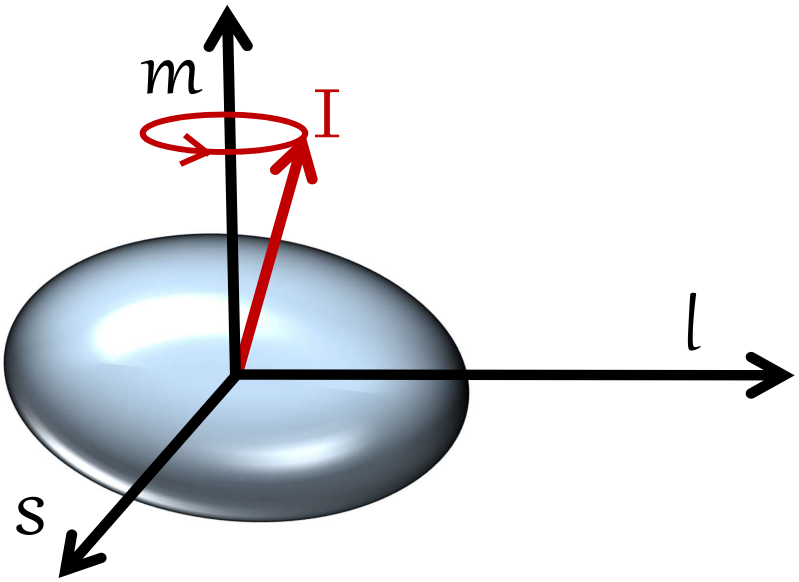

Figure 2.19: Pictorial representation of a simple wobbler where l, m, and s correspond to the long, medium, and short axes. I is the total angular momentum of nuclei, which processes about the medium axis.

attempts to rotate about the medium axis, which has the maximum moment of inertia. A precession of the body-fixed total angular momentum with respect to the medium axis can be reproduced by the non-zero values of the other two moments of inertia along, that is, along the short and long axes. This is termed a “simple” wobbler (Fig. 2.19). It is possible to express the energy levels in the wobbling band as

$$E = E_{rot} + (n_\omega + 1/2)\hbar\omega_{wob} \tag{2.34}$$

where n_ω represents the wobbling quanta, E_{rot} is the rotational energy resulting from the rotation around the medium axis, and $\hbar\omega_{wob}$ is the wobbling frequency with wobbling energy $E_{wob} = \hbar\omega_{wob}$. However, no such "simple" wobbling motion with zero quasi-particle configuration has been observed for even-even nuclei.

The wobbling motion is only seen in a few odd-A nuclei and is considered one of the experimental signatures of triaxiality in odd-mass nuclei. This motion can be classified into two types based on the coupling of the angular momenta of the triaxial core and the odd particle [49]:

I. Transverse wobbling (TW)

II. Longitudinal wobbling (LW)

The angular momentum of the valence particle aligns along the medium axis in the case of LW motion and either with the short or long axes in the case of TW motion (Fig. 2.20). For LW, it has been noted that the measured wobbling frequency increases with angular momentum, I. On the other hand, for all TW that have been detected so far, the wobbling frequency has been found to decrease with I. The energy differences between the $n_\omega = 0$ yrast band and the $n_\omega = 1$ wobbling partner band can be used to estimate the experimental wobbling frequency ω_{wob} as follows:

$$E_{wob} = \hbar\omega_{wob} = E(I, n_\omega = 1) - \frac{E(I+1, n_\omega = 0) + E(I-1, n_\omega = 0)}{2} \tag{2.35}$$

where the level energy with angular momentum I is denoted by E(I). The experimental

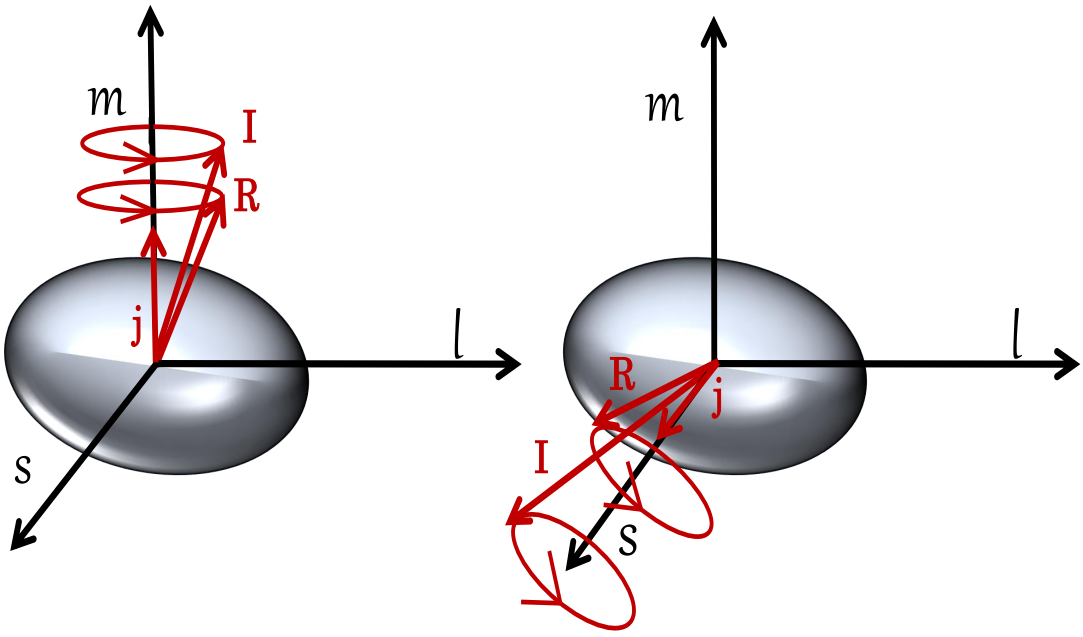

Figure 2.20: Pictorial representation of a longitudinal (left) and a transverse (right) wobbler. j, R and I are the odd particle, rotor and total angular momenta, respectively.

indicators of the wobbling motion in nuclei are as follows:

- The wobbling motion is represented by a series of rotational bands on top of the vibrational states corresponding to the wobbling quanta n_ω.

- The primary rotational band is connected to the wobbling bands via ΔI = 1 transitions whose M1+E2 mixing ratio is significantly larger and are predominantly E2 in nature.

- The ratio of the reduced transitions strengths of the intraband to interband E2 transitions, i.e., $B(E2)_{out}/B(E2)_{in}$, is large.

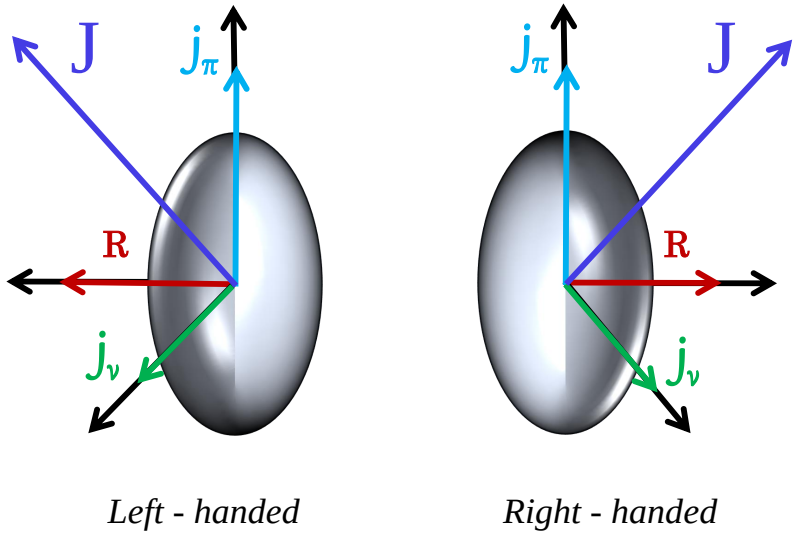

Figure 2.21: Schematic representation of left and right handed chiral systems for a triaxial odd-odd nucleus. R, j_ν, j_π and J are the rotor, neutron, proton and total angular momentum, respectively.

Spin chirality

Frauendorf and Meng made the first prediction on spin chirality in nuclei in 1997 [51]. This phenomenon arises in triaxially deformed nuclei containing high-j valence holes and particles. Given the torus-like density distribution of the valence particles, $\mathbf{j}_p$, which maximizes overlap with the triaxial core, the angular momentum contribution from them is aligned along the short axis. The maximum overlap of the dumbbell shape density distribution with the triaxial core causes the high-j hole angular momentum $\mathbf{j}_h$ to align along the long axis. The largest moment of inertia results from the core angular momentum vector R tending to align along the intermediate axis. Depending on the direction of the

core angular momenta **R**, these three mutually perpendicular angular momenta in the lab frame can produce two systems of opposite-handedness, right-handed and left-handed, as shown in Fig. 2.21. The total angular momentum, **J** does not lie in any plane formed by the three angular momentum vectors, $\mathbf{j}_p$, $\mathbf{j}_h$, and **R**. A pair of degenerate doublet dipole $\Delta I = 1$ bands of the same parity are obtained by restoring the chiral symmetry in the laboratory frame. The first experimental observation of nuclear chiral doublet bands was observed in ^{134}Pr [52] and later was interpreted as spin chirality.

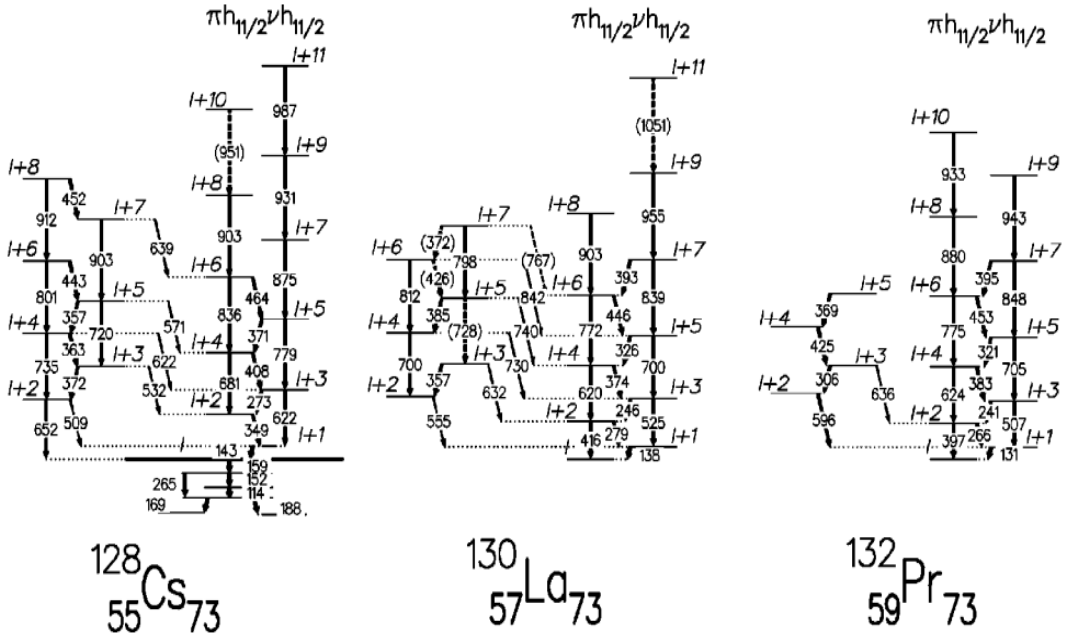

Figure 2.22: Partial level schemes showing chiral doublet bands in N = 73 isotones [50].

Spin chirality has several experimental fingerprints:

1. Using the same single-particle arrangement, observation of an almost degenerate dipole band with similar spin and parity (For example, see Fig. 2.22). The planer solution admixtures cause a higher energy separation between the doublet bands close to the band-head.

2. Because there is no Coriolis interaction between perpendicularly aligned core and particle-hole angular momenta, the quantity S(I) [defined as S(I) = [E(I) - E(I - 1)]/2I] should be independent of spin in the chiral region and the chiral doublet bands should display smooth variation in energy.

3. For these bands, all the physical observables including quasiparticle alignment, the

moment of inertia, and electromagnetic transition rates should be similar. These observations validate the identical configurations for the chiral partner bands.

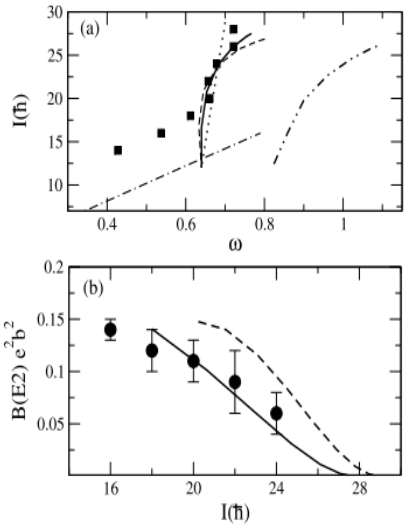

Figure 2.23: The measured I(ω) plot (shown in (a)) and B(E2) rates (shown in (b)) in ^{110}Cd. The calculated B(E2) values for AMR + rotation and pure AMR are shown in panel (b) by the solid and dotted lines, respectively [53].

2.4.3 Interplay between single-particle and collective contributions

In many nuclei, the high spin level structures exhibit the interplay or coexistence between the two different mechanisms discussed in this section. For example, in ^{104}Ag, the signature bands show the falling trend of B(M1)/B(E2) rates [27] thereby, showing the coexistence of shears mechanism and collective rotation. In ^{106}Ag, the reported negative parity band was found to originate due to the interplay between the shears mechanism and collective rotation of the core [54]. The work in Ref. [55] demonstrated for the first time that the generation of high angular momentum states (beyond 18^{+}) in the ^{110}Cd yrast band is caused by the interaction between antimagnetic and core rotation. The measured B(E2) rates, which exhibit a more gradual fall (shown in Fig. 2.23) in comparison to the pure AMR bands in ^{106,108}Cd, provide strong evidence for this effect.

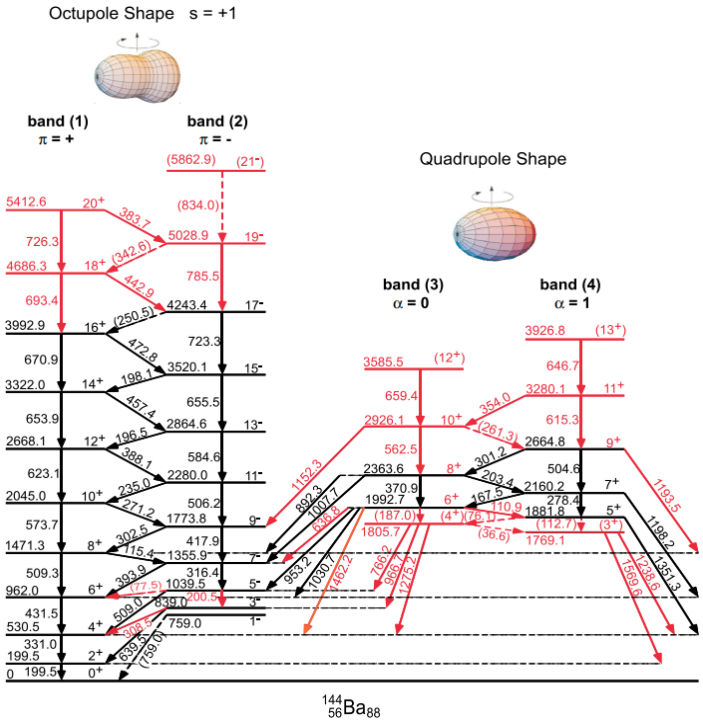

Figure 2.24: The partial level scheme of ^{144}Ba illustrating both symmetric and reflection asymmetric band structures. Figure taken from Ref. [56].

An already established transverse wobbler ^{135}Pr [57] demonstrates chiral band-like structures also. The angular distributions have been precisely measured to demonstrate the predominant magnetic dipole character of the $\Delta I = 1$ transitions between the chiral-doublet bands. This observation has established the triaxial nature of nuclear shapes on a more solid foundation than ever, as both signatures of triaxiality in nuclei – chirality and wobbling–have been observed in the same nucleus [58]. On the other hand, in the neutron-rich ^{144}Ba, an octupole band structure with a reflection asymmetric shape and a non-yrast quadrupole band structure with a reflection symmetric shape have been identified. This result demonstrates the coexistence of symmetric and asymmetric reflection shapes (shown in Fig. 2.24) [56].

This chapter briefly discussed the theoretical frameworks and the symmetry arguments, which have been used to explain observed properties of ^{100,101}Ru, ^{98}Mo and ^{105}Pd. Next, I discuss the experimental and analysis approaches employed to study the high spin characteristics of these nuclei.

Bibliography

[1] Bohr and B R Mottelson. Nuclear structure. volume ii. nuclear deformations.

[2] P. Ring and P. Schuck. The nuclear many-body problem. Springer-Verlag, New York, 1980.

[3] Aage Bohr and Ben R. Mottelson. Rotational states in even-even nuclei. Phys. Rev. C **90**:717–719, May 1953.

[4] D. R. Inglis. Particle derivation of nuclear rotation properties associated with a surface wave. Phys. Rev., **96**:1059–1065, Nov 1954.

[5] D. R. Inglis. Dynamics of nuclear deformation. Phys. Rev. C **97**:701–706, Feb 1955.

[6] Stefan Frauendorf. Spontaneous symmetry breaking in rotating nuclei. Rev. Mod. Phys., 73:463–514, Jun 2001.

[7] Arnold J. Sierk. Macroscopic model of rotating nuclei. Phys. Rev. C, **33**:2039–2053, Jun 1986.

[8] A.V. Afanasjev and I. Ragnarsson. Gradual loss of collectivity in rotational bands in the A $\approx$ 110 (Z $\approx$ 50, N $\approx$ 60) mass region. Nucl. Phys. A, **591**(3):387–420, 1995.

[9] C. M. Petrache *et. al.* Evolution from spherical single-particle structure to stable triaxiality at high spins in ^{140}Nd. Phys. Rev. C **72**:064318, Dec 2005.

[10] C. M. Petrache *et. al.* Tilted axis rotation, candidates for chiral bands, and wobbling motion in ^{138}Nd. Phys. Rev. C, **86**:044321, Oct 2012.

[11] G. N. Sylvan *et. al.* Deformation driving intruder orbitals in ^{77}Kr. Phys. Rev. C, 56:772–781, Aug 1997.

[12] C. M. Petrache *et. al.* Switch from short-axis to intermediate-axis rotation in ^{138}Nd. Phys. Rev. C, **88**:051303, Nov 2013.

[13] M. J. A. de Voigt, J. Dudek, and Z. Szymanski. High-spin phenomena in atomic nuclei. Rev. Mod. Phys., **55**:949–1046, Oct 1983.

[14] R. Casten. Nuclear Structure from a Simple Perspective. Oxford science publications. Oxford University Press, 2000.

[15] Maria G. Mayer. On closed shells in nuclei. Phys. Rev., **74**:235–239, Aug 1948.

[16] Maria Goeppert Mayer. On closed shells in nuclei. ii. Phys. Rev., **75**:1969–1970, Jun 1949.

[17] Otto Haxel, J. Hans D. Jensen, and Hans E. Suess. On the "magic numbers" in nuclear structure. Phys. Rev., **75**:1766–1766, Jun 1949.

[18] Sven Gösta Nilsson. Binding states of individual nucleons in strongly deformed nuclei. Technical Report 16, 1955.

[19] M. Ogawa, R. Broda, K. Zell, P. J. Daly, and P. Kleinheinz. Lowest 2+ state in $^{146}_{64}Gd_{82}$ and the energy gap at Z = 64. Phys. Rev. Lett., **41**:289–292, Jul 1978.

[20] Subhendu Rajbanshi. Generation of Angular Momentum for Weakly Deformed Nuclei in A $\approx$ 140 Mass Region. PhD thesis, 2016.

[21] R.M. Clark *et. al.* First observation of a collective dipole rotational band in the A = 200 mass region. Physics Letters B, **275**(3):247–251, 1992.

[22] G. Baldsiefen *et. al.* Oblate collective bands in ^{199}Pb and ^{200}Pb. Physics Letters B, **275**(3):252–258, 1992.

[23] M. Neffgen *et. al.* Lifetimes of shears bands in ^{199}Pb. Nucl. Phys. A, **595**(4):499–512, 1995.

[24] H. Hübel. Magnetic rotation in nuclei. Progress in Particle and Nuclear Physics, **54**(1):1–69, 2005.

[25] S. Frauendorf. Tilted cranking. Nucl. Phys. A, **557**:259–276, 1993.

[26] A. O. Macchiavelli *et. al.* Semiclassical description of the shears mechanism and the role of effective interactions. Phys. Rev. C, **57**:R1073–R1076, Mar 1998.

[27] P. Datta *et. al.* Observation of magnetic rotation in odd-odd ^{104}Ag. Phys. Rev. C, **69**:044317, Apr 2004.

[28] S. Chmel, S. Frauendorf, and H. Hübel. Deformation parameters and transition probabilities for shears bands in Pb isotopes. Phys. Rev. C, **75**:044309, Apr 2007.

[29] P. H. Regan *et. al.* Anomalous bend-crossings in the N = 57 isotones ^{103}Pd and ^{105}Cd. Journal of Physics G, Nuclear and Particle Physics, **19**(11): L157–L162, 1993.

[30] S. Zhu *et. al.* Investigation of antimagnetic rotation in ^{100}Pd. Phys. Rev. C, **64**:041302, Sep 2001.

[31] N. Rather *et. al.* Antimagnetic rotation in ^{104}Pd. Phys. Rev. C, **89**:061303, Jun 2014.

[32] S. Rajbanshi *et. al.* Antimagnetic rotation in the shape-phase transition point nucleus ^{82}Kr. Phys. Rev. C, **109**:064308, Jun 2024.

[33] W. Nazarewicz, M.A. Riley, and J.D. Garrett. Equilibrium deformations and excitation energies of single-quasiproton band heads of rare-earth nuclei. Nuclear Physics A, **512**(1):61–96, 1990.

[34] Ikuko Hamamoto. Signature inversion at low spins of odd-odd nuclei: Triaxial shape? Physics Letters B, **235**(3):221–224, 1990.

[35] Samuel M. Harris. Higher order corrections to the cranking model. Phys. Rev., **138**:B509–B513, May 1965.

[36] J. A. Sheikh and K. Hara. Triaxial projected shell model approach. Phys. Rev. Lett., **82**:3968–3971, May 1999.

[37] Nazira Nazir *et. al.* Triaxial projected shell model approach for negative parity states in even-even nuclei. Phys. Rev. C, **108**:044308, Oct 2023.

[38] Nazira Nazir and J. A. Sheikh. Private communication.

[39] P A Butler. Octupole collectivity in nuclei. Journal of Physics G: Nuclear and Particle Physics, **43**(7):073002, Jun 2016.

[40] P. A. Butler and W. Nazarewicz. Intrinsic reflection asymmetry in atomic nuclei. Rev. Mod. Phys., **68**:349–421, Apr 1996.

[41] P. Butler. Pear-shaped atomic nuclei. Proceedings of the Royal Society A: Mathematical, Physical and Engineering Sciences, **476**:20200202, 07 2020.

[42] I. Ahmad and P. A. Butler. Octupole shapes in nuclei. Ann. Rev. Nucl. Part. Sci., **43**:71–116, 1993.

[43] P. A. Butler *et. al.* The observation of vibrating pear shapes in Radon nuclei. Nature Communications, **10**(1):2473, Jun 2019.

[44] J. F. Smith *et. al.* Contrasting behaviour in octupole structures observed at high spin in ^{220}Ra and ^{222}Th. Phys. Rev. Lett., **75**:1050–1053, Aug 1995.

[45] P.A. Butler and W. Nazarewicz. Intrinsic dipole moments in reflection-asymmetric nuclei. Nucl. Phys. A, **533**(2):249–268, 1991.

[46] Aage Bohr and Ben R Mottelson. Nuclear Structure. World Scientific Publishing Company, 1998.

[47] N. V. Zamfir, P. von Brentano, and R. F. Casten. Phenomenological signature for the onset of strong octupole correlations. Phys. Rev. C, **49**:R605–R607, Feb 1994.

[48] B. Ackermann *et. al.* Collective E1 transitions in even-A Ra, Th, and U nuclei. Nucl. Phys. A, **559**(1):61–82, 1993.

[49] S. Frauendorf and F. Dönau. Transverse wobbling: A collective mode in odd-A triaxial nuclei. Phys. Rev. C, **89**:014322, Jan 2014.

[50] T. Koike *et. al.* Observation of chiral doublet bands in odd-odd N = 73 isotones. Phys. Rev. C, **63**:061304, May 2001.

[51] S. Frauendorf and Jie Meng. Tilted rotation of triaxial nuclei. Nucl. Phys. A, **617**(2):131–147, 1997.

[52] K. Starosta *et. al.* Chirality in odd–odd triaxial nuclei. Nucl. Phys. A, **682**(1):375–386, 2001.

[53] L.K. Kostov *et. al.* Absolute E1 and E2 transition rates in ^{110}Cd. Eur. Phys. J. A, **2**(3):269– 273, 1998.

[54] B. Das *et. al.* Three proton hole structures in ^{106}Ag. Phys. Rev. C, 93:064322, Jun 2016.

[55] Santosh Roy *et. al.* Systematics of antimagnetic rotation in even–even Cd isotopes. Physics Letters B, **694**(4):322–326, 2011.

[56] S. J. Zhu *et. al.* Coexistence of reflection asymmetric and symmetric shapes in ^{144}Ba. Phys. Rev. Lett., **124**:032501, Jan 2020.

[57] N. Sensharma *et. al.* Two-phonon wobbling in ^{135}Pr. Physics Letters B, **792**:170–174, 2019.

[58] N. Sensharma *et. al.* Evolution of chirality from transverse wobbling in ^{135}Pr, arXiv:2403.10749 2024.

Chapter 3

Experimental Techniques

This chapter covers the various experimental aspects related to the in-beam experiments, data acquisition, and offline analysis used in the thesis. The technique of discrete γ-spectroscopy follows the scheme:

1. Populating the high spin states of the nucleus of interest through the fusion-evaporation reaction involving the appropriate choice of the target and the accelerated projectile nucleus.

2. Use of an array of gamma detectors with very high resolution and adequate solid angle coverage.

3. Use of a digital data acquisition system for the collection of time-stamped data from which γ-γ coincidence events can be reconstructed offline.

4. Offline data sampling techniques are used to prepare the data samples for the measurements of the various properties of the gamma rays, which originate from the decay of the excited levels.

5. Obtain the spectroscopy information of the nuclear levels through these measurements.

In this chapter, I shall give a short description of each of the above-mentioned steps.

3.1 Fusion-evaporation reaction

In a fusion-evaporation reaction, two atomic nuclei merge to form a compound nucleus as shown pictorially in Fig. 3.1. The fusion process requires accelerated projectile nuclei, whose energy is adequate to overcome the repulsive Coulomb force between the positively charged protons within the target and projectile nuclei. The compound nucleus is formed at high excitation energy. In order to stabilize, it emits multiple particles, such as neutrons, protons or α particles, through the process known as evaporation. When the excitation energy falls below the threshold of particle emission, discrete γ-rays are emitted and the different residual nuclei reach their ground state as shown in Fig. 3.2. These gamma decays predominantly follow the "yrast line", which refers to the sequence of nuclear states with the lowest possible energy for a given value of angular momentum. The fusion-evaporation method offers several benefits, including the ability to synthesize a nucleus with specific numbers of protons or neutrons, transfer a desired amount of angular momentum, and combine these features. These capabilities allow researchers to investigate various structural phenomena associated with the nucleus, based on their specific areas of interest.

3.2 Interactions of γ-ray with matter

The emitted γ-rays are detected through their interactions with the detector materials [1]. The three interactions are i) Photoelectric Absorption, ii) Compton Scattering and iii) Pair Production.

Photoelectric Absorption : During the photoelectric process, a photon interacts with the absorber atom's electron, which is knocked out of one of the atom's shells and deposits all of its energy. For a typical γ - ray, the photoelectron is most likely to come out of the K shell, whose binding energy typically ranges from a few keV for low-atomic-number

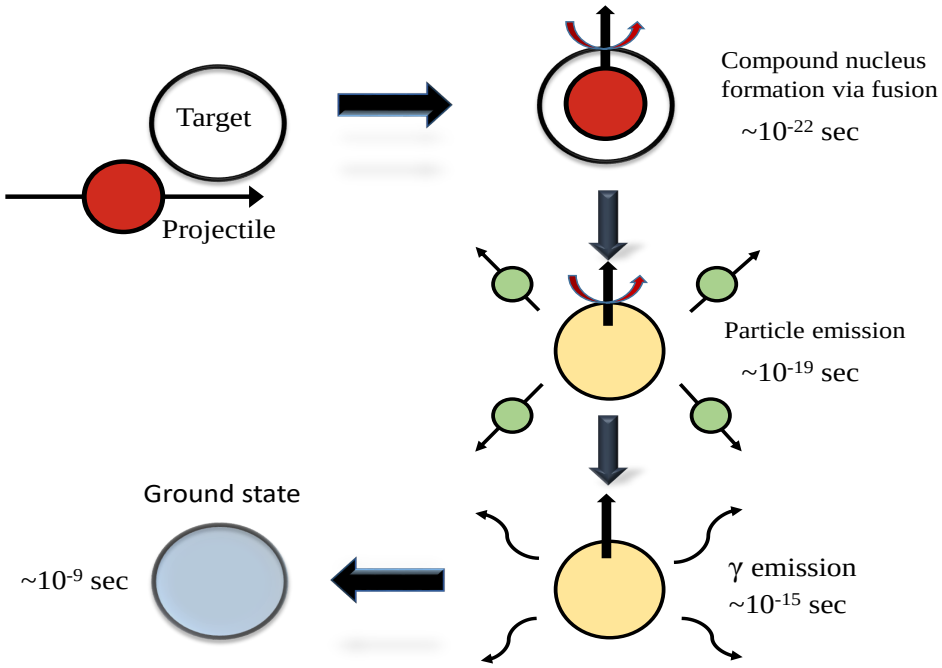

Figure 3.1: Schematic diagram depicting the mechanism of fusion evaporation reaction.

(Z) materials to tens of keV for high - Z materials. The incident photon energy (hν), the electron's binding energy in its initial shell ϕ_e and the electron's kinetic energy are related by:

$$E_e = \hbar\omega - \phi_e \tag{3.1}$$

The term ϕ_e is also referred to as the work function of the material.

The photoelectric process is the dominant interaction mode for gamma rays (or X-rays) with lower energy, and its cross-section increases when the absorber material has a higher atomic number Z.

Compton Scattering: Compton scattering is a primary mechanism for the interaction between incident γ - ray photons and electrons in the absorbing material. The incoming photon is deflected at an angle θ with respect to its initial direction during Compton scattering. The recoil electron receives a fraction of the energy from the photon. The energy

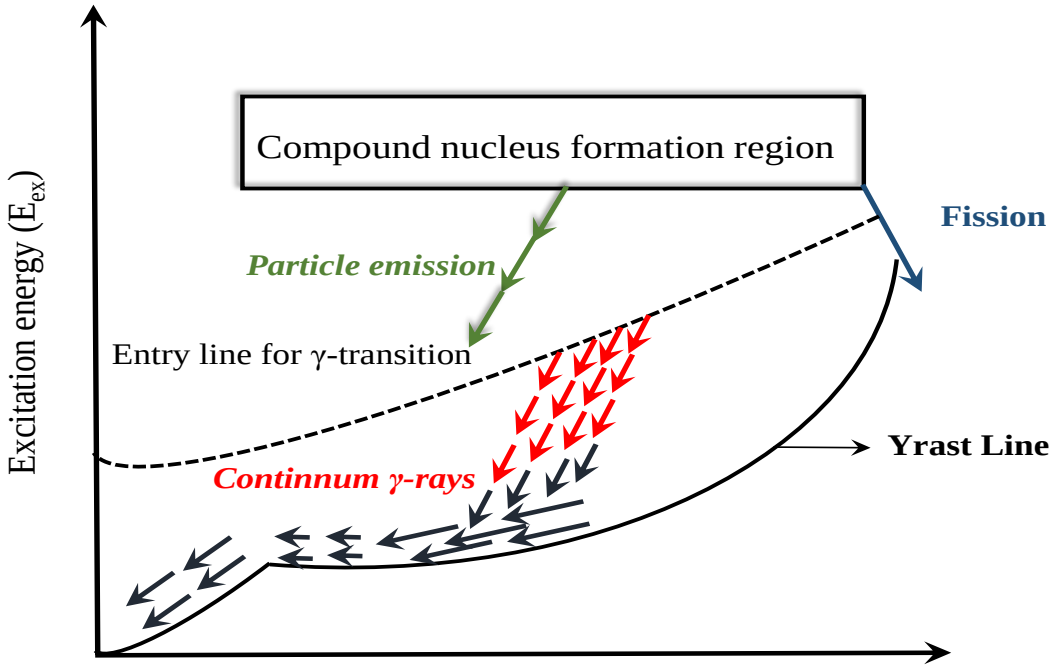

Figure 3.2: The decay scheme of a compound nucleus.

delivered to the electron can vary from zero to a substantial fraction of the incident γ-ray's energy E_γ since scattering can happen at any angle. These scattered electron, in turn, gets absorbed in the detector and produces a continuous energy spectrum, if the scattered γ-ray escapes the volume of the detector. These events produce the unwanted Compton background and can be suppressed by using an anti-compton shield. On the other hand, if the γ-ray deposits its full energy through multiple scattering and photoelectric absorption, then the photopeak is generated.

The energy $E_\gamma^{'}$ is carried by the scattered photon and can be determined by the following equation:

$$E_\gamma^{'} = \frac{E_\gamma}{1 + \frac{E_\gamma}{m_e c^2}(1 - \cos\theta)} \tag{3.2}$$

The probability of Compton scattering per absorber atom is determined by electron numbers present as potential scattering targets, and hence, exhibits a linear increase with the atomic number (Z) of the absorber [1].

Pair Production: An electron-positron (e^- - e^+) pair can be created by a γ - ray interacting

with detector material, provided that the initial γ - ray energy is greater than twice the electron's rest mass energy (1.02 MeV). The extra energy beyond the 1.02 MeV gets shared as the kinetic energies of the positron and electron. Within a few millimetres of travel, the generated e^- - e^+ pair will get absorbed by the detector material. Because of its extremely short lifetime, the e^+ annihilates with an electron of the medium to produce two γ - rays of 511 keV, which in turn experience the Compton scattering in the detector volume. There is no straightforward formula for the probability of pair production per nucleus, but it is roughly proportional to the square of the atomic number of the absorber. The three above-mentioned processes are shown pictorially in Fig. 3.3

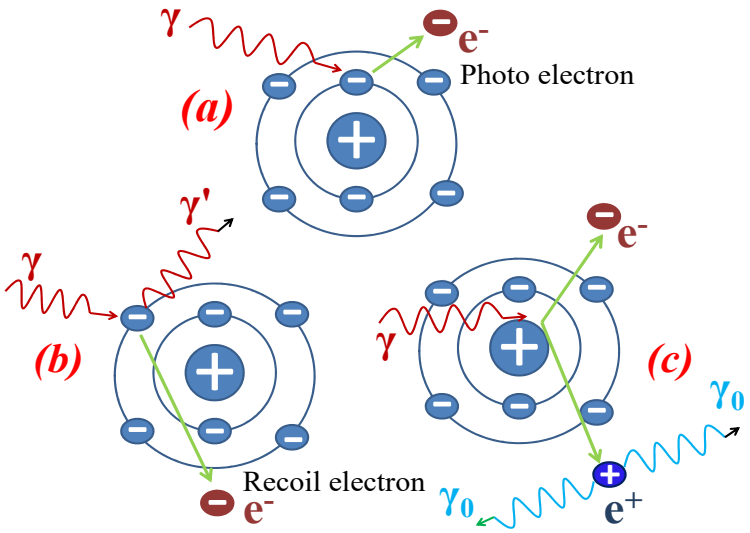

Figure 3.3: The three mechanisms through which a γ-ray interacts with matter are illustrated as follows: (a) Photoelectric Effect; (b) Compton Scattering; and (c) Pair Production.

3.3 Experimental set-up

The experimental setup entirely depends on the nuclei that need to be populated and in turn on the choice of target, projectile and energy of the beam. In the present thesis work, three experiments were conducted, two of them with α beam from K-130 cyclotron at

Variable Energy Cyclotron Centre (VECC), Kolkata; another one with ^{12}C beam from Pelletron at TIFR, Mumbai with currents in the range of pico-amperes to nano-amperes. Using light-ion projectiles has several advantages over heavier counterparts. One major advantage is the large production cross-section of nuclei of interest with minimal contamination from neighbouring channels. Light-ion beams also facilitate the study of non-yrast bands leading to the horizontal spectroscopy and identification of exotic excitation modes at low spins. However, heavier ions can populate higher angular momentum states, and thus, are very useful in the investigation of nuclear structures at high spins. Thus, the choice of beam is crucial for the problem one wants to address.

To ensure high statistics and distinguish between γ-rays that are close in energy, a γ-ray detector requires both high efficiency and high resolution. However, different types of detectors have trade-offs between these properties. For instance, High-Purity Germanium (HPGe) semiconductor detectors have excellent energy resolution but low detection efficiency. On the other hand, scintillation detectors made of Sodium Iodide (NaI) or Bismuth Germanate ($Bi_4Ge_3O_{12}$) (BGO) have high efficiency but poor energy resolution. In order to achieve better results, a combination of both semiconductor and scintillation detectors is commonly used in spectroscopic studies.

3.3.1 Clover Detectors

The effectiveness of a gamma spectrometer is determined by its ability to provide high energy resolution, photo-peak detection efficiency at higher energies, and identification of photo peaks from the background. In γ-spectroscopy, semiconductor detectors are preferred due to their superior resolution. In a semiconductor detector, a reverse bias is applied across the p-n junction diode, and radiation incident on the depletion region produces electron-hole pairs that move toward the respective collector ends under the influence of the applied electric field, producing a corresponding electric current. To achieve a good energy resolution, the work function, which is the average energy required

to create an electron-hole pair in HPGe detectors, needs to be low. However, with a value of about 3 eV, it is not possible to operate the HPGe detectors at room temperature due to the large dark current. Therefore, the detectors are cooled down to 77 K using liquid nitrogen to reduce thermal excitation across the valence-conduction band gap. A higher resolution is achieved with a greater depletion width, which is inversely proportional to the doping (impurity) concentration, leading to the 'high-purity' Ge detectors [1]. In reactions induced by heavy ions, the energy resolution is affected by Doppler broadening. Therefore, in addition to having high detection efficiency, gamma detectors with a narrow opening angle are necessary to minimize this broadening.

To address these issues, Clover detectors have been developed, which consist of an arrangement of four 'high-purity' Ge crystals housed in a single cryostat like a clover leaf as seen in Fig. 3.4. Each crystal is typically 50 mm in diameter and 70 mm in length. The crystals are closely packed with an average Ge-Ge distance of about 0.2 mm. The active volume of commercially available clover detectors is $\approx$ 475 cm^3, which is about 89% of the geometric volume. This design overcomes the Doppler broadening problem while maintaining high detection efficiency for gamma energies in the MeV range in the 'add-back' mode (discussed later in section 1.4.1).

3.3.2 Detector Geometry at INGA

The Indian National Gamma Array (INGA) is a collaboration between the Saha Institute of Nuclear Physics (SINP), Tata Institute of Fundamental Research (TIFR), Bhabha Atomic Research Centre (BARC), Variable Energy Cyclotron Centre (VECC), UGC DAE Consortium for Scientific Research, Inter University Accelerator Center (IUAC), and several universities across India. INGA is a multi-detector array consisting of Compton-suppressed Clover detectors. The anti-compton shield consists of sixteen Bismuth Germanate (BGO) scintillators, which surround the Clover crystals entirely. The Compton events are suppressed by recording the events where only the Clover detector has fired.

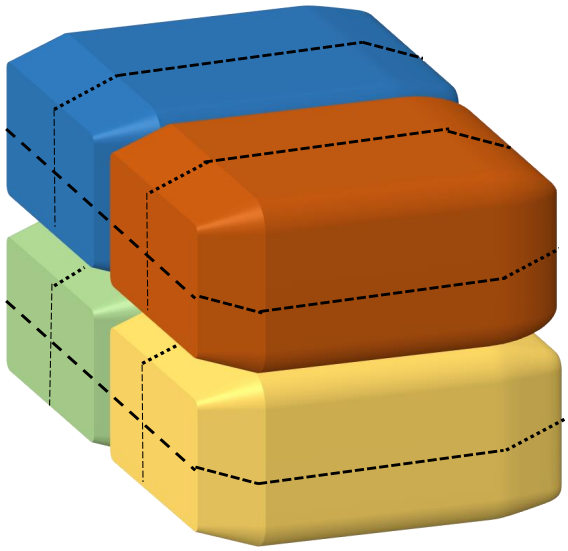

Figure 3.4: Schematic diagram of a typical clover detector. The four crystals have been depicted in distinct colours.

At TIFR, the detector mounting stand accommodates 24 Compton-suppressed Clover detectors, strategically positioned at six different angles: three detectors each at 23°, 40°, 65°, 115°, 140° and 157°, and six detectors positioned at 90° relative to the beam axis [2]. Similarly, at VECC, the stand supports 12 clover detectors arranged at three different angles: three detectors each at 40° and 125° and six detectors positioned at 90° with respect to the beam direction [3]. The experimental set-up of VECC and TIFR are shown in the left and right panels of Fig. 3.5, respectively. The IUAC stand likewise accommodates 24 clover detectors positioned at five distinct angles: four detectors at 32°, 57°, 123°, and 148°, and eight detectors at 90° with regard to the direction of the beam. The actual number of detectors utilized during experiments varied based on availability. In the context of this thesis, in-beam time-stamped data were collected from experiments conducted at TIFR and VECC utilizing INGA as the detection system, comprising of 18 and 11 Compton-suppressed clover detectors, respectively. The arrays at TIFR and VECC have photopeak efficiency of 5% and 4.2% around 1 MeV, respectively.

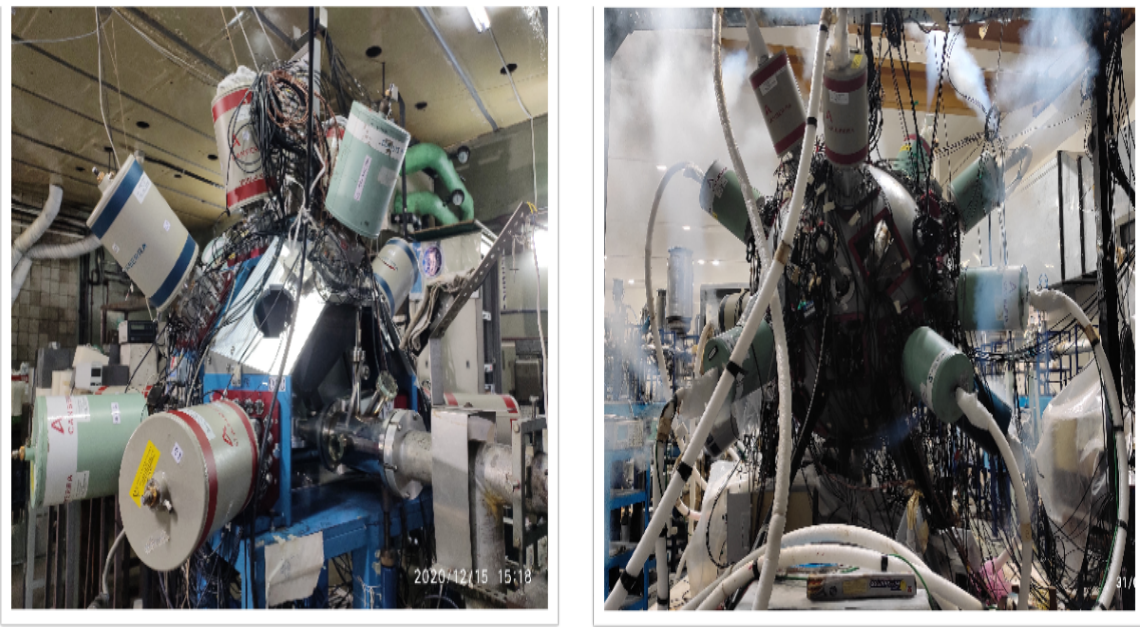

Figure 3.5: Experimental setup of VECC - INGA (left panel) and TIFR - INGA (right panel).

A fast data acquisition system is essential to record energy and timing information (time-stamped events) from all the crystals and to store the in-beam time-stamped data as single or multi-fold events. The detectors positioned at different angles are employed to study the angular distribution, polarization asymmetry, and lifetime of excited nuclear states utilizing the Doppler Shift Attenuation Method (DSAM).

3.3.3 Target

In the first experiment at VECC, a 98% pure self-supporting 2 mg/cm^2 of ^{100}Mo was utilized as the target (shown in Fig. 3.6). In the second experiment, the same target material was used but with an increased thickness of 10 mg/cm^2. For the experiment at TIFR, a 1 mg/cm^2 layer of ^{96}Zr target was used, which was backed by a 9 mg/cm^2 layer of natural Pb. The target was positioned approximately 25 cm from the centre of the array. The thick targets in the second and third experiments, respectively, were employed to

stop the recoiling nuclei in the targets. The energies of γ-rays emitted by the residual nuclei during the stopping process exhibit continuous line shapes due to Doppler shift instead of a sharp peak. These line shapes can be utilized to measure the lifetimes in the sub-picosecond range. The selection of lead (Pb) as the backing material was primarily motivated by two factors: its high atomic number, which ensures a smaller stopping time, and its higher Coulomb barrier compared to the target material, which prevents fusion-evaporation reactions between the thick backing and the incident beam nuclei. However, no backing heavy material could be used for the 45 MeV α beam as the beam energy was above the coulomb barrier for any backing material. Thus, a thick 10 mg/cm^2 target was employed.

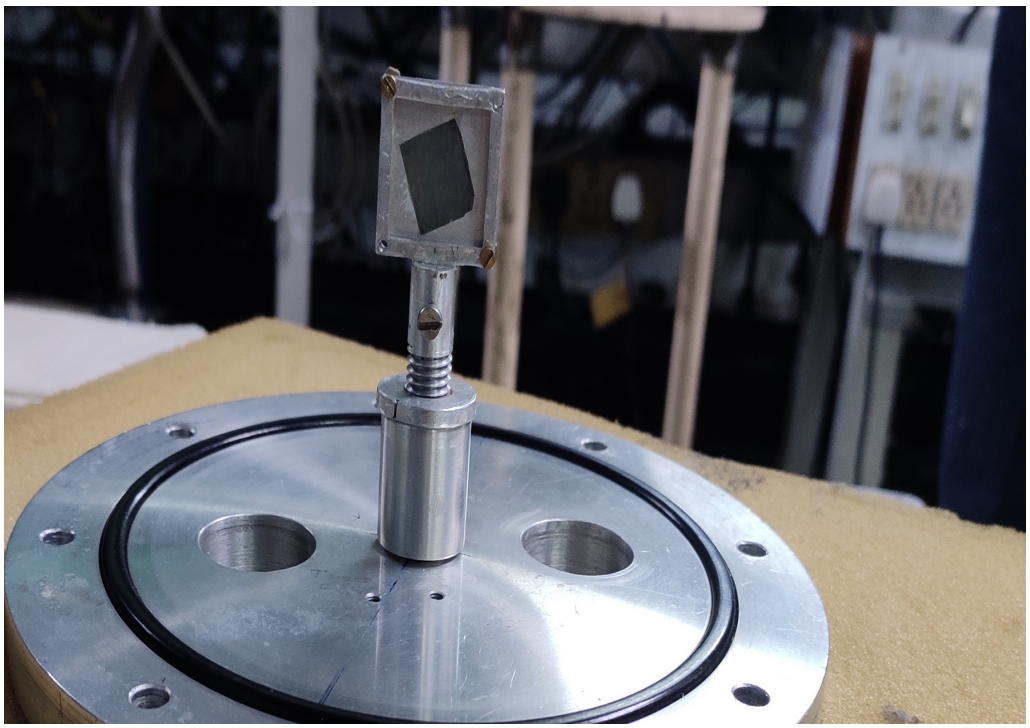

Figure 3.6: The mounting of the self - supporting ^{100}Mo target used in the first experiment at VECC

3.3.4 Data Acquisition

In nuclear spectroscopy, the introduction of digitizer-based pulse processing and data acquisition systems (DAQ) brought a new era of fast and effective experimental setups for massive detector arrays. These facilities collect time-stamped list mode data that is subjected to standard data reduction techniques and analysis. They are also capable of managing increasing event rates, which are frequently found in such arrays at the modern heavy-ion accelerators. It is well known that the events recorded would primarily consist of a single γ-ray transition recorded in a detector without considering time coincidence with any other emission detected in a different detector if there was no need for coincidence on the data acquisition. These events take up sufficiently large storage space and are frequently removed during data reduction. However, a condition of recording data only when two or more detectors have fired simultaneously (within a very small time window) is often implemented to obtain 2-fold or higher order multiplicity events. These data are usually obtained in list mode format, which is an event-by-event log of the detectors firing i.e. detecting and the corresponding energy and timing of the detected pulses. An event is defined by the user-defined (master) trigger condition. In modern spectroscopic studies, this trigger condition is usually based on a predetermined multiplicity of detectors firing simultaneously (within a time frame of approximately 100 ns). Four 32-bit words are recorded in the data for each channel (one crystal of the Clover detector) in the current digitizer system that has detected a pulse in an event. These words include the requisite information utilised in the following reduction and analysis. The first is the identification of the detector (channel) that triggered; this information is taken from the data's Slot ID and Channel Number. The timing of the detected pulse, which is determined from the 48-bit time stamp and the Constant Fraction Discriminator (CFD) value, is the next quantity of interest. A validated pulse's time stamp is latching at the point of threshold crossing on the leading edge of the corresponding fast filter output, measured in relation to a global clock that is initialized at the start of a new run (typically a length of 1800

s). The time stamp on the 250 MHz board is measured in 125 MHz clock ticks, which implies that there should be a minimum of 8 ns between two consecutive time stamps. The energy of the detected pulse, stored as the ADC address, is the final set of information. After sorting the data with a small coincidence window ($\approx$ 100 ns), the events are transformed into matrices of two or three dimensions. The two-dimensional E_γ-E_γ matrix, with three coordinates, is created from the two-fold coincidence data, where the x- and y-axes represent the two ADC channels corresponding to the 2-fold coincidence and the z-axis records the counts. By slicing a single gate on one axis, the gated spectrum is projected onto the other axis. Both symmetric and asymmetric matrices can be formed using "IUCPIX" [4], a package developed by UGC-DAE CSR, Kolkata and 'BINDAS' [5], a package developed by VECC, Kolkata. The three-dimensional matrices, called cubes, are formed from the 3-fold coincidences. The spectra are one-dimensional, and they, along with the matrices and cubes, can be analyzed using the software packages RADWARE [6], INGASORT [7] and BINDAS [5].

3.4 Data Analysis

3.4.1 Calibration

Gain Matching

One of the significant benefits of the Clover detector is the recovery of the photopeak from a Compton scattered event. In a Clover detector, after a portion of the energy is deposited in one crystal, the scattered gamma-ray can travel to the neighbouring crystals and may deposit the remaining energy. When the ADC channels corresponding to these Compton-scattered energies are added in a time-correlated manner for an "event," a count in the photopeak energy can be regenerated in the spectrum. This improves the photopeak efficiency and the peak-to-background ratio. This technique is known as "add back." For

a perfect add-back to happen, the crystals must have identical correspondence between the energy and the ADC channel. Generally, a polynomial fit as shown below is used to achieve the gain matching. The effect of gain matching and energy calibration is shown in Fig. 3.7.

$$E = \sum_{k=0}^{n} a_n x^n = a_0 + a_1 x + a_2 x^2 \tag{3.3}$$

The quadratic term is implemented to account for the slight non-linearity for large pulse heights. The term x^3 can be utilised to a better fit for energies above 1.5 MeV whereas, a term $\sqrt{x}$ may be added to the polynomial can get the correct energy below 200 keV. However, in most of the analysis processes, fitting energy with a 2^{nd} order polynomial is sufficient.

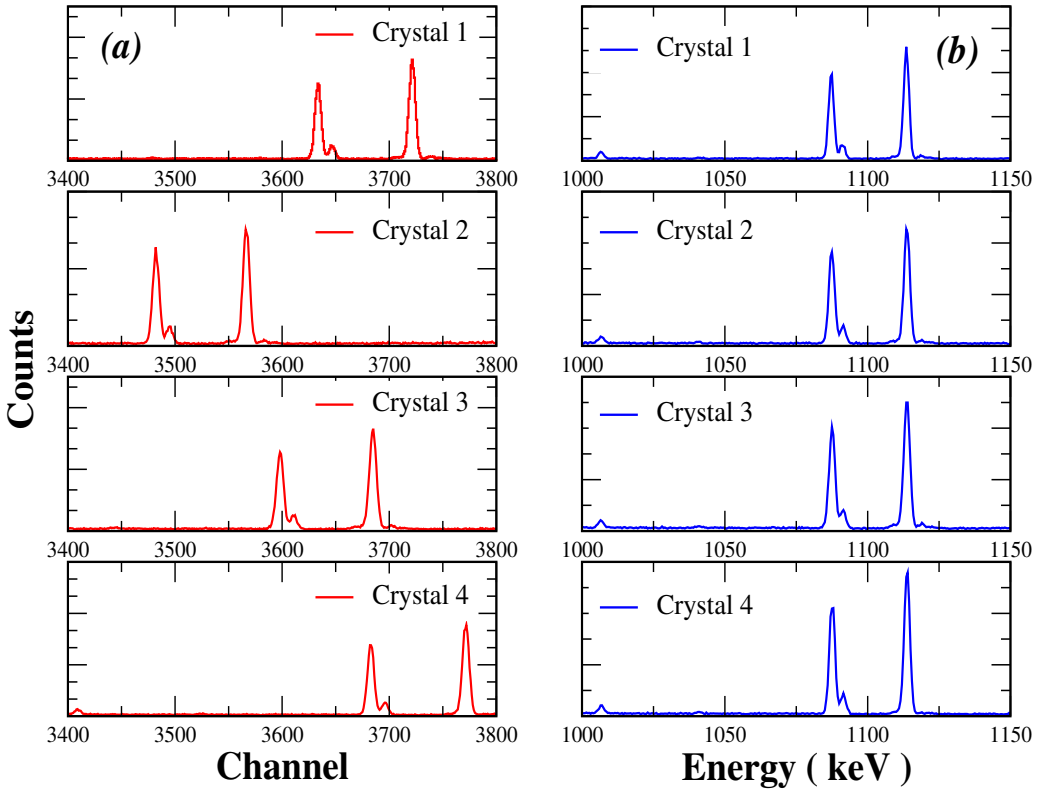

Figure 3.7: On panel (a): before gain matching and energy calibration, On panel (b): after the said processes. The data were acquired for the ^{152}Eu radioactive source during the VECC-INGA campaign 2020.

Energy Calibration

The primary expectation from a gamma-ray spectrometer is to determine precisely the energy of the incident irradiation. For this purpose, it is very important to know the exact energy corresponding to the ADC channel number of an observed spectrum [8]. In general, known γ rays from the ^{152}Eu and ^{133}Ba sources are used at target positions for the energy calibration.

Efficiency Calibration

The knowledge about detector efficiency is required for the determination of the absolute gamma-ray emission rate. Estimating the efficiencies of germanium detectors using published measurements or calculations for similarly sized detectors may only yield results with an accuracy of around 10-20%. This is due to several challenges, such as the lack of standardization in the dimensions of these detectors, which makes it difficult to determine their active volume accurately. Additionally, changes in the charge collection efficiency and/or window thickness over an extended period can result in fluctuations in the detector's efficiency. For these reasons, people normally carry out the periodic efficiency calibrations of their germanium detectors using calibrated sources. Any error in assumed detector dimensions will then apply both to the calibration and actual measurements and will not affect the accuracy of activity measurements. The source-detector distance still must be accurately measured and reproduced to avoid errors in the relative solid angle. Based on the area under the peak and the quoted relative intensities for the known γ rays from the source, the relative photopeak efficiencies of the respective γ rays are calculated and plotted as a function of γ ray energy. ^{152}Eu is quite a popular choice because of its long half-life of 13 years as well as the presence of a wide range of gamma-ray energies in its decay spectrum. The Radware subroutine "Effit" is used for this purpose [9]. Typically,

the following equation is used for the relative efficiency calibration::

$$\ln(\text{eff}) = [(A + Bx + Cx^2)^{-G} + (D + Ey + Fy^2)^{-G}]^{-1/G} \tag{3.4}$$

Here, the parameters A, B, and C control the lower-energy portion of the efficiency curve, while D, E, and F govern the higher-energy region. The parameter G specifically influences the shape of the curve in the low-energy turnover region. C and F parameters are usually set to zero and G determines the turnover region of the efficiency curve. In the above equation, x = ln(E_γ/100) and y = ln(E_γ/1000), where E_γ is the energy in keV for which the efficiency is being calculated. A typical example is shown in Fig. 3.8.

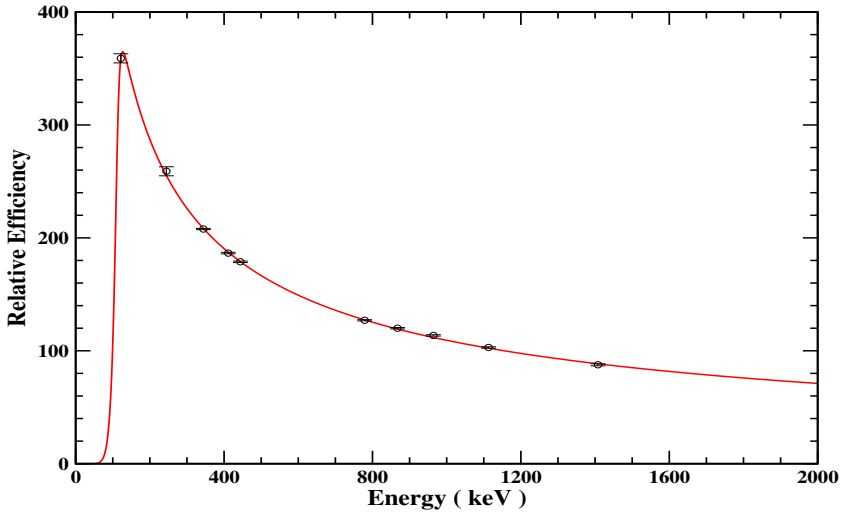

Figure 3.8: The relative efficiency of clover detectors in the VECC-INGA as a function of γ-ray energy as obtained using the radioactive source ^{152}Eu.

3.4.2 Coincidence technique between the γ transitions

A nuclear level scheme is a visual representation of its excited states, which are identified by energy, angular momentum and parity. The information obtained from various gated spectra is very similar to a jigsaw puzzle, which can have only one consistent solution. The first step is to establish the level scheme, which satisfies all the gating conditions. To

extend the level scheme to higher excitation energies, the spin and parity of the ground state of the nuclei must be known. Fig. 3.9 illustrates the basic concept of the coincidence method. For instance, setting a single gate on E2 produces coincidence spectrum transitions E1, E3 and E4 through direct feed; whereas, E8, and E9 through E5 decay. But E6 will not be seen when a gate is placed on E2. Similarly, if a double gate is set on E1 and E7 lines, the coincidence spectrum will only show gamma lines E6, E8, and E9, but E5 will not be visible as it is parallel to E7.

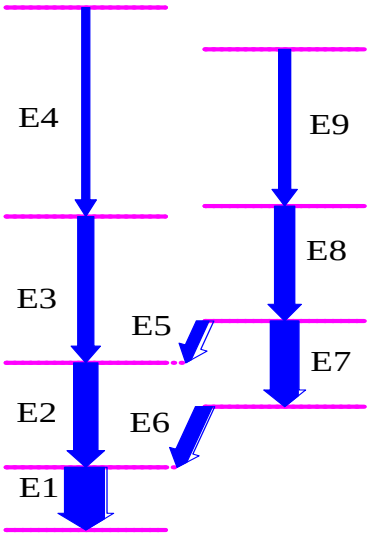

Figure 3.9: Example of a typical level scheme constructed using coincidence method.

3.4.3 Identification of Spin and Parity of the excited states

Angular Distribution Method

In a fusion evaporation reaction, the projectile transfers orbital angular momentum to the compound nucleus. The spin alignment of the residual nucleus alters slightly with the emission of γ-ray transitions or nucleons. The angular distribution is based on this principle. The usual geometry for this study is shown in Fig. 3.10. In a fusion-evaporation reaction, the residual nuclei are produced with their spin aligned perpendicular to the beam axis. The γ-rays emitted from these aligned states exhibit an angular distribution. This

angular distribution, as expressed in Eqn. 3.5, depends on the mixing ratio, multipolarity, and their associated spins:

$$W_l(\theta) = \sum_{k=0}^{l} A_{2k} P_{2k}(\cos\theta) = A_0 + A_2 P_2(\cos\theta) + A_4 P_4(\cos\theta) + \cdots + A_{2l} P_{2l}(\cos\theta) \quad (3.5)$$

where P_{2k}'s and A_{2k}'s represent the Legendre polynomials and corresponding coefficients,

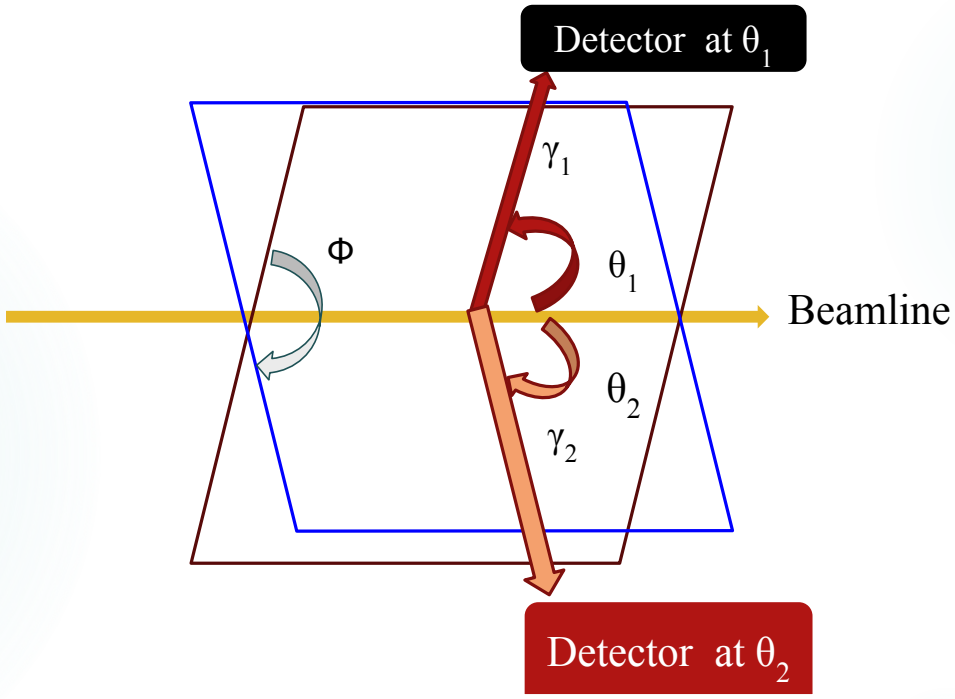

Figure 3.10: Geometry of angular correlation where angles θ_1 and θ_2 represent respective angles of the two detectors with beam axis. ϕ represents the angle between the two planes containing the detectors.

respectively. In the fusion evaporation reactions, the nuclei are mainly populated in states near the yrast line, leading to predominantly dipole ($\Delta l = 1$) and quadrupole ($\Delta l = 2$) transitions. Therefore, higher-order terms beyond k = 2 have a negligible effect on the angular distribution of the γ-rays, allowing us to express the angular distribution as:

$$W(\theta) = A_0 + A_2 P_2(\cos\theta) + A_4 P_4(\cos\theta) = A_0[1 + a_2 P_2(\cos\theta) + a_4 P_4(\cos\theta)] \quad (3.6)$$

The angular distribution coefficients A_0, A_2, and A_4 (or a_0, a_2, and a_4) can be determined by measuring the intensity of the γ-rays at different angles θ with respect to the beam axis. The values of the coefficients provide information about the multipolarities of the γ-rays. For a pure dipole (E1 or M1) transition, the values of a_2 and a_4 are approximately -0.50 and 0, respectively, while for a pure quadrupole (E2 or M2) transition, the values become approximately +0.30 and -0.10, respectively. These are termed 'stretched values' which correspond to the m = 0 substrate population. In the case of mixed γ-ray transitions, the values of the angular distribution coefficients deviate from those of pure transitions. Fig. 3.11 shows the angular distribution and associated coefficients for pure dipole, pure quadrupole, and mixed γ-ray transitions.

Mixing Ratio Calculation

To better understand the residual nuclei's de-excitation mechanism, both the multipole order of the transition and the dipole-quadrupole mixing ratio must be determined. Once the width of the sub-state population is specified, it is utilized to calculate the electric and magnetic mixing ratio (mostly M1+E2 mixing) for the mixed type of transition.

The conventional method to estimate the mixing ratio is from the fitting of experimentally observed angular distribution coefficients. This method could be implemented in our data from TIFR as four distinct angles were available in this array. The spin alignment of a residual nucleus, populated in a nuclear reaction, undergoes slight changes due to the emission of particles or γ-rays. The A_{2K} coefficients reach their maximum values for γ-rays emitted from completely aligned states. In such cases, Eqn. 3.5 can be expressed as:

$$W(\theta) = \sum_{k} A_{2k}^{max} P_{2k}(\cos\theta) \tag{3.7}$$

However, in the case of partial alignment, the angular distribution equation is modified by

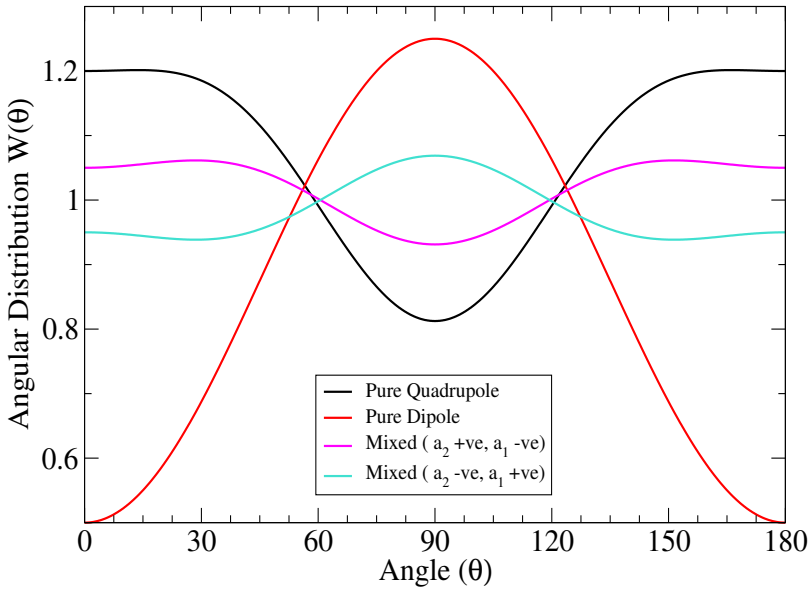

Figure 3.11: Theoretical angular distributions of γ-rays with different multipolarities and mixing ratios.

the presence of attenuation coefficients as follows:

$$W(\theta) = \sum_{k} \alpha_{2k} A_{2k}^{max} P_{2k}(\cos\theta) \tag{3.8}$$

The coefficients A_{2k}^{max} are defined as,

$$A_{2k}^{max}(J_i L_1 L_2 J_f) = \frac{1}{1+\delta^2}[f_{2k}(J_f L_1 L_1 J_i) + 2\delta f_{2k}(J_f L_1 L_2 J_i) + \delta^2 f_{2k}(J_f L_2 L_2 J_i)] \tag{3.9}$$

where δ is the mixing ratio. The sign of this mixing ratio determines the nature of the theoretical angular distribution. As shown in Fig. 3.12, the nature of theoretical plots are opposite for positive and negative values of δ, shown in green and blue lines, respectively. The red line gives the fitting of the obtained experimental data points (shown in the green circle) and matches quite well with the theoretical plot with positive δ. Thus, by accurately fitting the experimental data points, the coefficients as well as the sign of the mixing ratio can be determined.

The γ-γ Correlation Technique

The angular distribution is measured from the singles data and thus, can only be carried out for the strong γ-transitions which do not have contamination from any other residual channels. These criteria are satisfied by only a few observed transitions. Additionally, in the present INGA set-up at VECC, detectors have only been placed at three angular positions, which limits the ability to determine the multipolarities through angular distribution measurements. However, the quantization axis can be established by detecting one of the coincident γ-rays in a specific direction. In this case, the other γ-ray will exhibit angular anisotropy. As discussed earlier, angular correlation can be considered a special case of angular distribution, where a particular orientation is fixed by observing one transition in a specific direction as illustrated in Fig 3.10. The angular correlation of the coincident γ transitions depends on the multipolarities of both transitions. This approach is known as Directional Correlation from the Oriented states (DCO)-ratio, as prescribed by Krämer-Flecken et al. [10]. The DCO ratio is then defined as the ratio of the probability of the two angular distributions with an exchange in their detection angles.

$$R_{DCO} = \frac{W(\theta_2, \theta_1, \phi)}{W(\theta_1, \theta_2, \phi)} \tag{3.10}$$

where θ_1 and θ_2 denote the detectors' angular positions with respect to the beam axis. ϕ is the relative azimuthal angle formed by two planes each for the detector and the beam. In the data sorting, asymmetric matrices are created by recording the energies of gamma rays detected by two detectors placed at different angles θ_1 and θ_2, respectively. The DCO-ratio for a gamma ray with intensity $I_{\gamma 1}$ detected at θ_1 and coincident with another gamma ray with intensity $I_{\gamma 2}$ detected at θ_2 can be calculated from Eqn. 3.11

$$\mathrm{R_{DCO}} = \frac{I_{\gamma_1}(\theta_1) \text{ (Gated by } \gamma_2 \text{ at } \theta_2)}{I_{\gamma_1}(\theta_2) \text{ (Gated by } \gamma_2 \text{ at } \theta_1)} \tag{3.11}$$

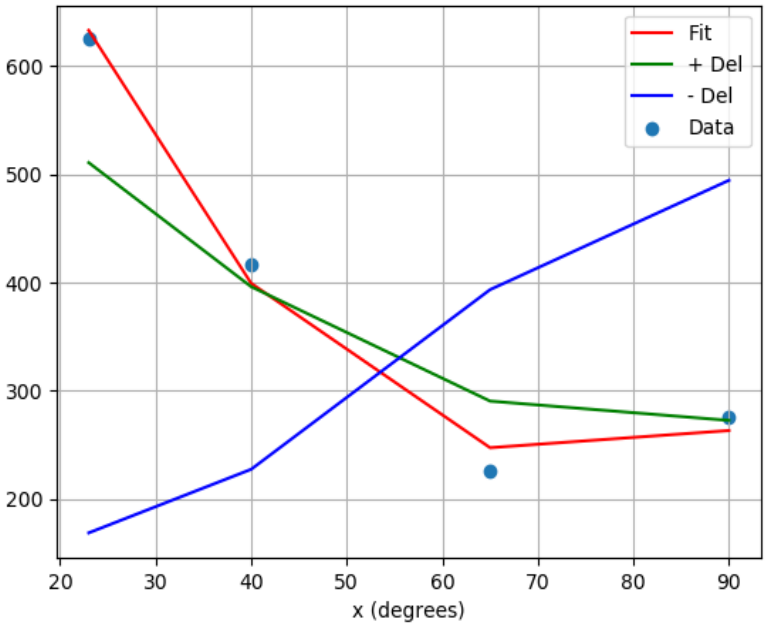

Figure 3.12: Angular distribution fit of 991 keV γ-ray in ^{105}Pd from the dataset of TIFR-INGA. Here, the angle is plotted up to 90° as the plot is symmetric around θ = 90°.

To replicate the experimentally obtained DCO-ratio, the ANGCOR code [11] is employed by fixing σ and adjusting the mixing ratio (δ). The DCO and polarization values for the parity changing transitions can be calculated with this code assuming no mixing i.e. pure E1. In this case, multiple contour plots can be obtained for different combinations of the spins and parities of the initial and final levels. This helps in the unambiguous assignment of the electromagnetic character of a transition. Such an estimation is crucial for the determination of the spin-parity of an excited band. An example of 888 keV E1 transition ($6^- \rightarrow 6^+$) is shown in Fig. 3.13, which helped to identify an even spin and negative parity band in ^{100}Ru.

In the current experimental configuration of VECC, the DCO matrix was prepared with the γ-rays detected at 90° and 40°. For a stretched transition with a gate on the transition of the same multipolarity, the ratio is 1. The DCO ratio value is around 0.5 and 2 for a dipole transition with quadrupole gating and vice versa for the extreme forward and 90° combination. The R_{DCO} value obtained for a pure dipole transition gated by a quadrupole

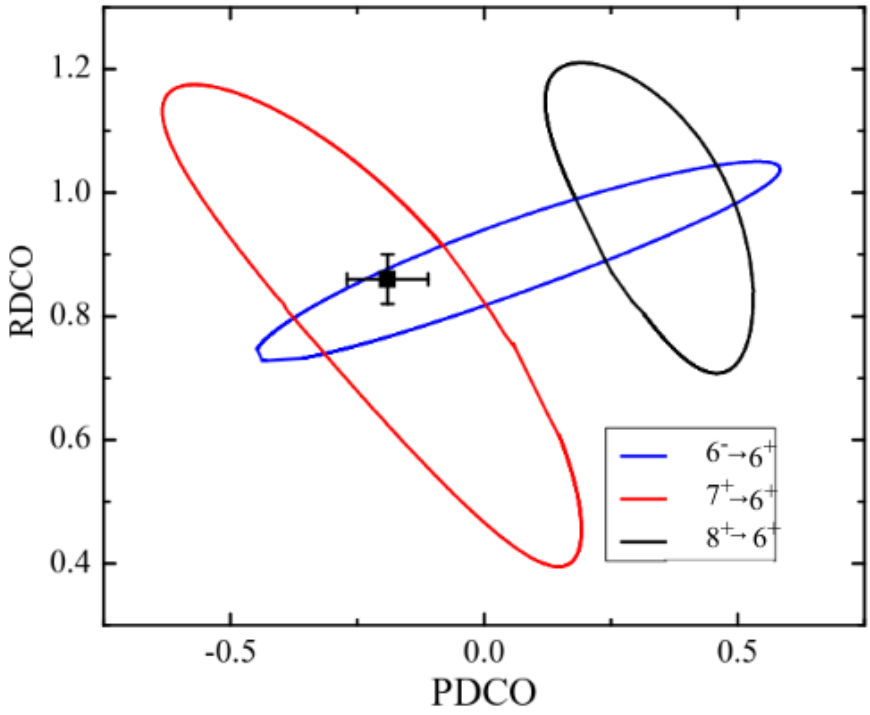

Figure 3.13: The contour plots for different combinations of initial and final levels as a function of mixing ratio (δ) with R_{DCO} in one axis and polarization in another. The black point indicates the experimental value for the 888 keV transition in ^{100}Ru which matches with the contour for $6^- \rightarrow 6^+$ transition.

transition was about 0.65, whereas, for the reversed scenario, the R_{DCO} value is around 1.55. For the TIFR setup, the same angles of 90° and 40° have been considered and thus the DCO ratios have similar values for pure dipole and quadrupole transitions.

Width of sub-states

The spins of the initial and the final levels, multipolarities, mixing ratios of γ transitions, and the m-substate population distribution of the initial state all impact the angular correlation of γ rays emitted from oriented states. To produce a compound nucleus, a target nucleus is bombarded with a projectile. Since the emission of neutrons and γ-rays occurs in random directions, the alignment of spin does not change significantly. Thus, a Gaussian distribution centred at m = 0 with a half width of a for a given spin can be used to describe the m-substate population. This quantity ($\frac{\sigma}{I}$) remains relatively constant over a

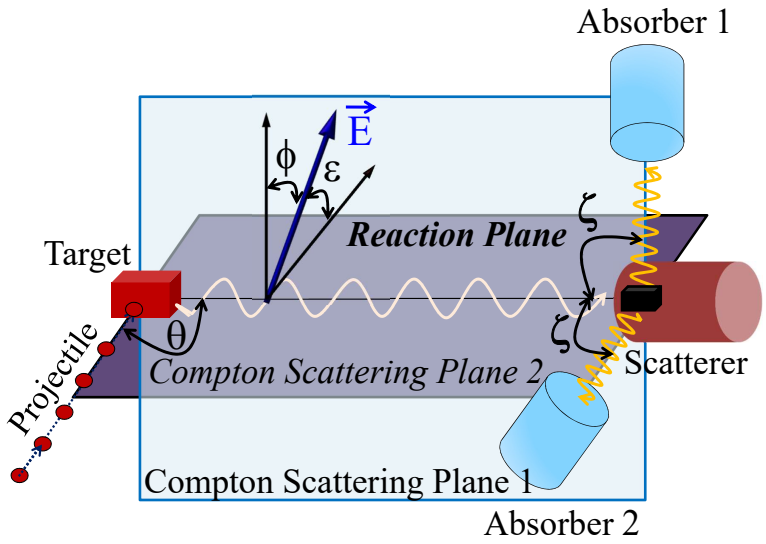

Figure 3.14: A schematic representation of the angles and planes relevant to the linear polarization measurement of a γ-ray [12].

broad spin range, with a deviation from this empirical fact only occurring in the low-spin region I $\leq$ 6. To determine this width, several pure electric dipole (E1) transitions of the nuclei populated in the same reaction have been chosen. The DCO ratios for these E1 transitions have been calculated using a stretched E2 as the gating transition. The DCO ratios are then compared to theoretical R_{DCO} values calculated using ANGCOR [11], with the spin alignment $\frac{\sigma}{I}$ being adjusted as a parameter to determine the best compliance. This value has been estimated to be around 0.3 in the present thesis work. Ideally, no change in alignment is expected if the decaying transitions are stretched in nature.

Linear Polarization measurement

The determination of the spin and parity of any level depends on the multipolarity and electromagnetic nature of the γ-transitions involved. While the method for determining the multipolarity has already been discussed, this section focuses on the estimation of the polarization of γ-transitions using the Clover detector and how their electromagnetic character has been determined. In addition to the detector angle with respect to the beam axis, the direction of the electric vector is also a crucial factor for linearly polarized γ-

rays. When performing polarization measurements using a clover detector, it is important to consider the three planes and four angles (refer to Fig. 3.14) as follows:

Reaction Plane: The angle between the ion-beam and the emitted γ-transition is denoted by θ and lies in the plane formed by them.

Electric field Plane: The plane that includes the electric vector of the emitted γ-transition and the emitted γ-transition is defined as the electric field plane. The angle between the electric vector and the reaction plane is denoted by ϵ, while the angle between the electric vector and the plane perpendicular to the reaction plane is represented by φ.

Scattering Planes: The polarization measurement using the clover detector involves the consideration of two scattering planes. These planes are formed by the incident γ-ray upon the detector and the corresponding scattered γ-rays. They are perpendicular and parallel to the reaction plane, and the angle between them is denoted by ξ.

The add-back events of a clover detector are utilized to estimate the linear polarization of γ transitions from excited nuclear states. The differential cross-section of an incident γ-rays with energy E_γ and Compton-scattered energy $E\gamma'$ is given by the Klein-Nishina formula:

$$\sigma_C(\xi,\varphi) = \frac{d\sigma}{d\Omega}(\xi,\varphi) = \frac{r_0^2}{2}\left(\frac{E'_\gamma}{E_\gamma}\right)^2\left[\frac{E'_\gamma}{E_\gamma} + \frac{E_\gamma}{E'_\gamma} - 2\sin^2\xi\cos^2\varphi\right] \tag{3.12}$$

Here, the angles are of the same notation as discussed before. r_0 is the classical electron radius, equal to $e^2/(m_e c^2)$, with m_e being the mass of the electron and c being the speed of light. The energy of the scattered γ-ray (E'_γ), which depends on ξ, can be obtained from the well-known Compton scattering formula. Eqn. 3.12 shows that the differential Compton scattering cross-section becomes maximum when ϕ is 90°, i.e., in the direction perpendicular to the electric field vector $\vec{E}$ of the incident γ-ray transition.

The clover detectors used in the present experiments serve as Compton polarimeters. Each crystal of a clover detector functions as a scatterer, while two adjacent crystals serve as the analyzers. The linear polarization measurements were carried out using clover detectors

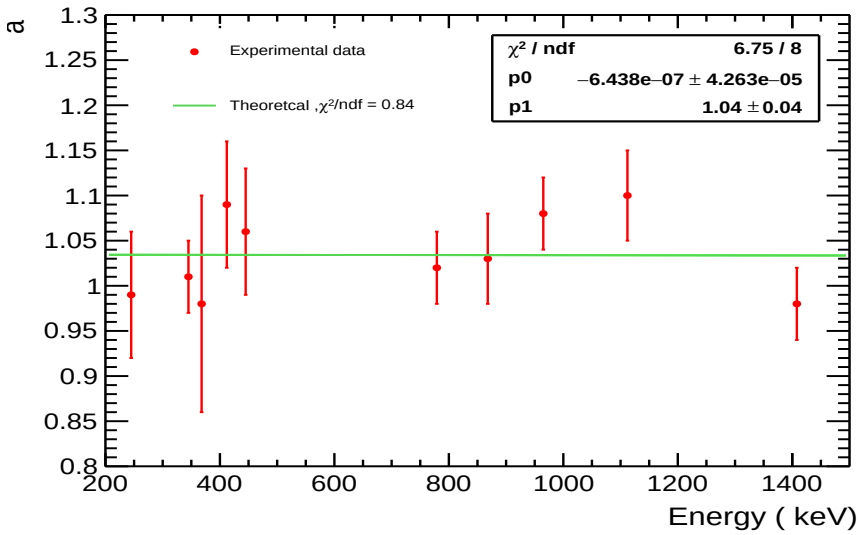

Figure 3.15: The values of the geometrical asymmetry correction factor a(E_γ) for various energies of ^{152}Eu source. The data points are fitted with a linear function, represented by the solid line

at a 90° angle since the degree of linear polarization reaches its maximum at this angle. The reference plane of each γ-ray is defined by the beam axis and the direction of γ-ray emission. In the list mode data sorting process, Compton scattered events in neighbouring pairs of Ge crystals of the clover detectors have been identified from the add-back events which lead to the photo peak. Two matrices, one for horizontally scattered γ-rays and the other for vertically scattered γ-rays were created with E_γ - E_γ on one axis and coincident γ-rays from all detectors on another.

The observed polarization asymmetry can be calculated using the following:

$$\Delta = \frac{a(E_\gamma)N_\perp - N_\parallel}{a(E_\gamma)N_\perp + N_\parallel} \tag{3.13}$$

The equation has the term a(E_γ), which is the geometrical asymmetry correction and is expressed as:

$$a(E_\gamma) = \frac{N_\parallel}{N_\perp} \tag{3.14}$$

The values of $N_\parallel$ and $N_\perp$ represent the photopeak counts in the parallel and perpendicular directions to the reference plane, respectively. The geometrical asymmetry correction

factor is used to correct the effects of detector geometry on polarization measurement. Its value depends on the energy of the gamma-ray, E_γ. The determination of a(E_γ) as a function of energy is based on the condition that the asymmetry Δ , measured with a radioactive source without spin alignment, should be zero. Typically, the value of a is found to be very close to 1.

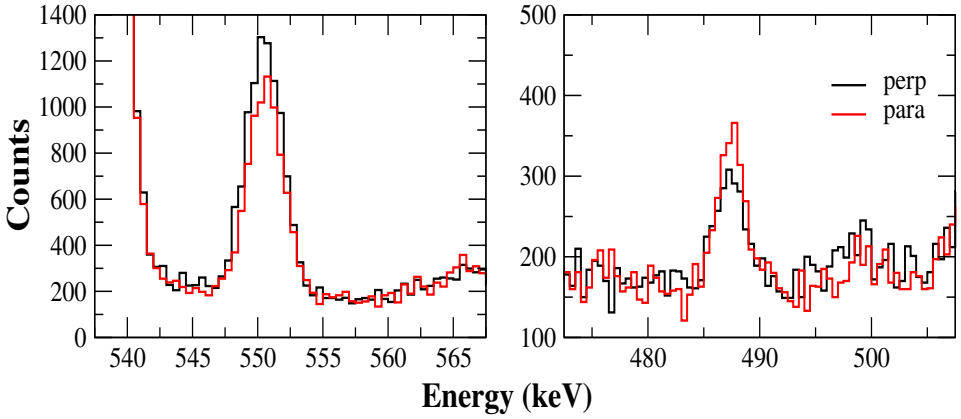

Figure 3.16: A typical gated spectrum for an electric type (left panel) and a magnetic type (right panel) transition.

This correction term has been determined by using the ^{152}Eu radioactive source located at the target position. The energy dependence of the parameter a(E_γ) can be obtained by the following expression: a(E_γ) = a + b×E_γ. The fitting of the data, as shown in Fig. 3.15, gives the coefficients a = 1.035(38) and b $\approx 10^{-7}$ for the VECC-INGA experiment. The γ-transitions can be classified into electric, magnetic, and mixed types based on the polarization asymmetries values which are positive, negative, and near-zero, respectively. The polarization measurement has been determined to have a lower energy cut-off of around 200 keV as the number of Compton scattered events leading to a photopeak becomes negligible for smaller γ energies. Fig. 3.16 shows that the parallel component (red solid line) is more for 488 keV (right panel), which is an established Magnetic M1 type of transition, whereas, for 552 keV (left panel), the perpendicular component (black solid line) is more, thus establishing it as an Electric E1 type of transition in ^{100}Ru.

The polarization sensitivity Q(ξ, E_γ) is a characterization parameter for a Compton po-

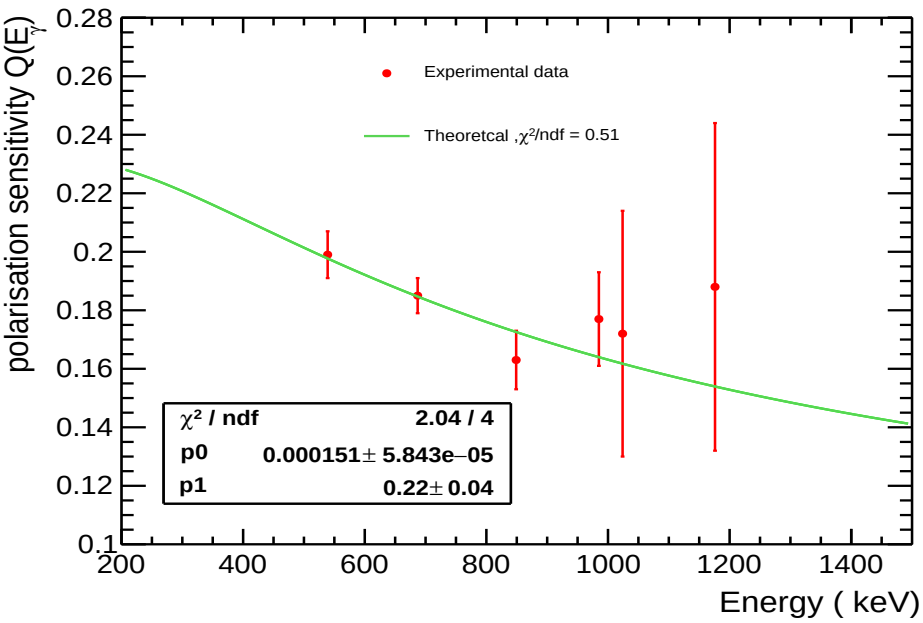

Figure 3.17: The energy-dependent polarization sensitivity of the Clover detectors used in the experiments.

larimeter that is dependent on both the incident γ-ray energy E_γ and the Compton-scattering angle ξ [13]. For a given incident γ-ray energy, it is known that the sensitivity is optimised close to $\xi = 90°$. For this reason, the scatterer and the analyzer are ideally positioned perpendicular to the direction of the incident γ-ray. However, a realistic Compton polarimeter subtends a finite solid angle, which leads to the polarization sensitivity. This has been estimated using a parameterized function that is linearly dependent on the energy of the incident γ-ray as $Q = Q_0(p_0 \times E_\gamma + p_1)$ where $Q_0 = \frac{1}{\left(\frac{E_\gamma}{0.511}\right)+\left(\frac{0.511}{E_\gamma+0.511}\right)}$ and Eγ is in keV [13]. Here, Q_0 represents the sensitivity for a point-like absorber, and E_γ is in units of MeV. The extended solid angle of the polarimeter (i.e. the segmented clover detector) is taken into account by two parameters p_0 and p_1. These parameters and the sensitivity Q are experimentally determined using γ lines with known polarization values. For the experiment performed at VECC, $p_1 = 0.22(3)$ and $p_0 = 1.5(6) \times 10^{-4}$ keV^{-1} have been estimated as shown in Fig. 3.17. Therefore, by knowing the sensitivity Q as a function of the incident γ-energy, the linear polarization can be obtained from the measured asymmetry (Δ) values using the relation:

$$P = \frac{\Delta}{Q(E_\gamma)} \tag{3.15}$$

3.4.4 Level Lifetime Measurements

The determination of lifetimes for excited levels following fusion-evaporation reactions holds significant importance due to the limited availability of the observables for excited nuclear levels. Various techniques have been employed to measure level lifetimes across a wide range, of 10^{-14} to 10^{-7} seconds. In terms of their applicability for the longer to the shorter lifetimes, these techniques are:: the delayed coincidence (10^{-7} to 10^{-8} seconds), the fast coincidence (10^{-8} to 10^{-11} seconds), the Recoil Distance Method (10^{-11} to 10^{-12} seconds) and the Doppler Shift Attenuation Method (DSAM) (10^{-12} to 10^{-14} seconds).

In DSAM, the sub-picosecond level lifetimes are measured by analysing the history of the slowing down process of the recoiling nuclei inside the target-backing medium. This leads to the observation of a continuous line shape at a particular angle (θ) for a γ-ray due to Doppler shift. The pictorial representation of the process is shown in Fig. 3.18.

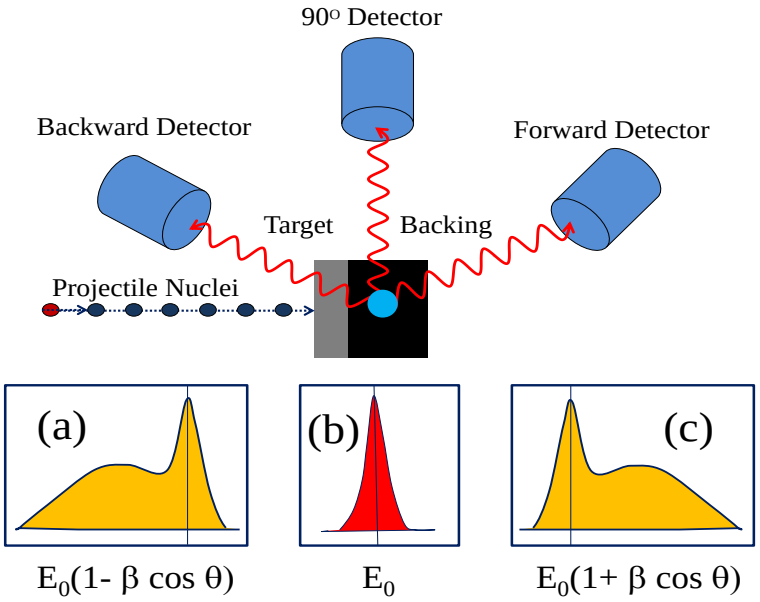

Figure 3.18: The experimental lineshapes of a γ transition depopulating from a state with a sub-picosecond lifetime are schematically represented in (a) the shape at the backward angle (-θ) detector, (b) the unshifted peak of energy E_0 at the 90° detector, and (c) the shape at the forward angle (+θ) detector, as the recoil velocity (β) decreases continuously to zero.

By fitting these line shapes with the LINESHAPE analysis code, the level lifetimes of the

states can be derived. It is made up of three separate programmes: Lineshape, Histaver, and Dechist. Using the Monte Carlo method, Dechist models the velocity histories of the recoiling nuclei across the backing medium and target. Using Monte Carlo methods with a time step of 0.001 ps, the slowing down history of 10,000 recoil nuclei traversing the target and supporting medium has been simulated. These computations have been performed using SRIM [14]. These are merited with lesser uncertainties ($\approx$ 5%) [15] relative to the stopping powers represented by either the Northcliffe-Schilling or Ziegler algorithms [16] in the original framework of LINESHAPE.

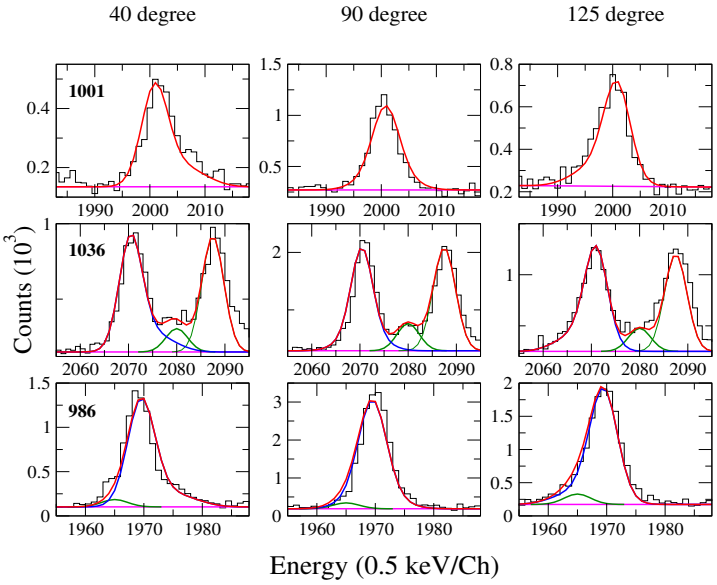

Figure 3.19: Typical experimental line-shapes and the corresponding fits produced using Wells and Johnson's LINESHAPE algorithm. The background is represented by the colour magenta, the contamination peak(s) by green, the line shape fit by blue, and the overall experimental data fit by red.

E_γ-E_γ asymmetric matrices were used to generate background-subtracted gated spectra for the extraction of the line shapes. These matrices record coincidence events of all detectors on one axis and events detected by other detectors at particular angles (forward, backwards, and 90°) along the other. To derive level lifetimes, the line shapes at different angles were fitted simultaneously. The spectra at 90° are crucial to locate the contaminant peaks. The outcomes of the line-shape fits for transitions of 1001, 1036 and 986 keV are displayed in Fig. 3.19. The line shapes at forward (40°), 90°, and backward (157°) angles

are displayed in the left, middle, and right panels, respectively. The solid line represents the best fit to the line shape. To reduce the inaccuracy of the estimated level lifetime, these fits are performed concurrently. The behaviour of the χ^2 at the minimum is used to derive the uncertainties in the lifetime measurements. The uncertainty in the side-feeding intensity, which originates from the uncertainties in the top-feeding and feed-out γ-transition intensities at the level of interest, constitutes the second source of error in this measurement. The level lifetimes for the extreme values of side feeding intensities are found in order to estimate this. The estimation of the side-feeding time is the third source. The side-feeding lifetime has been varied by ±10% to assess this uncertainty. The quadrature sum of the uncertainties resulting from side-feeding intensity, side-shape fitting, and side-feeding lifetime yields the total statistical uncertainty. It should be stated that this uncertainty does not include the systematic uncertainty coming from the estimation of the stopping powers, which can be around 5%. It is important to note that the uncertainties resulting from the side-feeding can be avoided if a line shape can be obtained from a top gate. As a result, the level lifetime is estimated more precisely. But most often, the statistics in the observed line shapes for high spin states are poor in the top gate.

3.4.5 Transition probability

The excited nuclear levels originate due to various angular momentum generation mechanisms and each of them leaves a specific signature on the γ-transition rates from these levels. The transition rates are estimated from the measured level lifetime using the following relation::

$$T_{fi}(\lambda L) = \frac{\ln 2}{T^{\gamma L}_{1/2}} = \frac{8\pi(L+1)}{\hbar L[(2L+1)!!]^2}\left(\frac{E_\gamma}{\hbar c}\right)^{2L+1} B(\lambda L : I_i \rightarrow I_f) \tag{3.16}$$

where symbols have their standard meaning. The reduced transition probability for the electric and magnetic type of transitions, $B(EL)$ and $B(ML)$, respectively, are given in

terms of Weisskoff units as follows:

$$B(ML) = \frac{(\ln 2)L([2L+1)!!]^2\hbar * BR}{80(1.2)^{2L}(L+1)A^{(2L-2)/3}T_{1/2}^{exp}(1+\alpha)[\mu_N^2(fm)^{2L-2}]}\left(\frac{\hbar c}{E_\gamma}\right)^{2L+1}\left(\frac{L+3}{3}\right)^2 [W.u.] \tag{3.17}$$

and

$$B(EL) = \frac{(\ln 2)L([2L+1)!!]^2\hbar * BR}{(1.2)^{2L}(L+1)A^{2L/3}T_{1/2}^{exp}(1+\alpha)[e^2(fm)^{2L}]}\left(\frac{\hbar c}{E_\gamma}\right)^{2L+1}\left(\frac{L+3}{3}\right)^2 [W.u.] \tag{3.18}$$

Thus, given knowledge of the branching ratio and lifetime, one can estimate the reduced transition probability [17]. However, in cases where the statistics are poor, the lifetime measurement may prove to be difficult. In such cases, the ratios of B(M1)/B(E2) and B(E1)/B(E2) become a useful tool for the determination of the single particle configuration of a band structure. The aforementioned ratios can be estimated from the energy expressed in MeV (E), intensity (I_γ), and mixing ratio (δ) of the inter-band dipole and the intra-band electric quadrupole γ-transitions as follows:

$$\frac{B(M1_{out}; I \to I-1)}{B(E2_{in}; I \to I-2)} = 0.697\frac{E_2^5(E2)}{E_1^3(M1)}\frac{1}{1+\delta^2}\frac{I_\gamma(M1)}{I_\gamma(E2)} \text{ in } \left(\frac{\mu_N}{eb}\right)^2 \tag{3.19}$$

$$\frac{B(E2_{out}; I \to I-1)}{B(E2_{in}; I \to I-2)} = \frac{E_2^5(E2_{in})}{E_1^5(E2_{out})}\frac{\delta^2}{1+\delta^2}\frac{I_\gamma(E2_{out})}{I_\gamma(E2_{in})} \tag{3.20}$$

and

$$\frac{B(E1_{out}; I \to I-1)}{B(E2_{in}; I \to I-2)} = \frac{1}{1.3\times 10^6}\frac{E_\gamma^5(E2)}{E_\gamma^3(E1)}\frac{I_\gamma(E1)}{I_\gamma(E2)} \text{ in fm}^{-2} \tag{3.21}$$

In the following chapters, I shall discuss the spectroscopy measurements carried out in ^{100}Ru, ^{98}Mo, ^{105}Pd and ^{101}Ru using the techniques described in this chapter.

Bibliography

[1] Glenn F. Knoll. Radiation Detection and Measurement, 3rd ed. John Wiley and Sons, New York, 2000.

[2] R. Palit Application of Accelerators in Research and Industry: Twenty-First International Conference, AIP Conf. Proc. No. 1336, edited by F. D. McDaniel and B. L. Doyle p. 573 (AIP, New York) (2011).

[3] Soumik Bhattacharya *et. al.* VECC-INGA: An exploration of nuclear structure with light ions DAE-BRNS symposium on nuclear physics: contributed papers. V. **63**, 2018.

[4] S. Das *et. al.* A Compton-suppressed detector multiplicity trigger-based digital DAQ for gamma-ray spectroscopy. NIM A: **893**:138–145, 2018.

[5] S. S. Nayak and G. Mukherjee. Development of an advanced, multi-function, multi-DAQ compatible data sorting and analysis software suite-bindas. IEEE Transactions on Nuclear Science, **70**(12):2561–2571, 2023.

[6] D.C Radford. Escl8r and Levit8r: Software for interactive graphical analysis of HPGE coincidence data sets. NIM A: **361**(1):297–305, 1995.

[7] R.P. Singh, Ranjan Bhowmik, S. Muralithar. Ingasort, a new program for the analysis of multi-clover array. DAE-BRNS symposium on nuclear physics: contributed papers. V. **44B**, 2001.

[8] L. Satpathy. Structure of Atomic Nuclei. Narosa Publishing House, 1999.

[9] D.C Radford. Background subtraction from in-beam HPGE coincidence data sets. NIM A: **361**(1):306–316, 1995.

[10] A. Krämer-Flecken, T. Morek, R.M. Lieder, W. Gast, G. Hebbinghaus, H.M. Jäger and W. Urban. Use of DCO ratios for spin determination in-coincidence measurements. NIM A: **275**(2):333–339, 1989.

[11] E.S. Macias, W.D. Ruhter, D.C. Camp, and R.G. Lanier. A program for calculating gamma-gamma directional correlation coefficients and mixing ratios. Comp. Phys. Comm., **11**(1):75–93, 1976.

[12] Subhendu Rajbanshi. Generation of Angular Momentum for Weakly Deformed Nuclei in A $\approx$ 140 Mass Region. PhD thesis, 2016.

[13] Ch. Droste, B. Czajkowska, Z. Marcinkowska, R.M. Lieder, T. Morek, T. Rzaca-Urban, W. Gast Polarisation sensitivity of the CLUSTER detector used in EUROBALL array NIM A: **556**:182–186, 2006.

[14] www.srim.org

[15] S. Das *et. al.* Extending the application of DSAM to atypical stopping media. NIM A: **841**:17–23, 2017.

[16] L.C. Northcliffe and R.F. Schilling. Range and stopping-power tables for heavy ions. Atomic Data and Nuclear Data Tables, **7(3)**:233–463, 1970.

[17] Michel Baranger and Erich Vogt (eds) Advances in Nuclear Physics , Volume 10, New York, 1978.

Chapter 4

Spectroscopic Studies in ^{100}Ru

4.1 Introduction

Nuclei possess octupole deformation due to the long-range octupole - octupole correlations among the nucleon orbitals close to the Fermi surface, whose total (J) and orbital (L) angular momenta differ by $3\hbar$. A reflection asymmetric pear shape of a nucleus can be realised by superimposing octupole deformation (characterized by β_3) on a prolate shape (characterized by β_2). Its rotation for an even-even nucleus is characterized by a unique band structure, where the levels of two alternating parity bands are connected by relatively fast electric dipole (E1) transitions. The presence of these transitions is the signature of an intrinsic dipole moment, which arises due to the separation between the centre of mass and the centre of charge as the concentration of protons is higher in the region of higher curvature, which is the narrower end of the pear [1].

Such a band structure was first reported in ^{218}Ra [2] and since then, stable octupole deformation has been reported in a number of even-even isotopes of Ra – Th ($Z \approx 88$ and $N \approx 134$) [3, 4, 5, 6] and Sm – Ba ($Z \approx 56$ and $N \approx 88$) nuclei [7, 8, 9, 10]. There exist other nucleon numbers, namely 34 and 56, where the octupole shape can be favoured [11, 12, 13, 14]. However, a recent theoretical study concluded that the nuclei in the A $\approx$

100 regions are unlikely to possess stable octupole deformation [15]. This has been found to be true as no well-defined rotational band structures have been found in the two N = 56 isotones, namely ^{96}Zr (Z = 40) [16] and ^{98}Mo (Z = 42) [17], although they exhibit the existence of the octupole degree of freedom. In ^{100}Pd (Z = 46), however, a parity doublet structure is observed but the bands become interspaced for I $\geq 16\hbar$, where the TRS calculations predict the emergence of the octupole deformation [18]. But, the interleaved E1 transitions were not observed in this spin domain. On the other hand, ^{100}Ru (Z = 44) has two interspaced opposite parity bands beyond I = $11\hbar$ [19, 20]. This led us to search for the E1 transitions between these alternating parity bands, whose presence would indicate a novel excited octupole band in ^{100}Ru.

4.2 Experimental details

The previous experiment on ^{100}Ru [19] was focused on studying band termination and thus, the high spin states were populated using the heavy ion ^{36}S beam on ^{70}Ge target. The γ rays were detected in EUROGRAM-2 spectrometer [21]. However, only about 3% of the 6×10^8 4-fold coincidence events corresponded to ^{100}Ru as a large number of residual nuclei were produced in this fusion-evaporation reaction. In the present experiment, excited levels of ^{100}Ru were populated through the fusion-evaporation reaction involving a 98% pure 2-mg/cm^2 thick ^{100}Mo target and a 50 MeV alpha beam from the K-130 cyclotron at VECC, India. The reaction and the beam energy were chosen such that the yield of ^{100}Ru was nearly 90% of the total fusion cross-section. About 5×10^9 2-fold γ-γ coincidence data were recorded by the PIXIE-16 digitizer-based data acquisition system [22] and these time-stamped data were sorted into γ-γ matrices with a coincidence window of 200 ns using the IUCPIX package [22]. The light alpha beam populated intermediate spin levels (I $\approx 16\hbar$), where we planned to search for the elusive E1 transitions by collecting a large data sample.

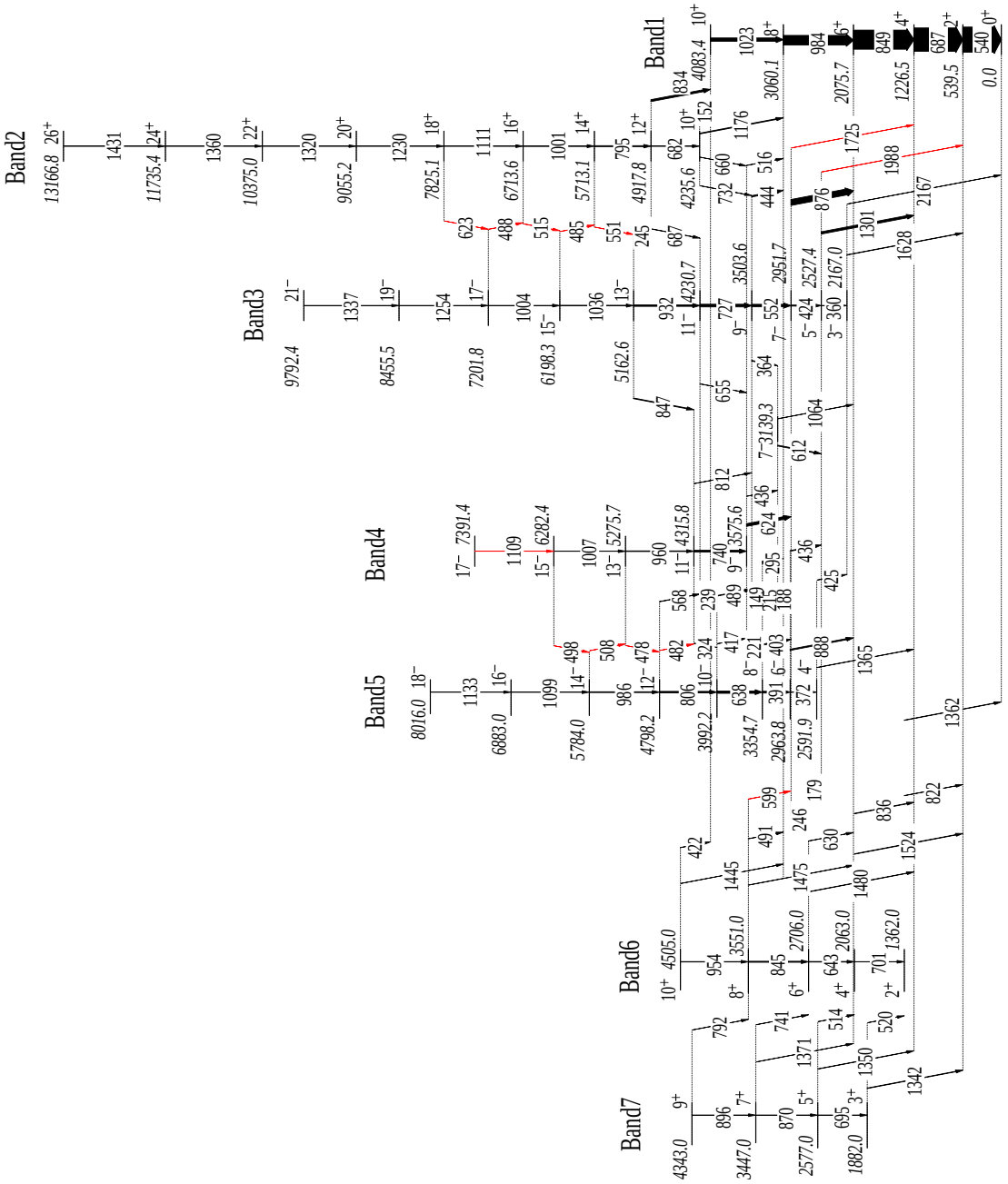

Figure 4.1: The partial level scheme of ^{100}Ru established from the present work. Seven inter-leaved transitions between Band2 and Band3 have been observed in the present work. The level and transition energies are expressed in keV. Gamma-ray energies have been rounded off to their closest integer. The thicknesses of the arrows are proportional to the relative intensities of the de-exciting γ-rays. The transitions marked in red are newly observed in the present data set. The high spin levels beyond I = 20$\hbar$ were reported in Ref. [19] but not observed in the present experiment.

4.3 Results

The symmetric matrix was analyzed using the RADWARE program ESCL8R [23] to build the partial level scheme of ^{100}Ru, which is shown in Fig. 4.1. There are three pairs of bands:

1. Band2 and Band3 form an alternate parity structure with interleaved E1 transitions.

2. Band4 and Band5 are negative parity bands interconnected by M1 transitions.

3. Band6 and Band7 are positive parity bands interconnected by M1 transitions.

Two new E3 transitions from 5^- and 7^- states to the levels of the ground state band were observed in the present data. It may be noted that this is a rare occurrence and points towards the presence of octupole collectivity at low spins in ^{100}Ru. These transitions are shown in the inset of the 552 keV gated spectrum (marked in red) of Fig. 4.2. It is observed from this figure that the 1036 keV transition is more intense than the 1004 keV transition. Thus, their placements were interchanged with respect to Ref. [19]. In Fig. 4.2, these two transitions have been labelled in green. The intensities of the γ rays in different gated spectra have been obtained by fitting the observed photo peaks to the Gaussian function using the INGASORT software [24]. The intensities of the weak interleaved E1 transitions between Band2 and Band3 were estimated from the γ-gated spectra at 90° using the following prescription:

245 keV ($13^- \rightarrow 12^+$): from the two top γ-gates of 1036 and 1004 keV.

551 keV ($14^+ \rightarrow 13^-$): from the two top γ-gates of 1001 and 1111 keV. This peak is well resolved from the 552 keV transition.

485 keV ($15^- \rightarrow 14^+$): from the immediate top and bottom γ-gates of 1004 and 795 keV, respectively.

515 keV ($16^+ \rightarrow 15^-$): from the immediate top γ-gate of 1111 keV. In this gate, the contamination due to 516 keV transition ($9^-_{\text{Band4}} \rightarrow 8^+$) was found to be negligible. To validate this observation, the branching ratio for the 14^+ level was also evaluated in the 444 keV

gate, which is not in coincidence with the 516 keV transition.

488 keV ($17^- \rightarrow 16^+$): from the two immediate bottom γ-gates of 1001 and 795 keV.

623 keV ($18^+ \rightarrow 17^-$): from the two bottom γ-gates of 552 and 727 keV since the higher gamma gates of Band3 are contaminated by the 624 keV transition ($9^-_{\text{Band4}} \rightarrow 7^-$). These two gating transitions are not in coincidence with the 624 keV transition.

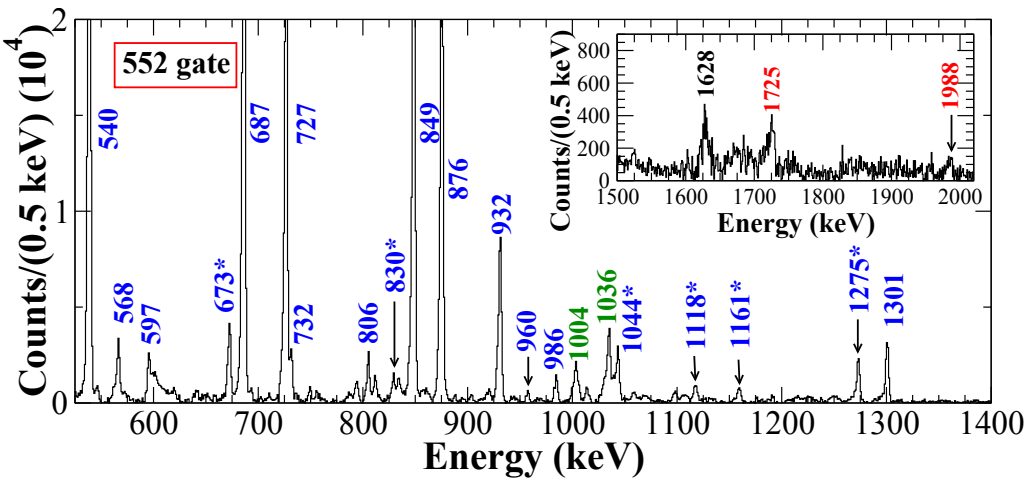

Figure 4.2: The γ-ray spectrum in coincidence with the 552- keV ($9^- \rightarrow 7^-$) transition. The gamma energies have been rounded off to the nearest integer. The higher energy section of the gated spectrum is shown in the inset. The γ rays marked with * are from other excited levels of ^{100}Ru [25], which are not part of the partial level scheme shown in Fig. 4.1.

In the estimation of the E1/E2 branching ratios, the enhancement of the intensities of E1 transitions observed at 90° has to be corrected. The correction factor was determined by measuring the branching ratios for (444 and 552 keV), (516 and 624 keV) and (876 and 424 keV) γ-rays at 90° and at 125° (at this angle the angular distribution effects are negligible). The weighted mean of the ratio of the branching ratios was found to be 1.58 ± 0.06. Thus, the E1/E2 branching ratios determined at 90° have been divided by this number to correct for the angular distribution effects. The energies and intensities of the observed transitions of ^{100}Ru are listed in Table 4.1.

Table 4.1: The energy (E_γ) and the relative intensity (I_γ) of the γ rays of ^{100}Ru along with the spin and parity of the initial (J^i_π) and the nal (J^f_π) states, measured values of R_{DCO}, Δ_{iPDCO} and the energy of the initial state (E_i) are shown. R_{DCO} values are obtained with gates on pure quadrupole transitions except as noted. The quoted uncertainties in the intensities include statistical and fitting errors only. The systematic error due to the efficiency determination has been estimated to be around 3%.

E_i (keV)	E_γ (keV)	$J^i_\pi \rightarrow J^f_\pi$	I_γ	R_{DCO}	Δ_{iPDCO}	Type
539.5(2)	539.5(2)	$2^+ \rightarrow 0^+$	100.0(3)	1.00(1)	0.11(1)	E2
1226.4(1)	686.9(1)	$4^+ \rightarrow 2^+$	93.2(4)	0.99(1)	0.09(1)	E2
2075.7(1)	849.2(2)	$6^+ \rightarrow 4^+$	76.1(3)	1.02(1)	0.08(1)	E2
2167.0(3)	1627.5(4)	$3^- \rightarrow 2^+$	1.42(3)	-	-	E1$^\#$
	2167.0(3)	$3^- \rightarrow 0^+$	0.46(7)	-	-	E3$^\#$
2527.4(3)	360.4(5)	$5^- \rightarrow 3^-$	0.73(9)	1.03(5)	-	E2$^\#$
	1300.9(3)	$5^- \rightarrow 4^+$	9.02(2)	0.70(3)	0.05(1)	E1
	1987.9(3)	$5^- \rightarrow 2^+$	0.12(3)	-	-	E3*
2951.9(2)	424.3(5)	$7^- \rightarrow 5^-$	4.20(44)	0.99(2)	0.07(2)	E2
	876.0(2)	$7^- \rightarrow 6^+$	23.19(22)	0.65(1)	0.09(1)	E1
	1725.2(4)	$7^- \rightarrow 4^+$	0.24(7)	-	-	E3*
2591.9(2)	1365.4(4)	$4^- \rightarrow 4^+$	1.01(1)	-	-	E1$^\#$
	424.9(4)	$4^- \rightarrow 3^-$	0.48(5)	-	-	M1+E2$^\#$
2963.8(1)	371.9(5)	$6^- \rightarrow 4^-$	1.66(17)	1.02(4)	-	E2$^\#$
	888.1(2)	$6^- \rightarrow 6^+$	4.77(3)	0.78(2)	-0.12(8)	E1
	436.4(3)	$6^- \rightarrow 5^-$	2.71(2)	0.84(3)	-	M1+E2
3060.1(2)	984.4(2)	$8^+ \rightarrow 6^+$	38.48(24)	0.99(1)	0.08(1)	E2
3139.5(4)	187.6(3)	$7^- \rightarrow 7^-$	1.94(20)	-	-	
	1063.6(2)	$7^- \rightarrow 6^+$	0.75(8)	0.62(4)	-	E1$^\#$
	611.9(6)	$7^- \rightarrow 5^-$	3.36(5)	1.03(4)	-	E2$^\#$
3503.6(2)	364.3(3)	$9^- \rightarrow 7^-$	4.13(39)	1.02(3)	-	E2$^\#$
	443.5(3)	$9^- \rightarrow 8^+$	5.13(31)	0.66(1)	0.08(1)	E1
	551.9(4)	$9^- \rightarrow 7^-$	5.78(34)	0.97(4)	0.10(3)	E2

	148.9(3)	$9^- \rightarrow 8^-$	1.87(2)	0.71(8)	-	M1+E2$^{\#}$
3354.7(1)	390.9(3)	$8^- \rightarrow 6^-$	7.13(3)	1.00(2)	-	E2$^{\#}$
	294.6(5)	$8^- \rightarrow 8^+$	0.54(6)	-	-	E1$^{\#}$
	403.0(3)	$8^- \rightarrow 7^-$	4.10(3)	-	-	M1+E2$^{\#}$
	215.4(3)	$8^- \rightarrow 7^-$	0.44(4)	0.71(4)	-	D*
3575.6(2)	623.9(4)	$9^- \rightarrow 7^-$	10.51(50)	1.01(3)	0.08(3)	E2
	515.5(3)	$9^- \rightarrow 8^+$	0.92(4)	0.69(4)	0.08(4)	E1
	436.3(3)	$9^- \rightarrow 7^-$	0.52(6)	1.05(6)	-	E2
	220.9(4)	$9^- \rightarrow 8^-$	0.08(1)	-	-	
3992.2(3)	637.5(2)	$10^- \rightarrow 8^-$	9.35(3)	0.98(3)	0.06(4)	E2
	416.6(3)	$10^- \rightarrow 9^-$	0.23(7)	0.74(5)	-0.04(5)	M1+E2*
	488.6(4)	$10^- \rightarrow 9^-$	2.20(8)	0.74(1)	-0.05(2)	M1+E2
4083.4(1)	1023.3(2)	$10^+ \rightarrow 8^+$	13.5(2)	0.99(1)	0.09(1)	E2
4230.7(1)	727.1(2)	$11^- \rightarrow 9^-$	6.57(4)	1.00(3)	0.07(2)	E2
	655.1(1)	$11^- \rightarrow 9^-$	0.76(2)	1.02(2)	0.06(4)	E2*
	238.5(3)	$11^- \rightarrow 10^-$	1.07(4)	0.73(7)	-	M1+E2$^{\#}$
4235.6(4)	1175.8(2)	$10^+ \rightarrow 8^+$	3.11(13)	1.03(2)	0.13(3)	E2*
	152.2(3)	$10^+ \rightarrow 10^+$	0.28(5)	-	-	
	732.0(2)	$10^+ \rightarrow 9^-$	0.21(7)	-	-	
	660.0(4)	$10^+ \rightarrow 9^-$	0.05(1)	-	-	
4315.8(3)	740.2(3)	$11^- \rightarrow 9^-$	7.33(60)	1.08(4)	0.11(4)	E2
	323.6(3)	$11^- \rightarrow 10^-$	0.09(2)	0.60(7)	-0.22(16)	M1+E2*
	812.2(3)	$11^- \rightarrow 9^-$	0.34(3)	1.07(5)	-	Q*
4798.2(2)	806.0(3)	$12^- \rightarrow 10^-$	6.07(4)	0.99(4)	0.07(5)	E2
	482.4(3)	$12^- \rightarrow 11^-$	0.35(4)	0.72(5)	-0.09(6)	M1+E2*
	567.5(4)	$12^- \rightarrow 11^-$	1.20(3)	0.77(2)	-0.06(4)	M1+E2*
4917.8(2)	682.2(2)	$12^+ \rightarrow 10^+$	1.41(2)	1.05(3)	0.09(4)	E2*
	687.1(4)	$12^+ \rightarrow 11^-$	0.34(8)	-	-	E1$^{*\#}$

	834.4(5)	$12^+ \rightarrow 10^+$	7.65(10)	0.98(2)	0.05(3)	E2
5162.6(3)	931.9(2)	$13^- \rightarrow 11^-$	6.19(4)	1.00(1)	0.08(1)	E2
	244.8(4)	$13^- \rightarrow 12^+$	0.017(4)	0.67(7)	-	E1*
	846.8(4)	$13^- \rightarrow 11^-$	2.86(13)	1.06(1)	0.05(4)	E2*
5275.7(2)	959.9(4)	$13^- \rightarrow 11^-$	2.52(7)	1.00(4)	0.07(4)	E2
	477.5(5)	$13^- \rightarrow 12^-$	0.27(3)	0.74(6)	0.04(11)	M1+E2*
5713.1(1)	795.3(3)	$14^+ \rightarrow 12^+$	3.91(2)	0.99(1)	0.13(2)	E2
	550.5(4)	$14^+ \rightarrow 13^-$	0.15(4)	-	-	E1*#
5784.0(4)	985.8(3)	$14^- \rightarrow 12^-$	3.03(4)	1.03(6)	0.04(3)	E2
	508.3(4)	$14^- \rightarrow 13^-$	0.11(2)	0.55(6)	-0.21(13)	M1+E2*
6198.3(2)	1035.7(3)	$15^- \rightarrow 13^-$	2.39(2)	1.01(3)	0.02(1)	E2
	485.2(4)	$15^- \rightarrow 14^+$	0.037(8)	0.65(9)	-	E1*
6282.4(6)	1006.7(5)	$15^- \rightarrow 13^-$	0.85(6)	0.97(7)	0.05(3)	E2*
	498.4(4)	$15^- \rightarrow 14^-$	0.09(2)	0.58(6)	-0.37(23)	M1+E2*
6713.6(1)	1000.5(3)	$16^+ \rightarrow 14^+$	2.31(2)	1.00(1)	0.21(2)	E2
	515.3(3)	$16^+ \rightarrow 15^-$	0.04(1)	1.06(10)[1]	-	E1*
6883.0(5)	1099.2(4)	$16^- \rightarrow 14^-$	1.44(20)	0.96(4)	0.15(3)	E2
7201.8(2)	1003.5(4)	$17^- \rightarrow 15^-$	1.24(2)	0.99(3)	0.05(4)	E2
	488.2(5)	$17^- \rightarrow 16^+$	0.03(1)	-	-	E1*#
7391.4(6)	1109.1(5)	$17^- \rightarrow 15^-$	0.51(20)	1.01(5)	0.12(8)	E2*
7825.1(2)	1111.4(4)	$18^+ \rightarrow 16^+$	1.13(1)	1.03(3)	0.04(3)	E2
	623.3(4)	$18^+ \rightarrow 17^-$	0.06(2)	-	-	E1*#
8016.0(5)	1133.0(4)	$18^- \rightarrow 16^-$	0.32(3)	0.96(6)	0.06(4)	E2
8455.5(5)	1253.7(5)	$19^- \rightarrow 17^-$	0.28(2)	1.02(4)	0.11(8)	E2*
9055.2(3)	1229.5(5)	$20^+ \rightarrow 18^+$	0.81(3)	1.01(3)	0.09(3)	E2

- *: New measurement from current data.
- #: The M2 mixing has been assumed to be negligible following the discussions given in the text.

- [1]: Gate on dipole transition (444 keV $9^- \rightarrow 8^+$).

A similar prescription was used to determine the intensities of the transitions of Band4 and Band5 and the interleaved M1 transitions which are listed in Table 4.1. The placement of two low spin bands namely 6 and 7, were confirmed [25] from the present high statistics data. These positive parity bands are also partners connected by M1 transitions.

Table 4.2: E1 and E2 branching ratios and the estimated values of B(E1)/B(E2) for the low spin levels of ^{100}Ru. The gamma energies were expressed in MeV for calculating the B(E1)/B(E2) ratios.

E_{level} [J^π] (keV)	E_γ (keV)	γ-gates	I(E1)/I(E2)	B(E1)/B(E2) (10^{-8} fm^{-2})
2527 [5^-]	1301 (E1)	552	12.34 ± 1.51	2.61 ± 0.32
	360 (E2)			
2964 [6^-]	888 (E1)	391	2.87 ± 0.30	2.25 ± 0.24
	372 (E2)			
2952 [7^-]	876 (E1)	552	5.52 ± 0.57	8.63 ± 0.90
	424 (E2)			
3355 [8^-]	295 (E1)	638	0.08 ± 0.01	2.08 ± 0.25
	391 ((E2)			
3504 [9^-]	444 (E1)	727	1.24 ± 0.14	6.94 ± 0.76
	364 (E2)			
3576 [9^-]	516 (E1)	740	0.09 ± 0.01	4.63 ± 0.29
	624 (E2)			

In order to measure the γ -ray multipolarities by the Ratio of Directional Correlations from Oriented states (R_{DCO}) method [26], an angle-dependent matrix was constructed with the γ-ray energy detected at 90° along one axis and the coincident γ-ray energy at 125° on the other axis. The linear polarization measurements were also performed to extract the electromagnetic character of the de-exciting γ rays using the integrated Polarization from the Directional Correlation of Oriented states method (iPDCO) [27]. The analysis was performed for all the E2 transitions of the alternate parity bands except for the top-most transition (1337 keV) of Band3, as the data were insufficient. The measured iPDCO and R_{DCO} values have been plotted in Fig. 4.3. The E1 character of the 444 and 876 keV transitions is evident from the figure. This establishes the negative parity assignment for Band3. It may be noted that iPDCO values for the weak E1 transitions were not obtained

from the present data set. However, DCO measurements for the 245 ($13^- \rightarrow 12^+$), 485 ($15^- \rightarrow 14^+$) and 515 ($16^+ \rightarrow 15^-$) keV transitions were performed. The R_{DCO} values for the 245 and 485 keV transitions were 0.67 ± 0.07 and 0.65 ± 0.09, when gated on the ΔI = 2 transitions of 834 and 795 keV, respectively. This value was 1.06 ± 0.10 for 515 keV when gated on the ΔI = 1 transition of 444 keV. All these values match with the calculated R_{DCO} value for a pure ΔI = 1 transition for the given detector geometry. Thus, the dipole transitions between the positive parity Band2 and negative parity Band3 have been assigned as E1 since the M2 mixing is negligible. The measured R_{DCO} and iPDCO values are tabulated in Table 4.1. The present results are in agreement with previous measurements [19, 25].

Table 4.3: E1 and E2 branching ratios and the estimated values of B(E1)/B(E2) for the levels of the alternate parity band. The gamma energies were expressed in MeV for calculating the B(E1)/B(E2) ratios. The evaluated branching ratio is the weighted average of the values obtained from the two independent gates.

E_{level} [J^π] (keV)	E_γ (keV)	γ-gates	I(E1)/I(E2) (10^{-2})	B(E1)/B(E2) (10^{-8} fm^{-2})
4918[12^+]	687(E1)	795 and 687	24.21 ± 5.37	8.47 ± 1.88
	682 (E2)			
5163[13^-]	245 (E1)	1036 and 1004	0.27 ± 0.05	9.84 ± 1.93
	932 (E2)			
5713[14^+]	551 (E1)	1111 and 1001	3.93 ± 1.04	5.88 ± 1.55
	795 (E2)			
6198[15^-]	485 (E1)	1004 and 795	1.54 ± 0.35	12.56 ± 2.83
	1036 ((E2)			
6714[16^+]	515 (E1)	1111 and 444	1.72 ± 0.41	9.75 ± 2.35
	1001 (E2)			
7202[17^-]	488 (E1)	1001 and 795	2.53 ± 0.80	17.07 ± 5.41
	1004 (E2)			
7825[18^+]	623 (E1)	727 and 552	5.17 ± 1.56	27.92 ± 8.40
	1111 (E2)			

The B(E1)/B(E2) rates were determined from the following relation.

$$\frac{B(E1, I_i \rightarrow I_i - 1) \downarrow}{B(E2, I_i \rightarrow I_i - 2) \downarrow} = \frac{1}{1.3 \times 10^6} \frac{I(E1)}{I(E2)} \frac{E_\gamma^5(E2)}{E_\gamma^3(E1)} fm^{-2}$$

where the energies of the γ-rays (E_γ) are expressed in MeV and I(E1)/I(E2) is the mea-

sured branching ratio. The B(E1)/B(E2) ratios for low spin levels of ^{100}Ru are listed in Table. 4.2. The E1 and E2 branching ratios for each level of the alternate parity bands were estimated from two different γ-gated spectra. The values listed in Table. 4.3 are the weighted average of the two values obtained from the two independent γ-gates. These gated spectra are shown in Fig. 4.4.

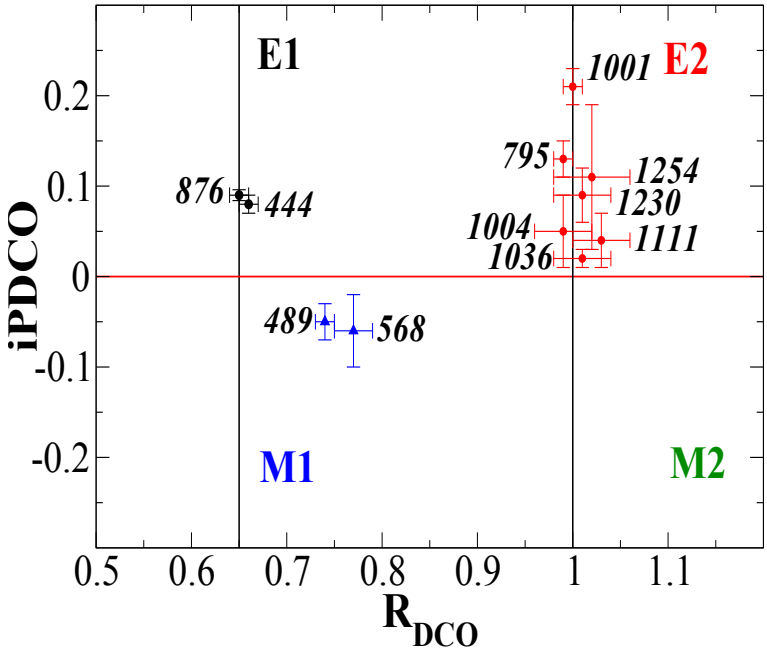

Figure 4.3: The measured values of Ratio of Directional Correlations from Oriented states (R_{DCO}) and integrated Polarization from the Directional Correlation of Oriented states (iPDCO) for different γ transitions of ^{100}Ru. The vertical lines represent the calculated R_{DCO} values of 0.65 and 1.0 for pure $\Delta I = 1$ and $\Delta I = 2$ transitions, respectively, in a stretched E2 gate.

The B(M1)/B(E2) ratio have been estimated following the relation

$$\frac{B(M1, I_i \rightarrow I_i - 1)\downarrow}{B(E2, I_i \rightarrow I_i - 2)\downarrow} = 0.697 \times \frac{I(M1)}{I(E2)} \frac{E_\gamma^5(E2)}{E_\gamma^3(M1)} \mu_N^2/e^2b^2$$

where the quantities have the usual meaning. These values for Bands4 - Band5 and Band6 - Band7 are given in Table 4.4 and Table 4.5, respectively.

Table 4.4: M1 and E2 branching ratios and the estimated values of B(M1)/B(E2) for the spin levels of Band4 and 5 of ^{100}Ru. The gamma energies were expressed in MeV to calculate the B(M1)/B(E2) ratios.

E_{level} [J^{π}] (keV)	E_{γ} (keV)	I(M1)/I(E2) (10^{-2})	B(M1)/B(E2) ($\mu_N^2/(eb)^2$)
4798 [12^-]	482 (M1)	5.76 ± 0.66	0.12 ± 0.02
	806 (E2)		
5276 [13^-]	478 (M1)	10.71 ± 1.23	0.56 ± 0.06
	960 (E2)		
5784 [14^-]	508 (M1)	3.63 ± 0.66	0.18 ± 0.03
	986 (E2)		
6282 [15^-]	498 (M1)	10.59 ± 2.47	0.61 ± 0.14
	1007 ((E2)		

Table 4.5: M1 and E2 branching ratios and the estimated values of B(M1)/B(E2) for the spin levels of Band6 and 7 of ^{100}Ru. The gamma energies were expressed in MeV to calculate the B(M1)/B(E2) ratios.

E_{level} [J^{π}] (keV)	E_{γ} (keV)	I(M1)/I(E2)	B(M1)/B(E2) ($\mu_N^2/(eb)^2$)
2577 [5^+]	514 (M1)	0.32 ± 0.06	0.27 ± 0.05
	695 (E2)		
3447 [7^+]	741 (M1)	0.58 ± 0.07	0.49 ± 0.06
	870 (E2)		
4343 [9^+]	792 (M1)	0.29 ± 0.08	0.23 ± 0.06
	896 ((E2)		

4.4 Discussion

4.4.1 Octupole and strongly couple bands

In Fig. 4.1, Band1 is the ground state band of ^{100}Ru, which corresponds to the vacuum configuration for this even-even nucleus. Band2 has been proposed to originate from the rotational alignment (RAL) of a pair of neutrons in the $h_{11/2}$ orbitals [19]. This is observed as a sharp discontinuity in the band structure of the ground state Band1 at I = 10$\hbar$, beyond which Band2 (s-band of Band1) becomes favoured in energy. This phenomenon [28] happens when the Coriolis interaction decouples a pair of nucleons and aligns their angular momentum vectors along the rotational axis.

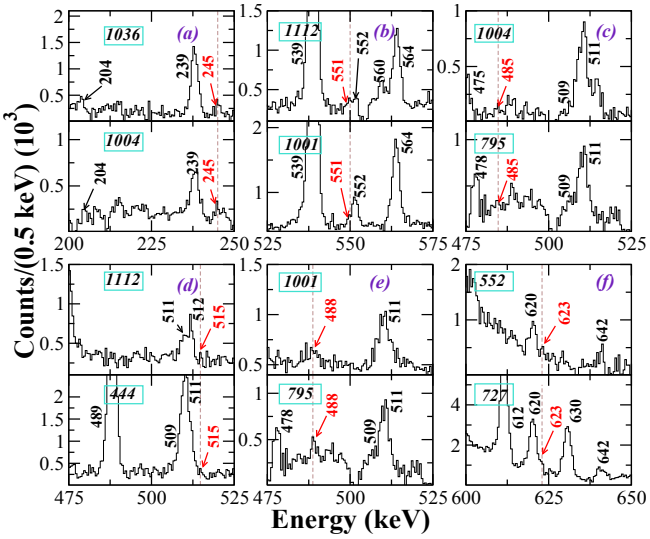

Figure 4.4: Coincident γ spectra observed with the detectors of the 90° ring. The E1 transitions connecting Band2 and Band3 are marked by the dotted line. Each E1 transition is shown in two gamma-gated spectra. The numbers in the rectangular box represent the γ-ray energy of the gating transitions. The gamma energies have been rounded off to their closest integer.

The lowest observed negative parity level in ^{100}Ru is 3^-. The hindrance factor for E1 transition estimated from the lifetime measurement for this level is 1.0×10^{-5} [20]. A similar retardation factor of 1.2×10^{-5} has been estimated for the 5^- level using the observed intensity ratio of the E1 and E2 transitions from this level and assuming $Q_0 \approx 200$ efm^2 for ^{100}Ru following the systematics of the B(E2, $2^+ \rightarrow 0^+$) transition rate [29]. This hindrance is similar to the $1-2\times10^{-5}$ factor observed for the single neutron transitions in odd Cd isotopes [18], which indicates that there is no permanent octupole deformation in ^{100}Ru at low spins. Thus, the presence of the E3 transitions from the low spin negative parity levels indicates that these levels originate due to the collective octupole vibration around a reflection symmetric shape.

At higher spins, three negative parity bands are seen in Fig. 4.1. Interleaved M1 transitions have been observed till $I^\pi = 15^-$ between Band4 and Band5 while these transitions with Band3 are observed only up to $I^\pi = 11^-$ although Band3 is the negative parity yrast sequence. This observation indicates that Band4 and Band5 are signature partners while the presence of M1 transitions between Band3 and Band5 is probably due to the mixing

of 9^- and 11^- levels of Band3 and Band4 as they lie very close in energy ($\approx$ 100 keV). This assumption is supported by the large $B(E2)_{out}/B(E2)_{in}$ value (0.74(4)) observed for the 13^- level of Band3 evaluated from the observed intensities of the 847 (between 5162.6 and 4315.8 keV levels) and 932 keV (between 5162.6 and 4230.7 keV levels) transitions. In the two previous experiments and from the present data set, no unfavoured signature partner of Band3 could be identified. However, its absence may also indicate that this band is shifted to higher energies due to the large signature splitting.

In order to explore the presence of the octupole correlations in ^{100}Ru, the ratio of the inter-band E1 and intra-band E2 transition rates, $B(E1)_{out}/B(E2)_{in}$, have been plotted in Fig. 4.5. These values for the 6^- (E_x = 2963.8 keV) and 8^- (E_x = 3354.7 keV) levels have been extracted by assuming a pure E1 character for the $6^- \rightarrow 6^+$ and $8^- \rightarrow 8^+$ transitions and were found to be similar to that for the 5^- level (E_x = 2527.4 keV). For the 7^- (E_x = 2951.9 keV), 9^-_{Band3} (E_x = 3503.6 keV) and 9^-_{Band4} (E_x = 3575.6 keV) levels, the observed retardation factor lies between $4-7\times10^{-5}$ assuming Q_0 = 200 efm^2. This apparent increase can be understood from the calculations of E1 rates by Hamamoto and Sagawa [30] between the two quasi-neutron band (ν = 2) and ground state band (ν = 0), which predict B(E1) values as large as 10^{-4} e^{2}fm^2 for $\Delta\nu$ = 2 E1 transitions without incorporating octupole deformation. The calculations were also performed for $\Delta\nu$ = 0 transitions and the rates were found to be considerably smaller than the $\Delta\nu$ = 2 transitions. However, these calculated values underestimated the observed B(E1) values by one to three orders of magnitude in the odd-A rare-earth nuclei, which are stable against octupole deformation. It has been proposed [31] that such large enhancement in the E1 rates may arise due to the particle octupole vibrational coupling and the observed rates can be reproduced by tuning the amplitude of an additional term in the E1 transition operator, which accounts for the octupole vibrations in quadrupole-deformed nuclei. However, in all these cases, the two opposite parity bands are not interspaced and their moments of inertia are different. In the mass 100 regions, interspaced opposite parity bands have been reported in ^{104}Pd [32], ^{103}Pd [33] and ^{102}Ru [34] following the neutron $h_{11/2}$ alignment. But in these

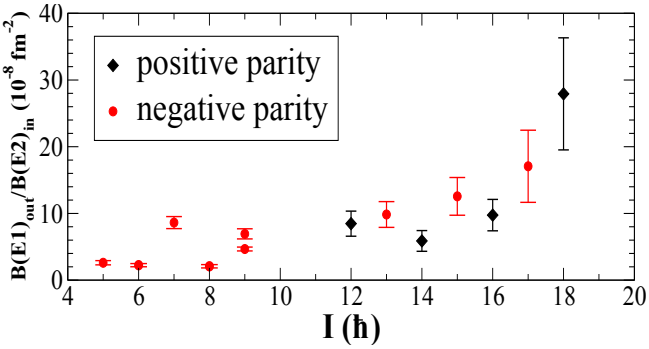

Figure 4.5: Ratios of the inter-band E1 and the intra-band E2 transition rates from the excited levels of ^{100}Ru as a function of spin, I. The lower value of the ratio for the 9^- level corresponds to Band4. The values for I $\leq 9\hbar$ corresponds to $\Delta\nu$ =2 E1 transitions between Band3 and Band1, while for the higher spins, $\Delta\nu$ = 0 E1 transitions between Band3 and Band4 are considered.

cases also the moments of inertia (MOI) of the two bands are significantly different. This difference indicates that the negative and the positive parity bands in these nuclei originate from $\nu[\{d_{5/2}/g_{7/2}\} \bigotimes h_{11/2}]$ and $\nu h^2_{11/2}$ configurations, respectively. In addition, the interleaved transitions have not been reported between the alternate parity bands. Thus, ^{100}Ru is the first nucleus in the A $\approx$ 100 region for which seven inter-leaved E1 transitions have been observed and the moments of inertia of the two alternate parity bands are found to be nearly identical for I > $16\hbar$ (as seen from Fig. 4.6(e)). These observations can be simultaneously accounted for by considering the alignment to occur in the mixed parity orbitals of $[\{d_{5/2}/g_{7/2}\}/h_{11/2}]$ in the intrinsic frame and the parity partners originate due to the parity projection in the laboratory frame. Such a configuration in ^{100}Ru is possible due to the proximity of the octupole driving orbitals of $h_{11/2} - d_{5/2}$ states for N = 56 [35]. It may be noted that the emergence of stable octupole deformation above the first band crossing has already been reported in even - even Lanthanide nuclei [36, 37, 38].

The level energies and B(E1) transition probabilities for N = 88 isotones have been calculated by Garrote *et. al.* [39] within the framework of the Cranked Hartree-Fock-Bogoliubov approximation with the parity breaking Gogny-interaction. The comparison with the observed energy splitting between the alternate parity levels and the B(E1)/B(E2) rates shows a good agreement. These calculations indicate a phase transition from an oc-

tupole vibration to an octupole deformation at a higher spin (I $\approx 10\hbar$) in N = 88 isotones, which is characterized by the vanishing of the parity splitting and the enhancement of the B(E1)/B(E2) rates. It is interesting to note that the B(E1)/B(E2) rates for the alternate parity bands at low spins (I $\leq 16\hbar$) of ^{100}Ru are similar to that observed from the octupole vibrational level of 7^- (E_x = 2951.9 keV) (as seen from Fig. 4.5). On the other hand, the rates increase significantly and also the parity splitting vanishes beyond I = $16\hbar$ (as seen from Fig. 4.6(f)). Thus, from the perspective of Ref. [39], ^{100}Ru seems to exhibit the octupole vibration to octupole deformation phase transition at I = $16\hbar$ [40].

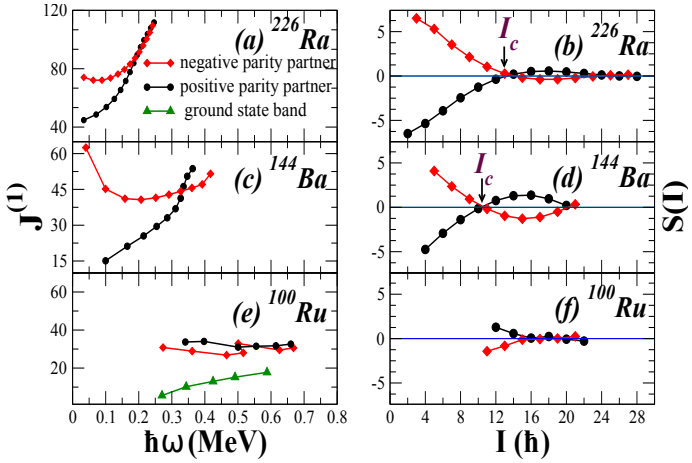

Figure 4.6: Moment of inertia $J^{(1)}$ and parity splitting index S(I) for the positive (black dots) and the negative parity (red diamonds) partner bands of ^{226}Ra, ^{144}Ba and ^{100}Ru are plotted on the left and right panels as a function of rotational frequency (ω) and angular momentum I, respectively.

However, it is important to note that the weighted average value of B(E1)/B(E2) beyond I = $16\hbar$ is 2.0(5) $\times 10^{-7}$ fm^{-2}, which is an order of magnitude smaller than those observed in the Lanthanide and Actinide regions [38, 41]. This indicates that the electric dipole transitions are less enhanced in ^{100}Ru and thus, the octupole deformation is lower. On the other hand, the $\nu h^2_{11/2}$ and $\nu[d_{5/2}/g_{7/2}\}/h_{11/2}]$ assignments for Band2 and Band3 respectively, can not be ruled out. Thus, to establish the stable octupole deformation in ^{100}Ru, it is essential to measure the level lifetimes for the alternate parity bands and compare the measured B(E1) values with the calculated rates for the two separate configurations for Band2 and Band3.

With this goal in mind, a second experiment was performed with the same target projectile combination. But this time, the alpha beam of energy 45 MeV was bombarded on a foil of 10 mg/cm^2 thick ^{100}Mo foil. A total of 4×10^9 γ-γ coincidence events were sorted within a time window of 100 ns by using the sorting program BINDAS [42]. About 58% events were found to belong to the ^{100}Ru channel. The data were sorted to form three angle-dependent asymmetric matrices. The lineshapes are extracted using 1023 keV ($10^+ \rightarrow 8^+$) for Band2, 727 keV ($11^- \rightarrow 9^-$) for Band3, 624 keV ($9^- \rightarrow 7^-$) for Band4 and 638 keV ($10^- \rightarrow 8^-$) for Band5. The lineshape analysis was carried out using the LINESHAPE package [43] along with the development reported in Ref. [44]. The velocity profiles for the ^{100}Ru residues at the three angles of 40°, 90° and 125° were simulated using the stopping powers calculated by SRIM. These profiles were calculated in time steps of 0.001 ps for 10000 trajectories while considering their origins distributed across the expanse of the thick self-supporting target. It may be noted that only an insignificant ($\approx 4\%$) proportion of trajectories remain unfinished within the target, that do not impact the subsequent analysis. The γ-ray energies and intensities were treated as the inputs to the line shape fit. The side-feeding intensities at each level were calculated from the measured intensities tabulated in Table 4.1. The detailed procedure for lineshape fitting has been described in Chapter 3.

The global fit for each band was carried out simultaneously at 40°, 90° and 125°. Lineshape fits for four γ transitions namely 1111 keV ($18^+ \rightarrow 16^+$ for Band2), 1004 keV ($17^- \rightarrow 15^-$ for Band3), 1007 keV ($15^- \rightarrow 13^-$ for Band4) and 986 keV ($14^- \rightarrow 12^-$ for Band5) are presented in Fig. 4.7. The measured level lifetimes and the evaluated transition rates are listed in Table. 4.6 and 4.7. The weighted average of the quadrupole moment (Q_0) are 279(14), 261(9), 202(10) and 215(9) (efm^2) for Band2, Band3, Band4 and Band5 respectively. The Q_0 values corresponding to Bands (2,3) and (4,5) are shown in Fig. 4.8 and Fig. 4.9, respectively. As seen in these figures, the Q_0 value is nearly the same for the alternate parity bands (Band2 and Band3) while the value for the signature partner bands (Band4 and Band5) is marginally smaller. In this regard, it may be noted that the

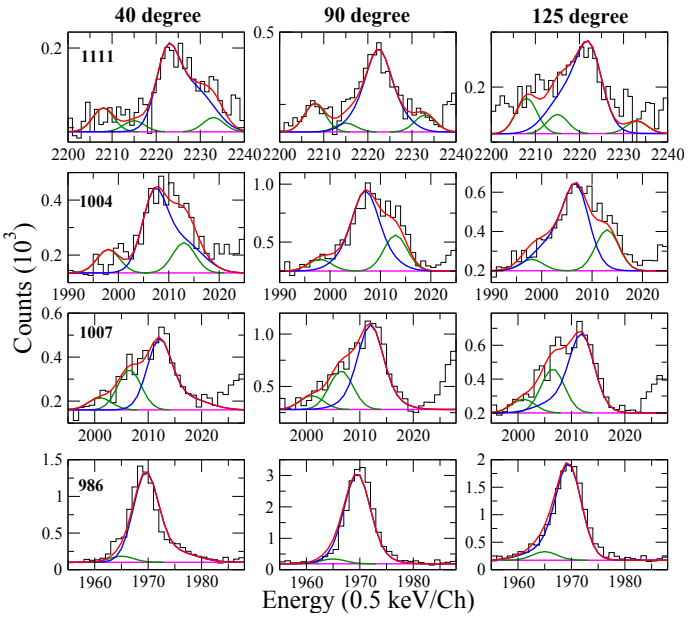

Figure 4.7: The line-shape fits for 1001 keV of Band2, 1036 keV of Band3 and 986 keV of Band5 at 40°, 90° and 157° to the beam direction. The fitted Doppler broadened line shapes are drawn in blue lines while the contaminant peaks are shown in green lines. The result of the fit to the experimental data is shown in red lines.

B(M1) values exhibit the characteristic staggering of inter-band transitions between the two signature partners [45].

Table 4.6: The measured lifetimes of electric quadrupole transitions of the ^{100}Ru levels for Band2, Band3, Band4 and Band5. The uncertainties in the lifetime measurements were derived from the behaviour of the χ^2 in the vicinity of the minimum for the simultaneous fit at the three angles.

E_i	E_γ	$J^i_\pi \rightarrow J^f_\pi$	τ	B(E2) (e^2fm^4)		Q_0 (efm^2)	
(keV)	(keV)		(ps)	Expt.	TPSM	Expt.	TPSM
			Band2				
5713.1(1)	795.3(3)	$14^+ \rightarrow 12^+$	1.01(9)	2444(220)	2557	269(24)	275
6713.6(1)	1000.5(3)	$16^+ \rightarrow 14^+$	0.31(2)	2573(180)	2573	277(19)	277
7825.1(2)	1111.4(4)	$18^+ \rightarrow 16^+$	0.15(1)	2975(241)	2522	292(24)	269
9055.2(3)	1229.5(5)	$20^+ \rightarrow 18^+$	0.14^u	2128^l	2081	248	245
			Band3				
5162.6(3)	931.9(2)	$13^- \rightarrow 11^-$	0.49(3)	1628(97)	2338	224(13)	268

6198.3(2)	1035.7(3)	$15^-\rightarrow13^-$	0.30(2)	2272(114)	2188	260(14)	255
7201.8(2)	1003.5(4)	$17^-\rightarrow15^-$	0.23(1)	3454(162)	1718	316(15)	223
8455.5(5)	1253.7(5)	$19^-\rightarrow17^-$	0.12^u	2202^l	1156	252	183
			Band4				
5275.7(2)	959.9(4)	$13^-\rightarrow11^-$	0.70(5)	1291(89)	1259	199(14)	197
6282.4(6)	1006.7(5)	$15^-\rightarrow13^-$	0.56(4)	1302(93)	676	197(14)	142
7391.4(6)	1109.1(5)	$17^-\rightarrow15^-$	0.41^u	1172^l	589	183	130
			Band5				
4798.2(2)	806.0(3)	$12^-\rightarrow10^-$	1.30(6)	1469(68)	2110	212(10)	254
5784.0(4)	985.8(3)	$14^-\rightarrow12^-$	0.50(3)	1670(120)	2319	223(16)	263
6883.0(5)	1099.2(4)	$16^-\rightarrow14^-$	0.40^u	1273^l	2393	195	267

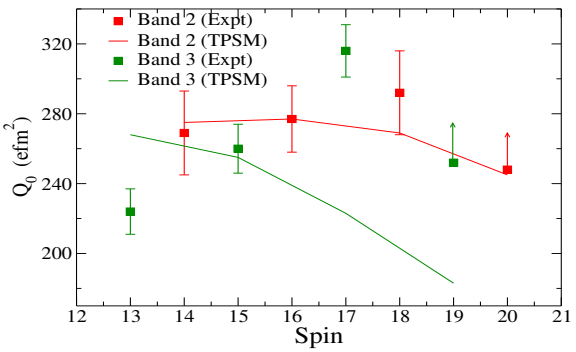

Figure 4.8: Intrinsic quadrupole moment (Q_0) values as a function of spin for Band2 and Band3. The solid line represents the values from TPSM calculations.

The B(E1) rate of 1.8(4) $\times$ 10^{-6} e^2fm^2 has been estimated for 10^+ $[h^2_{11/2}]\rightarrow 9^-$ $[h_{11/2} \bigotimes (g_{7/2}/d_{5/2})]$ transition in the neighbouring ^{110}Cd [46]. It may be observed from Table. 4.7 that the measured B(E1) rates in ^{100}Ru are two orders of magnitude enhanced compared to that observed for ^{110}Cd. This is a clear indication of the presence of octupole collectivity in ^{100}Ru. However, it may be noted that E1 transition rates can be dominated by single particle effects, which may be different for ^{110}Cd and ^{100}Ru. Thus, it is necessary to estimate these rates for ^{100}Ru. These numerical calculations have been carried out in the TPSM framework.

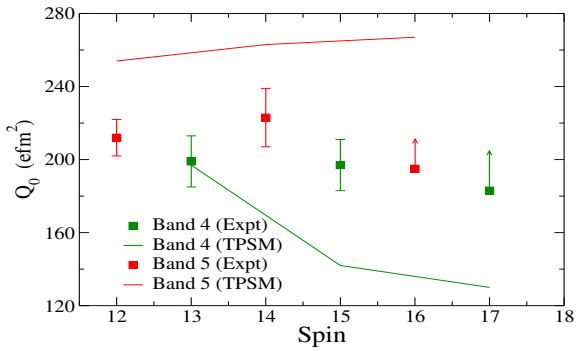

Figure 4.9: Intrinsic quadrupole moment (Q_0) values as a function of spin for Band4 and Band5. The solid line represents the values from the TPSM calculations.

In TPSM calculations, the valence particles were allowed to occupy two major oscillator shells (N = 4 and N = 5) [47]. This allowed the construction of the negative parity states with two quasiparticle configurations in ^{100}Ru. From the various projected bands, positive and negative yrast cascades were considered as Band2 and Band3, respectively. In these TPSM calculations, the Hamiltonian consisted of pairing and quadrupole-quadrupole interaction terms, which are parity-conserving. However, the observed enhanced E1 transition rates between the alternate parity bands indicated the presence of octupole correlations. As a first step to consider the octupole correlations in the TPSM approach, the Hamiltonian was augmented by including the octupole-octupole interaction terms among neutrons, protons and also between neutrons and protons. The coupling constant of the octupole interaction term was adopted to be ten times smaller than the quadrupole coupling constant, which follows from the hydrodynamical estimate [4]. The Hamiltonian was diagonalized with the angular-momentum projected wavefunction having parity as a good quantum number and, therefore, in the present work, octupole interaction has been considered as a perturbation [47]. The deformation parameters were chosen such that the in-band B(E2) rates are reasonably well reproduced at low spins as tabulated in Table. 4.6. The evaluated Q_0 values for Bands 2, 3, 4 and 5 are compared with the calculated values obtained from the TPSM calculations in Fig. 4.8 and Fig. 4.9. The experimental routhians were well described by the TPSM calculations as shown in Fig. 4.10.

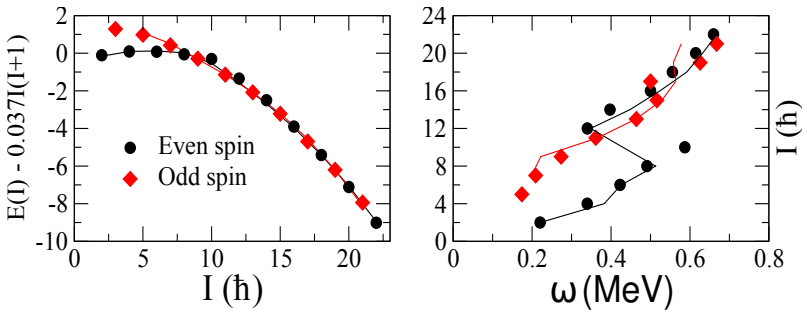

Figure 4.10: Level energies minus rotor contribution values and angular momentum as a function of spin (I) and rotational frequency (ω), respectively for positive parity Band1 and Band2 (black circles) and negative parity Band3 (red diamond). The solid line represents the values from TPSM calculations.

Using these TPSM wavefunctions, the B(E1) rates for the interleaved transitions between Band2 and Band3 were calculated with and without considering octupole-octupole perturbation as tabulated in Table. 4.7. As seen from Fig. 4.11, the TPSM values were enhanced by a factor of $\approx$ 1.5 after the incorporation of the perturbation term. However, the calculated values are still an order of magnitude lower at high spins (I $\geq 16\hbar$) compared to the experimental observations. This indicates clearly that the high spin levels of Band2 and Band3 originate due to octupole collectivity, while the lower spins may originate due to the octupole correlations.

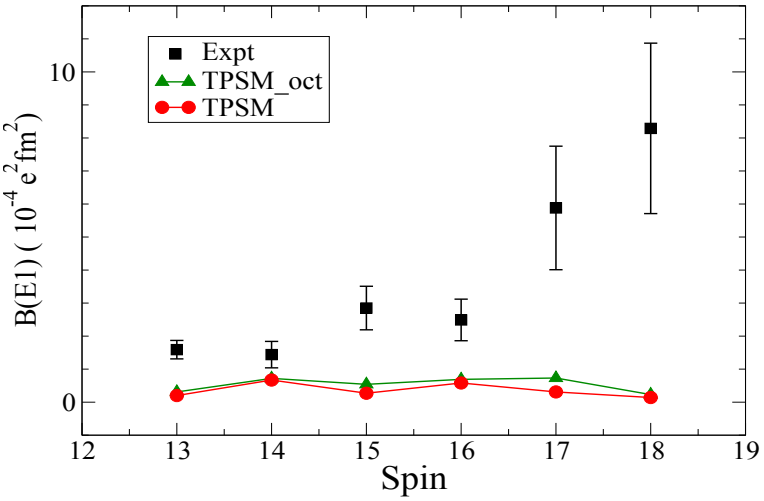

Figure 4.11: B(E1) values vs spin for Band2 and Band3. The solid line represents theoretical calculations using the TPSM framework.

Table 4.7: The measured lifetimes of dipole transitions of the ^{100}Ru levels for Band2 and Band3 along with the values from the two TPSM calculations; one considering only quadrupole-quadrupole and pairing term and the other one additionally considering octupole perturbation. The uncertainties in the lifetime measurements were derived from the behaviour of the χ^2 in the vicinity of the minimum for the simultaneous fit at the three angles.

E_γ	τ	B(E1) (10^{-4} e^{2}fm^2)			B(E1) (10^{-4} w.u.)		
(keV)	(ps)	Expt.	TPSM	TPSM$_{oct}$	Expt.	TPSM	TPSM$_{oct}$
			Band2				
550.5(4)	1.01(9)	1.44(40)	0.67	0.72	1.04(29)	0.49	0.52
515.3(3)	0.31(2)	2.49(63)	0.58	0.69	1.80(46)	0.42	0.50
623.3(4)	0.15(1)	8.29(258)	0.14	0.23	6.00(187)	0.10	0.17
			Band3				
244.8(4)	0.49(3)	1.59(28)	0.20	0.31	1.15(6)	0.15	0.22
485.2(4)	0.30(2)	2.85(66)	0.27	0.54	2.06(9)	0.20	0.39
488.2(5)	0.23(1)	5.88(187)	0.31	0.73	4.26(17)	0.22	0.53

It may be noted that the dynamic octupole deformation (i.e vibration) in ^{100}Ru can be ruled out following the two arguments:

1. For a band built on a rotationally aligned octupole phonon, the negative parity sequence is always shifted up in energy [31, 48] and thus, the two opposite parity bands are not interspaced and their moments of inertia are different.

2. Only the transitions $I^- \rightarrow (I-1)^+$ are allowed [48]. Thus, the interleaved E1 transitions will not be present.

These arguments establish that the high spin states of Band2 and Band3 originate due to the rotation of a stable octupole shape. To further explore the rotational characteristics of the two alternate parity bands of ^{100}Ru, the moments of inertia of the parity partner bands of two well-known pear-shaped nuclei, namely ^{226}Ra [5] and ^{144}Ba [7], have been compared with those of ^{100}Ru on the left panel of Fig. 4.6. On the right panel, the values

of parity splitting indices, S(I^+) and S(I^-) have been plotted, where S(I) is defined as the difference of the energy difference of the I, (I − 1) and (I − 2) levels [49].

For ^{226}Ra, the value of both the parity indices becomes zero at $I_c = 12\hbar$, which indicates the onset of strong octupole correlations [49]. At the corresponding frequency ($\hbar\omega = 0.18$ MeV), the MOI values of both the bands become similar as shown in Fig. 4.6(a). This marks the onset of stable octupole deformation in ^{226}Ra [14] and beyond I_c, the negative parity levels become favoured in energy. This phenomenon of parity inversion in the nuclei of the Actinide region has been explored by Jolos et.al [50] within the framework of the particle-rotor coupling model. These calculations indicate that the intrinsic configuration for the alternating parity bands changes from a fully paired configuration (K = 0, where K is the projection of I along the symmetry axis of the nucleus) before the parity inversion to one with rotationally aligned nucleons (K ≠ 0) after the inversion. Thus, the rotational alignment leads to the stabilization of octupole deformation as the pairing correlations become weaker [41]. With increasing spin, the potential barrier height at $\beta_3 = 0$ increases and the parity splitting due to the tunnelling between the two minima vanishes beyond the I = 23 $\hbar$ in ^{226}Ra, as seen in Fig. 4.6(b).

The nature of the S(I) plot for ^{144}Ba is very similar to that of ^{226}Ra as seen from (Fig 4.6(d)). The parity inversion happens around I = 10$\hbar$ [38], where the first band crossing takes place and beyond I = 20$\hbar$, the parity splitting vanishes. However, the MOI of the alternate parity bands continue to be significantly different till the highest observed frequencies as seen from Fig 4.6(c) and in this respect, the behaviour is different from ^{226}Ra.

The MOI and S(I) plots for ^{100}Ru are distinct from the above two cases as seen in Fig. 4.6. It is observed from Fig. 4.6(e) that the MOI values of the two parity bands are similar over the entire range of observed spins. This is the consequence of the RAL configuration for the alternate parity bands of ^{100}Ru, as the pairing correlation becomes substantially weaker. It may be noted that the MOI values of the pear-shaped odd-mass nuclei, for example, ^{223}Th [51] and ^{225}Th [52], also exhibit a similar weak dependence on rotational

frequency due to the presence of the odd nucleon, which lowers the pairing correlations due to Pauli blocking.

At lower spins, $12\hbar \leq I \leq 16\hbar$, the difference in the MOI values is probably due to the strong octupole correlations as indicated by the TPSM calculations. Beyond $I = 16\hbar$, the MOI values for the alternate parity bands become nearly identical and the parity splitting vanishes as seen from Fig. 4.6(e) and (f), respectively. This observation, along with the observed increase in the B(E1) rates (as seen from Fig. 4.11), seems to indicate the onset of stable octupole deformation in ^{100}Ru beyond $I = 16\hbar$.

To summarize, the seven interleaved E1 transitions have been observed between the two alternate parity bands of ^{100}Ru, whose moments of inertia are nearly identical. The enhancement of the B(E1)/B(E2) rates and the vanishing of the parity splitting beyond $I = 16\hbar$ indicate the emergence of stable octupole deformation in ^{100}Ru based on a RAL configuration.

It is possible to estimate the liquid drop contribution to the intrinsic dipole moment from the droplet model [53] following the prescription by Dorso *et. al.* [54]. In this formalism, D_0^{macro} is expressed as the difference between two terms, namely the redistribution term, which originates from the 'lightning rod' effect and the 'neutron skin' term. The different parameters of the droplet model have been chosen by Butler and Nazarewich [55]. This numerical calculation has been carried out for ^{100}Ru with $\beta_2 = 0.23$ and $\beta_4 = 0.03$. The β_2 values have been evaluated from the weighted average value of Q_0 for Band2 and Band3 [listed in Table. 4.6]. The D_0 value of 0.03 efm is found for $\beta_3 \approx 0.1$.

4.4.2 Band4 and Band5 - the signature partner bands

These two bands are connected by pure M1 transitions. The measured B(M1) rates have been given in Table 4.8. The characteristic staggering of the transition energies (Fig. 4.12) and transition rates establish them to be signature partners. These strongly-coupled neg-

Table 4.8: The measured lifetimes of dipole transitions of the ^{100}Ru levels for Band4 and Band5. The uncertainties in the lifetime measurements were derived from the behaviour of the χ^2 in the vicinity of the minimum for the simultaneous fit at the three angles.

E_i (keV)	E_γ (keV)	$J^i_\pi \rightarrow J^f_\pi$	τ (ps)	B(M1) (μ_n^2)
		Band4		
4315.8(3)	323.6(3)	$11^- \rightarrow 10^-$	2.77(14)	0.007(2)
5275.7(2)	477.5(5)	$13^- \rightarrow 12^-$	0.70(5)	0.072(8)
6282.4(6)	498.4(4)	$15^- \rightarrow 14^-$	0.56(4)	0.079(23)
		Band5		
4798.2(2)	482.4(3)	$12^- \rightarrow 11^-$	1.30(6)	0.018(3)
5784.0(4)	508.3(4)	$14^- \rightarrow 13^-$	0.50(3)	0.030(6)

ative parity sequences can only arise due to $\nu[h_{11/2} \bigotimes d_{5/2}/g_{7/2}]$ configuration as $h_{11/2}$ is the only negative parity intruder orbital present in this mass region.

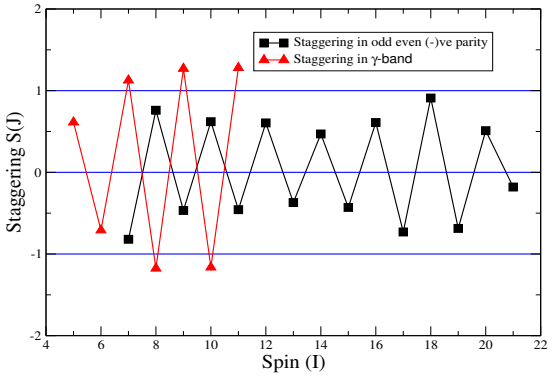

Figure 4.12: Energy staggering S(I) for the negative parity partners (black square) and the positive parity γ (red diamonds) partner bands of ^{100}Ru are plotted as a function of angular momentum I.

4.4.3 Band6 and Band7 - the γ - soft bands

The two γ-soft bands with positive parity are based on the 2^+ level. The odd-even spin energy staggering function is used to explain the difference between a γ-soft and a γ-rigid energy sequence [56].

The staggering function is defined as

$$S(I) = \frac{E(I) + E(I-2) - 2E(I-1)}{E(2_g^+)} \tag{4.1}$$

which yields positive values for even spins and negative values for odd spins in the case of a γ rigid rotation. For the γ soft rotor, on the other hand, the sign between the odd and even spins is inverted. The S(I) plot for ^{100}Ru shown in Figure 4.12 (in red), clearly establishes ^{100}Ru as a γ-soft rotor also. It is interesting to note that the phase of staggering is opposite for the strongly coupled bands (Band4 and Band5).

Thus, ^{100}Ru has been established as a unique nucleus of the A $\approx$ 100 mass region. On one hand, it exhibits collective rotation of a reflection asymmetric shape leading to the two inter-spaced opposite parity bands (Band2 and Band3), while on the other, it has a pair of strongly coupled bands leading to signature partner bands (Band4 and Band5). In addition to this co-existence of reflection symmetric and asymmetric shapes, ^{100}Ru has also been found to be γ-soft at low spins.

Bibliography

[1] Aage Bohr and Ben R Mottelson. Nuclear Structure. World Scientific Publishing Company, 1998.

[2] J. Fernández-Niello *et. al.* High-spin states in ^{218}Ra. Nuclear Physics A, 391(1):221–236, 1982.

[3] M. M. R. Chishti *et. al.* Direct measurement of the intrinsic electric dipole moment in pear-shaped Thorium-228. Nature Phys., 16(8):853–856, 2020.

[4] L. P. Gaffney *et. al.* Studies of pear-shaped nuclei using accelerated radioactive beams. Nature, 497(7448):199–204, 2013.

[5] J. F. C. Cocks *et. al.* Observation of octupole structures in radon and radium isotopes and their contrasting behaviour at high spin. Phys. Rev. Lett., 78:2920–2923, Apr 1997.

[6] P. A. Butler *et. al.* Evolution of octupole deformation in radium nuclei from coulomb excitation of radioactive ^{222}Ra and ^{228}Ra beams. Phys. Rev. Lett., 124:042503, Jan 2020.

[7] S. J. Zhu, *et. al.* Coexistence of reflection asymmetric and symmetric shapes in ^{144}Ba. Phys. Rev. Lett., 124:032501, Jan 2020.

[8] B. Bucher, S. Zhu et al. Direct evidence for octupole deformation in ^{146}Ba and the origin of large E1 moment variations in reflection-asymmetric nuclei. Phys. Rev. Lett., 118:152504, Apr 2017.

[9] Raymond K. Sheline and P. C. Sood. Octupole deformation at high spin in the Ba-Sm region. Phys. Rev. C, 34:2362–2364, Dec 1986.

[10] W. Andrejtscheff *et. al.* Octupole collectivity and spin dependence of the E1 transition moments in ^{150}Sm. Physics Letters B, 437(3):249–256, 1998. 36

[11] P. A. Butler and W. Nazarewicz. Intrinsic reflection asymmetry in atomic nuclei. Rev. Mod. Phys., 68:349–421, Apr 1996.

[12] P. A. Butler. Octupole collectivity in nuclei. J. Phys. G, 43(7):073002, 2016.

[13] P. Butler. Pear-shaped atomic nuclei. Proceedings of the Royal Society A: Mathematical, Physical and Engineering Sciences, 476:20200202, 07 2020.

[14]] I. Ahmad and P. A. Butler. Octupole shapes in nuclei. Ann. Rev. Nucl. Part. Sci., 43:71–116, 1993.

[15] Yuchen Cao *et. al.* Landscape of pear-shaped even-even nuclei. Phys. Rev. C, 102:024311, Aug 2020.

[16] H. Mach *et. al.* Strong octupole and dipole collectivity in ^{96}Zr: Indication for octupole instability in the A = 100 mass region. Phys. Rev. C, 42:R811–R814, Sep 1990.

[17] S. Lalkovski *et. al.* Octupole collectivity in ^{98,100,102}Mo. Phys. Rev. C, 75:014314, Jan 2007.

[18] G.E. Perez *et. al.* Structure of high-spin states in ^{100}Pd. Nuclear Physics A, 686(1):41– 63, 2001.

[19] J. Timár *et. al.* Terminating bands in ^{98,99,100}Ru nuclei: New information on the neutron $2d_{5/2}$ and $1g_{7/2}$ energy spacing. Phys. Rev. C, 62:044317, Sep 2000.

[20] Balraj Singh and Jun Chen. Nuclear data sheets for A=100. Nuclear Data Sheets, 172:1–542, 2021.

[21] P J Nolan, F A Beck, and D B Fossan. Large arrays of escape-suppressed gamma-ray detectors. Annual Review of Nuclear and Particle Science, 44(Volume 44,):561–607, 1994.

[22] S. Das *et. al.* A Compton suppressed detector multiplicity trigger-based digital DAQ for gamma-ray spectroscopy. NIM A:893:138–145, 2018.

[23] D.C Radford. Escl8r and levit8r: Software for interactive graphical analysis of HPGe coincidence data sets.NIM A: , 361(1):297–305, 1995.

[24] R.P. Singh Ranjan Bhowmik, S. Muralithar. Ingasort, a new program for the analysis of multi-clover array. DAE-BRNS symposium on nuclear physics: contributed papers. V. 44B, 2001.

[25] L. Genilloud *et. al.* Study of the vibrational nucleus ^{100}Ru by the ^{98}Mo(α,2nγ) and ^{99}Ru(n,γ) reactions. Nuclear Physics A, 662(1):3–43, 2000.

[26] A. Krämer-Flecken *et. al.* Use of DCO ratios for spin determination in - coincidence measurements. NIM A: , 275(2):333–339, 1989.

[27] K. Starosta *et. al.* Experimental test of the polarization direction correlation method (PDCO).NIM A: 423(1):16–26, 1999.

[28] A. Johnson, H. Ryde, and S.A. Hjorth. Nuclear moment of inertia at high rotational frequencies. Nuclear Physics A, 179(3):753–768, 1972.

[29] S. Raman *et. al.* Transition probability, B(E2)↑, from the ground to the first-excited 2^+ state of even-even nuclides. Atomic Data and Nuclear Data Tables, 36(1):1–96, 1987.

[30] I Hamamoto and H Sagawa. Electromagnetic transitions in rotating nuclei, Sep 1979.

[31] G. B. Hagemann, I. Hamamoto, and W. Satuła. Electric-dipole transitions and octupole softness in odd-a rare-earth nuclei. Phys. Rev. C, 47:2008–2018, May 1993.

[32] N. Rather *et. al.* Antimagnetic rotation in ^{104}Pd. Phys. Rev. C, 89:061303, Jun 2014.

[33] B. M. Nyakó *et. al.* Band terminations in ^{103}Pd. Phys. Rev. C, 60:024307, Jul 1999.

[34] D. Sohler *et. al.* High-spin structure of ^{102}Ru. Phys. Rev. C, 71:064302, Jun 2005.

[35] W. Nazarewicz and S. L. Tabor. Octupole shapes and shape changes at high spins in the Z ≈ 58, N ≈ 88 nuclei. Phys. Rev. C, 45:2226–2237, May 1992.

[36] W. R. Phillips *et. al.* Octupole deformation in neutron-rich Barium isotopes. Phys. Rev. Lett., 57:3257–3260, Dec 1986.

[37] W. Urban *et. al.* Evidence for coexistence of reflection asymmetric and symmetric shapes in ^{150}Sm. Physics Letters B, 185(3):331–335, 1987.

[38] S.J. Zhu *et. al.* Octupole deformation in ^{142,143}Ba and ^{144}Ce: new band structures in neutron-rich Ba-isotopes. Physics Letters B, 357(3):273–280, 1995.

[39] E. Garrote, J. L. Egido, and L. M. Robledo. Fingerprints of reflection asymmetry at high angular momentum in atomic nuclei. Phys. Rev. Lett., 80:4398–4401, May 1998.

[40] A. Karmakar *et. al.* Possibility of stable octupole deformation in ^{100}Ru. Phys. Rev. C, 109:054312, May 2024.

[41] W. Nazarewicz and P. Olanders. Rotational consequences of stable octupole deformation in nuclei. Nuclear Physics A, 441(3):420–444, 1985.

[42] S. S. Nayak and G. Mukherjee. Development of an advanced, multi-function, multi-daq-compatible data sorting and analysis software suite- BINDAS. IEEE Transactions on Nuclear Science, 70(12):2561–2571, 2023.

[43] N.R. Johnson J.C Wells. Oak Ridge National Laboratory Report No. ORNL-6689, 1991.

[44] S. Das *et. al.* Extending the application of DSAM to atypical stopping media. Nuclear Instruments and Methods in Physics Research Section A: 841:17–23, 2017.

[45] Santosh Roy *et. al.* Emergence of principal axis rotation in ^{110}Ag. Physics Letters B, 710(4):587–593, 2012.

[46] L.K. Kostov, W. Andrejtscheff, L.G. Kostova, L. Käubler, H. Prade, and R. Schwengner. Absolute e1 and e2 transition rates in ^{110}Cd. Eur. Phys. J. A, 2(3):269–273, 1998.

[47] Nazira Nazir and J. A. Sheikh. Private communication.

[48] X. Wang *et. al.* Structure of ^{240}Pu: Evidence for octupole phonon condensation? Phys. Rev. Lett., 102:122501, Mar 2009.

[49] N. V. Zamfir, P. von Brentano, and R. F. Casten. Phenomenological signature for the onset of strong octupole correlations. Phys. Rev. C, 49:R605–R607, Feb 1994.

[50] R. V. Jolos, N. Minkov, and W. Scheid. Inversion of parity splitting in alternating parity bands at high angular momenta. Phys. Rev. C, 72:064312, Dec 2005.

[51] M. Dahlinger *et. al.* Alternating parity bands and octupole effects in ^{221}Th and ^{223}Th. Nuclear Physics A, 484(2):337–375, 1988.

[52] J. R. Hughes, *et. al.* Octupole correlations in ^{225}Th. Nuclear Physics A, 512(2):275–293, 1990.

[53] P. Moller, J.R. Nix, W.D. Myers, and W.J. Swiatecki. Nuclear ground-state masses and deformations. Atomic Data and Nuclear Data Tables, 59(2):185–381, 1995.

[54] C.O. Dorso, W.D. Myers, and W.J. Swiatecki. Droplet-model electric dipole moments. Nuclear Physics A, 451(2):189–201, 1986.

[55] P.A. Butler and W. Nazarewicz. Intrinsic dipole moments in reflection-asymmetric nuclei. Nuclear Physics A, 533(2):249–268, 1991.

[56] E. A. McCutchan, Dennis Bonatsos, N. V. Zamfir, and R. F. Casten. Staggering in γ-band energies and the transition between different structural symmetries in nuclei. Phys. Rev. C, 76:024306, Aug 2007.

Chapter 5

Spectroscopic Studies in ^{98}Mo

The previous chapter reports the presence of permanent octupole deformation in ^{100}Ru for the configuration with two rotationally aligned $h_{11/2}$ quasi-neutrons. In order to establish this novel phenomenon, it is essential to study its neighbouring N = 56 nucleus namely, ^{98}Mo. The previous work on ^{98}Mo hinted at an octupole collectivity due to the presence of a 3^- state and observation of an E3 transition decaying from this 3^- state [1]. However, the alternate parity bands in ^{98}Mo have not been established. In the present chapter, I report the extension of the level scheme and the spin-parity assignment of all the observed levels of ^{98}Mo thereby establishing the alternate parity band structure. However, the present data volume was found to be inadequate for the observation of the interleaved E1 transitions.

5.1 Experimental details

The excited levels of ^{98}Mo were populated through the ^{100}Mo(^{4}He,α 2n)^{98}Mo fusion-evaporation reaction using a beam of energy 45 MeV and enriched 10 mg/cm^2 thick target. A total of 4×10^9 γ-γ coincidence events were sorted with a time window of 100 ns by using the sorting program BINDAS [2]. Only about 15% events were found to belong to the channel of interest.

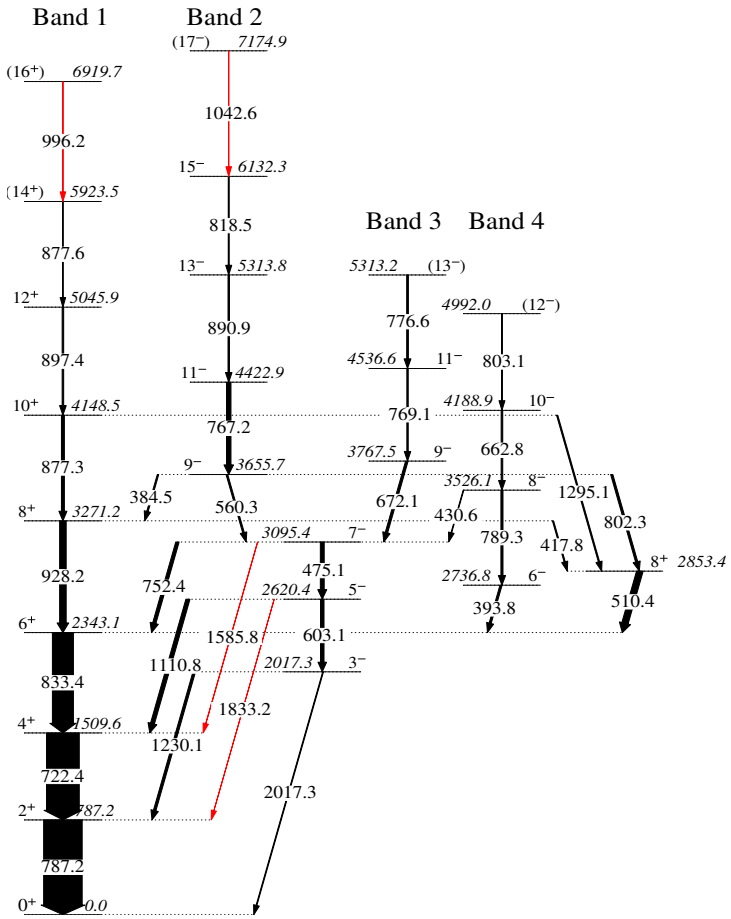

Figure 5.1: The partial level scheme of ^{98}Mo established from the present work. The level and transition energies are expressed in keV. The thicknesses of the arrows are proportional to the relative intensities of the de-exciting γ-rays. The transitions marked in red are newly observed in the present data set.

5.2 Results

Fig. 5.1 shows the partial level scheme established from the present data. Two new E3 transitions, namely 1833.2 keV and 1585.8 keV could be established. Bands 1 and 2 could be extended to spin 16^+ and 17^- spin levels through the placement of 996.2 keV and 1042.6 keV transitions, respectively. Fig. 5.2 shows the coincidence spectrum gated with 787.2 keV (ground state $2^+ \rightarrow 0^+$) transition, where the four newly placed transitions are identified with red. However, in the previous work on ^{98}Mo [1], the spin and parity of levels above I = 6$\hbar$ were unassigned. Hence, to establish the bands as an alternating parity sequence, it was necessary to determine the electromagnetic characters and multipolarities

of the transitions decaying from these levels. To achieve this, R_{DCO} and polarisation measurements have been carried out in this thesis.

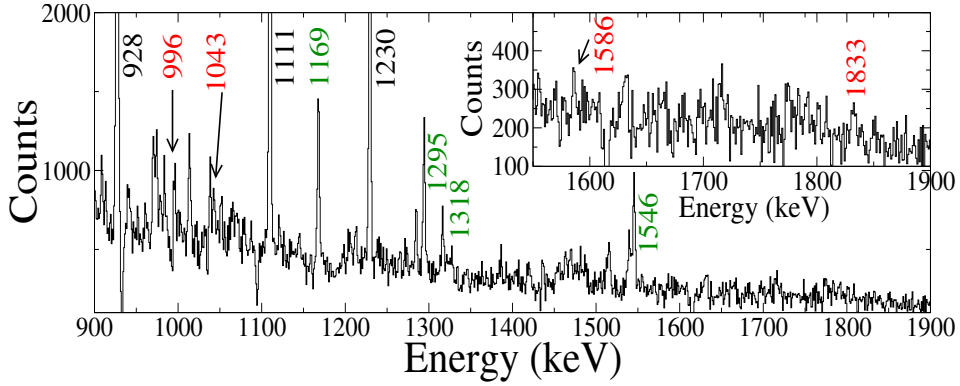

Figure 5.2: Gated spectrum of ^{98}Mo using 787.2 keV gate. The transitions marked in red are newly placed from the present experiment. However, those marked in green, are transitions from ^{98}Mo but not part of the partial level scheme. Transition energies are rounded off to the nearest integer value.

The measured DCO values for the previously reported pure E1 transitions of 1430 and 1206 keV between the positive and negative parity yrast band of ^{101}Ru [3], which was a major channel in our experiment, were fitted to estimate the attenuation coefficient for alignment. Calculation of R_{DCO} needs at least one strong transition whose multipolarity is already established. For this purpose, values for most of the transitions were estimated using the lowest 787.2 keV transition, which is established as a stretched $\Delta I = 2$ ($2^+ \rightarrow 0^+$) transition. However, this is a strong transition and was found to contain significant coincident Compton events, leading to a high background in the γ-gated coincidence spectrum. Thus, it is not suitable to measure weaker transitions in this gate. Hence, different gates of different multipolarities have been used, which will be discussed in detail. The polarisation asymmetry value for an electric type of transition is positive and thus, the photopeak counts for the gated addback events in the perpendicular direction are more than that of parallel. The vice versa is true for a magnetic type of transition. The values, unlike DCO calculations, do not depend on the nature of gating transitions. Hence, any strong γ-ray can be used as a gate for sufficient counts in the photopeaks.

In order to establish the spin-parity of a band, it is crucial to determine the spin and parity

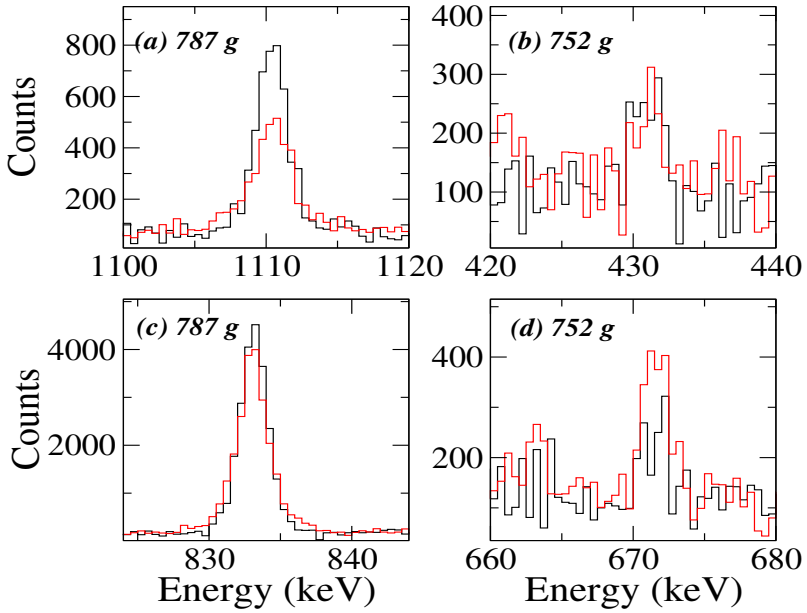

Figure 5.3: Spectrum for calculating R_{DCO} values showing four possible combinations of multipolarity of gating and observed transition. Panel (a), (b), (c) and (d) represent dipole transition (D) gated with the quadrupole transition (Q) gate, D in D gate, Q in Q gate and Q in D gate, respectively. The red and black lines represent the counts corresponding to 125° and 90°, respectively.

of the band head. In the case of Band 1, the first two levels were already assigned by Lalkovski *et. al.* 787.2 and 722.4 keV transitions were used as gates to assign the spin and parity of in-band transitions decaying from the higher energy levels. Unambiguous determination was possible up to I = 12$\hbar$. For example, as the counts of the 833.4 keV transition in both 90° angle and 125°should are approximately equal (Fig. 5.3(c)), it can be concluded to have the same multipolarity as the gate (787.2 keV E2) used. For the DCO and polarisation measurements of 877.6 keV ($14^+ \rightarrow 12^+$) transition decaying from the 5923.5 keV level, the only usable gate was 877.3 keV ($10^+ \rightarrow 8^+$) transition. However, the statistics were too low to determine the R_{DCO} value with reasonable uncertainty. From the R_{DCO} measurements of other transitions, Band 1 was established as an even spin positive parity band.

For Band 2, the 3^- state was already established [1]. To proceed further, DCO and polarization measurements of the 1110.8 keV transition were performed using the 787.2 keV

gate (Table 5.1). Fig. 5.3(a) shows 1110.8 keV transition having more photopeak counts in 90° angle than in 125° which is expected when a ΔI = 1 transition is observed in a ΔI = 2 gate due to effects of angular distributions. The Δ_{iPDCO} value was found to be positive (refer to Table 5.1). Thus, this transition was found to be a pure electric dipole (E1) and the 2620.4 keV level was established as 5^- level. A similar prescription was followed for Eγ = 752.4 keV to establish the next level as a 7^- state. For all the in-band transitions of Band 2 up to spin I = 15$\hbar$, DCO measurements were performed using the 787.2 keV gate and were found to be close to 1. The polarisation asymmetry values of all these transitions except 560.3 keV (due to fewer statistics) were positive. These values are tabulated in Table 5.1. This indicates that the in-band transitions are stretched electric quadrupole (E2) in nature. In the case of 560.3 keV, the transition was assumed to be E2 as it was already established as a ΔI = 2 transition (as seen from Table. 5.1) and a strong M2 transition is ruled out. Thus, Band 2 could be established as an odd spin negative parity band up to spin I = 15$\hbar$.

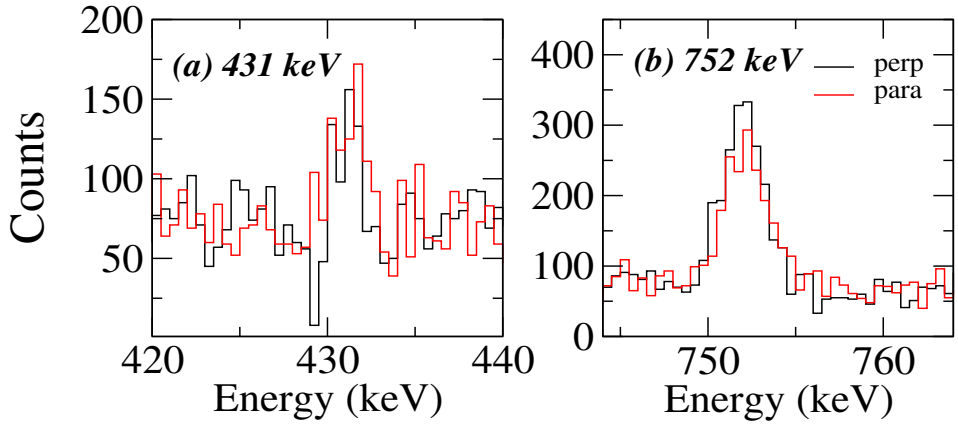

Figure 5.4: Typical polarisation spectrum for one magnetic type (left panel) and one electric type (right panel) transition of ^{98}Mo.

The 9^- state of Band 3 (E_{level} = 3767.5 keV) was established using the 752.4 keV gate. As per the angular distribution effects, ΔI = 2 transition shows more counts in 125° compared to that of 90° when gated on a ΔI = 1 transition. This is seen experimentally for the case of 672.1 keV when the 752.4 keV (E1) transition is used as shown in panel (d) of Fig. 5.3. In addition, the Δ_{iPDCO} value is positive. This establishes the 672.1 keV transition is an

E2 transition. Thus, Band 3 is an odd spin negative parity band.

The spin-parity of Band 4 could be unambiguously determined through the 430.6 keV transition using the 787.2 keV E2 gate. The projections from the DCO and polarization matrices are shown in Fig. 5.3(b) and Fig. 5.4(a), respectively. The extracted values for p_{DCO} and Δ_{iPDCO} are given in Table 5.1, which establishes the 430.6 keV transition as a magnetic dipole (M1) transition. The E2 nature of 662.8 keV (E_{level} = 4188.9 keV) and 789.3(E_{level} = 3256.1 keV) could also be established. Thus, Band 4 is identified as an even spin negative parity band.

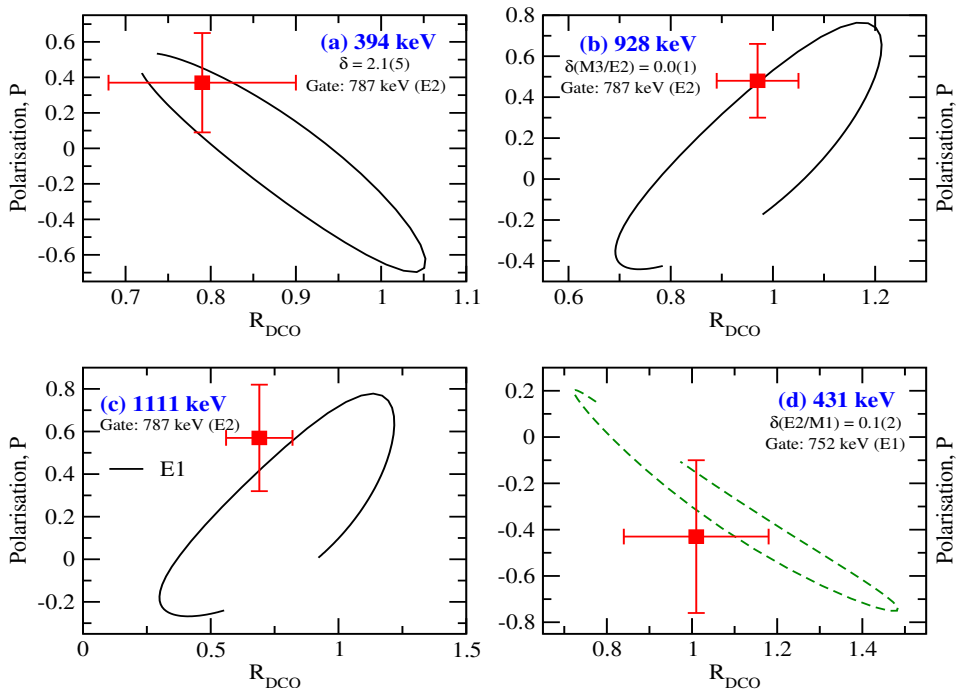

Figure 5.5: Contour plots of polarisation vs R_{DCO} as a function of varying mixing ratio for four different transitions.

Fig. 5.5 shows contour plots of DCO and polarisation value (P) of 4 transitions (393.8 keV, 928.2 keV, 1110.8 keV and 430.6 keV) as a function of mixing ratio δ. In all the cases, the values of the mixing ratio were found to be negligible.

Table 5.1: The energy (E_γ) and the relative intensity (I_γ) of the γ rays of Band2 and Band3 of ^{98}Mo along with the spin and parity of the initial (J^i_π) and the nal (J^f_π) states, measured values of R_{DCO}, Δ_{iPDCO} and the energy of the initial state (E_i) are shown. R_{DCO} values are obtained with gates on pure quadrupole transition except as noted. The quoted uncertainties in the intensities include statistical and fitting errors only. A systematic error due to the efficiency determination has been estimated to be around 4%.

E_i (keV)	E_γ (keV)	$J^i_\pi \rightarrow J^f_\pi$	I_γ	R_{DCO}	Δ_{iPDCO}	Type
787.2(3)	787.2(3)	$2^+ \rightarrow 0^+$	100.0(30)	1.02(5)	0.08(3)	E2*
1509.6(2)	722.4(2)	$4^+ \rightarrow 2^+$	84.9(24)	0.98(4)	0.10(2)	E2*
2017.3(2)	1230.1(2)	$3^- \rightarrow 2^+$	6.46(31)	0.72(9)	0.06(5)	E1*
	2017.3(3)	$3^- \rightarrow 0^+$	2.03(75)			E3
2343.1(4)	833.4(4)	$6^+ \rightarrow 4^+$	54.5(11)	1.03(6)	0.09(3)	E2*
2620.4(3)	603.1(2)	$5^- \rightarrow 3^-$	8.94(45)	0.96(12)	0.05(4)	E2*
	1110.8(3)	$5^- \rightarrow 4^+$	10.33(55)	0.69(8)	0.09(4)	E1*
	1833.3(5)	$5^- \rightarrow 2^+$	0.24(9)			E3*
2736.8(3)	393.8(4)	$6^- \rightarrow 6^+$	5.37(38)	0.79(11)	0.08(5)	Mixed*
3095.4(4)	475.1(2)	$7^- \rightarrow 5^-$	9.89(25)	1.02(10)	0.09(4)	E2*
	752.4(3)	$7^- \rightarrow 6^+$	8.52(40)	0.65(6)	0.07(4)	E1*
	1585.8(6)	$7^- \rightarrow 4^+$	0.74(16)			E3*
3271.2(3)	928.2(3)	$8^+ \rightarrow 6^+$	16.90(53)	0.97(8)	0.08(3)	E2*
3526.1(5)	789.3(5)	$8^- \rightarrow 6^-$	5.31(44)	1.07(21)	0.03(5)	E2*
	430.6(5)	$8^- \rightarrow 7^-$	1.66(41)	1.06(17)#	-0.09(7)	M1+E2*
3655.7(4)	802.3(3)	$9^- \rightarrow 8^+$	5.54(58)	0.73(13)	0.06(5)	E1*
	560.3(3)	$9^- \rightarrow 7^-$	4.17(42)	1.04(19)		Q
	384.5(3)	$9^- \rightarrow 8^+$	3.62(29)	0.69(10)		D
3767.5(4)	672.1(4)	$9^- \rightarrow 7^-$	6.25(24)	0.95(13)	0.07(5)	E2*
4148.5(4)	877.3(4)	$10^+ \rightarrow 8^+$	7.56(24)	0.99(13)	0.07(4)	E2*
	1295.1(3)	$10^+ \rightarrow 8^+$	3.12(41)			

4188.9(3)	662.8(3)	$10^- \rightarrow 8^-$	4.06(37)	0.95(19)	0.08(6)	E2*
4422.9(7)	767.2(7)	$11^- \rightarrow 9^-$	11.48(66)	0.99(14)	0.12(5)	E2*
4536.6(5)	769.1(5)	$11^- \rightarrow 9^-$	3.51(34)	1.04(19)	0.22(12)	E2*
4992.0(5)	803.1(5)	$12^- \rightarrow 10^-$	2.07(53)	-	-	
5045.9(3)	897.4(5)	$12^+ \rightarrow 10^+$	3.87(27)	0.99(34)	0.02(6)	E2*
5313.8(3)	890.9(3)	$13^- \rightarrow 11^-$	3.62(46)	1.05(22)	0.02(6)	E2*
6132.3(5)	818.5(5)	$15^- \rightarrow 13^-$	2.41(43)	1.03(26)	0.14(9)	E2*

- *: New measurement from current data.
- #: Gate on dipole transition.

5.3 Discussion

The level schemes of ^{98}Mo and ^{100}Ru show a number of common features:

1. There are four high spin bands out of which three have negative parity.

2. There is a pair of bands with interspaced levels of opposite parity, which are observed beyond 6^+ and 8^+ for ^{98}Mo and ^{100}Ru, respectively.

3. The two negative parity bands with interspaced levels of even and odd spins.

4. Three E3 transitions have been observed from the 3^-, 5^- and 7^- levels. In all the cases, the associated E1 transitions have been observed from these levels. The energy of the 3^- level in ^{98}Mo is lower in energy by 150 keV.

5. Beyond the 7^- level the odd spin negative parity sequence bifurcates in two bands.

Such detailed similarities between these two level structures imply similar mechanisms for the angular momentum generation for the two cases.

This comparison can be extended to the transition rates of the low spin states of the negative parity sequence, which in ^{100}Ru have been established to originate due to octupole vibrations [4]. In the present data with a thick target, the sub-picosecond level lifetimes can be measured through DSAM. But the lifetimes of these low spin levels are expected

Table 5.2: The E3 and E2 branching ratios and the estimated values of B(E3)/B(E2) for the low spin levels of ^{98}Mo and ^{100}Ru.

	E_{level}(keV) [J^π]	E_γ (keV)	B(E3)/B(E2) (fm^2)	B(E3) $\times 10^3$ (e^{2}fm^6)
^{98}Mo	2620.4 [5^-]	1833.3 (E3)	66.05 ± 27.01	108(44)
		603.1 (E2)		
	3095.4 [7^-]	1585.8 (E3)	153.81 ± 33.31	250(54)
		475.1 (E2)		
^{100}Ru	2527.4 [5^-]	1987.9 (E3)	17.39 ± 4.84	28(8)
		360.4 (E2)		
	2951.9 [7^-]	1725.2 (E3)	36.97 ± 11.45	60(19)
		424.3 (E2)		

to be an order of magnitude larger. In the absence of direct measurement, we have compared the B(E3)/B(E2) rates in Table 5.2. It is evident that The B(E3)/B(E2) values of ^{98}Mo are 4 times stronger than those in ^{100}Ru. The moments of inertia and its variation with spin were found to be very similar in both cases (beyond $I^\pi = 5^-$) for the negative parity band of the parity doublet as shown in Fig. 5.6. Thus, it is reasonable to assume a similar B(E2) value ($\approx$ 2000 e^{2}fm^4) for ^{98}Mo as measured for the negative parity band of ^{100}Ru [Chapter 4]. Using this value, the estimated B(E3) values are tabulated in Table 5.2.

The octupole deformation (β_3) parameters for the 7^- levels of ^{98}Mo and ^{100}Ru can be evaluated following equation [5]::

$$B(E3) = \frac{3}{4\pi}(ZeR^3)^2\beta_3^2$$

The large β_3 values of 0.12(6) and 0.06(2) for ^{98}Mo and ^{100}Ru respectively, indicate the presence of substantial octupole collectivity.

In order to explore the possibility of stable octupole deformation at low spins in ^{98}Mo, the B(E1)/B(E2) ratio has been plotted in Fig. 5.7 and listed in Table 5.3. This ratio should be enhanced in case of permanent octupole deformation due to the lighting-rod effect [6]. It is observed from the figure that the values of the ratio are very similar for ^{98}Mo and ^{100}Ru. These values correspond to a hindrance factor $\approx 1.0 \times 10^{-5}$, which is very

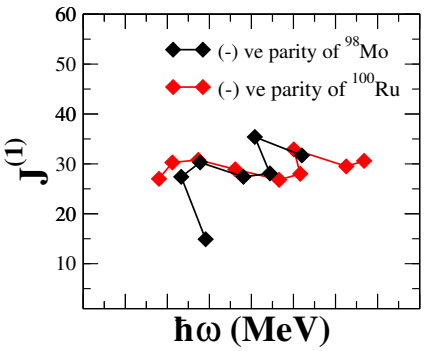

Figure 5.6: The moment of inertia $J^{(1)}$ as a function of rotational frequency (ω) for the negative parity partner of the alternate parity bands in^{98}Mo (black diamonds) and ^{100}Ru (red diamonds).

similar to those observed for the single neutron transitions in odd Cd isotopes [7]. Thus, there is no permanent octupole deformation in ^{98}Mo at low spins and the presence of the three E3 transitions from the low spin negative parity levels indicates that these levels originate due to the collective octupole vibration around a reflection symmetric shape and the magnitude of the shape oscillation has been found to be large ($\beta_3 \approx 0.12$).

Table 5.3: The E1 and E2 branching ratios and the estimated values of B(E1)/B(E2) for the low spin levels

E_{level}(keV) [J^{π}]	E_{γ} (keV)	I(E1)/I(E2)	B(E1)/B(E2) (10^{-8} fm^{-2})
^{100}Ru			
2527.4 [5^-]	1300.9 (E1) 360.4 (E2)	12.34 ± 1.51	2.61 ± 0.32
2951.9 [7^-]	876.0 (E1) 424.3 (E2)	5.52 ± 0.57	8.63 ± 0.90
3504 [9^-]	444 (E1) 552 (E2)	0.89 ± 0.06	39.97 ± 2.69
^{98}Mo			
2620.4 [5^-]	1110.8 (E1) 603.1 (E2)	1.16 ± 0.08	5.17 ± 0.38
3095.4 [7^-]	752.4 (E1) 475.1 (E2)	0.86 ± 0.05	3.76 ± 0.21
3655.7 [9^-]	384.5 (E1) 560.3 (E2)	0.87 ± 0.11	64.52 ± 8.30

It may be interesting to note that the 5^- level of ^{98}Mo does not follow the rotational sequence unlike in the case of ^{100}Ru as seen from Fig. 5.6. Thus, this state may have a

substantial contribution from E2-E3 two-phonon state. The possible origin of the 5^- level in A $\approx$ 100 mass region has been proposed by Pignanelli et. al. within the framework of the IBM model [8].

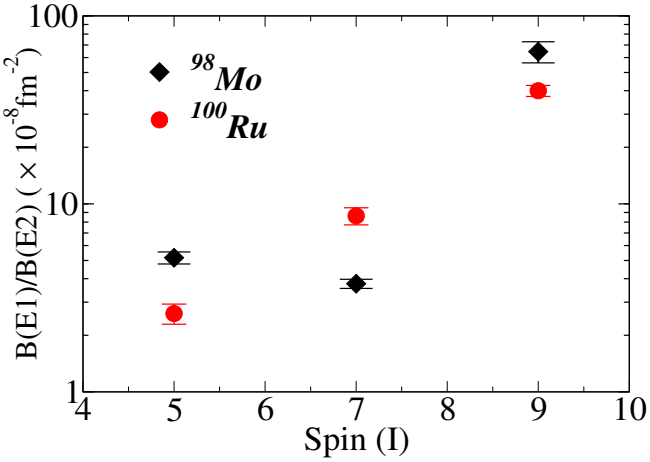

Figure 5.7: The ratio of the inter-band E1 and the intra-band E2 transition rates from the low spin excited levels of ^{98}Mo and ^{100}Ru as a function of spin, I.

There is an order of magnitude enhancement in the B(E1)/B(E2) value at $I^\pi = 9^-$ as observed in Fig. 5.7. This is a clear indication of the onset of strong octupole correlation at this level for ^{98}Mo, which is similar to ^{100}Ru. This fact is also supported by the observed inversion (marked by I_c) in the S(I) plot as shown in Fig. 5.8(a), which is the signature of the onset of strong octupole correlation [9]. In this figure, the S(I) plot for ^{100}Ru and ^{144}Ba has been shown for the comparison of the behaviour of the observed alternate parity bands of ^{98}Mo with increasing spin. It is interesting to note that the behaviour in all three cases is similar except that the vanishing of the parity splitting has not been observed for ^{98}Mo.

Thus, the high spin levels ($I \geq 9\ \hbar$) of Bands 1 and 2 in ^{98}Mo may originate due to the rotation of a permanent octupole shape. This can only be established through the observation of the interleaved E1 transitions between the levels of the two bands. However, these very weak transitions were not observed. This is due to inadequate data, which was an order of magnitude lower than that collected for ^{100}Ru.

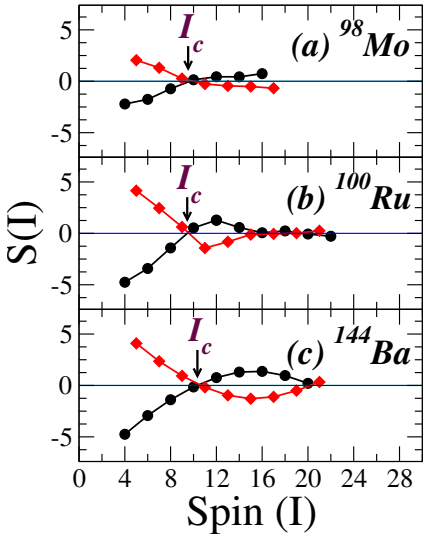

Figure 5.8: The parity splitting index S(I) as a function of angular momentum for the positive (black dots) and negative parity (red diamonds) partner bands of ^{98}Mo, ^{100}Ru, and ^{144}Ba.

In summary, four high spin bands have been established in ^{98}Mo. These band structures have been found to be similar to those observed in ^{100}Ru. The low spin negative parity levels were found to originate due to the octupole vibration. A large enhancement of octupole correlation has been observed at $I^{\pi} = 9^{-}$. The S(I) plots for ^{98}Mo, ^{100}Ru and ^{144}Ba are very similar thereby indicating the possibility of permanent octupole deformation in ^{98}Mo at high spins.

Bibliography

[1] S. Lalkovski *et. al.* Octupole collectivity in ^{98,100,102}Mo. Phys. Rev. C, **75**:014314, Jan 2007.

[2] S. S. Nayak and G. Mukherjee. Development of an advanced, multi-function, multi- DAQ-compatible data sorting and analysis software suite - BINDAS. IEEE Transactions on Nuclear Science, **70**(12):2561–2571, 2023.

[3] A. D. Yamamoto *et. al.* High- j proton and neutron alignments in γ-soft ^{101}Ru. Phys. Rev. C, **66**:024302, Aug 2002.

[4] A. Karmakar *et. al.* Possibility of stable octupole deformation in ^{100}Ru. Phys. Rev. C, **109**:054312, May 2024.

[5] P.A. Butler and W. Nazarewicz. Intrinsic dipole moments in reflection-asymmetric nuclei. Nuclear Physics A, **533**(2):249–268, 1991.

[6] P. A. Butler and W. Nazarewicz. Intrinsic reflection asymmetry in atomic nuclei. Rev. Mod. Phys., **68**:349–421, Apr 1996.

[7] L.K. Kostov, W. Andrejtscheff, L.G. Kostova, L. Käubler, H. Prade, and R. Schwengner. Absolute E1 and E2 transition rates in ^{110}Cd. Eur. Phys. J. A, **2**(3):269– 273, 1998.

[8] M Pignanelli *et. al.* Octupole excitations in vibrational nuclei and the SDF interacting boson model. Nuclear Physics A, **519**(3):567–601, December 1990.

[9] N. V. Zamfir, P. von Brentano, and R. F. Casten. Phenomenological signature for the onset of strong octupole correlations. Phys. Rev. C, **49**:R605–R607, Feb 1994.

Chapter 6

Spectroscopic Studies in ^{105}Pd

The existence of triaxial deformed nuclei has been predicted by numerous mean-field studies (see e.g. Ref. [1]). A special feature of triaxial nuclei is that they can exhibit the wobbling motion near the yrast line which was predicted by Bohr and Mottelson in 1975 [2]. However, this special high-spin mode for an even-even nucleus has not been observed yet. Instead, the first observation of wobbling was reported in 2001 for the odd-mass ^{163}Lu [3]. The authors interpreted their data in the framework of the particle + triaxial rotor (PTR) model (see e.g. Ref. [2]). Two bands, labelled as TSD1 and TSD2, were identified, which were associated with the triaxial strongly deformed (TSD) minimum with odd-proton occupying the $i_{13/2}$ configuration as obtained in the ultimate cranking calculations [4]. The lower TSD1 band corresponds to $n = 0$ and the excited TSD2 band to the $n = 1$ wobbling excitation. Using the Particle + Triaxial Rotor (PTR) model, Frauendorf and Dönau [5] classified the collective mode into longitudinal wobbling (LW) when the angular momentum vector precesses about the medium axis of the triaxial nuclear shape and transverse wobbling (TW) when it precesses around an axis transverse to the medium axis. For increasing angular momentum, the excitation energy of the wobbling quanta increases for LW, and decreases for TW up to a critical value I_c, above which the TW changes into the LW regime. The wobbling mode represents a periodic motion of the three

principal axes of the triaxial charge distribution, which generates strong E2 radiation. This is observed as collectively enhanced ΔI = 1 E2 transitions from the levels of band with n wobbling quanta to the band with n-1 wobbling quanta. Recently, TW mode has been reported in several odd-A nuclei [3]- [19].

The TW regime appears when the angular momentum **j** of the odd particle aligns with the short axis of the nucleus which is transverse to the medium axis. Of course, the particle alignment is not rigid and there are excitations which correspond to the reorientation of the odd particle's angular momentum **j**, such that it precesses about the short axis with the projection $j - 1$. The bands based on this configuration have been referred to as signature partner (SP) bands [6] because it is their traditional nomenclature in high-spin physics, where the rotational bands group into $\Delta I = 2$ signature sequences connected by strong intra-band E2 transitions. (The signature of the band is defined by $\alpha = I$ + even number.) In contrast to the TW bands, SP bands are connected by $\Delta I = 1$ M1 transitions to the $n = 0$ band. In all the reported cases [3]- [19], the SP band has been observed. Both the TW and signature partner bands have the signature, $-\alpha$, that is opposite to the signature α of the n=0 band. The appearance of the collective TW band, in addition to the signature partner band, represents stringent evidence for triaxial deformation.

If the two distinct modes keep their dominant character, the next bands with signature α are expected to be the double TW band ($n = 2$), the TW based on the SP band and the particle excitation, where **j** precesses about the short axis with the projection $j - 2$. The authors of Ref. [16] discussed the small amplitude limit of the particle triaxial rotor system, where the TW and SP modes appear as normal vibrational modes, which combine in an additive way.

In the case of ^{135}Pr the odd particle is an $h_{11/2}$ proton and accordingly, the $n = 0$ yrast band has $\alpha = -1/2$. The TW and SP bands with $\alpha = 1/2$ were identified in Ref. [6]. The authors of Ref. [17] demonstrated that a fourth band with $\alpha = -1/2$ has the characteristics of the double TW excitation. The present case study of ^{105}Pd has a structure that is

analogous to ^{135}Pr with the odd proton replaced by the odd $h_{11/2}$ neutron. The authors of Ref. [19] identified the $\alpha = -1/2$ yrast band (Band 1) and the $\alpha = 1/2$ TW (Band 3) and SP (Band 2) bands depicted in Fig. 6.1. This work also observed, at a somewhat larger energy, an $\alpha = -1/2$ band [20] and the authors speculated that it might be the double TW band by analogy to ^{135}Pr. However, they left the nature of the band an open problem because their data did not allow them to establish such an assignment. In the present thesis, the mixing ratios of all the inter-band transitions of ^{105}Pd have been measured. As will be elucidated below, the second $\alpha = 1/2$ band is not the double TW band as speculated, but is the first known example of a TW-on-SP band.

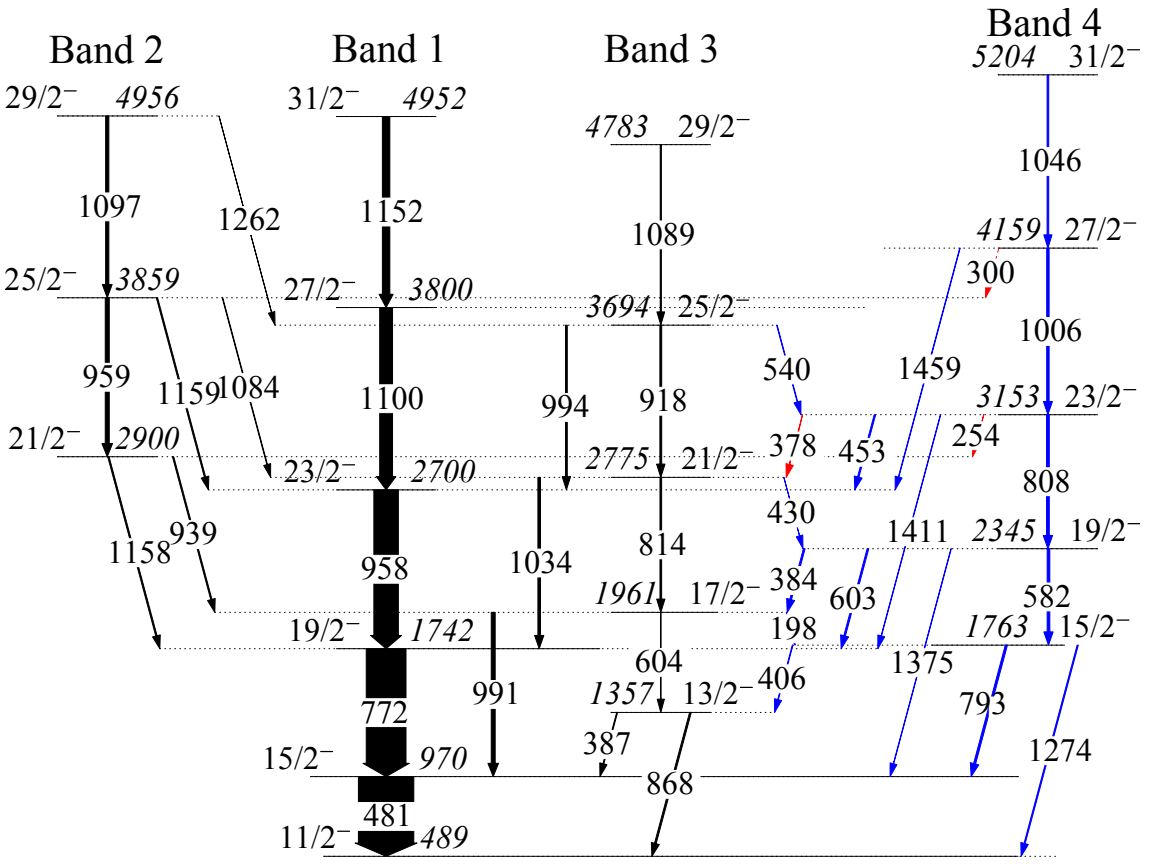

Figure 6.1: The partial level scheme of ^{105}Pd established from the present work. The level and transition energies are expressed in keV and have been rounded off to their nearest integer. The levels and transitions marked in Black were reported in [19] while those marked in Blue were reported [20] by the same group. Our data confirms all these levels and transitions and we have added three more transitions, which are marked in red. The spin and parities of Band 2 have been adapted from Ref. [19]

The authors of Ref. [21] questioned the interpretation of band 3 as TW. They studied the nucleus in the framework of the interacting boson-fermion model. The calculated energies of band 3 relative to band 1 *increase* with I in contrast to the observed decrease. As seen in Fig. 7(h) of Ref. [21], the calculated small mixing ratios disagree with the ones from Ref. [19] and the present study. A well-founded comparison with the data from Ref. [22] is not possible because the first two points do not indicate the uncertainties, which are large (see discussion below). Thus, in my view the authors of Ref. [21] have not substantiated their claim.

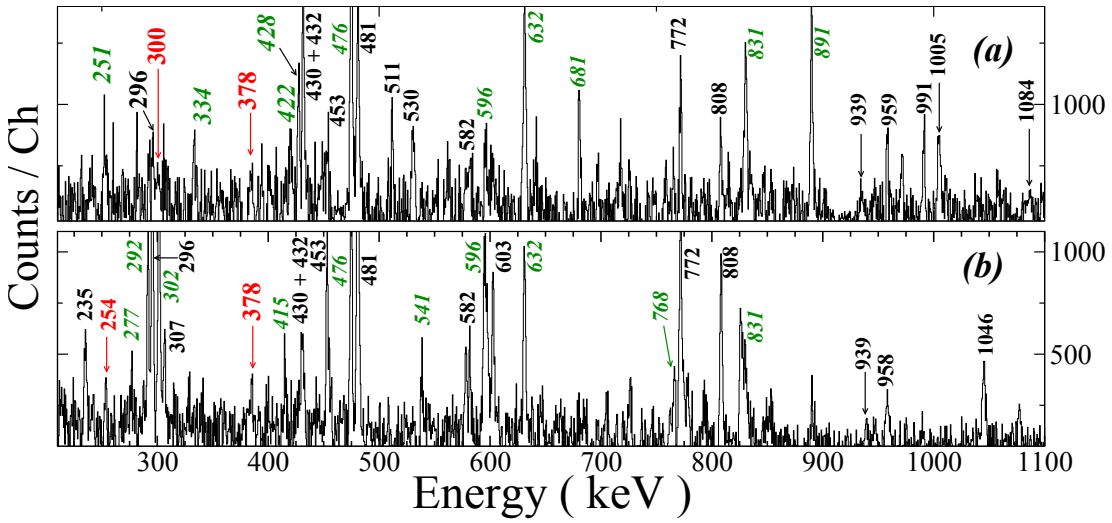

Figure 6.2: The gamma spectra in coincidence with (a) 1046 keV ($31/2^- \rightarrow 27/2^-$) keV and (b) 1006 ($27/2^- \rightarrow 23/2^-$) keV transitions of Band 4. The newly placed gamma transitions from Band 4 to Band 2 have been marked in red. The transitions marked in green belong to ^{102}Ru. This contamination is due to the presence of 1047 keV ($15^- \rightarrow 13^-$) and 1005 keV ($14^- \rightarrow 12^-$) transitions in ^{102}Ru.

6.1 Experimental Results

The partial level scheme of ^{105}Pd has been shown in Fig. 6.1, where the widths of the transitions are proportional to their relative intensities. The newly placed 254 keV ($23/2^- \rightarrow 21/2^-$) and 300 keV ($27/2^- \rightarrow 25/2^-$) transitions between Band 4 and Band 2 are shown in the coincidence spectrum with their respective top transitions, in Fig. 6.2. The relative intensities of the gamma transitions obtained from the present data agree well with

the evaluated intensities from Ref. [22]. However, the intensities of the newly observed gamma transitions in Ref. [19] and [20] were not reported. These have been evaluated in this thesis and tabulated in Table 6.1.

Table 6.1: Energies, relative intensities, DCO ratios using the detectors at 40° and 157° ring along with the detectors at 90° ring, linear polarizations, mixing ratios and deduced multipolarities of transitions of ^{105}Pd shown in Fig. 6.1.

E_γ (keV)	I_γ (rel.)	R_{DCO} (40°)	R_{DCO} (157°)	P	δ	Mult.
198	0.42(11)	0.60(24)	-	-	0.0(2)	M1
254	0.22(7)	0.91(34)	0.97(41)	-	$0.3^{+0.4}_{-0.3}$	Mixed
300	0.12(5)	0.89(38)	0.85(47)	-	$0.3^{+0.5}_{-0.3}$	Mixed
378	1.04(23)	0.61(23)	-	-	0.1(1)	M1
384	0.84(21)	0.66(18)	-	-	0.1(1)	M1
387	0.24(9)	-	-	-	-	Mixed
406	0.50(19)	-	-	-	-	M1
430	0.28(6)	0.65(17)	-	-	0.1(1)	M1
453	1.19(25)	0.84(20)	0.83(23)	-	$-0.6^{+0.5}_{-0.6}$	Mixed
481	65.9(3)	1.01(2)		0.57(3)	0.0(3)	E2
540	0.66(24)	0.65(26)	-	-	0.1(1)	M1
582	1.38(37)	1.06(21)	-	-	0.1(1)	E2
603	1.93(31)	0.84(16)	0.78(19)	-0.31(97)	$-0.6^{+0.4}_{-0.5}$	Mixed
604	0.64(11)	0.97(21)	-	-	0.1(1)	E2
772	47.93(22)	1.04(3)	-	0.64(8)	0.1(4)	E2
793	2.48(28)	-	-	-	-	Mixed
808	4.81(39)	0.96(10)	-	-	-0.1(1)	E2
814	1.98(27)	0.98(14)	-	-	0.0(5)	E2
868	0.42(11)	-	-	-	-	Mixed
918	2.18(29)	1.00(15)	-	-	0.0(1)	E2

939	1.01(10)	0.96(12)	-	-	0.0(2)	E2
958	29.51(29)	0.98(2)	-	0.46(14)	0.0(1)	E2
959	1.29(34)	-	-	-	-	-
991	4.75(16)	1.20(8)	1.27(12)	-0.43(97)	$1.9^{+0.4}_{-0.5}$	Mixed
994	2.16(15)	1.08(10)	1.23(14)	-0.35(108)	$2.4^{+0.8}_{-0.5}$	Mixed
1006	2.90(48)	1.05(19)	-	-	0.1(7)	E2
1034	3.11(16)	1.12(9)	1.15(14)	-0.33(99)	$2.2^{+0.5}_{-0.4}$	Mixed
1046	1.93(37)	1.03(20)	-	-	0.1(6)	E2
1084	0.48(16)	1.03(37)	-	-	0.1(1)	E2
1089	1.38(32)	1.05(28)	-	-	0.1(8)	E2
1097	1.25(33)	-	-	-	-	-
1100	15.48(47)	0.99(6)	-	0.30(23)	0.1(4)	E2
1152	8.96(91)	1.00(12)	-	0.25(22)	0.0(5)	E2
1158	1.08(17)	-	0.65(26)	-	-	M1
1159	0.43(17)	-	-	-	-	-
1262	0.18(9)	-	-	-	-	-
1274	1.37(35)	-	-	-	-	E2
1375	0.51(34)	1.09(37)	-	-	0.1(1)	E2
1411	0.51(32)	0.98(38)	-	-	0.0(1)	E2
1459	0.60(35)	0.98(32)	-	-	0.0(2)	E2

The γ - ray multipolarities were determined from the Ratio of Directional Correlations from Oriented states (R_{DCO}) method [23]. For this measurement, an asymmetric matrix was constructed with the γ -ray energy detected at 90° along one axis while the coincident γ -ray energy at 40° and 140° on the other axis. For the mixed transitions, the measured R_{DCO} values have been validated by re-measuring the value using the "157°" and "90°" matrix. For the R_{DCO} measurements, the stretched E2 gating transitions were used. The value for the attenuation coefficient of complete alignment (σ/J) of 0.31(3) was estimated

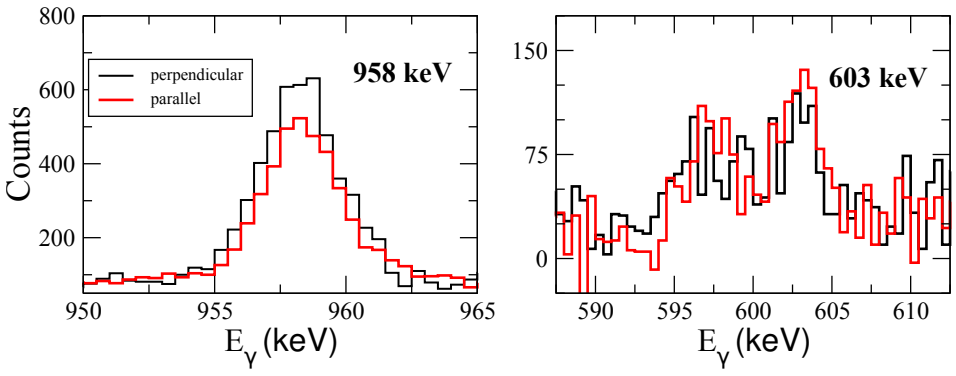

Figure 6.3: A typical polarisation spectrum for an electric (left) and a mixed (right) transition.

from the measured R_{DCO} values for 1100 keV E2 and 1331 keV E1 transitions, which were assumed to be pure stretched transitions. The R_{DCO} values for 40° (157°) were calculated using the computer code ANGCOR [24] (for σ/J = 0.31(3)) and were found to be 1.0 and 0.58 (1.0 and 0.51) for pure ΔI = 2 and ΔI = 1 transitions, respectively. The linear polarization (P) measurements were also performed to extract the electromagnetic character of the de-exciting γ rays. A typical spectrum for calculating polarisation asymmetry is shown in Fig. 6.3. The left panel shows a previously established electric transition and has more counts in the perpendicular combination of crystals in 90° detectors than in parallel combination. It can be observed from the figure that the present dataset was inadequate for the P measurements for the weak crossover transitions, like 603 keV. The electromagnetic characters could only be determined uniquely (considering the uncertainty) only for the lower transitions of the yrast band, for example, 958 keV. Thus, the present analysis relies mostly on the R_{DCO} values. The results obtained from the present measurements are tabulated in Table 6.1 and the R_{DCO} values are found to be consistent with previously known spin and parity assignments [19, 20]. It may be observed from Table. 6.1 that the experimental R_{DCO} values show a significant departure from the calculated values for the ΔI = 1 transitions between Band 3 $\rightarrow$ Band 1 and Band 4 $\rightarrow$ Band 2 and also for the ΔI = 0 transitions between Band 4 $\rightarrow$ Band 1. Only these transitions (labelled as mixed in Table. 6.1) have substantial M1/E2 mixing. The mixing ratios (δ) of 991 (E_x = 1961 keV), 603 (E_x = 2345 keV), 1034 (E_x = 2775 keV) and 994 (E_x = 3694 keV) keV transitions

have been unambiguously determined through the combined measurement of R_{DCO} and P. The mixing ratios for the 991, 1034 and 994 keV transitions between the wobbling bands were reported to be 1.8(5), 2.3(3) and 2.7(6), respectively [19]. The calculated values of the mixing ratio from polarization and R_{DCO} contour plots using the current experimental data for 991 keV and 1034 keV are shown in Fig. 6.4. It may be observed from the figure that the large error bars on polarisation values do not allow the unique determination of the electromagnetic characters. However, the correlation between the P and R_{DCO} values in the contour plot can be used to obtain the lowest minimum from the χ^2 minimization, thereby leading to the most probable value. This analysis has been shown in Fig. 6.5, where the minimum corresponding to the higher value of the mixing ratio for 991 keV, 1034 keV and 994 keV transitions is the lowest. The values obtained from the χ^2 variation near the minimum are $1.9^{+0.4}_{-0.5}$, $2.4^{+0.8}_{-0.5}$ and $2.2^{+0.5}_{-0.4}$ which are consistent with the previously reported values [19].

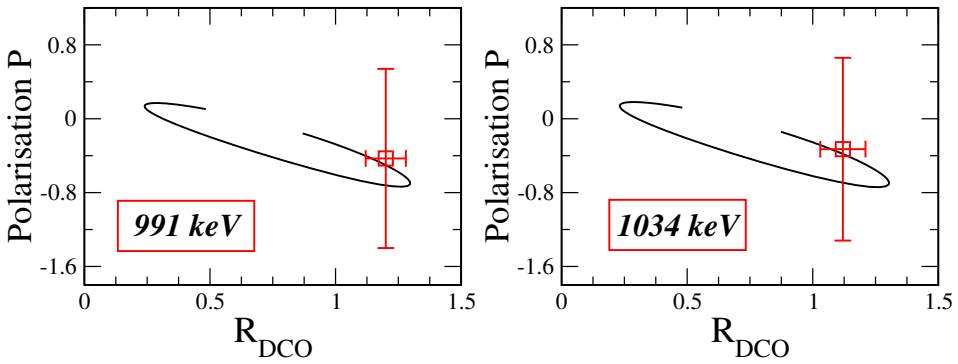

Figure 6.4: Values of the DCO ratios (R_{DCO}) and linear polarization (P) of the $\Delta I = 1$ transitions that decay from the negative parity wobbling band to the positive parity ground state band, computed (solid line) and experimental (symbol) for various mixing ratios (δ).

Alternately, the mixing ratio can be estimated by comparing the experimental R_{DCO} value with the corresponding calculated values for the different values of δ using σ/J = 0.31(3). These plots for the 991 and 1034 keV transitions are shown in Fig. 6.6 (a) and (b), respectively. The higher values of the mixing ratio obtained from this method were 1.8(4) and 2.2(5), respectively, which match with the values obtained from the previous method within $\pm 1\sigma$. Thus, this method has been followed to obtain the mixing ratios for the low energy transitions of 254, 453 (E_x = 3153 keV) and 300 keV (E_x =4159 keV), where the P

measurements were not possible due to inadequate statistics. The results for 300 and 254 keV transitions are shown in Fig. 6.6 (c) and (d), respectively. Due to low statistics, the R_{DCO} values of 254 and 300 keV transitions have larger error bars and give two different values for the mixing ratio. The higher δ values of Fig. 6.6(c) and (d) were found to be unrealistic as they predict a much stronger (about 15 times) $B(E2)_{out}$ rate in the $I \rightarrow I-1$ transitions than the $B(E2)_{in}$ rate in the $I \rightarrow I-2$ transitions. For the two $\Delta I = 0$ transitions of 453 and 603 keV from Band 4 to Band 3, the δ values were found to be $\approx$ -0.6(6) and -0.6(5), respectively. These values were reported as 0.0(7) and 0.0(5) by Rickey et. al. [22]. It is not possible to compare the two measurements as the reported uncertainties are very large in Ref. [22] and we may only conclude that the values match within $\pm 1\sigma$. The DCO ratios for all the observed $\Delta I = 1$ transitions between Band 3 and 4 agree well with the calculated value for a pure dipole transition. This was also found to be true for the 1158 keV transition from Band 2 (E_x = 2900 keV) to Band 1. Thus, for these transitions, the E2 mixing has been found to be negligible (E2 fraction $\leq$ 0.1%). It is worth mentioning that the $17/2^-$, $21/2^-$ and $25/2^-$ levels of Band 3 decay by two $\Delta I = 1$ transitions to Band 1 and Band 4. For the three transitions to Band 1, the E2 fraction ($\frac{\delta^2}{1+\delta^2}$) is $\approx$ 85%, while for the transitions to Band 4, the E2 fraction is $\leq$ 0.1% as obtained from Table 6.1. It may also be noted that the E2 fraction is $\approx$ 10% for the 254 and 300 keV transitions from Band 4 to Band 2, but the lower transition energies lead to large electric quadrupole transition rates (B(E2)) for these $\Delta I = 1$ transitions.

The ratios of the inter-band to intra-band transition rates have been plotted in Fig. 6.7, which show two distinct classes of inter-band $\Delta I = 1$ transitions. In one case, the B(E2) values for these transitions are of the same order as the intra-band B(E2) rates. Thus, these $\Delta I = 1$ transitions from Band 3 to Band 1 and Band 4 to Band 2 (Fig. 6.7(a) and Fig. 6.7(b)) have substantial collective enhancement in the B(E2) rates. On the other hand, the $\Delta I = 1$ transitions for Band 3 $\rightarrow$ Band 4 and Band 2 $\rightarrow$ Band 1 are predominantly M1 in nature. The $B(M1)_{out}/B(E2)_{in}$ values for the $\Delta I = 1$ transitions are plotted in Fig. 6.7(d), (e) and (f). The ratios for the out-band and in-band transition rates for Band 2 to Band 3

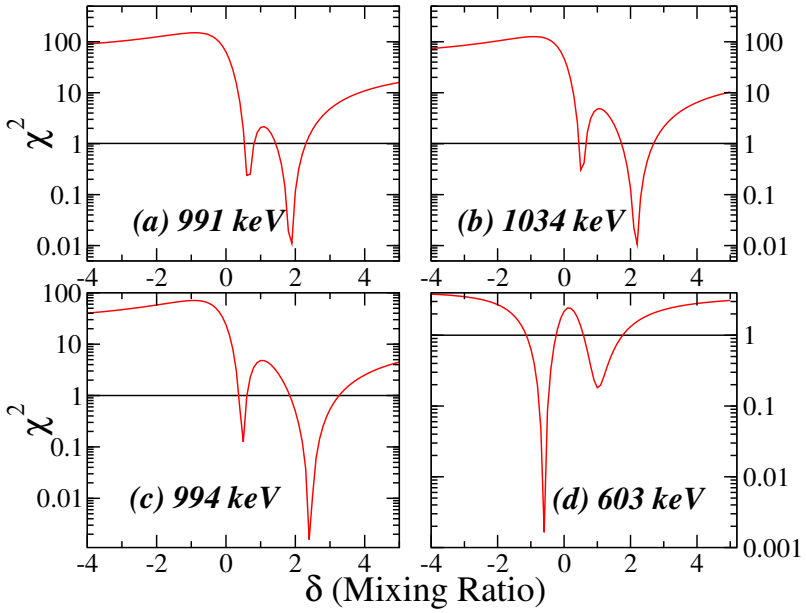

Figure 6.5: The χ^2 minimization plots for (a) 991 keV (b) 1034 keV (c) 994 keV and (d) 603 keV. The horizontal lines correspond to the +1 of the minima value for determining the uncertainties. For the first three transitions, the lower minima correspond to the higher δ values. However, for 603 keV, the lower delta value is more preferable.

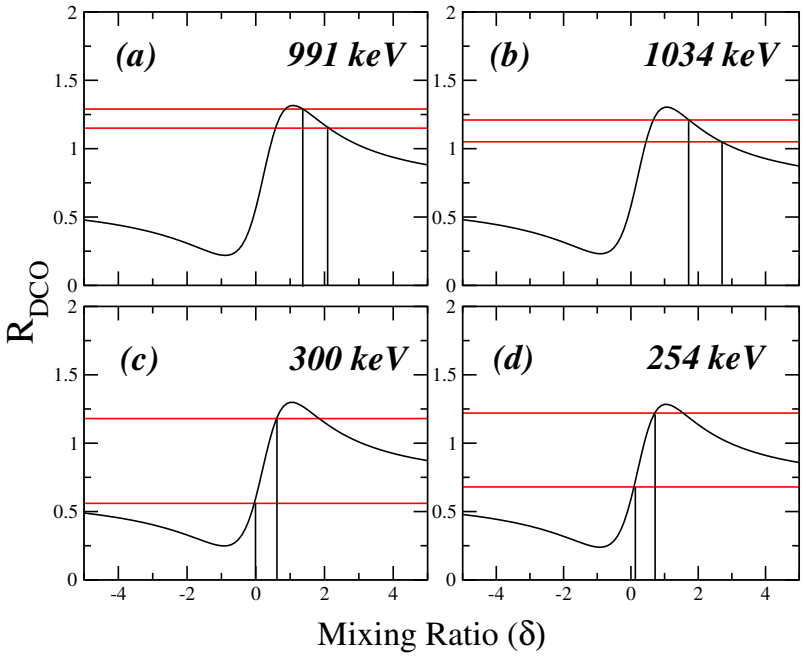

Figure 6.6: Variation of the calculated R_{DCO} as a function of mixing ratio (δ) for the ΔI = 1 transitions from Band 3 to Band 1 ((a) 991, (b) 1034 keV) and from Band 4 to Band 2 ((c) 300, (b) 254 keV). The horizontal lines correspond to the R_{DCO} values at 40° along with their uncertainties.

and Band 4 to Band 1 have been plotted in Fig. 6.8, which shows an increasing trend in the $B(M1)_{out}/B(E2)_{in}$ values for the ΔI = 0 transitions from Band 4 to Band 1 as a function of

spin (Fig. 6.8(b)). This analysis establishes that the inter-band ΔI = 1 transitions for Band

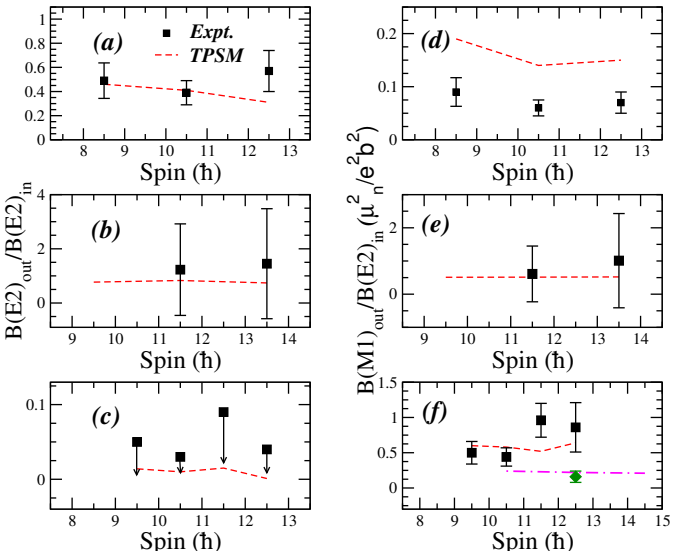

Figure 6.7: The ratio of the rates of the out-band ΔI = 1 transitions and the in-band E2 transitions of ^{105}Pd are plotted as a function of spin, I. The E2 and M1 rates for the ΔI = 1 transitions have been estimated using the evaluated values of the mixing ratios (Table 6.1) and are shown on the left and right panels, respectively. The values for the Band 3 → Band 1 transitions are shown in (a) and (d), the values for Band 4 → Band 2 transitions in (b) and (e), and the values for the Band 3 → 4 transition in (c) and (f). Fig. 6.7(f) also includes the value for the Band 2 → Band 1 transition (shown in green), assuming the E2 mixing to be negligible. In Fig. 6.7(c), the upper bounds correspond to the upper limit of the uncertainties of the mixing ratio values given in Table 6.1. The dotted line on each panel represents the calculated values from TPSM.

2 → Band 1 and Band 4 ⟷ Band 3 are predominantly M1, while the ΔI = 1 transitions for Band 3 → Band 1 and Band 4 → Band 2 shows large enhancement in B(E2) rates.

6.2 Discussion

To provide an insight into the nature of the band structures observed in ^{105}Pd, triaxial projected shell model (TPSM) [25] calculations have been performed. This model has been shown to provide a unified description of the interplay between collective and single-particle degrees of freedom in deformed odd-mass nuclei [9, 26] - [28]. In the present study of ^{105}Pd, the deformed basis states have been obtained by solving the triaxial Nilsson potential with $\epsilon = 0.26$ and $\epsilon' = 0.11$ [19]. The monopole pairing interaction is employed

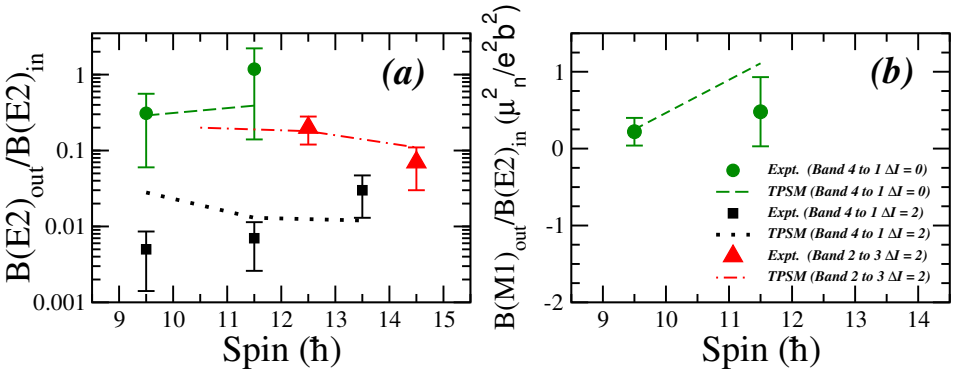

Figure 6.8: The ratio of the rates of the out-band ΔI = 0 and ΔI = 2 transitions from Band 4 to Band 1, Band 2 to Band 3 and the in-band E2 transition of Band 4 as a function of spin, I. The M1 and E2 rates have been estimated using the evaluated values of the mixing ratios (Table. 6.1) and plotted in (a) and (b), respectively. The dotted line on each panel represents the calculated values from TPSM.

by solving standard Bardeen-Cooper-Schriefer (BCS) equations and the resulting Nilsson + BCS states are then projected onto good angular-momentum states [29]. For odd-neutron nuclei, the basis states are composed of one-neutron and one-neutron coupled to two-proton states, which are sufficient for the discussion of the observed low-lying band structures in ^{105}Pd. We have also evaluated the transition probabilities with the effective charges of 1.6e for protons and 0.6e for neutrons [30, 31, 32].

The experimental energies $E(I)$ and the derived rotational frequencies $\hbar\omega(I)$ are compared with the TPSM values in Fig. 6.9. The calculations reproduce the experimental values for all four bands quite well. The levelling of Band 1 at $\hbar\omega$ = 0.58 MeV ("upbend" of the function $I(\omega)$) reflects the rotational alignment of an additional pair of $h_{11/2}$ quasineutrons, which is seen in Fig. 6.10 as the bands originating from the three-quasineutron configuration at 4.17 MeV become yrast. A similar levelling is found in the TPSM results for Bands 2, 3, and 4 and reflects the crossing of the three-quasineutron configurations. The TPSM levelling is seen in the experimental frequencies of Bands 3 and 4 as well. However, the two experimental frequency points of Band 2 do not confirm the TPSM prediction.

The TPSM wavefunctions have been used to calculate the M1 and E2 transition probabilities between the excited levels of ^{105}Pd, which are listed in Table 6.2. Figs. 6.7 and

Table 6.2: Transition rates of different bands from TPSM Calculations used for the comparison plots with experimental values.

Band 2

Spin ($\hbar$)	B(E2)$_{in}$ (e^2b^2)	B(E2)$_{out}$ (e^2b^2)	B(M1)$_{out}$ (μ_n^2)	Decay to
10.5	0.54	0.008	0.13	Band 1
			0.11	Band 3
12.5	0.82	0.008	0.18	Band 1
			0.15	Band 3
14.5	0.89	0.001	0.19	Band 1
			0.09	Band 3

Band 3

Spin ($\hbar$)	B(E2)$_{in}$ (e^2b^2)	B(E2)$_{out}$ (e^2b^2)	B(M1)$_{out}$ (μ_n^2)	Decay to
8.5	0.72	0.33	0.14	Band 1
		0.01	0.41	Band 4
10.5	0.80	0.32	0.12	Band 1
		0.01	0.46	Band 4
12.5	0.72	0.23	0.11	Band 1
		0.001	0.46	Band 4
14.5	0.70	0.18	0.11	Band 1

Band 4

Spin ($\hbar$)	B(E2)$_{in}$ (e^2b^2)	B(E2)$_{out}$ (e^2b^2)	B(M1)$_{out}$ (μ_n^2)	Decay to
7.5	0.63	0.02	0.51	Band 3
		0.23	0.08	Band 1 (ΔI = 0)
		0.02	-	Band 1 (ΔI = 2)
9.5	0.69	0.01	0.42	Band 3
		0.53	0.35	Band 2
		0.20	0.17	Band 1 (ΔI = 0)
		0.02	-	Band 1 (ΔI = 2)
11.5	0.72	0.01	0.38	Band 3
		0.60	0.37	Band 2
		0.28	0.79	Band 1 (ΔI = 0)
		0.01	-	Band 1 (ΔI = 2)
13.5	0.74	0.004	0.35	Band 3
		0.55	0.38	Band 2
		0.27	0.65	Band 1 (ΔI = 0)
		0.01	-	Band 1 (ΔI = 2)

6.8 compare the pertaining ratios with the observed inter-band to intra-band ratios of the transition rates. For all the transitions, the agreement was found to be quite well, which

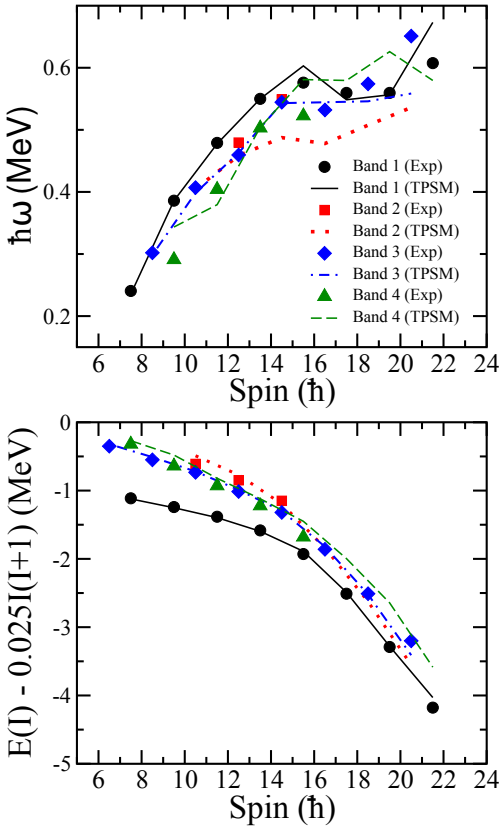

Figure 6.9: Experimental and calculated values from TPSM for the rotational frequency (upper panel) and the level energies minus the rotor contribution (lower panel) as functions of the spin I for Bands 1, 2, 3 and 4.

substantiates the suggested interpretation.

The E2 probability for Band 3 → Band 1 is enhanced, as expected for collective transition connecting the $n = 1$ TW state with the $n = 0$ yrast state. The transitions Band 2 → Band 1 are weak, expected for the SP band, which has a different orientation of the $h_{11/2}$ quasineutron than the yrast band. The transitions Band 4 → Band 2 are enhanced, as speculated for the collective E2 transition connecting the $n = 1$ TW excitation on top of the SP states with the SP states. The transitions Band 4 → Band 3 are small because the orientation of the $h_{11/2}$ quasineutron differs in the two bands. For the same reason, the transitions Band 4 → Band 1 are weak.

In order to further investigate the structure of the observed bands in ^{105}Pd, Fig. 6.10 shows the energies of the bands projected from the quasiparticle configurations before the TPSM Hamiltonian is diagonalized. It is important to point out that the short principal axis is

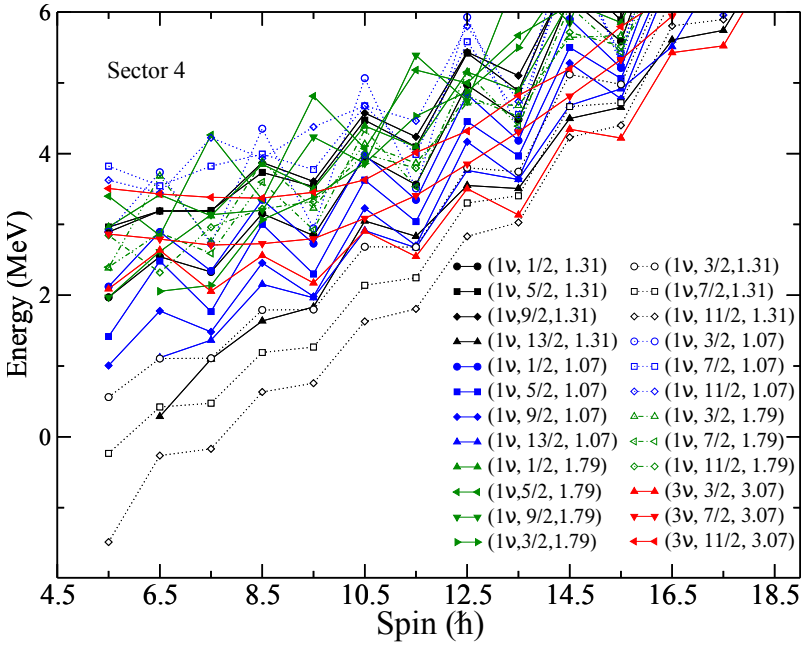

Figure 6.10: Energies of the projected K configurations, where the short axis is chosen as the quantization axis 3 to which K refers. The curves are labelled by three quantities: quasiparticle character, K quantum number and energy of the quasiparticle state. For instance, [1,1/2,1.31] designates the one quasineutron state with K= 1/2 having intrinsic energy of 1.31 MeV.

chosen as the 3-axis of quantization, and "K" denotes the angular moment projection on the short axis. This is different from the TPSM calculations published so far where the long principal axis is chosen as the 3-axis. This choice simplifies the interpretation because, in the TW regime, the odd quasineutron tends to align its angular momentum with the short axis. This has the consequence that the final states are much less mixed with respect to K. Of course, such a change of the quantization axis leaves the observables invariant. Technically, it is achieved by changing the triaxiality parameter γ to an equivalent value in another sector. The TPSM parameters $\epsilon = 0.26$ and $\epsilon' = 0.11$ correspond to $\epsilon = \epsilon_0 \cos\gamma$ and $\epsilon' = \epsilon_0 \sin\gamma$ with $\epsilon_0 = 0.28$ and $\gamma = 23°$ and the 3-axis being long principal axis. Changing $\gamma \rightarrow -120° - \gamma = -143°$ leaves the results invariant but moves the 3-axis to the short principal axis and the TPSM calculations were performed for $\epsilon = 0.22$ and $\epsilon' = -0.17$.

Fig. 6.11 displays the diagonal components of the K-distribution of the wavefunctions for various angular momentum states for the four observed bands. The lowest sequences of

basis states in Fig. 6.10 are projections from the one-quasineutron configuration at 1.307 MeV onto different values of K. As seen in Fig. 6.11, for the states I = 11/2, 15/2 19/2, ... of Band 1 the largest components are the K = 11/2 states. Decomposing these basis states into their quasineutron factors and collective factors (defined as the projections from the quasiparticle vacuum) shows that the main quasineutron component is $h_{11/2}$ with the projection of the triaxial Nilsson state along the s-axis, k = 11/2. For the I = 13/2, 17/2, 21/2, ... states of Band 3 band, the same K = 11/2 basis states appear with the largest probability. The higher energies of the I = 13/2, 17/2, 21/2, ... states compared to the I = 11/2, 15/2 19/2, as seen in Fig. 6.10, are due to a larger fraction of the collective angular momentum. This is the expected structure for the TW mode with the angular momentum of the $h_{11/2}$ quasineutron being aligned with the s-axis.

For I = 17/2, 21/2, ... of band Band 2, the dominating basis state is K = 7/2 and decomposing it into the quasineutron and collective factors shows that the most probable component is $h_{11/2}$ with the k = 7/2 projection. It has the characteristic signature partner structure, with the angular momentum of the quasineutron being tilted away from the s-axis. The reorientation of the quasineutron's angular momentum suppresses the collective E2 transitions Band 2 $\rightarrow$ Band 1 and Band 2 $\rightarrow$ Band 3, and the transitions acquire the M1 character. For the I = 15/2, 19/2, 23/2, ... of Band 4, the largest component is K = 7/2. The energies of the states are larger as compared to the 13/2, 17/2, 21/2, ..., because of the additional collective angular momentum of the wobbling motion. The similar orientation of the quasineutron's angular momentum allows enhanced E2 Band 4 $\rightarrow$ Band 2 transitions. For Band 4 $\rightarrow$ Band 3 transitions, the change of the quasineutron's angular momentum alignment with the s-axis suppresses the collective E2 radiation and generates the M1 part.

The above interpretation in terms of the leading basis states loses relevance with increasing I because of the mixing of different K states projected from the quasineutron configuration at 1.307 MeV as well from the configurations at 1.074 MeV and 1.792 MeV.

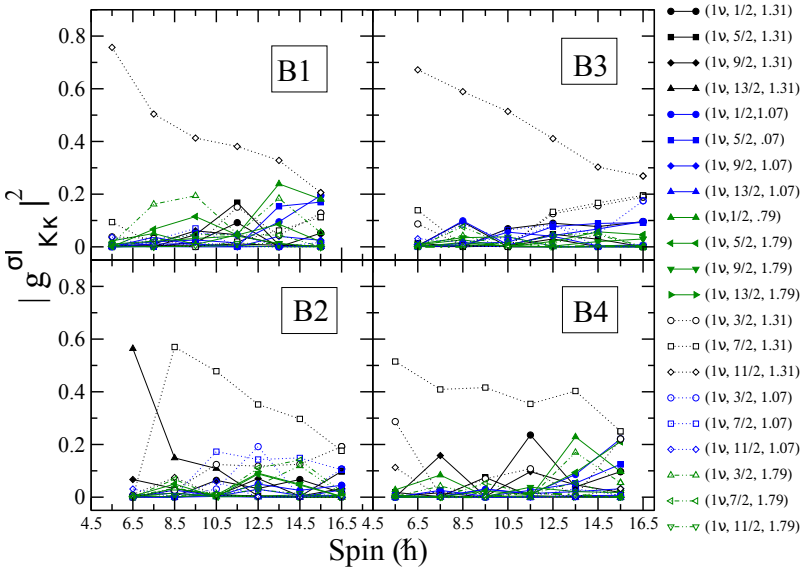

Figure 6.11: Probabilities of various projected K configurations in the orthonormal basis shown in Fig. 6.10. The curves are labelled by three quantities: quasiparticle character, K quantum number and energy of the quasiparticle state. For instance, [1,1/2,1.31] designates one quasineutron state with K= 1/2 having an intrinsic energy of 1.31 MeV. The symbols and line types agree with Fig. 6.10.

This is reflected by the decrease in the probability of the configuration at 1.307 MeV with increasing I.

The nucleus ^{105}Pd has a structure that is analogous to ^{135}Pr, where the odd $h_{11/2}$ quasineutron replaces the odd quasiproton. The latter has been studied in Refs. [5, 6, 17] using the TPSM and the PTR model. Both approaches predict that the second band with the signature 11/2, 15/2, 19/2, ... has the character of the $n = 2$ double TW excitation mode, which is in agreement with the strong E2 transition to the $n = 1$ single TW band observed in ^{135}Pr [17]. As shown in the present work, this band has a different nature in ^{105}Pd. The TPSM accounts for the different nature of these bands in ^{105}Pd and ^{135}Pr. At variance, the PTR model predicts a $n = 2$ double TW excitations for Band 4 in ^{105}Pd as well [33]. The PTR model predicts the SP band in both nuclei at twice the energy above the yrast band than observed [19, 17], while the TPSM approach reproduces the experimental energy difference quite well. The TPSM takes the anti-symmetrization between the odd nucleon and the nucleons of the collective rotor core into account, while the PTR model neglects it. This could be the reason for the discrepancy between the two models.

In summary, the multipolarities and the electromagnetic characters of the gamma transitions from the excited levels of Band 4 have been determined through the R_{DCO} and polarization measurements. The transitions connecting it with the previously known single transverse wobbling band (Band 3) are dominated by the M1 component with only weak E2 admixtures. This excludes the interpretation as a double transverse wobbling excitation, which has been suggested for the analogue band in ^{135}Pr. Instead, the band has been interpreted as a transverse wobbling excitation built on the signature partner band (Band 2). Accordingly, the inter-band $\Delta I = 1$ transitions show a large enhancement in the B(E2) rates. The TPSM calculations account well for the observed energies and ratios of the transition probabilities. Analyzing the calculated eigenstates, the doublet wobbling nature of the bands observed in ^{105}Pd has been demonstrated.

In general, the collective excitations in a triaxial nucleus are expected to appear not only based on the yrast band but also on quasiparticle excitations. The present work identified the first example of the transverse wobbling mode of a quasineutron, which is not aligned with the s-axis i.e. the wobbling partner of a SP band.

Bibliography

[1] P. Möller, R. Bengtsson B. G. Gillis, P. Olivius, T. Ichikawa, Phys. Rev. Let. **97** 162502 (2006).

[2] A. Bohr and B. R. Mottelson, *Nuclear Structure* (W. A. Benjamin, New York, 1975), Vol. II, Chap. 4.

[3] S. W. Ødegård *et al.* Phys. Rev. Lett **86**, 5866 (2001).

[4] R. Bengtsson and H. Ryde, Eur. Phys. J. A **22**, 355 (2004).

[5] S. Frauendorf and F. Dönau, Phys. Rev. C **89**, 014322 (2014).

[6] J. T. Matta *et al.* Phys. Rev. Lett. **114**, 082501 (2015).

[7] S. Nandi *et al.* Phys. Rev. Lett. **125**, 132501 (2020).

[8] S. Chakraborty *et al.*Phys. Lett. B **811**, 135854 (2020).

[9] A. Mukherjee *et al.* Phys. Rev. C **107**, 054310 (2023).

[10] D. R. Jensen *et al.* Phys. Rev. Lett. **89**, 142503 (2002).

[11] P. Bringel *et al.* Eur. Phys. J. A **24**, 167 (2005).

[12] G Schönwaßer *et al.* Phys. Lett. B **552**, 9 (2003).

[13] H Amro *et al.* Phys. Lett. B **553**, 197 (2003).

[14] D. J. Hartley *et al.* Phys. Rev. C **80**, 041304(R) (2009).

[15] S. Biswas *et al.* Eur. Phys. J. A **55**, 159 (2019).

[16] Kosai Tanabe and Kazuko Sugawara-Tanabe Phys. Rev. C **95**, 064315 (2017).

[17] N. Sensharmaa *et al.* Phys. Lett. B **792** 170 (2019).

[18] N. Sensharma *et al.* Phys. Rev. Lett. **124**, 052501 (2020).

[19] J. Timár *et al.* Phys. Rev. Lett. **122**, 062501 (2019).

[20] J. Timár *et al.* J. Phys.: Conf. Ser. **1555** 012025 (2020).

[21] K. Nomura and C. P Petrache, Phys. Rev. C **105**, 024320 (2022)

[22] F. A. Rickey, J. A. Grau, L. E. Samuelson and P. C. Simms, Phys. Rev. C **15**, 1530 (1977).

[23] A. Krämer-Flecken *et al.* Nuclear Instruments and Methods in Physics Research Section A: Accelerators, Spectrometers, Detectors and Associated Equipment **275**, 333 (1989).

[24] E. S. Macias, W. D. Ruhter, D. C. Camp and R. G. Lanier Comp. Phys. Comm. **11**, 75 (1976).

[25] J. A. Sheikh and K. Hara, Phys. Rev. Lett. **82**, 3968 (1999).

[26] S. Jehangir, G. H. Bhat, N. Rather, J. A. Sheikh and R. Palit, Phys. Rev. **C 104**, 044322 (2021).

[27] J. A. Sheikh, G. H. Bhat, Y. Sun and R. Palit, Phys. Lett. **B 688**, 305 (2010).

[28] J. Marcellino *et al.* Phys. Rev. **C 96**, 034319 (2017).

[29] P. Ring and P. Schuck, *The Nuclear Many Body Problem* (Springer-Verlag, New York), (1980).

[30] G. H. Bhat, W. A. Dar, J. A. Sheikh and Y. Sun, Phys. Rev. C **89**, 014328 (2014).

[31] G. H. Bhat, J. A. Sheikh W. A. Dar, S. Jehangir, R. Palit and P. A. Ganai, Phys. Lett. B **738**, 218 (2014).

[32] G. H. Bhat, R. N. Ali, J. A. Sheikh and R.Palit, Nucl. Phys. A **922**, 150 (2014).

[33] Q. B. Chen Private Communication

Chapter 7

Spectroscopic Studies in ^{101}Ru

The wobbling motion has been reported only in ^{105}Pd among the nuclei of A $\approx$ 100 mass region. This has been discussed in the previous chapter. In order to establish nuclear wobbling as an alternate mechanism for the generation of low spin states of nuclei of this mass region, it is essential to explore other neighbouring isotopes. In the present thesis, ^{101}Ru was selected for this search as Yamamoto et. al. had concluded that the observed band crossing frequencies were consistent with a significant triaxial rigidity, which persists into the medium-spin regime [1]. In their study, only the negative parity yrast cascade was established and thus, the primary focus of the present experiment was to search for the wobbling and SP partner bands for this negative parity band.

7.1 Experimental details and results

With this motivation the excited levels of ^{101}Ru were populated through the fusion-evaporation reaction ^{100}Mo(^{4}He,3n)^{101}Ru. The 45 MeV ^{4}He was delivered by the K-130 cyclotron at Variable Energy Cyclotron Centre, Kolkata and the enriched ^{100}Mo target was 10 mg/cm^2 thick. The γ - rays were detected by an array of 11 Compton-suppressed Clover detectors of the Indian National Gamma Array (INGA) at VECC. About 35% events of acquired

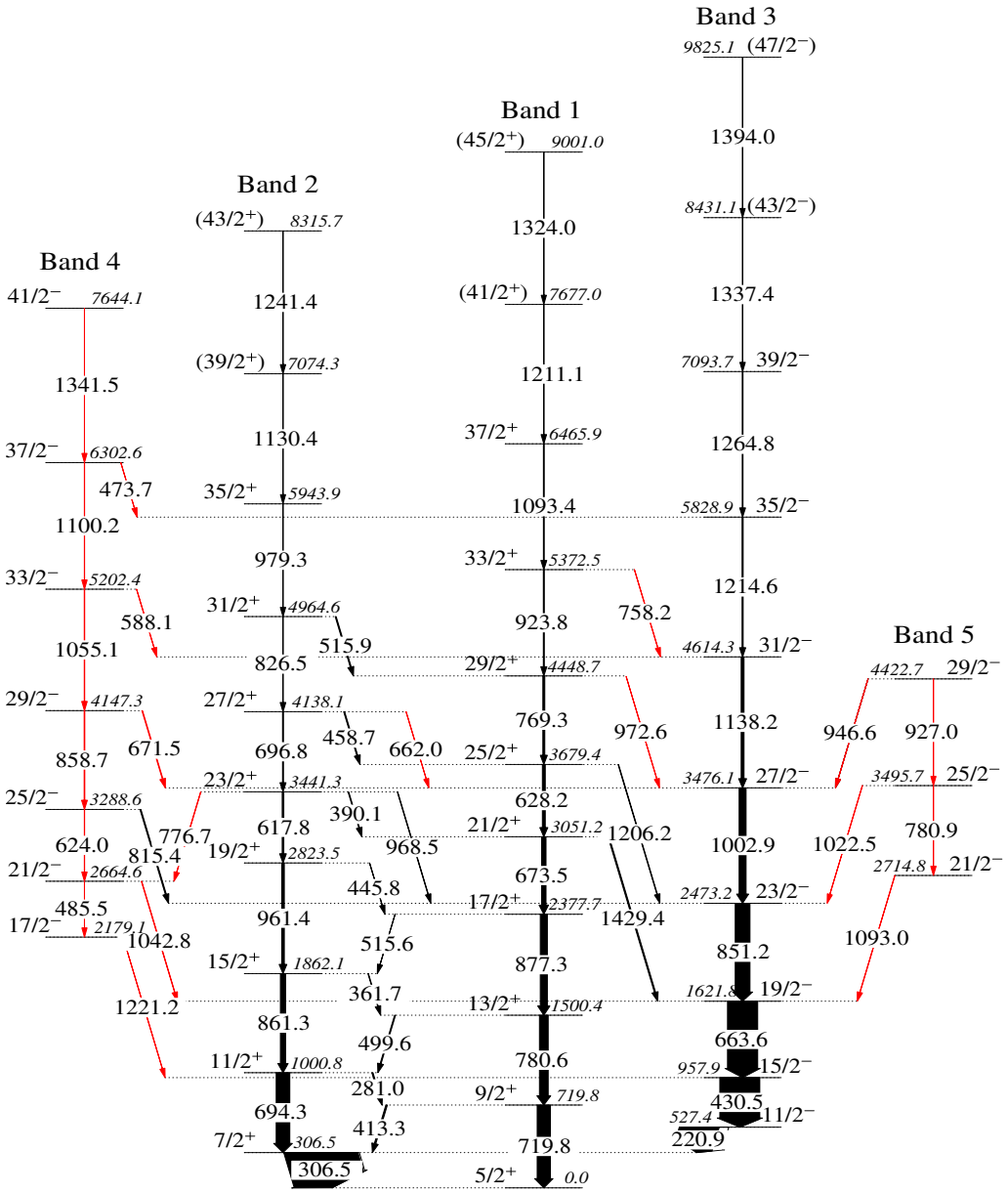

Figure 7.1: The partial level scheme of ^{101}Ru established from the present work. The level and transition energies are expressed in keV. The thicknesses of the arrows are proportional to the relative intensities of the de-exciting γ-rays. The transitions and levels marked in red are newly observed in the present data set. The high spin levels beyond 39/2 were reported in Ref. [1] but not observed in the present experiment.

data [2] were found to belong to the ^{101}Ru channel [3]. The present level scheme built from the coincidence spectra is shown in Fig. 7.1, where the newly placed transitions have been marked in red. Bands 1, 2 and 3 were reported by Yamamoto et. al. [1] and the placement of γ transitions in the level scheme has been found to be consistent with

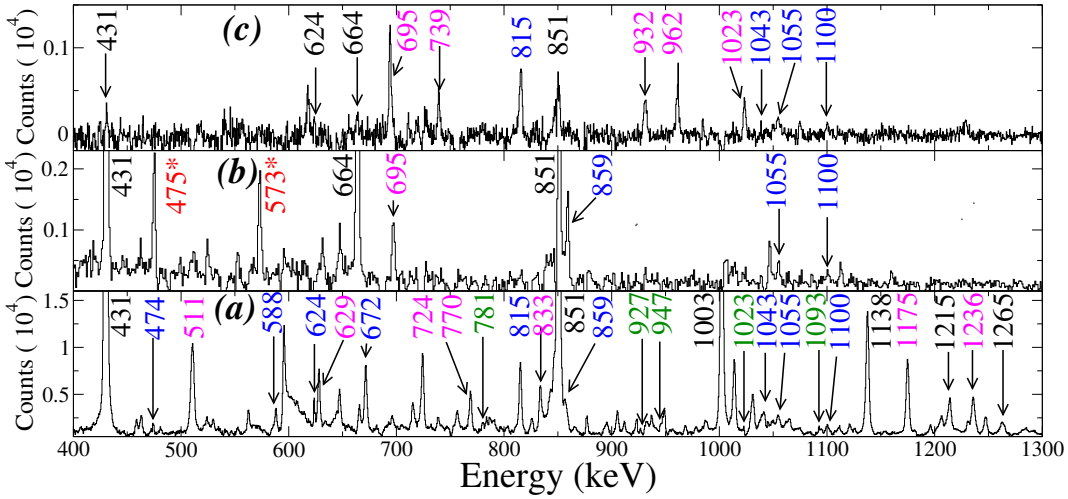

Figure 7.2: γ - γ coincidence spectra with 663.6, 815.4 and 858.7 keV gates in ^{101}Ru. The transitions marked in black, green and blue belong to Bands 1, 2 and 3 respectively, while those marked in magenta are from the other bands of ^{101}Ru, which are not shown in the current level scheme. It may be noted that the 858.7 keV gate has contamination from the strong 861 keV transition ($15/2^+ \rightarrow 11/2^+$) in positive parity sequence of ^{101}Ru. The transitions marked in red are contamination from ^{98}Mo.

the present data. The two new bands namely 4 and 5, are shown in Fig. 7.1. The gated spectrum with 664 keV γ transition is shown in Fig. 7.2(a), where the presence of an 815 keV transition can be identified. This transition was also reported in the previous work by Yamamoto et. al. [1]. The coincidence spectrum with the 815 keV gate revealed the presence of a cascade of 858.7, 1055.1 and 1100.2 keV transition as shown in Fig. 7.2(b). The transitions belonging to the negative parity non-yrast band were in turn, identified from the 858.7 keV gate (Fig. 7.2(c)). The transitions belonging to Band 3, 4 and 5 are marked in black, green and blue respectively, in this figure. It may be noted that the energies of the excited levels of Band 4 and 5 are well fixed because of the presence of the interband transitions from these bands to Band 3. Four new interband transitions namely 972.6 and 758.2 keV from Band 1 and 662.0 and 776.7 keV from Band 2, have been observed. The newly placed E1 transitions from Band 1 to Band 3 have been shown in the γ gated spectra of 923.8 and 1138.2 keV in Fig. 7.3. No E1 transitions could be observed beyond $I^\pi = 33/2^+$. This is probably due to two factors: (a) the intensity beyond I = 16 $\hbar$ falls sharply for the fusion-evaporation reactions involving the alpha beam and (b) the E1 branching for

the next $I^{\pi} = 35/2^{-}$ level will be 18 times smaller due to the $E_{\gamma}(I-(I-2))^5/E_{\gamma}(I-(I-1))^3$ dependence. The intensities of the γ-rays were estimated from the γ-gated spectra at 90° following the prescription described in Ref. [4].

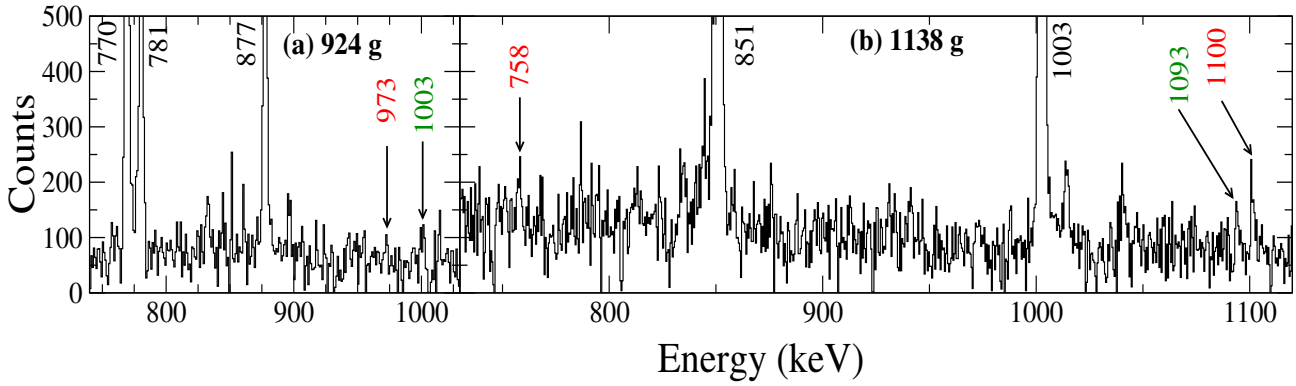

Figure 7.3: γ - γ coincidence spectra with (a) 923.8 and (b) 1138.2 keV gates in ^{101}Ru. The transitions marked in red are newly placed from the present experiment. The transitions marked in green represent previously placed transitions used for confirmation of placements of new transitions.

The spins and parities of the levels of Band 4 were unambiguously assigned through the simultaneous measurement of directional correlation from oriented states (DCO) and linear polarisation (P) of the interconnecting transitions between Bands 3 and 4. For the DCO analysis, we have used stretched E2 transitions and the attenuation coefficient for alignment was estimated by fitting the measured DCO values for the previously known pure E1 transitions of 1430 and 1206 keV between Band 1 and 3. The current measurements were validated by estimating the DCO ratio and P value for previously assigned [1] E2 (851 keV) and M1 (307 keV) transitions as shown in the two top panels of Fig. 7.4. The lower four panels show the measurements for the new interconnecting transitions. In all the cases, uncertainties in the P values did not allow the unique identification of their electromagnetic characters. However, the simultaneous measurements of the DCO ratio and P values for the 1042.8, 815.4, 671.5 and 588.1 keV indicate the $\Delta I = 1$ M1+E2 multipolarity with the mixing ratio (δ) = $2.4^{+1.4}_{-0.8}$, $2.5^{+1.5}_{-0.5}$, $0.5^{0.3}_{-0.2}$ and $0.4^{+0.5}_{-0.2}$, respectively. The corresponding χ^2 analysis (discussed in detail in Chapter 6) is shown in Fig. 7.5. Thus, the E2 mixing for 1042.8 and 815.4 is as large as 85% while the mixing is about 19%

for 671.5 and 588.1 transitions. The P measurement for the 473.7 keV transition was not possible due to inadequate statistics and the mixing ratio was estimated by comparing the experimental DCO ratio with the corresponding calculated values (using ANGCOR [5]) for different values of δ. This plot is shown in the top panel of Fig. 7.6. The small value of δ indicates the predominant M1 character for the 473.7 keV transition which is in contrast to the observed values for the other inter-band transitions.

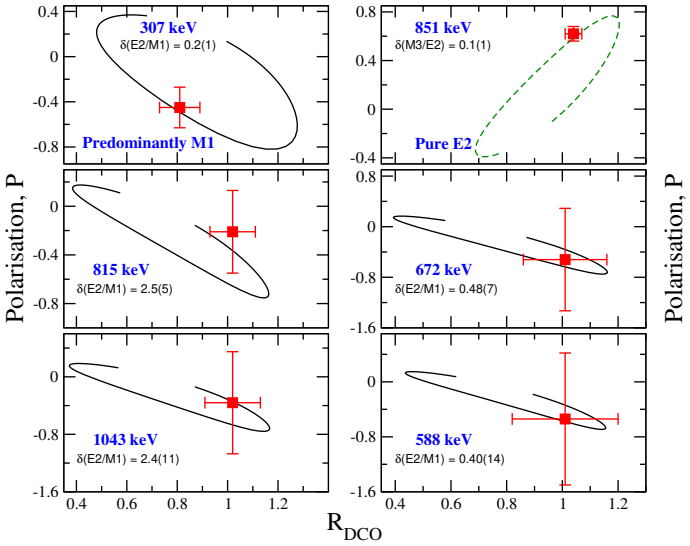

Figure 7.4: Experimental (symbol) and calculated (solid line) values of DCO ratios and linear polarization (P) for varying mixing ratios δ for transitions decaying from Band 4 to Band 3. In the top two panels, previously established magnetic dipole (M1) and electric quadrupole (E2) transitions are shown in order to validate the present measurements.

A similar small value was also obtained for the 1022.5 keV transition between Bands 2 and 1, which established I = 25/2$\hbar$ for the 3497.0 keV level (refer to Fig. 7.1). The parity of the level could be established because of the observed lineshapes for the 1023 keV transition at 40° and 125° degrees. The fitting of those lineshapes (discussed in the following paragraph) leads to an effective lifetime of 0.87(17) ps for the = 25/2$\hbar$ level. Assuming the E1 character for this 1023 keV transition and the observed retardation factor of 0.3×10^{-5} or more [6], the level lifetime is expected to be 141 ps or more. This large discrepancy establishes the M1 character of the 1023 keV transition. Thus, Band 5 is also a negative parity band which decays to Band 3 through M1 transitions. It may be noted that these measurements establish Band 5 as the signature partner (SP) band for Band 3

and Band 4 as its wobbling band. All the measured properties for the observed γ-rays have been tabulated in Table. 7.1.

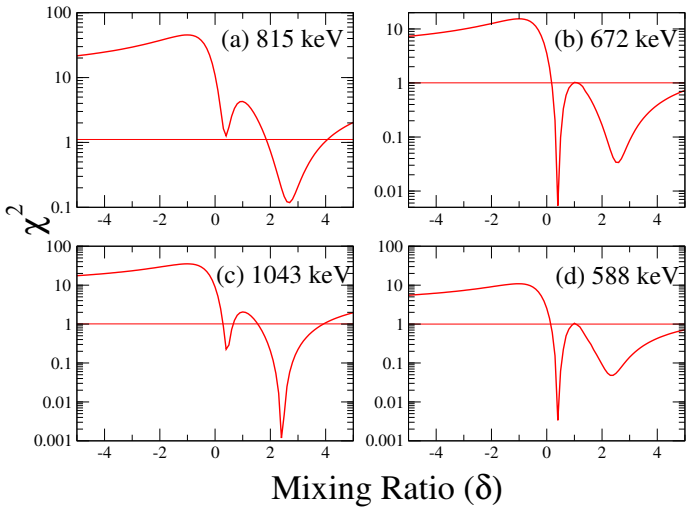

Figure 7.5: The χ^2 analysis to establish the true minima of the mixing ratio values for the transitions from Band 4 to Band 3. The horizontal lines correspond to the +1 of the minima value for determining the uncertainties.

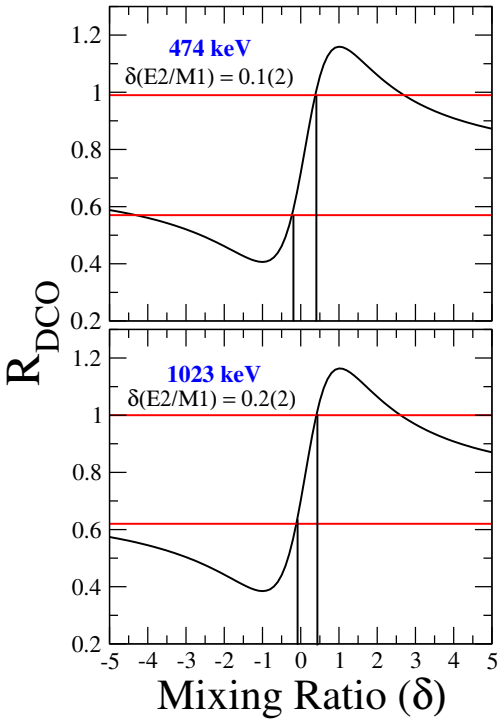

Figure 7.6: Variation of the calculated R_{DCO} as a function of mixing ratio (δ) for the ΔI = 1 transitions from Band 4 to Band 3 (i.e. 473.7 keV) and from Band 5 to Band 3 (i.e. 1022.5 keV). The horizontal lines correspond to the R_{DCO} values at 125° along with their uncertainties.

In the present data with 10 mg/cm^2 thick ^{100}Mo target, distinct lineshapes were observed

at 40° and 125° degrees for the γ-rays deexciting the levels above 29/2 for Band 1, 27/2 for Band 2 and Band 3 and 25/2 for Band 4. The lineshape analysis was carried out using the LINESHAPE package [7] along with the development reported in Ref. [8]. The details of the lineshape fitting procedure have been described in Chapter 3 (Ref. [9, 10]).

Table 7.1: Energies, relative intensities, DCO ratios using the detectors at 125° ring and the detectors at 90° rings, linear polarization, mixing ratios and deduced multipolarities of transitions of the five reported bands of ^{101}Ru. The quoted uncertainties in the intensities include statistical and fitting errors only. The systematic error due to the efficiency determination has been estimated to be around 4%.

E_{level} (keV)	E_γ (keV)	I_γ (rel.)	R_{DCO} (125°)	P	δ	Type
306.5	306.5(2)	186(3)	0.81(4)	-0.45(18)		M1+E2
527.4	220.9(4)	100(1)	0.95(7)			M2
719.8	719.8(2)	34.2(17)	1.01(4)			E2
	413.3(2)	3.72(12)	0.67(4)	-0.17(9)		M1 + E2
1000.8	694.3(2)	35.0(23)	0.99(4)	0.14(3)		E2
	281.0(2)	2.81(22)	0.71(4)	-		M1 + E2
957.9	431.1(2)	102.6(10)	1.01(2)	0.64(7)	0.0(1)	E2
1500.4	780.6(2)	22.5(17)	1.02(5)			E2
	499.6(3)	2.37(25)	0.69(5)	-0.22(20)		M1 + E2
1621.8	663.6(3)	77.9(21)	0.99(2)	0.56(10)	0.0(1)	E2
1862.1	861.3(2)	13.3(15)	0.99(4)			E2
	361.7(3)	1.31(11)	0.72(7)	-0.23(27)		M1 + E2
2179.1	1220.6(5)	0.10(2)	-	-	-	-
2377.7	877.3(3)	18.2(14)	0.98(6)			E2
	515.6(3)	1.01(17)	0.70(7)	-		M1 + E2
2473.2	851.1(3)	38.04(45)	1.04(3)	0.62(26)	0.1(1)	E2
2664.6	1042.8(4)	0.95(11)	1.02(11)	-0.36(71)	$2.4^{+1.4}_{-0.8}$	M1+E2

	485.5(6)	0.021(5)	1.01(25)	-	-	Q
2714.8	1093.0(5)	0.55(8)	0.76(16)	-	0.2(3)	D
2823.5	961.4(2)	6.7(7)	1.02(6)			E2
	445.8(3)	0.62(9)	0.62(11)			M1 + E2
3051.2	673.5(2)	11.2(9)	1.03(10)			E2
	1429.4(3)	2.97(24)	0.67(7)	0.34(11)	-	E1
3288.6	815.4(3)	2.48(21)	1.02(9)	-0.21(34)	$2.5^{+1.5}_{-0.5}$	M1+E2
	624.0(5)	0.61(16)	0.96(28)	-	-	Q
3441.3	617.8(2)	3.97(44)	0.99(8)			E2
	390.1(3)	1.8(6)	0.78(8)	-0.41(33)		M1+E2
	776.7(4)	0.7(2)				
	968.5(3)	1.1(3)				E1
3476.1	1002.6(3)	17.86(34)	1.02(4)	0.31(18)		E2
3679.4	628.2(2)	7.3(6)	0.99(5)			E2
	1206.2(4)	1.3(3)	0.70(11)	0.24(35)	-	E1
3495.7	780.9(4)	0.54(14)	1.07(21)			Q
	1022.5(4)	0.15(4)	0.81(19)		0.2(2)	D
4138.1	696.8(4)	2.2(3)	1.00(11)	0.31(47)		E2
	458.7(3)	1.7(5)	0.77(10)	-0.30(49)		M1+E2
	662.0(5)	0.23(8)				E1
4147.3	671.5(3)	1.54(17)	1.01(15)	-0.52(81)	$0.5^{0.3}_{-0.2}$	M1+E2
	858.7(4)	1.52(37)	1.05(28)	-	0.3(3)	Q
4422.7	927.0(5)	0.14(4)	-	-	-	
	946.6(6)	0.17(4)	-	-	-	
4448.7	769.3(3)	4.8(4)	1.02(7)			E2
	972.6(4)	0.27(12)				
4614.3	1137.9(4)	7.23(18)	1.02(3)	0.28(25)	0.1(2)	E2
4964.6	826.5(4)	1.3(2)	0.99(14)			E2

	515.9(3)	1.2(3)				
5202.4	588.1(4)	0.42(12)	1.01(19)	-0.59(96)	$0.4^{+0.5}_{-0.2}$	M1+E2
	1055.1(5)	0.98(24)	0.99(25)			Q
5372.5	923.8(3)	2.3(3)	1.00(12)			E2
	758.2(5)	0.28(12)				
5828.9	1214.6(4)	2.65(10)	1.01(4)	0.31(29)	0.0(2)	E2
5943.9	979.3(3)	0.5(1)	1.06(17)			E2
6302.6	473.7(4)	0.11(3)	0.78(21)	-	0.1(2)	M1+E2
	1100.2(4)	0.50(11)	1.0(24)			Q
6465.9	1093.4(4)	1.98(65)	1.03(36)			E2
7093.7	1264.8(4)	1.77(20)	0.98(15)	0.25(21)	0.0(3)	E2
7074.3	1130.4(5)	0.31(11)				E2
7644.1	1341.5(5)	0.24(10)				E2
7677.0	1211.1(4)	0.80(32)	1.03(26)			E2

The topmost transition with adequate statistics in the lineshape namely 1214.6 keV for Band 3 and 1055.1 keV for Band 4, respectively, were assumed to have 100% side feed. This led to the estimation of the effective lifetimes for the $39/2^-$ and $33/2^-$ levels of Bands 1 and 3, respectively. For the following levels, these effective lifetimes were considered as the input parameters. In this way, further lower levels were added one by one and fitted until all the line shapes for Bands 1 (three) and 3 (two) were included in the global fits where only the in-band and side feeding lifetimes were allowed to vary. This global fit for each band was simultaneously carried out for all three angles. A similar prescription was employed for the estimation of the level lifetimes of Band 1, where line shapes were observed for $I^\pi \geq 29/2^+$. For this band, the effective lifetime was estimated for I^π = 6465.9 keV level by fitting line shape for 1093.4 keV transition.

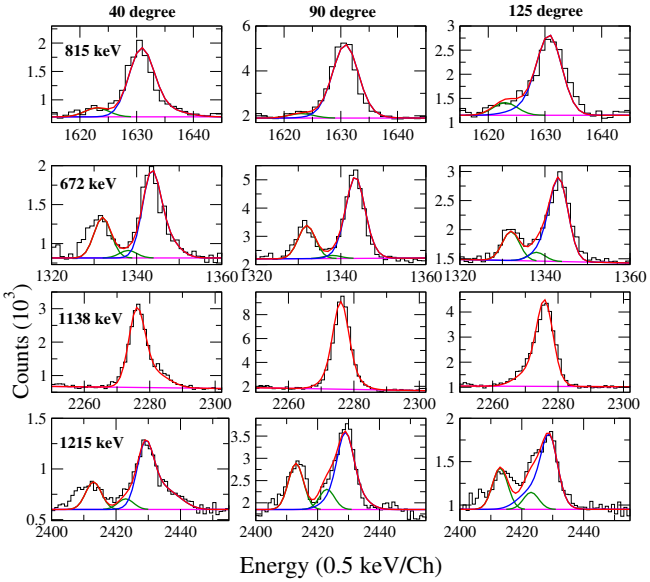

Figure 7.7: The line-shape fits for 815.4 keV, 671.5 keV of Band 4 and 1138.2 keV, 1214.6 keV transitions of Band 3 at 40°, 90° and 157° to the beam direction. The fitted Doppler broadened line shapes are drawn in blue lines while the contaminant peaks are shown in green lines. The result of the fit to the experimental data is shown in red lines.

The uncertainties in the lifetime measurements were estimated from the χ^2 behaviour in the vicinity of the minimum for this simultaneous fit. The other source of error is due to uncertainty in the estimation of the side feeding, which in turn originates due to the uncertainties in the estimation of the intensities of the top feeding and the feed out γ transitions for the level under consideration. In the present analysis, this error was estimated by finding the level lifetime for the minimum and maximum allowed values of side feeding intensity at that level. Thus, the final uncertainty on the level lifetime was calculated by adding in quadrature the uncertainties due to the fitting and side feeding intensity. The estimated values of the level lifetimes and the extracted transition rates are tabulated in Table 7.2.

Fig. 7.7 shows the experimental lineshapes observed in the 663.6 keV γ-gate at the three different angles for two in-band transitions of Band 3 (1137.9 keV and 1214.6 keV) and two inter-band transitions from Band 4 (815.4 keV and 671.5 keV) along with the corresponding fits from DSAM. The estimated level lifetime values are given in Table. 7.2. Note that, for Band 5, only the effective lifetime for the I = 25/2$^-$ level could be esti-

Table 7.2: The measured lifetimes of the levels of Bands 1, 3, 4 and 5 of ^{101}Ru and the derived transition rates.

E_{level}	τ_{level}	$B(E2)_{in}$ (e^2b^2)		$B(E2)_{out}$ (e^2b^2)		$B(M1)_{out}$ (μ^2_N) (μ^2_N)		$B(E1)_{in}$ $\times 10^{-4}$ (e^2fm^2)	
(keV)	(ps)	(Expt)	(Theo)	(Expt)	(Theo)	(Expt)	(Theo)	(Expt)	(Theo)
					Band 1				
4448.7(3)	1.07(36)	0.29(10)	-	-	-	-	-	0.37 ± 0.17	-
5829.3(2)	0.6(2)	0.22(7)	-	-	-	-	-	3.13 ± 1.38	-
6465.9(5)	0.27^u	0.19^l	-	-	-	-	-	-	
					Band 3				
3476.8(2)	0.38(9)	0.20(5)	0.20	-	-	-	-	-	-
4614.7(3)	0.18(5)	0.24(6)	0.24	-	-	-	-	-	-
5829.3(2)	0.15(4)	0.22(6)	0.18	-	-	-	-	-	-
7094.1(4)	0.18^u	0.14^l	0.18	-	-	-	-	-	-
					Band 5				
3497.0(3)	0.87^u	0.25^l	0.23	-	-	0.02^l	0.19	-	-
					Band 4				
3289.6(4)	0.86(12)	0.20(5)	0.22	0.18(5)	0.23	0.014(4)	0.14	-	-
4148.3(4)	0.40(11)	0.22(6)	0.24	0.14(4)	0.21	0.19(5)	0.17	-	-
5202.8(5)	0.28^u	0.15^l	0.22	0.17^l	0.11	0.30^l	0.22	-	-

mated. The corresponding B(E2) values for the ΔI = 2 transitions and the B(E2) and B(M1) values for the ΔI = 1 transitions have been extracted from these measured level lifetime values and tabulated in Table. 7.2. This is only the second instance [11] where the large interband B(E2) rates from a wobbled band have been extracted from the measured level lifetimes. However, it may be noted that the lifetimes were not measured for all the levels and thus, the ratios of the inter-band to intra-band transition rates have been plotted in Fig. 7.8.

For the low spin levels of $21/2^-$ and $25/2^-$, the $B(E2)_{out}$ and $B(E2)_{in}$ values are nearly equal while the $B(M1)_{out}/B(E2)_{in}$ values are small ($\approx 0.1\ \frac{\mu^2_N}{e^2b^2}$). This is the common feature for all the observed wobbled bands. However, beyond this spin, the $B(M1)_{out}/B(E2)_{in}$ values increases sharply and $B(E2)_{out}/B(E2)_{in}$ remains ≈ 1.0 till I = $33/2\hbar$ and drops suddenly to 0.33(21) for I = $37/2\hbar$ level. These features of the wobbled band of ^{101}Ru are distinct from all the other reported wobbled bands of the Segre Chart. In this regard, it may be noted that there is a band crossing in ^{101}Ru around $\hbar\omega \approx 0.55$ MeV as shown by the aligned

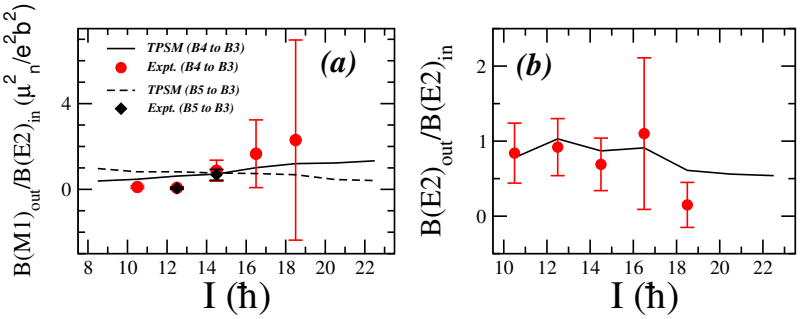

Figure 7.8: Experimental transitional rate ratios of ΔI = 1 transitions decaying from Band 5 (plotted in black) and Band 4 (plotted in red) to Band 3. The ratio for the 29/2$^-$ level for Band 5 has been extracted assuming pure M1 character for the 946.6 keV transition. The solid and dashed lines represent calculated values using the Triaxial Projected Shell Model (TPSM) approach.

angular momentum plot (i_x) for ^{101}Ru in Fig. 7.9(a). This band crossing around I = 33/2 $\hbar$ also leads to the vanishing of the wobbling energy (Fig. 7.9(b)) and causes a signature inversion between the levels of Bands 3 and 4 (Fig. 7.9(c)).

7.2 Discussion of the Results

In order to shed light on the unique wobbling behaviour of ^{101}Ru, theoretical calculations using the TPSM approach have been carried out. In the present study of ^{101}Ru, the single-particle deformed basis states were obtained by solving the triaxial Nilsson potential with $\epsilon = 0.26$ and $\epsilon' = 0.12$. This choice of the deformation parameters has been validated by comparing the calculated B(E2)$_{in}$ rates with the observed values. The calculated values are tabulated in the sixth column of Table. 7.2 and show a good agreement. The general procedure to perform the TPSM calculations can be found in refs. [12, 13, 14].

The experimental and calculated energies for the three observed bands of ^{101}Ru are compared in Fig. 7.10. It is noted that the TPSM approach reproduces the experimental energies quite well. The alignment (i_x) as a function of the rotational frequency is depicted in Fig. 7.9(a) and it is noted that the observed band-crossing, occurring about $\hbar\omega \approx 0.55$ MeV in Bands 1 and 2, is well reproduced by the TPSM calculations. This band crossing

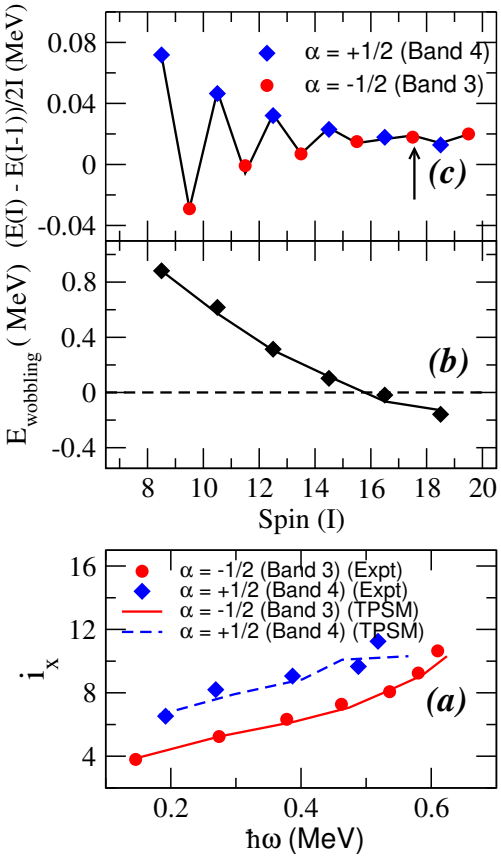

Figure 7.9: The variation of the three derived parameters with increasing spin from Bands 3 and 4 of ^{101}Ru namely, aligned angular momentum (panel (a)), wobbling energy (panel (b)) and signature spitting (panel (c)). α is the favoured signature and the arrow in Fig. 7.9(c) marks the signature inversion point in ^{101}Ru. The calculated values from TPSM, shown as solid lines in the figures, show good agreement with the experimental values.

is associated with the rotational alignment of a pair of $g_{9/2}$ quasi protons, as is evident from Fig. 7.11. In this figure, the projected energies are displayed for each configuration as a function of angular momentum before the diagonalization is performed. These unmixed band structures can cross each other and therefore provide information regarding the band crossing. It is interesting to note that the 3-qp particle band ($\nu h_{11/2} \bigotimes \pi g^2_{9/2}$) becomes nearly degenerate in energy with the one quasineutron ground-state band around I = 29/2 $\hbar$ and eventually becoming yrast beyond I = 33/2 $\hbar$. This earlier alignment for the quasi-protons in ^{101}Ru (Z = 44) compared to ^{105}Pd (Z = 46) is expected as the proton-pair occupy low $g_{9/2}$ Ω orbitals in ^{101}Ru. The proximity of the 1-qp and 3-qp configurations is observed in Fig. 7.11 for a considerable range of spin states and mixing of the two con-

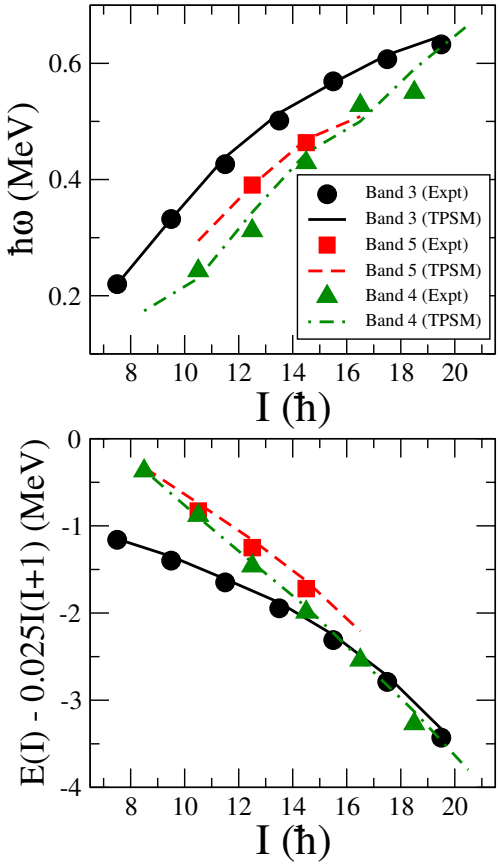

Figure 7.10: Experimental and calculated values from TPSM for the rotational frequency (upper panel) and the level energies minus the rotor contribution (lower panel) as functions of the spin I for Bands 1, 2 and 3

figurations will affect the calculated M1 and E2 transition rates for these spin states. The electric transition probabilities have been evaluated with the effective charges of 1.6 e and 0.6 e for protons and neutrons, respectively. In the calculations of the B(M1) values, the spin factors g_s^p and g_s^n were assumed to be 0.6 times the free nucleon values while g_l^p = 1.0, g_l^n = 0.0, and g_R = Z/A were used. The calculated rates are tabulated in Table. 7.2 and show a good agreement with the observed values extracted from the level lifetime measurements. The calculated ratios of the transition rates are shown by the continuous lines in Fig. 7.8. The observed variations in the $B(M1)_{out}/B(E2)_{in}$ and $B(E2)_{out}/B(E2)_{in}$ as a function of spin for all the three bands are well reproduced by the TPSM calculation.

To further probe the nature of the band structures, the quantisation axis has been chosen as the short principal axis, following the prescription given in Ref. [15]. As the wob-

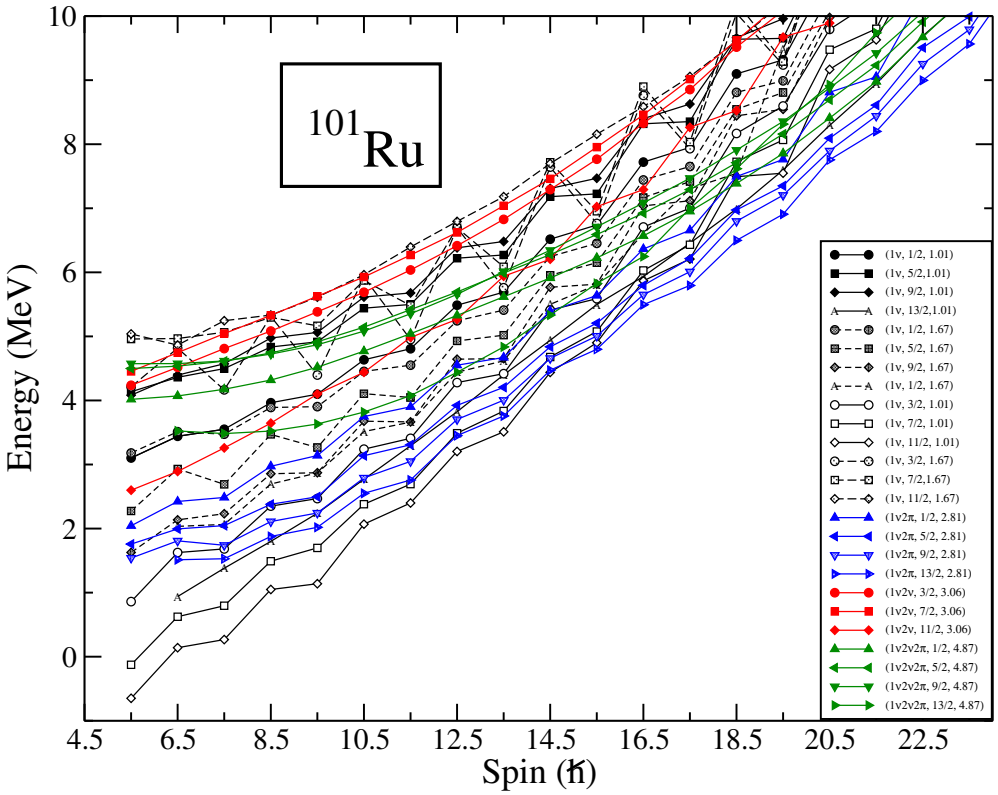

Figure 7.11: Energies of the projected K configurations for the negative parity levels, where the short axis is chosen as the quantization axis, to which the "K" refers. The curves are labelled by three quantities: quasiparticle character, K quantum number and energy of the quasiparticle state. For instance, [1,1/2,1.01] designates the one quasineutron state with K= 1/2 having intrinsic energy 1.01 MeV.

bling motion is expected to have a transverse character, the wavefunctions should have a dominant component along this axis. In Fig. 7.12, the probabilities of different projected K-configurations in the orthonormal basis are plotted for the three observed bands. It is noted from the figure that the low-spin levels of Bands 3 and 5 have K = 11/2 and 7/2 as the largest components, respectively. Decomposing these deformed basis states in terms of spherical components, the most dominant component is $1h_{11/2}$. It is evident from the figure that in Band 3, the odd-neutron is aligned towards the s-axis and Band 5 has the characteristic structure for the signature partner band where the quasiparticle angular momentum is tilted away from the short axis. The low spin levels of Band 4 are also found to originate predominantly from the angular momentum projected, K = 11/2 state. This similar orientation of the quasineutron leads to the enhancement of the B(E2) rates between

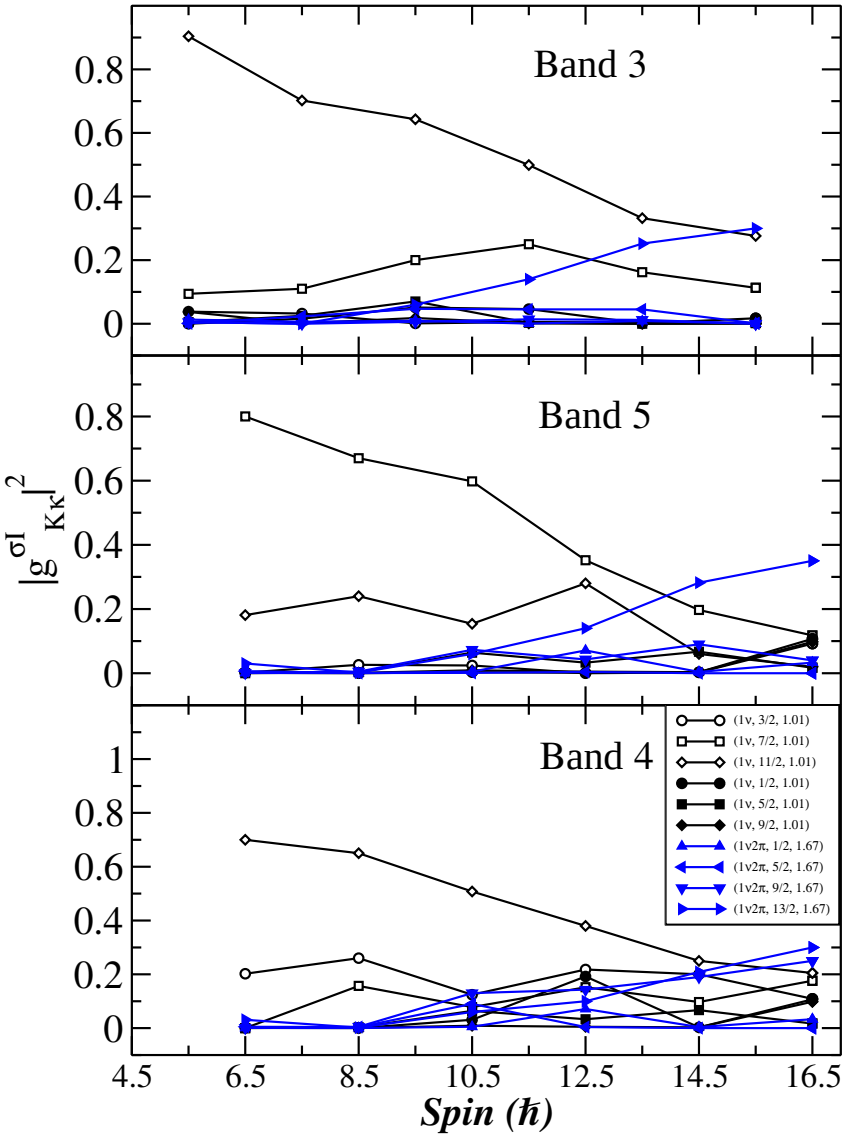

Figure 7.12: Probabilities of various projected K configurations for the negative parity levels in the orthonormal basis shown in Fig. 7.11. The curves are labelled by three quantities: quasiparticle character, K quantum number and energy of the quasiparticle state for the negative levels. For instance, [1,1/2,1.01] designates one quasineutron state with K= 1/2 having an intrinsic energy of 1.01 MeV. The symbols and line types agree with Fig.7.11.

Band 4 and 3 due to the collective contribution from the intrinsic quadrupole moment. However, after the quasiproton alignment, the high spin levels of Bands are found to originate predominantly from the angular momentum of the three-quasiparticle, which has a K = 13/2 configuration. It may be noted from Fig. 7.12 that the amplitude for the K =

11/2 configuration for Band 3 falls sharply after the band crossing. This results in the loss in the E2 collectivity and the B(E2)$_{(I \rightarrow I-1)}$ for the 37/2$^-$ level falls sharply, which leads to the predominant M1 character for the 473.7 keV transition from Band 4. Thus beyond the band crossing, the wobbling motion ceases and the high-spin states are generated by quasiparticle angular momentum and principal axis rotation. This inference has also been supported by the observation that the wobbling energy vanishes at the band crossing as seen from Fig. 7.9(b). It is interesting to note that the change in the K-component from 11/2 to 13/2 for Band 2 due to the quasi-particle alignment also reverses the favoured signature from α = -1/2 to +1/2 as the 3-qp band becomes yrast. This inversion has been observed experimentally (Fig. 7.9(c)). The calculated values from TPSM, shown as solid lines in the figures, show good agreement with the experimental values.

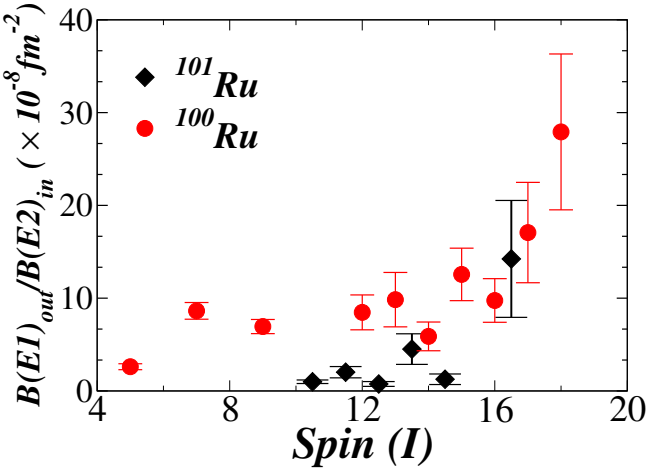

Figure 7.13: Ratios of the interband E1 and the intraband E2 transition rates from the excited levels of ^{100}Ru (red circles) and ^{101}Ru (black diamonds) as a function of spin, I.

An interesting possibility to explore is the shape of ^{101}Ru at high spins, where the nucleus exhibits the principal axis rotation. It may be noted that the ^{100}Ru core exhibits permanent octupole deformation after the rotational alignment of two $h_{11/2}$ neutrons, as established in Chapter 4. In order to explore the possibility of octupole deformation in ^{101}Ru, the values of B(E1)$_{out}$ /B(E2)$_{in}$ ratio for the four levels of Band 1 and two levels of Band 2 have been plotted in Fig. 7.13 along with the observed rates of ^{100}Ru [4]. It is interesting to note the variation of the ratio as a function of spin is very similar in both cases, which

exhibit an order of magnitude increase at high spins. The B(E1) rate extracted from the lifetime measurement for the $33/2^+$ level has been found to be 3.1(14) $\times$ 10^{-4} e^2fm^2 (as given in Table. 7.2), which is two orders of magnitude higher than the B(E1) rate of 1.8(4) $\times$ 10^{-6} e^2fm^2 estimated for the 10^+ $[h^2_{11/2}] \rightarrow 9^-$ $[h_{11/2} \bigotimes (g_{7/2}/d_{5/2})]$ transition in ^{110}Cd [16]. This large enhancement compared to the measured single particle rate establishes the presence of octupole collectivity in ^{101}Ru beyond I = 29/2.

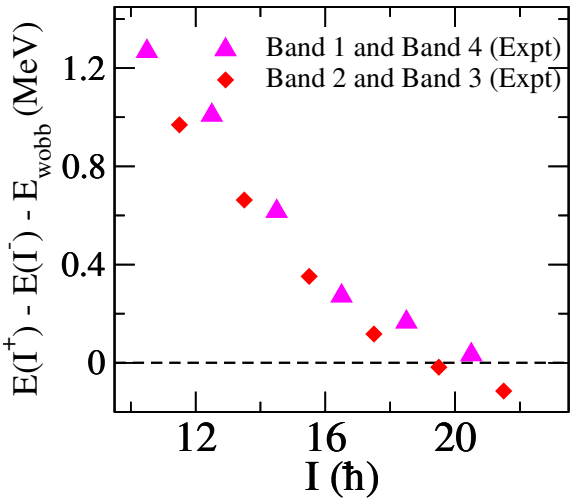

Figure 7.14: Variation of the parity splitting between the simplex partners as a function of the spin I. The wobbling energy has been subtracted from the corresponding level energies of Band 4.

It is interesting to note that in this spin domain after the $h_{11/2}$ neutron alignment, Bands 1 and 3 have been found to constitute the simplex (s) = +i sequence, while Bands 2 and 4 correspond to s = -i. In Fig. 7.14 the ΔE (= $E(I^+)$ – $E(I^-)$) values for s = $\pm$i has been plotted as a function of spin. The figure shows a significant parity splitting at low spins, which smoothly vanishes with increasing spin. This observation is typical for all the reported odd-A reflection asymmetric nuclei [17, 18, 19]. The s = $\pm$i corresponds to the rotations of the two mirror shapes in the two degenerate minima at the $\pm$ β_3^{min} separated by a finite barrier at β_3 = 0 (discussed in Chapter 2). At low spins, the barrier height is small and tunnelling between the two minima is possible, which leads to the observed parity splitting in the laboratory frame. With the increase in rotational frequency the barrier height increases due to the lowering of the pairing correlations [18]. This

leads to the eventual vanishing of the parity splitting. It is worth noting that at low spins (below I $\leq$ 25/2), the levels of Band 4 exhibit the primary feature of wobbling motion i.e large E2 transition rates in inter-band ΔI = 1 transitions while the B(M1) values are small. Subsequently, as the spin increases the simplex structure develops in ^{101}Ru and the B(M1) rates for the inter-band transitions between Band 4 and 3 were found to increase smoothly (refer to Fig. 7.8(a)) thereby indicating an admixture of principal axis rotation of a reflection asymmetric case. Beyond I = 33/2, the parity splitting among the simplex partners nearly vanishes and the 473.7 keV transition ($37/2^- \rightarrow 35/2^-$) exhibits nearly pure M1 character as seen from Fig. 7.8. Thus, in this high spin domain, the wobbling motion stops and we observe only the principal axis rotation of a reflection asymmetric triaxial shape.

Bibliography

[1] A. D. Yamamoto *et. al.* Phys. Rev. C **66**, 024302 (2002).

[2] S. Das *et. al.* Nucl. Instrum. Methods A: Accelerators, Spectrometers, Detectors and Associated Equipment **893**, 138 (2018).

[3] S. S. Nayak and G. Mukherjee, IEEE Transactions on Nuclear Science, **70**, 12, 2561-2571 (2023).

[4] Possibility of stable octupole deformation in ^{100}Ru A. Karmakar *et. al.* Phys. Rev. C **109**, 054312 (2024).

[5] E. S. Macias, W. D. Ruhter, D. C. Camp and R. G. Lanier Comp. Phys. Comm. **11**, 75 (1976).

[6] S. Chattopadhyay *et. al.* Phys. Rev. C **57**, R471(R) (1998).

[7] J. C. Wells and N. R. Johnson, Oak Ridge National Laboratory Report No. ORNL-6689, 1991.

[8] S. Das *et. al.* Nucl. Instrum. Methods A **841** (2017)

[9] F James, M Roos Comput. Phys. Commun. 10 (1975) 343-67.

[10] N. Rather *et. al.* Phys. Rev. C **89**, 061303(R) (2014)

[11] A. Görgen *et. al.* Phys. Rev. C **69**, 031301(R) (2004)

[12] G. H. Bhat, W. A. Dar, J. A. Sheikh and Y. Sun, Phys. Rev. C **89**, 014328 (2014).

[13] G. H. Bhat, J. A. Sheikh W. A. Dar, S. Jehangir, R. Palit and P. A. Ganai, Phys. Lett. B **738**, 218 (2014).

[14] G. H. Bhat, R. N. Ali, J. A. Sheikh and R. Palit, Nucl. Phys. A **922**, 150 (2014).

[15] A. Karmakar et al, Phys. Lett. B (submitted) arXiv:2403.08235.

[16] L.K. Kostov, W. Andrejtscheff, L. G. Kostova, L. Käubler, H. Prade, R. Schwengner Eur. Phys. J. A **2**, 269 (1998).

[17] S. Frauendorf. Rev. Mod. Phys. **73** 463, (2001).

[18] P. A. Butler and W. Nazarewicz, Rev. Mod. Phys. **68**, 349 (1996).

[19] I. Ahmad and P. A. Butler, Ann. Rev. Nucl. Part. Sci. **43**, 71 (1993).

Chapter 8

Summary

This thesis reports a comprehensive experimental investigation of four nuclei in A $\approx$ 100 region, namely, ^{100,101}Ru, ^{98}Mo and ^{105}Pd. The high-spin states of ^{100,101}Ru and ^{98}Mo were populated through the reactions ^{100}Mo(^{4}He, 4nγ)^{100}Ru, ^{100}Mo(^{4}He, 3nγ)^{101}Ru and ^{100}Mo(^{4}He, α2nγ)^{98}Mo using the α beam of 50 MeV and 45 MeV from K - 130 cyclotron at VECC. In another experiment at TIFR, the high spin levels of ^{105}Pd were populated through the reaction ^{98}Zr(^{13}C, 4nγ)^{105}Pd using the ^{13}C beam of 63 MeV from 14-UD BARC-TIFR Pelletron.

These four nuclei exhibit a wide range of angular momentum-generation mechanisms (discussed in detail in Chapter 2), as shown by the current experimental study and comparison with the Triaxial Projected Shell Model (TPSM) calculations. The necessary tools for carrying out the data analysis are discussed in Chapter 3. The experimental observations include:

1. The two alternate parity bands of similar moments of inertia and vanishing parity splitting for I $\geq 16\hbar$, connected by seven inter-leaved E1 transitions with enhanced B(E1) rates establishes ^{100}Ru (N = 56 nucleus) as the first stable octupole deformed nucleus in A $\approx$ 100 mass region.

2. The spin and parity determination of the previously unassigned levels ^{98}Mo (another N

= 56 nucleus) establishes two opposite parity partners. The similarity between the level structures of ^{98}Mo and ^{100}Ru establishes ^{98}Mo as another prospective nucleus for exhibiting stable octupole deformation in A $\approx$ 100 mass region.

3. In ^{105}Pd, the existence of two wobbling bands both having one phonon configuration and originating from the coupling of the wobbling phonon to the ground state band and its signature partner have been observed. The doublet one-phonon wobbling bands are, in turn, found to be the signature partner bands. These observations have been drawn from the measured ratios of the inter-band and intra-band gamma transition rates. This is the first observation of the wobbling mode of a quasineutron excitation.

4. Two new bands were identified in ^{101}Ru which are the wobbling and signature partner to the yrast negative parity band, which establishes the wobbling mode in ^{101}Ru. The wobbling motion has been found to evolve smoothly to a one-dimensional rotation of a triaxial shape at high spins. The simplex symmetry at high spins in ^{101}Ru seems to indicate a reflection asymmetric triaxial shape. This is a novel observation.

Based on this thesis work, the following future directions of research may be pursued:

1. To establish ^{98}Mo as a stable octupole deformed nuclei, an order of magnitude larger dataset is essential in order to extend the level scheme to higher spins and observe the elusive weak E1 transitions between the energy levels of the opposite parity partners. This data set can be collected using the same reaction but with a larger array of 30 Clover detectors and a beam time spanning over 10 days.

2. The first evidence of stable octupole deformation outside of the Lanthanide and Actinide regions has been established in the current work. However, additional study in the mass $\approx$ 100 region is required. Another nucleus worth studying is ^{102}Pd, which also has two pairs of alternate parity bands and the same neutron number as ^{98}Mo and ^{100}Ru.

3. Two nuclei in this mass region, namely ^{101}Ru (N = 57) and ^{105}Pd (N = 59) have been found to exhibit the wobbling motion. The other odd mass isotopes of these nuclei i.e. ^{103}Ru (N = 59) and ^{103}Pd (N = 57) can be investigated in order to establish this mass

region as another island for wobbling excitations.

4. The search for the interleaved E1 transitions at high spin levels in ^{101}Ru and ^{103}Pd may be carried out in order to establish the reflection asymmetric shape for these triaxial nuclei. Thus, they may be the first candidates to observe the rotation of heart-shaped nuclei of the Segre Chart.

5. In the present thesis, multiple E3 transitions have been identified in ^{98}Mo and ^{100}Ru. It will be interesting to measure these level lifetimes through the method of fast coincidence and explore the evolution of octupole collectivity at low spins in A $\approx$ 100 mass region.

This thesis work reports the first evidences of exotic shapes in A $\approx$ 100 mass region due to the presence of the $h_{11/2}$ intruder orbital. Further experimental investigations using a larger INGA array are necessary to explore the shapes of the neutron-rich isotopes of this mass region.